Studies of non-hydrodynamic processes in ICF implosions on OMEGA and the National Ignition Facility

by

Hans G. Rinderknecht

A.B. Physics, Princeton University (2008)

Submitted to the Department of Physics
in partial fulfillment of the requirements for the degree of

Doctor of Philosophy

at the

MASSACHUSETTS INSTITUTE OF TECHNOLOGY

June 2015

Author ..... Signature redacted
.....
Department of Physics
February 20, 2015

Certified by... Signature redacted
.....
Richard D. Petrasso
Division Head, High Energy Density Physics
Thesis Supervisor

Certified by.. Signature redacted
.....
Miklos Porkolab
Professor of Physics
Thesis Co-Supervisor

Signature redacted

Accepted by .....
.....
Krishna Rajagopal
Professor of Physics and MacVicar Faculty Fellow
Chairman, Department Committee on Education

Studies of non-hydrodynamic processes in ICF implosions on OMEGA and the National Ignition Facility

by

Hans G. Rinderknecht

Submitted to the Department of Physics
on February 20, 2015, in partial fulfillment of the
requirements for the degree of
Doctor of Philosophy

Abstract

Ion kinetic effects are expected to modify plasma dynamics when ion mean-free-paths and collision-times become comparable to the scale sizes of the plasma. Such conditions arise during the shock-convergence phase of inertial confinement fusion (ICF) implosions, when they may modify the compression and ignition of the fuel from the evolution predicted by main-line hydrodynamic simulations. Kinetic plasma dynamics relevant to ICF implosions have been studied experimentally using strongly-shocked ICF implosions containing multiple ion species, and diagnosed using both new and established nuclear diagnostics and techniques.

Implosions of deuterated plastic shells filled with equivalent-mass-density mixtures of deuterium and ^{3}He gas have demonstrated for the first time ion diffusive mixing of the fuel and shell material through observations of the D^{3}He-proton and DD-neutron yields. Implosions with initially-separated populations of D in the shell and ^{3}He in the gas produced D^{3}He-fusion from the mixed region on par with implosions filled with equimolar D^{3}He fuel and an order of magnitude larger than is produced by hydrodynamic models of fuel/shell mix. An extensive survey of kinetic mix- and yield-generation mechanisms and their signatures in nuclear diagnostics establishes ion diffusion as the best candidate to explain these observations.

A series of shock-driven implosions of D^{3}He-gas filled glass shells has demonstrated two signatures of significant ion kinetic plasma effects for the first time: ion thermal decoupling and ion species separation. In low-initial gas density implosions, for which the thermal equilibration times were much longer than the burn duration, the burn-averaged ion temperatures were observed to be anomalously invariant with ion species fraction. This behavior has been shown to signify thermal decoupling of the D and ^{3}He ion species between the shock- and fusion-phases. Comprehensive nuclear diagnostic information has been used to infer the burn-averaged deuterium fraction, which was reduced from the expectations of hydrodynamic simulations, the first direct measurement of species separation in an ICF implosion. When corrected for these effects, simulations agreed better with the observed anomalously low nuclear yields.

These results have demonstrated the significant modification of ICF-relevant shocked plasmas by kinetic plasma dynamics, motivating further experimental and theoretical investigation of these highly dynamic and poorly understood regimes.

Thesis Supervisor: Richard D. Petrasso
Title: Division Head, High Energy Density Physics

Thesis Co-Supervisor: Miklos Porkolab
Title: Professor of Physics

Acknowledgments

"The ocean takes care of each wave till it gets to shore. You need more help than you know."
— Rumi

I first came to MIT with the intention of working on magnetic confinement research, but a fifteen minute conversation with Dr. Rich Petrasso changed all that. Rich's unstoppable enthusiasm and energy were and are infectious, and I thank him first and foremost for his dedication to helping me and all of us in the High Energy Density Physics division to pursue scientific research of the highest possible quality. All the scientists in the HEDP division were critical partners in the success of this work. I thank Dr. Johan Frenje for his guidance and perspective, especially during my months of research at Livermore. Dr. Chikang Li provided steadfast support for my experiments at the Laboratory for Laser Energetics and invaluable commentary on my interpretation of the data. Dr. Fredrick Séguin developed most of the diagnostic methods and experimental techniques used throughout this work, and his unparalleled precision was extremely valuable to me in developing new techniques. Lastly, I thank Dr. Maria Gatu Johnson for her uncountable hours of support for my research 'in the trenches' at MIT, LLE, and LLNL — in particular for her contributions to the PTOF project — and for always demonstrating how to perform exceptional science.

It was a pleasure and an honor for me to work with my fellow graduate students in the HEDP division. I cannot count the conversations I have had with Dr. Mike Rosenberg and (soon-to-be) Dr. Alex Zylstra during the past seven years, or the number of experiments, presentations, and manuscripts we have collaborated on: none of this work would have succeeded without your innumerable contributions. Dr. Dan Casey, Dr. Mario Manuel, and Dr. Nareg Sinenian all provided plentiful support and guidance for developing my experiments, and frequently pitched in to help make sure they were a success, both in the lab at MIT and at OMEGA. Thanks also to Hong Sio, Caleb Waugh and Brandon Lahmann, who I am sure will continue to discover great things.

On a practical level, I owe a huge debt of gratitude to the work of our research technicians: Jocelyn Schaeffer, Irina Cashen, Bob Frankel, and Ernie Doeg. Each OMEGA shot-day generated over 100 pieces of CR-39, and every piece passed through their lab to be etched and scanned (often several times) by one of them. Thanks also to Eric Gentry and Jimmy Rohas-Herrera, two MIT undergraduates with whom I worked extensively in the lab at MIT.

Most of the experimental work in this thesis was performed on the OMEGA laser at the Laboratory for Laser Energetics at the University of Rochester in New York. I thank Dr. Robert McCrory, Director of LLE, and all of the scientists at LLE for the extensive support they have shown me and all my fellow researchers in HEDP at MIT. Shot time on the OMEGA laser was primarily provided through the NLUF program and was crucial to performing this research. In particular, I thank Dr. Vladimir Glebov and Dr. Christian Stoeckl for their expertise on nuclear bang-time diagnostics and CVD-diamond detectors; Dr. Fred Marshall and Nicholas Whiting for support with x-ray diagnostics; Dr. Jacques Delettrez for extensive simulation support; Dr. Radha

Bahukutumbi for consultation on secondary yield analysis; Jason Magoon and Tony Agliata for the MagPTOF engineering design; Milt Shoup III for support of PTOF and MagPTOF engineering; Michelle McCluskey and Joe Katz for continual diagnostics support; Dr. David Meyerhofer for comprehensive feedback and consultation on my manuscripts; and especially Dr. Craig Sangster for extensive support of this experimental research, in particular for providing two additional shots in the thin-CD campaign that demonstrated that the surprising yield results were not a fluke and lead directly to my first PRL.

From 2011 to 2013 I spent a great deal of time at Lawrence Livermore National Laboratory, collaborating on the National Ignition Campaign and supporting the implementation of PTOF and design of MagPTOF. I would like to thank Dr. Andy Mackinnon for hosting me at the lab during that time, Dr. Nino Landen for frequently providing opportunities to present my research and excellent feedback on the research itself, and Dr. Rip Collins for always asking interesting questions. I was lucky to work with Dr. Peter Amendt, who not only provided simulations for many of the studies in this thesis but also helped develop the theoretical underpinnings for the ion diffusion discussions. Thanks also to Dr. Claudio Bellei and Dr. Scott Wilks for many valuable discussions on kinetic physics and simulation methods. Dr. Andy MacPhee contributed a significant amount of work on the initial implementation of PTOF. Dr. Ryan Rygg helped me develop the PTOF diagnostic and analysis methods in relationship to other experimental observables, and helped develop the early stages of the MagPTOF conceptual design. Joe Kimbrough and Francisco Barbosa have worked tirelessly to keep the PTOF system documented and in good working order, and Shannon Ayers led the Livermore contributions to the MagPTOF project. Most importantly, through thick and thin Dr. Joe Kilkenny has been a tireless advocate for these diagnostics: thank you for giving us the chance to get it right and for pointing us in directions that proved so fruitful.

Two theorists at Los Alamos National Laboratories were involved in interpreting the results of these experiments. Many thanks to Dr. Nels Hoffman for bringing ion diffusion to my attention as a possible mix mechanism, and for bringing his reduced ion kinetic simulations to bear on this experimental data. Thanks also to Dr. Grisha Kagan for several valuable discussions.

I would like to express my deep thanks to my co-supervisor and thesis reader Dr. Miklos Porkolab, and to the members of my thesis committee, Dr. Earl Marmar and Dr. Gunther Roland. Their many suggestions and insightful questions contributed greatly to the quality of this thesis.

Graduate school is a tough time, but as a Graduate Resident Tutor at Simmons Hall, I certainly had the best neighbors. To the Simmons housemasters Dr. John and Ellen Essigman and the assistant housemaster Dr. Steve Hall, thank you for your support and for many delicious evenings. Thank you to my fellow Simmons GRTs both for many memorable and fun times and for being a GRT for me when I needed one. Thanks also to Josh Gonzales for making everyone's life better. I'm sure we will never live anywhere a quarter as interesting or half as friendly.

I would not have completed this PhD without the support of my friends and family, which they gave prolifically regardless of how well they understand my papers. Thanks Tim, for music, chess, and reminding me I'm a human; Jakob, for brewing expertise, word selection advice and a role model for rigor; Luke, for more music, fine consumables and optimism; and Zac, for good books and better conversations. Phil and Cesca, thank you for your love and appreciation, and for proofreading this entire thesis! I look forward to yet more wonderful times together. Thank you to my mother and father: your love for me and each other never ceases to amaze me. And finally, to Mariah, for everything you do that nobody else can, and nobody else knows to. Like Rumi says, we are the universe in ecstatic motion — dancing and dancing and dancing.

Contents

List of Publications

This dissertation is based on several peer-reviewed journal publications and manuscripts to be submitted for publication:

1. H. G. Rinderknecht, M. G. Johnson, A. B. Zylstra *et al.*, "A novel particle time of flight diagnostic for measurements of shock- and compression-bang times in D^3He and DT implosions at the NIF," Review of Scientific Instruments, **83**(10), 10D902 (2012)

2. H. G. Rinderknecht, H. Sio, C. K. Li *et al.*, "First Observations of Nonhydrodynamic Mix at the Fuel-Shell Interface in Shock-Driven Inertial Confinement Implosions," Physical Review Letters, **112**, 135001 (2014)

3. H. G. Rinderknecht, H. Sio, C. K. Li *et al.*, "Kinetic mix mechanisms in shock-driven inertial confinement fusion implosions," Physics of Plasmas, **21**(5), 056311 (2014)

4. H. G. Rinderknecht, H. Sio, J. A. Frenje *et al.*, "A magnetic particle time-of-flight (MagPTOF) diagnostic for measurements of shock- and compression-bang time at the NIF (invited)," Review of Scientific Instruments, **85**(11), 11D901 (2014)

5. H. G. Rinderknecht, M. J. Rosenberg, C. K. Li *et al.*, "Ion thermal decoupling and species separation in shock-driven implosions," Physical Review Letters, **114**, 025001 (2015)

6. H. G. Rinderknecht, M. J. Rosenberg, A. B. Zylstra *et al.*, "Using relative secondary DT-neutron and D^3He-proton yields to evaluate fuel ρR, electron temperature, and mix in deuterium-filled implosions at the NIF," to be submitted to Physics of Plasmas (2015)

7. H. G. Rinderknecht, J. Rojas-Herrera, A. B. Zylstra *et al.*, "Impact of x-ray dose on track formation for CR-39-based proton spectrometers," to be submitted to Review of Scientific Instruments (2015)

8. H. G. Rinderknecht, M. J. Rosenberg, C. K. Li *et al.*, "Measurements of species separation and reduced compression in shock-driven implosions," to be submitted to Physics of Plasmas (2015)

During the course of this work, the author contributed as a coauthor to 42 peer-reviewed journal publications.

List of Figures

List of Tables

List of Acronyms

AFM	Atomic Force Microscopy
ALE	Arbitrary Lagrangian-Eulerian simulation framework
BT	Bang Time
CBET	Cross Beam Energy Transfer
CCB5	Configuration Control Board (NIF committee)
CCMS	Cable-Chain Management System for PTOF
CD	Deuterated plastic
CR	Convergence ratio
ConA	Convergent Ablator backlit-radiography experimental platform (NIF)
CPS	Charged Particle Spectrometer (OMEGA)
CVD	Chemical Vapor Deposition technique to make diamond wafers
D^3He	Deuterium-helium 3 fuel
DIM	Diagnostic Instrument Manipulator (NIF)
DIME	Defect Induced Mix Experiments
DISC	DIM Imaging Streak Camera (NIF)
DPP	Distributed Phase Plates
DSR	Down-Scattered Ratio
DT	Deuterium-Tritium fuel
EOS	Equation of State
ExplPush	Exploding Pusher campaign (NIF)
FABS	Full-aperture backscatter stations (OMEGA)
FFLEX	Filter-Fluorescer Diagnostic for high-energy x-ray spectra (NIF)
FWHM	Full-Width at Half Maximum of a peak
GCD	Gas Cherenkov Detector for gammas (OMEGA)
GRH	Gamma Reaction History diagnostic (NIF)
GXD	Time-Gated X-ray Detector (NIF)
HDC	High Density Carbon
HED	High Energy Density
HGXD	Hardened Gated X-ray Detector (NIF)
hGXI	Hardened Gated X-ray Imager (NIF)
ICF	Inertial Confinement Fusion
IDEP	Indirect-drive Exploding Pusher (NIF)
IRF	Instrument Response Funciton
ITFX	Ignition Threshold Factor - eXperimental
KH	Kelvin-Helmholtz instability
LANL	Los Alamos National Laboratory
LEH	Laser Entrance Hole of a hohlraum

LEIA	Linear Electrostatic Ion Accelerator for diagnostic development (MIT)
LLE	Laboratory for Laser Energetics
LLNL	Lawrence Livermore National Laboratory
LPI	Laser-Plasma Interactions
MagPTOF	Magnetic Particle Time of Flight diagnostic
MCP	Micro-channel plate
MIT	Massachusetts Institute of Technology
MRS	Magnetic Recoil Spectrometer for neutrons
multiPTD	Multiple Particle Temporal Diagnostic (OMEGA)
NIC	National Ignition Campaign
NIF	National Ignition Facility
NLUF	National Laser Users Facility program for granting OMEGA shot time
NTD	Neutron Temporal Diagnostic (OMEGA)
nTOF	neutron Time of Flight detectors
NVH	Near Vacuum Hohlraum
PCIS	Proton/Penumbral Core Imaging System (OMEGA)
PD	Photodiode
PDD	Polar Direct Drive
PIC	Particle In Cell kinetic simulation technique
PMT	Photomultiplier Tube
PTD	Proton Temporal Diagnostic (OMEGA)
PTOF	Particle Time of Flight diagnostic
RIK	Reduced Ion Kinetic models incorporated into hydrodynamic simulations
RM	Richtmyer-Meshkov instability
RMS	Root mean square
RS	Responsible Scientist (NIF)
RT	Rayleigh-Taylor instability
SG	Super-Gaussian
SPBT	South-Pole Bang-time diagnostic for x-rays (NIF)
SPIDER	Streaked Polar Instrumentation for Diagnosing Energetic Radiation (NIF)
SRC	Solid Radiochemistry
SSD	Smoothing by Spectral Dispersion
SymCap	Symmetry Capsule experimental platform (NIF)
TCC	Target Chamber Center
TDR	Time-Domain Reflectometry
TIM	Ten-Inch Manipulators diagnostic platform (OMEGA)
VISAR	Velocity Interferometer System for Any Reflector
WRF	Wedge Range Filter compact proton spectrometer
XRFC	X-ray Framing Camera (OMEGA)
YOC	Yield-over-clean (observed yield divided by simulated yield)
YOCn	Yield-over-clean normalized

1

Introduction

This thesis experimentally explores the impact of kinetic physics on the evolution of high-energy-density (HED) plasmas, in particular those relevant for inertial confinement fusion (ICF) studies. Such HED plasmas have been studied both theoretically and in the laboratory for decades, because they show promise as one path towards attaining controlled fusion and can provide unique insight into astrophysical phenomena. Because of the small scales (~100 μm), short timescales (~1 ns), and extremely dynamic nature of these plasmas, computational simulations are extensively used to design and understand the results of experiments. These simulations are nearly all based on hydrodynamic theory, which presumes the plasma evolves as a fluid. More specifically, hydrodynamic codes assume that the ions and electrons in the plasma are locally collisional and self-thermalized. If this is true, the evolution of the plasma can be determined completely from the local pressure, density and temperature of the fluids, the relationship between these three properties (called the *equation of state*), and any energy or pressure source terms. Kinetic physics refers to conditions in which the hydrodynamic assumption breaks down. When the dynamical timescales are shorter than the time it takes for the particles to thermalize, or when the size of the plasma is smaller than the range of a particle, the hydrodynamic quantities of pressure and temperature are no longer well defined. Additionally, most experiments include multiple ion species (for example, a mixture of deuterium and tritium is the most common fuel) and the relative motion of these species is not accounted for in hydrodynamic simulations. In such situations, the experimental results will deviate from the hydrodynamic predictions.

The National Ignition Facility (NIF) has recently performed implosions that approach fusion ignition. However these experiments do not perform as well as predicted by hydrodynamic simulations: the final pressure in the fusing plasma is less than half of the predicted value. A possible partial explanation for this discrepancy is that kinetic physics affects the evolution of the implosion. In the standard ignition design, a strong shock transits the low-density (~0.3 mg/cc) central plasma of the target. The plasma behind this shock has a high temperature and a low density: conditions that are a prerequisite for kinetic behavior. In particular, the mean-free-path of ions in this plasma is predicted to be comparable to the size of the plasma. Kinetic dynamics during this phase of the implosion would modify the initial conditions for the subsequent fuel compression and stagnation. In addition, recent theory predicts that the strong pressure, temperature, and electric potential gradients in the implosion cause diffusive flow between the ion species, leading to species separation. Both of these effects might play a role in the discrepancies between the experiments and hydrodynamic simulations.

The research presented in this thesis examines the kinetic dynamics of plasmas with multiple ion species. The contributions of this work include both the development of new nuclear bang-time diagnostics, and the experimental demonstration that ion diffusion and ion thermal decoupling,

two ion kinetic effects, significantly perturb the evolution of ICF-relevant plasmas.

In support of this research and the broader ICF effort, two diagnostic instruments were designed and implemented at the NIF to look for signatures of kinetic effects by measuring the time of peak nuclear emission ("bang time"). By using multiple fusion products, the particle time-of-flight (PTOF) diagnostic measures both the shock-bang time, which is associated with the rebounding strong shock from the center of the implosion, and the compression-bang time, which occurs near peak convergence of the implosion. The time difference between these two values is expected to be sensitive to kinetic physics that affect the dynamics of the shock propagation. The PTOF has added significant capability to the NIF diagnostic suite, as it is the only diagnostic capable of measuring the shock-bang time using D^{3}He-protons and the compression-bang time using DD-neutrons at yields below 10^{13}. An upgrade (MagPTOF) is currently being implemented to measure the shock- and compression-bang times on experiments with large x-ray backgrounds. The design, implementation, analysis procedure, and resulting data from the PTOF diagnostic, and the design of the MagPTOF diagnostic, are presented in Chapter 2, and resulted in References [1] and [2].

Experiments studying the effects of kinetic physics relevant to the shock-phase of ICF implosions were performed at the OMEGA laser. The first series of experiments studied ion diffusion by imploding targets with initially separated fusion reactants: deuterated plastic shells filled with helium-3 gas. These shock-driven implosions generated D-^{3}He-fusion yields at levels suggestive of full atomic mix of the deuterium into the ^{3}He fuel, and an order of magnitude greater than predicted by hydrodynamic models of fuel-shell mix. Of several kinetic mechanisms investigated, ion diffusion was found to produce sufficient fuel-shell mix in these experiments to explain the observed data. The findings, which demonstrate clear evidence of ion diffusion playing a significant role in an ICF-relevant plasma, are presented in Chapter 3, and resulted in References [3] and [4]. A second series of experiments investigated the impact of kinetic effects in a multiple-species fuel by imploding shock-driven targets containing various ratios of deuterium to ^{3}He gas at either high (3.3 mg/cc) or low (0.4 mg/cc) initial gas density. Comprehensive nuclear diagnostic information showed anomalous trends compared to the hydrodynamic predictions as the D:^{3}He ratio was varied. The anomalous observations were shown to be signatures of two multiple-ion kinetic effects — thermal decoupling of the deuterium and ^{3}He populations in the low density implosions, and separation of the ion species in the high density implosions. These findings are presented in Chapter 4 and resulted in Reference [5].

This chapter introduces the necessary background for the new research presented in the remainder of this thesis. Section 1.1 provides a brief summary of nuclear fusion, the theory of ICF, the shock-driven implosions used in the experimental campaigns, and the ICF facilities used for the experiments. Section 1.2 presents an overview of hydrodynamic theory as implemented in the simulation codes and some relevant kinetic extensions to hydrodynamics that have been previously proposed. Section 1.3 introduces the nuclear diagnostic techniques and instruments that were used extensively to obtain the experimental data presented in this work. Finally, Section 1.4 presents an overview for the remainder of this thesis.

1.1 Inertial Confinement Fusion

Since the discovery in the early 20th century that thermonuclear fusion provides the power source for the stars, scientists have dreamed of capturing fusion in laboratories and power-plants on Earth. ICF is one approach toward obtaining net energy gain from thermonuclear fusion reactions. The research presented in this thesis uses and develops the experimental techniques of ICF to explore the physics of HED plasmas relevant to ICF applications.

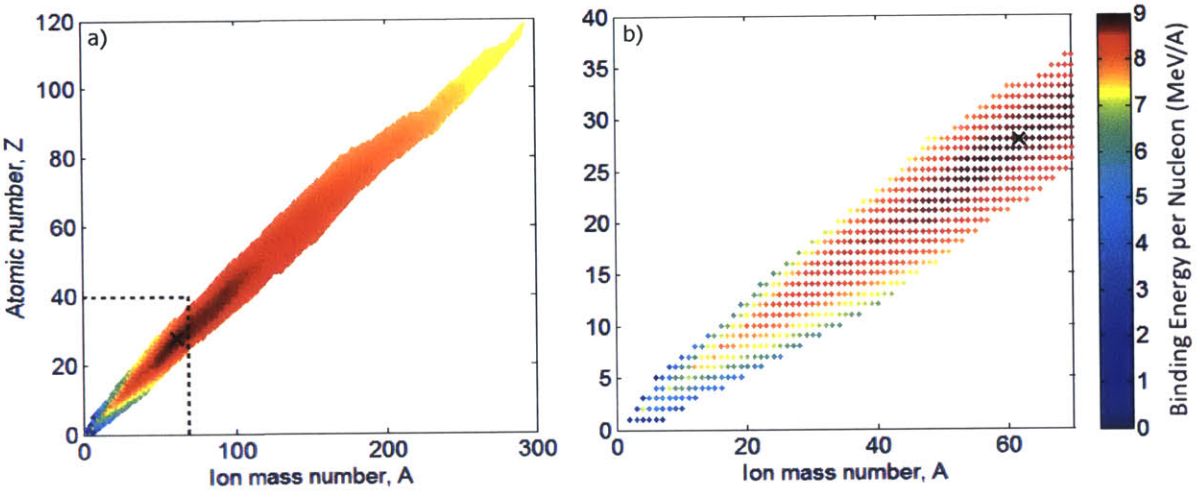

Figure 1.1. a) Binding energy per nucleon (MeV/A) for all stable nuclei as a function of atomic number (Z) and ion mass number (A). Iron ($^{62}_{26}$Fe, indicated with a black X) has the highest binding energy per nucleon, 8.7945 MeV/A. b) Zoom in on the mass range A = 0–70, Z = 0–40. Data taken from Reference [10].

1.1.1 Nuclear fusion

The groundwork for the discovery of nuclear fusion was laid by Einstein's derivation of the mass-energy equivalence relation, $E = mc^2$ in 1905.[6] This famous relation implies that in nuclear reactions, if the mass of the products is less (or greater) than the mass of the reactants, this difference must be made up by a release (or absorption) of an equivalent amount of energy. By comparing the masses of ions as measured by Aston, Eddington inferred in 1920 that the energy released by the fusion of light nuclei would provide a sufficient source of energy for the sun and other stars.[7] Building on calculations of the rate of nuclear fusion at stellar temperatures pioneered by Atkinson and Houtermans,[8] Bethe later developed the theory of stellar nucleosynthesis in 1939.[9]

The difference between the ion mass and the sum of the rest masses of its component nucleons is proportional to the binding energy, B:

$$B = (Zm_P + (A - Z)m_n - m_i)c^2, \tag{1.1}$$

where Z and A are the atomic number and mass number, respectively; m_p, m_n, and m_i are the rest masses of the proton, neutron, and ion, respectively; and c is the speed of light. In general, B as defined in Eqn. 1.1 is positive for stable nuclei. Figure 1.1 shows the binding energy per nucleon (B/A) plotted as a function of atomic mass and atomic number. The nucleus with maximum binding energy per nucleon is iron ($^{62}_{26}$Fe). Nuclear fusion of ions lighter than iron and nuclear fission of ions heavier than iron tends to be exothermic, as the binding energy of the products is higher than that of the reactants. The amount of energy released in light-ion fusion reactions is typically on the order of 1 to 10 MeV.

For two nuclei to fuse, they must approach close enough for the strong nuclear force to overcome the electrostatic repulsion between them. Coulomb's law indicates that the electric potential between the two ions is a function of their charges Z_i and the distance r between them, as $V_C(r) = \left(Z_1 Z_2 e^2\right) / \left(4\pi\epsilon_0 r\right)$.[a] This potential assumes point-like particles, and breaks down as r

[a] Throughout this thesis, the SI unit system will be used for equations, with some modifications. Energy and

approaches the sum of the nuclear radii, $\sim 1.4(A_1^{1/3} + A_2^{1/3})$ fm. Combining these formulas, the electric potential barrier to nuclear fusion is calculated to be on the order of 1 MeV, and is proportional to the product of the nuclear charges. Classically, reacting ions would require at least this energy to overcome the potential barrier and fuse. However, quantum mechanics allows the ions to 'tunnel' through the potential barrier with a probability dependent on the size of the barrier and the energy of the collision. Because the potential barrier increases proportionally to $Z_1 Z_2$, the fusion cross-section at a given collision energy drops rapidly with ion charge, and fusion fuels of interest are generally isotopes of hydrogen and helium. Several fusion reactions of particular interest for controlled fusion research are:

$$\begin{array}{llllllll} {}^2_1D & + & {}^2_1D & \rightarrow & {}^3_1T & (1.01\text{ MeV}) & + \; p & (3.02\text{ MeV}) \quad (50\%), \\ & & & \rightarrow & {}^3_2He & (0.82\text{ MeV}) & + \; n & (2.45\text{ MeV}) \quad (50\%), \\ {}^2_1D & + & {}^3_1T & \rightarrow & {}^4_2He & (3.5\text{ MeV}) & + \; n & (14.1\text{ MeV}), \\ {}^2_1D & + & {}^3_2He & \rightarrow & {}^4_2He & (3.6\text{ MeV}) & + \; p & (14.7\text{ MeV}). \end{array} \tag{1.2}$$

A common parametrization of the fusion cross-section σ is[11]

$$\sigma(\epsilon) = \frac{S(\epsilon)}{\epsilon} \exp\left(-\sqrt{\epsilon_G/\epsilon}\right), \tag{1.3}$$

where $\epsilon = m_r v^2/2$ is the center-of-mass energy of the reactants, $\epsilon_G = 986.1 Z_1^2 Z_2^2 A_r$ keV is the Gamow energy for the reaction, and the astrophysical S-factor $S(\epsilon)$ is typically a slowly-varying function of ϵ. (The masses with subscript 'r' indicate the reduced mass of the reactants, $m_r = m_1 m_2/(m_1 + m_2) \approx A_r m_p$.) From Eqn. 1.3, it is clear that the cross-section increases rapidly with increasing center-of-mass energy up to approximately the Gamow energy. Figure 1.2a) shows the fusion cross-section for the reactions in Eqn. 1.2. The deuterium-tritium (DT) fusion reaction has the highest cross-section of any known light-ion fusion reaction due to a large resonance near $\epsilon =$ 100 keV. As such, DT is the fuel of choice for fusion experiments seeking net energy production.

The cross-sections for fusion are not sufficiently high enough for directly accelerated ions incident on a target (beam-target fusion) to produce a net fusion yield. Consider a beam of energetic deuterium ions incident on a tritiated target, such that the fusion cross-section is near the maximum of approximately 5 barns ($E_D \approx 170$ keV). Assuming a gaseous tritium target with density ρ_T, the deuteron would stop after traversing a path length $L \sim 0.17$ mg/cm$^2/\rho_T$. Ignoring the reduction in the cross section as the deuteron slows, an upper bound for the probability of fusion is calculated to be less than 0.02%, resulting in an average ratio of energy produced to energy expended of less than 2%.

For this reason, experimental studies focus on creating a *thermonuclear* plasma in which colliding thermalized ions are sufficiently energetic to fuse. In a thermalized plasma, the kinetic energy of elastic collisions is redistributed within the plasma, rather than being lost as in the beam-target scenario. Assuming a thermalized plasma with ions in a Maxwell-Boltzmann velocity distribution, the fusion cross-section can be numerically integrated over the distribution of colliding ions to generate an average thermal reactivity $\langle \sigma v \rangle$ with units of cm^3/sec. The rate of fusion production is

temperature ($k_B T$) will be expressed in electron volts (eV) or multiples thereof (10^3 eV = 1 keV, 10^6 eV = 1 MeV); distances will frequently be expressed in centimeters (cm) or microns (μm); and time will often be expressed in nanoseconds (1 ns = 10^{-9} sec) or picoseconds (1 ps = 10^{-12} sec). These "ICF units" are commonly used in HED research as they are comparable to the scales of interest.

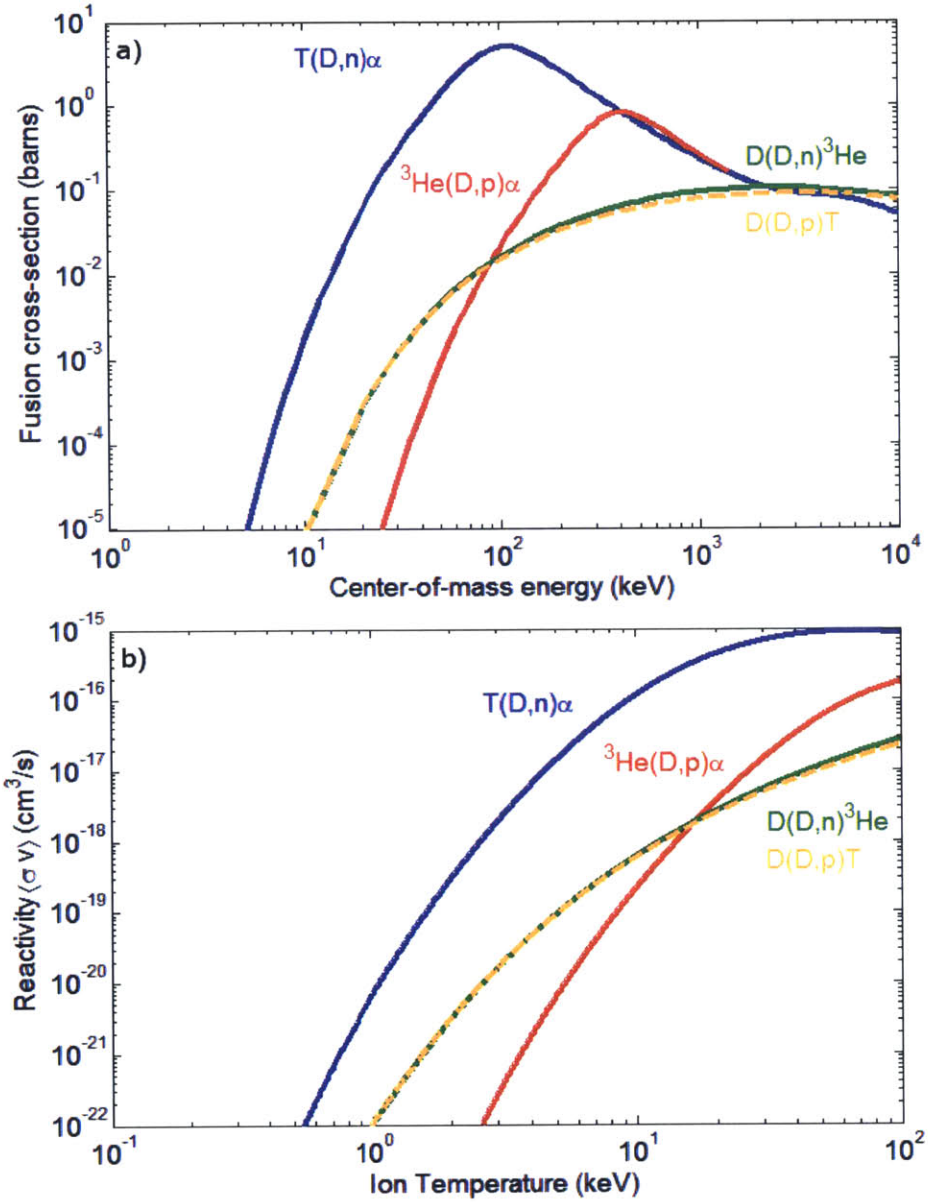

Figure 1.2. a) Fusion cross-sections as a function of center-of-mass energy for the nuclear fusion reactions T(D,n)α (blue), ^{3}He(D,p)α (red), D(D,n)^{3}He (green), and D(D,p)T (orange dashed). Data taken from Reference [12]. b) Fusion reactivity as a function of ion temperature. The reactivity $\langle \sigma v \rangle$ is calculated for each reaction by averaging the cross-section times the center-of-mass velocity over the velocity distributions of both reactant species, assuming a thermalized plasma with ions in a single-temperature Maxwell-Boltzmann distribution. Parametrization taken from Reference [13].

then given by:

$$\frac{dY_{ij}}{dt} = \int \frac{n_i n_j}{1+\delta_{i,j}} \langle \sigma v \rangle dV. \tag{1.4}$$

For each fusion reaction, the thermal reactivity is a function of plasma ion temperature only,

and is shown in Figure 1.2b for the four reactions discussed here. As the fusion cross-section increases rapidly with the center-of-mass energy of the reactants, the energy of the fusing ions is typically several times the ion temperature. Parametrizations of the cross-sections and reactivities are available from a number of authors; for the work contained in this thesis, the parametrizations from Reference [13] is primarily used.

1.1.2 Theory of Inertial Confinement Fusion

ICF seeks to generate conditions in which the energy created by fusion reactions is deposited locally, thereby increasing the local temperature and reactivity, generating a run-away self-heating scenario in which a substantial fraction of the fuel in the plasma burns. The primary requirement for such a burning plasma is that self-heating due to fusion exceeds power losses. The total losses include radiative losses (primarily bremsstrahlung) and diffusive losses, and are written in terms of the density, temperature, and energy confinement time τ_E as follows:[11]

$$C_{brems} n_e^2 T^{1/2} + \frac{3nT}{\tau_E} = \frac{1}{5}\frac{n^2\langle\sigma v\rangle Q_{DT}}{4} \quad \rightarrow \quad n\tau_E = \frac{3T}{Q_{DT}\langle\sigma v\rangle\frac{1}{20} - C_{brems}T^{1/2}}. \tag{1.5}$$

From the left, the terms in Eqn. 1.5 are: bremsstrahlung power loss with the coefficient $C_{brems} = 5.34 \times 10^{-24}$ erg cm^3 sec^{-1} keV$^{-1/2}$; diffusive power loss; and the fusion heating of the plasma. Most of the DT-fusion reaction energy $Q_{DT} = 17.6$ MeV escapes, carried by the 14.1 MeV neutron. The fusion heating comes from the DT-fusion α, which deposits its 3.5 MeV locally; this introduces the factor of 1/5 in the fusion heating term. Note that in this treatment additional external sources of heating have not been included. While such outside heating sources play an important role in steady-state fusion designs, ICF relies on the burn of the assembled hotspot for subsequent heating and ignition. The formula has been re-written on the right to generate a balance condition for density and energy confinement time. For the fuel to ignite, the product $n\tau_E$ must exceed the value given by Equation 1.5, which is a function of temperature and the properties of the fusion reaction. This requirement is known as the Lawson criterion, and was first derived in Reference [14]. It is convenient to rewrite this requirement as a condition on $nT\tau_E$, which is equivalent to $P\tau_E$, because for DT-fusion the ignition condition becomes roughly constant: $nT\tau_E \geq 3.3 \times 10^{15}$ cm^{-3}s keV = 5.3 Gbar ns in the range $T = 10$–20 keV.

In an inertially-confined experiment, the confinement time is set primarily by the rate at which the pressure of the plasma releases into the surrounding area, mediated by a rarefaction wave. Assuming a spherical plasma with a radius R, the confinement time scales as $\tau_E = R/4c_s$, where $c_s = \sqrt{\gamma P/\rho}$ is the sound speed. (The factor of 4 arises from the spherical geometry.) Multiplying this time with the rate of fusion production given in Eqn. 1.4, the total fusion yield of an experiment is approximately[11]

$$N_{fus} \approx \frac{n_i n_j}{1+\delta_{ij}}\langle\sigma v\rangle V_0 \frac{R}{4c_s} = \rho R \frac{\langle\sigma v\rangle}{8m_f c_s} N_{ij}, \tag{1.6}$$

where $N_{ij} = n_0 V_0/(2-\delta_{ij})$ is the number of fuel ion pairs in the plasma, m_f is the average fuel ion mass, and it has been assumed that the fuel species are equimolar [$n_i = n_j = n_0/(2-\delta_{ij})$]. The burn efficiency thus scales primarily with the *areal density* ρR. The fraction on the right-hand side of Eqn. 1.6 is referred to as the 'burn parameter,' often defined as the inverse such that $H(T) = 8m_f c_s/\langle\sigma v\rangle$. This quantity is a function of temperature only and has units of areal density.

Equation 1.6 is valid only in the limit of low burn $N_{fus} \ll N_{ij}$, which is equivalent to $\rho R \ll H(T) \sim 7$ g/cm^2 for DT fuel. This sets a scale for the areal densities required for ignition and high gain, and provides the motivation for why compression of the fuel is necessary for controlled

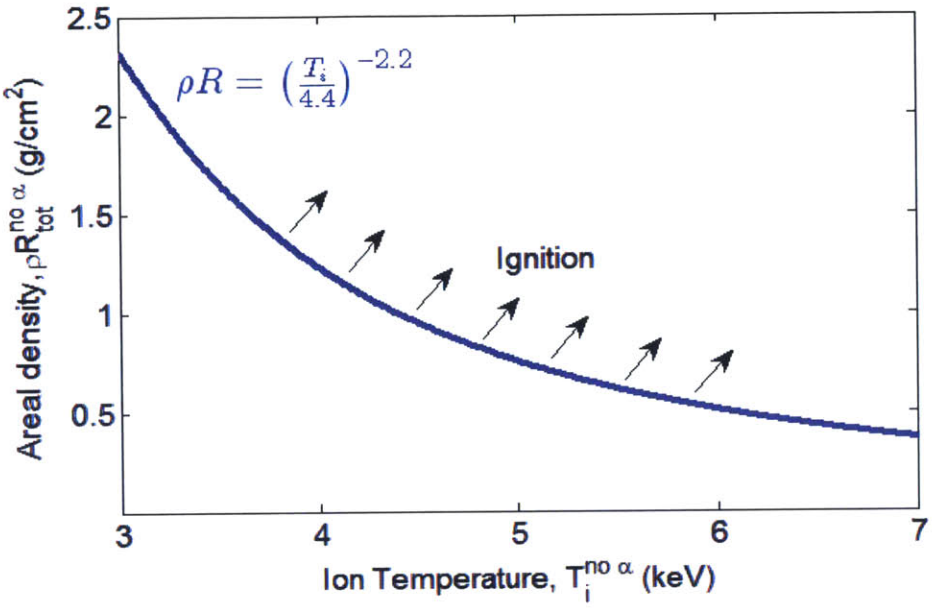

Figure 1.3. Areal density (ρR) as a function of ion temperature (T_i) for marginal ignition in an ICF implosion. To ignite, ρR and T_i must be larger than indicated by the blue curve. Quantities shown are "no-α", i.e. the expected value neglecting the effects of alpha heating; in an igniting target, the fusion reactions will additionally heat the plasma. For more information see Reference [15].

fusion. A sphere of cryogenic DT-ice with a density of approximately 0.225 g/cc would require a radius on the order of 10 cm to burn a substantial fraction of the fuel. Such a target would contain approximately a kilogram of DT-ice, and total nuclear yield would be on the order of 100 kilotons of TNT. Compression is required to achieve ignition with controllable fusion power output.

Recent work has demonstrated that the Lawson criterion for ICF can equivalently be written as a function of the areal density and temperature, as expected based on Eqn. 1.6:

$$\chi_{1D} \approx \left(\rho R_{tot}^{no-\alpha}\right)^{0.8} \left(\frac{T_i^{no-\alpha}}{4.4}\right)^{1.8}, \tag{1.7}$$

where χ_{1D} is unity for marginal 1D-ignition.[15] This formulation can be corrected to account for 3-dimensional effects by incorporating the ratio of the observed nuclear yield to the 1D-simulated yield ("Yield-over-clean" or YOC $\equiv Y_{obs}/Y_{1D}$): $\chi_{3D} = \chi_{1D} YOC^{\mu}$, where $\mu \approx 1$. Based on Eqn. 1.7, the marginal ignition condition is described by a power law in the range T_i = 3–7 keV: $\rho R = (T_i/4.4)^{-2.2}$, as shown in Figure 1.3. The areal density and temperature are therefore the primary metrics for the performance of ICF implosions. Areal density is closely related to the compression of the fuel: to zeroth order, spherical compression will increase the density proportionally to R^{-3}, such that $\rho R \propto R^{-2}$. Importantly, both the areal density and the temperature can be inferred using nuclear diagnostic techniques.[16,17] Measurements of the ion temperature from nuclear diagnostics are used extensively in this thesis, and will be discussed in detail in Sec. 1.3.

Laser Inertial Confinement Fusion

A method for producing the required compression of the fusion fuel using lasers was first proposed openly by Nuckolls and colleagues in a seminal paper in 1972.[18] However the concept of achieving controlled thermonuclear fusion through compression of the fuel with an intense power source dates back to classified research during the late 1950s. Following the advent of the laser in 1960, several researchers proposed the use of lasers as a driver for fuel compression, and as a consequence laser-plasma interaction experiments and theory developed around the world throughout the decade. The concept of laser-driven ICF was declassified in the United States in 1971,[11] shortly before the Nuckolls paper was published. Nuckolls' paper identifies and addresses several important areas of research for laser-driven ICF, which are discussed in this section.

Compression of the fuel is of primary importance, for reasons already discussed. Since a high density (and a high ρR) is required, it is valuable to compress the fuel while maintaining as low an entropy as possible. The quantum mechanical Fermi exclusion principle determines the maximum electron density that can be obtained for a given pressure to be

$$n_{e,degen} = \left[\frac{20 P m_e}{h^2}\left(\frac{\pi}{3}\right)^{\frac{2}{3}}\right]^{\frac{3}{5}} = \left(\frac{P}{1\text{ Gbar}}\right)^{3/5} 9.52 \times 10^{24}\text{ cm}^{-3}. \tag{1.8}$$

Achieving such a Fermi-degenerate state minimizes the implosion pressure required in order to achieve the required densities. The fuel can be initialized in a cryogenic state to minimize its initial entropy. High pressures must then be obtained while avoiding significant heating of the fuel.

Nuckolls discusses an "optimal, isentropic compression" of the fuel that can be performed by sufficiently fine-tuning the laser pulse. An isentropic compression scheme requires a detailed pressure time-history to maintain the adiabatic relationship $d(\ln P)/dt = \gamma d(\ln \rho)/dt$. In realistic systems, it has proven difficult to control the drive at the required level for such an optimal compression. Instead, a more robust experimental solution has been to compress the fuel with a series of weak shocks, before imploding it with a strong primary drive.

A shock is a discontinuous jump in the pressure, density, and flow velocity of a fluid, which travels faster than the speed of sound in the unshocked fluid. In Sec. 1.2.1, the jumps in pressure and density at the shock front are derived as a function of the Mach number M, the ratio of the shock velocity to the upstream sound speed (see Eqn. 1.24 and 1.25). The compression ratio ρ_2/ρ_1 and the pressure ratio P_2/P_1 at the shock front for both isentropic and shock-compression is shown in Figure 1.4; the subscripts 1 and 2 designate the unshocked (upstream) and shocked (downstream) plasmas, respectively. In the limit of weak shocks ($M \sim 1$), the density and pressure both increase linearly with M, and the compression is nearly isentropic, as desired. A series of weak shocks can thus compress a spherical shell of fuel to high density while maintaining a low entropy. The current ignition design uses a carefully tuned laser drive pulse shape to launch four weak shocks, which set the fuel density and adiabat prior to the spherical implosion.[19] Strong shocks ($M \gg 1$) increase the density ratio across the shock front up to a limiting value $(\gamma + 1)/(\gamma - 1)$ dependent on the ratio of specific heats, γ. For an ideal gas with $\gamma = 5/3$, the maximum density increase due to a shock is 4, and further increases in the shock pressure will add heat to the fuel. Careful timing of the weak shocks is required to prevent them merging into a single stronger shock while in the cryogenic fuel, which would generate a higher than desired entropy in the fuel.

To achieve the highest possible pressure in the fuel, the standard laser ICF design implodes a spherical shell of solid fusion fuel which then stagnates around a 'hotspot' at the center of the implosion. The calculation of the hotspot pressure as a function of experimental parameters is complex, and continues to be developed; however a simple kinematic argument explains the

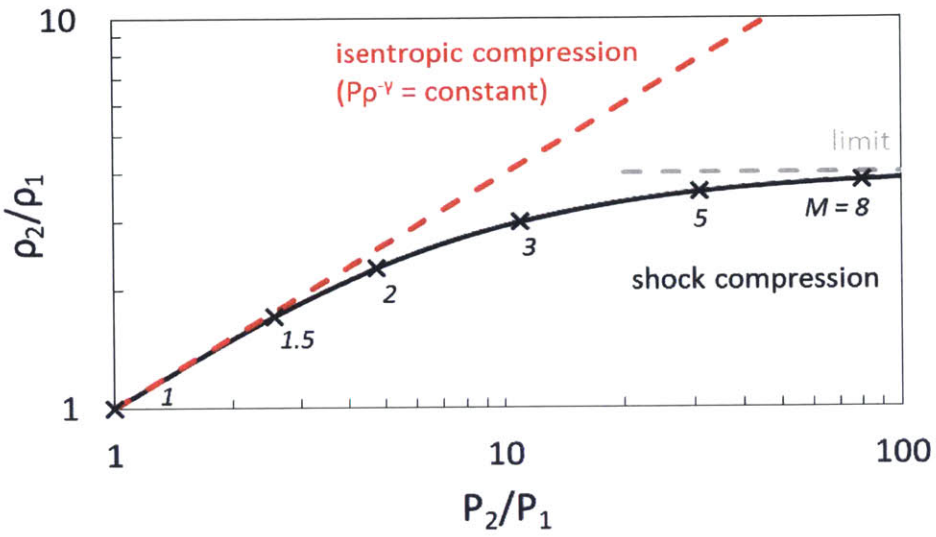

Figure 1.4. Density ratio (ρ_2/ρ_1) as a function of pressure ratio (P_2/P_1) for compression by a shock (black line), assuming a ratio of specific heats $\gamma = 5/3$ (as for an ideal gas). The Mach number M of the shock is labeled at several points (black x). In the limit of weak shocks ($M \sim 1$), the shock compression ratio approaches isentropic compression (red dashed), whereas in the limit of strong shocks ($M \gg 1$), the ratio approaches a limit of $(\gamma+1)/(\gamma-1) = 4$ (grey dashed). In laser ICF, a series of weak shocks are used to compress the fuel to attain maximum density with minimum pressure.

enhancement of pressure by the implosion process. The laser does not directly push the shell material, but rather ablates the outer layers of the shell; the ablation pressure then drives the implosion. Consider a shell with initial mass M_0 and initial radius R_0 driven to implode spherically by a constant pressure P_{abl}. The kinetic energy absorbed by the shell material is approximately given by $E_K \approx P_{abl}(4\pi R_0^3/3)(1-(R'/R_0)^3)$. Here, R' is the radius of the shell at the time when the drive stops. Part of this energy is lost to the ablated mass. The remaining kinetic energy of the imploding shell $E_{K,sh}$ is assumed to scale as the absorbed kinetic energy multiplied by the fraction of remaining mass, $f_M = M_{sh}/M_0$.[b] The imploding shell with remaining mass M_{sh} then compresses the central gas adiabatically, resulting in a stagnated hotspot pressure of $P_{HS}V_{HS} \approx E_{K,sh}$ (neglecting the initial hotspot pressure). Combining these relations provides a lower bound on the hotspot pressure:

$$P_{HS} \gtrsim P_{abl}\,(\mathrm{CR})^3\, f_M \left[1-\left(R'/R_0\right)^3\right], \tag{1.9}$$

where the convergence ratio $\mathrm{CR} = R_0/R_{HS}$ is defined in terms of the hotspot radius $R_{HS} = (3V_{HS}/4\pi)^{1/3}$. While the fraction of mass remaining is typically in the range 0.2 to 0.5, depending on the experimental design, and the final geometric term is always less than 1, typical ICF designs can feature convergence ratios of ~30 or more. Thus, with an ablation pressure on the order of 100 Mbar, a hotspot pressure on the order of hundreds of Gbar can be obtained.

Let us consider more specifically the hotspot pressure produced by the imploding shell. When the spherical shock rebounds, re-transits the fuel, and encounters the remaining mass of the shell, the incipient hotspot already has a certain pressure and volume, P_0 and V_0. The energy contained

[b] This condition provides a lower bound on the shell kinetic energy, since it assumes the entire shell is accelerated before the ablated mass vanishes. To calculate the actual energy absorbed by the imploding shell requires integrating the rocket equation in spherical geometry.

in the radially-converging mass at peak velocity is transferred into compressing the fuel, and energy balance dictates that the maximum compression occurs when $P_{max}V_{max} = P_0V_0 + E_{K,sh}$. Assuming the compression occurs isentropically such that PV^γ is constant, the final pressure and volume are calculated to be as follows:

$$P_{max} = P_0\left(1 + \frac{\frac{1}{2}M_{sh}v_{imp}^2}{P_0V_0}\right)^{\frac{\gamma}{\gamma-1}}, \tag{1.10}$$

$$V_{max} = V_0\left(1 + \frac{\frac{1}{2}M_{sh}v_{imp}^2}{P_0V_0}\right)^{-\frac{1}{\gamma-1}}. \tag{1.11}$$

Since $\gamma = 5/3$ in an ideal gas, the exponent on the pressure equation is 5/2, while the exponent on the volume equation is $-3/2$. For large compressions, the initial hotspot energy must be small compared to the energy in the inflowing shell. In this regime the maximum pressure scales with the initial hotspot pressure to the $-3/2$ power. To achieve a high hotspot pressure at peak compression it is therefore important to minimize the adiabat of the hotspot as well as that of the main fuel.

The symmetry of the implosion is also critical to obtaining high pressures in the hotspot. Both low mode-number and high mode-number asymmetries in the implosion velocity and radius have detrimental impacts on the performance of the implosion and must be sufficiently controlled.[c] The radial implosion aggravates these detrimental effects, as asymmetry must be controlled to much better than the scale of the final fuel assembly, which is a factor of ~ 30 smaller than the initial capsule radius. Furthermore, the Rayleigh-Taylor (RT) instability drives the exponential growth of initial perturbation seeds[20] in any region with oppositely directed gradients of pressure and density:[11]

$$\frac{d\rho}{dr}\frac{dP}{dr} < 0. \tag{1.12}$$

During the ablation and acceleration phase the ablation front is susceptible to RT instability, as well as to the Richtmyer-Meshkov (RM)[21,22] and Kelvin-Helmholtz (KH) instabilities.[23] Sufficient growth of perturbations early in the implosion can violate the integrity of the shell, reducing the effectiveness of compression and introducing jets of ablator material into the fuel. During the deceleration and stagnation phase, the fuel-shell interface is also vulnerable to RT growth, seeded by the perturbations that developed during the acceleration phase of the implosion.

Asymmetries in the implosion velocity or radius result in several negative consequences for the implosion, as illustrated in Figure 1.5. Asymmetries with low mode numbers ($\ell < 5$) can result in non-stagnated fuel velocity at peak compression, reducing the peak pressure as compared to an ideal implosion in which all of the available kinetic energy is converted to thermal energy. Sufficient growth of mid-range mode-numbers ($4 < \ell \lesssim 20$) can introduce 'fingers' of cold fuel or ablator mass penetrating the hotspot, reducing the effective volume and ρR of the hotspot and inhibiting nuclear performance. High mode numbers ($\ell \gg 10$) lead to the introduction of atomic mix between the hotspot and the ablator, which cools the hotspot by increased radiative loss and dilutes the fuel.

Two main approaches to laser ICF have different merits in terms of asymmetry control, as illustrated in Figure 1.6. In direct-drive ICF (Fig. 1.6a), the lasers directly irradiate the target. Assuming a large number of lasers positioned with spherical symmetry around the target, this approach can result in very good low-mode symmetry. However the overlap of the laser spots on

[c] Asymmetry is often characterized by the mode number of Legendre polynomials, with a mode modifying the radius by $P_\ell(\cos\theta)$. The conventional terminology in spherical coordinates associates "P modes" (e.g. P2, P4) with the polar angle θ and "M modes" with the azimuthal angle ϕ.

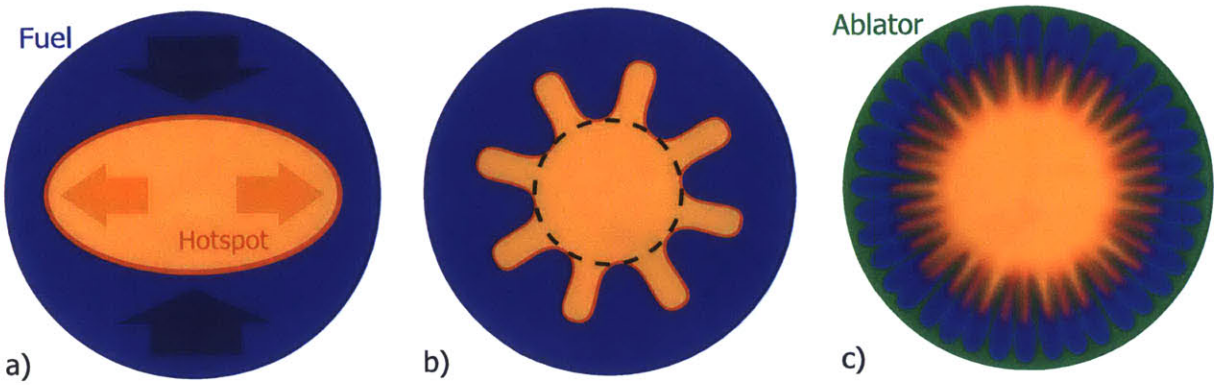

Figure 1.5. Illustration of the possible effects of a) low-mode ($\ell = 2$), b) mid-mode ($\ell = 8$) and c) high-mode ($\ell \approx 40$) implosion asymmetries on the fuel assembly (blue) and hotspot (orange). Low-mode asymmetries can result in non-stagnated fuel velocity (arrows). Medium modes introduce fingers of cold fuel into the hotspot, reducing the effective hotspot volume (black dashed circle). High modes can lead to turbulent mixing of ablator material (green) into the hotspot, diluting and radiatively cooling it.

the target inherently introduces high-mode asymmetries, with a characteristic mode set by the number and geometry of the laser beams. In contrast, indirect-drive ICF (Fig. 1.6b) uses the lasers to illuminate the inside of a secondary target made of high-Z elements, referred to as a 'hohlraum' (German for cavity, or hollow space). The hohlraum converts the laser energy to a blackbody x-ray radiation source, which drives the ablation and implosion of the target. This conversion smooths out high-mode asymmetries in the drive, as the black-body x-ray radiation is isotropic. Moreover, the indirect-drive x-rays deposit their energy deeper into the ablating plasma than the direct-drive UV laser light, due to the higher-frequency of the driving photons. This deeper penetration reduces the thickness of the RT-unstable layer in the ablation front. However the hohlraum's cylindrical symmetry, as well as laser-plasma interactions (LPI) at the laser entrance hole (LEH) through which all the lasers must cross, can distort the low-mode symmetry of the x-ray drive. As a consequence, the laser power balance history must be carefully tuned to achieve a spherical drive throughout the implosion, avoiding mode 2 perturbations such as prolate ('sausaged') and oblate ('pancaked') shapes, as well as higher mode perturbations.[d]

The targets for ICF experiments are also optimized for control of asymmetries. During the acceleration phase, the rate of mass ablation has a stabilizing effect on RT instability growth. The choice of an ablator with a high ablation velocity, such as beryllium or high-density carbon, can reduce the rate of instability growth during the acceleration phase. Developing the ability to fabricate targets from these more exotic materials has itself required significant amount of research and development. Target manufacturing has developed a high level of precision, to reduce or eliminate as much as possible any surface perturbations that act as seeds for instability growth. Much of the target development for the ICF program in the United States is contracted from General Atomics, who have also provided the targets used in this thesis.[24]

A hydrodynamic simulation of an ignition implosion is presented in Figure 1.7. This simulation illustrates several of the processes described so far, including shock compression of the DT-ice, shock

[d]Indirect- and direct-drive each have additional benefits and disadvantages related to drive efficiency. The deeper penetration of the x-rays increases the efficiency of the mass ablation by x-ray drive relative to UV laser light. However the added conversion step from UV to x-rays reduces the total efficiency of the drive when comparing kinetic energy of the implosion to the initial laser energy. The physics of mass ablation, x-ray drive and laser-plasma interaction are beyond the scope of this thesis and will not be described herein. Chapters 7, 9, and 11 of Reference [11] provide an excellent discussion of these topics.

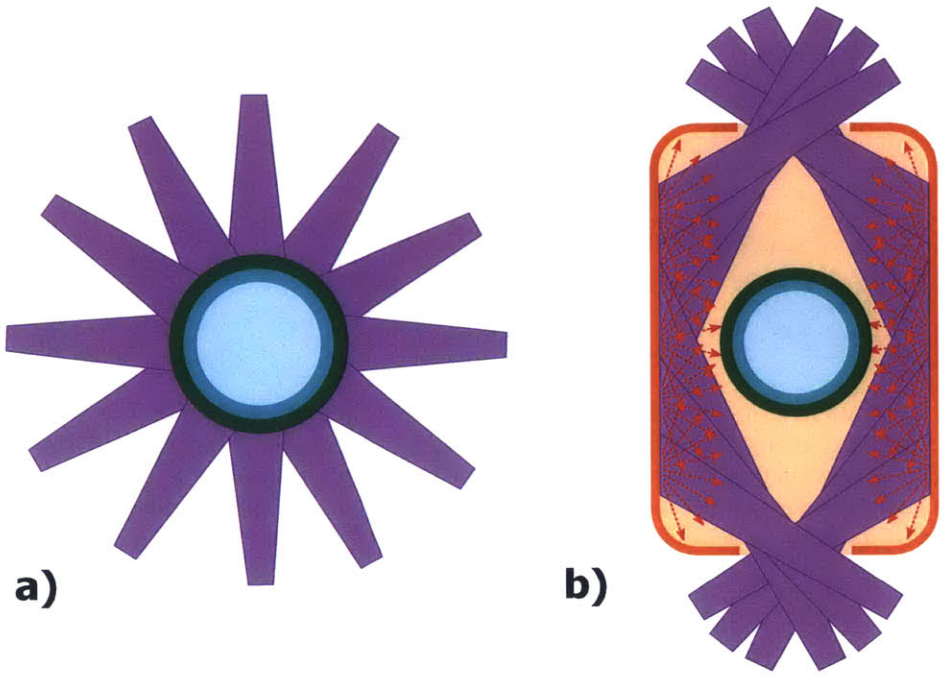

Figure 1.6. Cartoons of the two main approaches to laser ICF: a) direct-drive and b) indirect-drive. In direct-drive experiments, the lasers (magenta) directly illuminate the capsule, ablating the outer shell layer ('ablator', green) to implode the solid fuel-ice layer (blue) and fuel-vapor core (light blue). Direct-drive can achieve high efficiency of laser energy coupling to the implosion and good low-mode symmetry at the cost of mid- and high-mode asymmetry. In indirect-drive experiments, the lasers instead illuminate the inside of a cavity made of high-Z material, often gold or uranium, called the hohlraum (orange). The high-Z plasma generates isotropic black-body x-ray radiation (red), which in turn drives the capsule. Indirect-drive achieves very good high-mode uniformity and reduces ablation-phase RT instability growth at the cost of significantly reduced energy coupling to the target and increased difficulty achieving low mode drive symmetry.

coalescence inside the DT-vapor, acceleration of the fuel, shock rebound, onset of deceleration, final compression and hotspot formation, and ignition. Some of the physics underlying the 1D-radiation hydrodynamic simulations used to model ICF implosions is described in Section 1.2.

1.1.3 Shock-driven implosions

As introduced in Section 1.1.2, ICF implosions typically generate two periods of nuclear production. The *shock bang* occurs just after the shock front reaches the center of the implosion and rebounds. In the ICF ignition platform shown in Figure 1.7, four shocks are launched by the laser to shock-compress the cryogenic fuel, and these four shocks coalesce into a single shock just inside the ice layer. However more generally, a sufficiently strong laser drive will generate a shock in spherical implosions. The spherical convergence amplifies the strength of the incoming shock as it approaches the center, such that it is typically a strong shock with a Mach number $M \gg 1$. The rebounding shock encounters an inflowing, shocked plasma created by the first passage of the shock. The combination of initial shock, spherical convergence, and rebound shock can generate densities and temperatures sufficiently high for fusion to occur.

Consider a simplified ICF target consisting only of a spherical shell with thickness w and initial radius R_0, which is filled with a fuel gas with initial mass density ρ_0. The volume at maximum

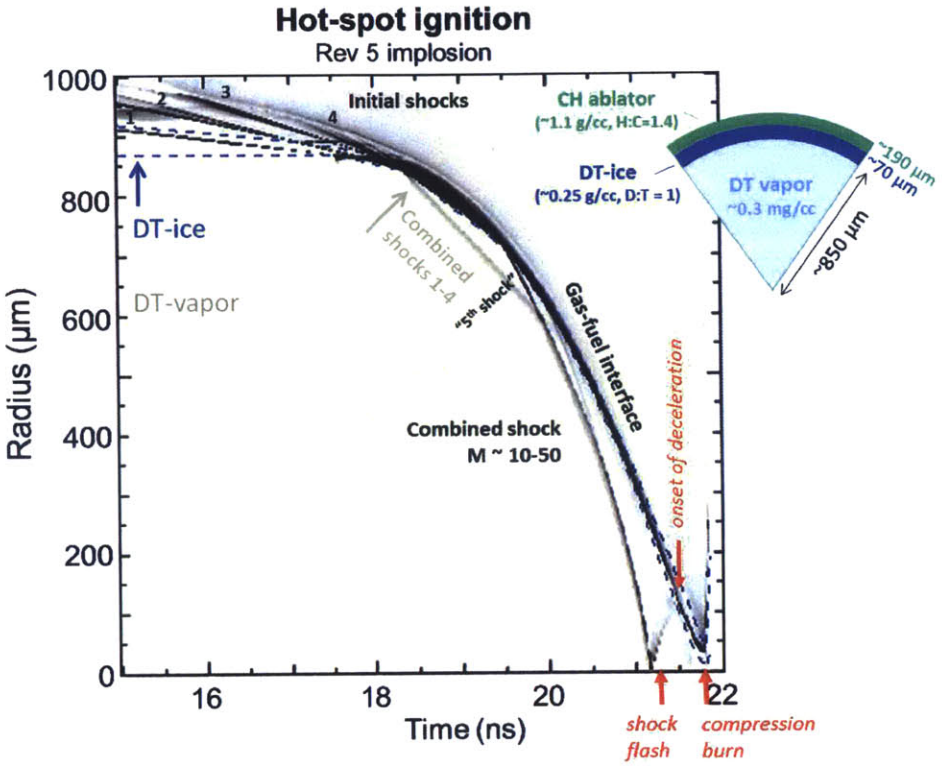

Figure 1.7. A Lagrangian plot from a 1D-hydrodynamic simulated "Rev 5" ignition implosion designed for the NIF. The Rev 5 design is described in Reference [19]. Gradients in $\log P$ are shown as a function of radius and time, depicting the trajectory of shocks and the gas/fuel interface. Four weak shocks compress the DT-ice layer before the main laser impulse drives radial implosion. (A fifth shock is also launched at some point during the main drive.) The shocks merge in the DT-gas into a strong shock with Mach number $M \sim 10$–50. The combined shock rebounds at the center of the implosion, initiating a brief period of nuclear production ('shock-flash') and setting the initial hotspot adiabat. The rebounding shock then interacts with the imploding dense fuel mass, initiating shell deceleration and culminating in peak compression and peak nuclear production ('compression-burn'). Hydrodynamic simulation techniques are discussed in Section 1.2. Simulation and plot courtesy of H. Robey, LLNL.

compression derived in Equation 1.11 indicates that the further compression of the fuel by the shell depends on the condition $M_{sh}v_{imp}^2/2 \gg P_0V_0$, which means that the kinetic energy contained in the inflowing shell is substantially larger than the energy already contained in the hotspot. If this is true, the shock bang is followed by the deceleration of the inflowing shell, which causes an increase in the hotspot pressure and an associated period of nuclear production called *compression burn*. However if the opposite is true ($E_{K,sh} \ll E_{HS,0}$), no additional compression (and no compression burn) occurs. In this scenario, peak pressure occurs when the rebounding shock strikes the fuel-shell interface, and is immediately followed by rarefaction of the fuel as the rebounding shock continues into the shell plasma. Such an implosion is called a *shock-driven* implosion.

One way to create a shock-driven implosion is to use a thin shell, such that the entire shell is ablated prior to the deceleration phase. The ablating shell will compress the material behind the shock, increasing the plasma density and therefore the shock yield. Figure 1.8 presents a 1D-radiation hydrodynamic simulation of a thin-shell implosion, generated using the code HYADES.[25] Because the thin shell has little inertia, its acceleration is rapid enough that it continuously catches

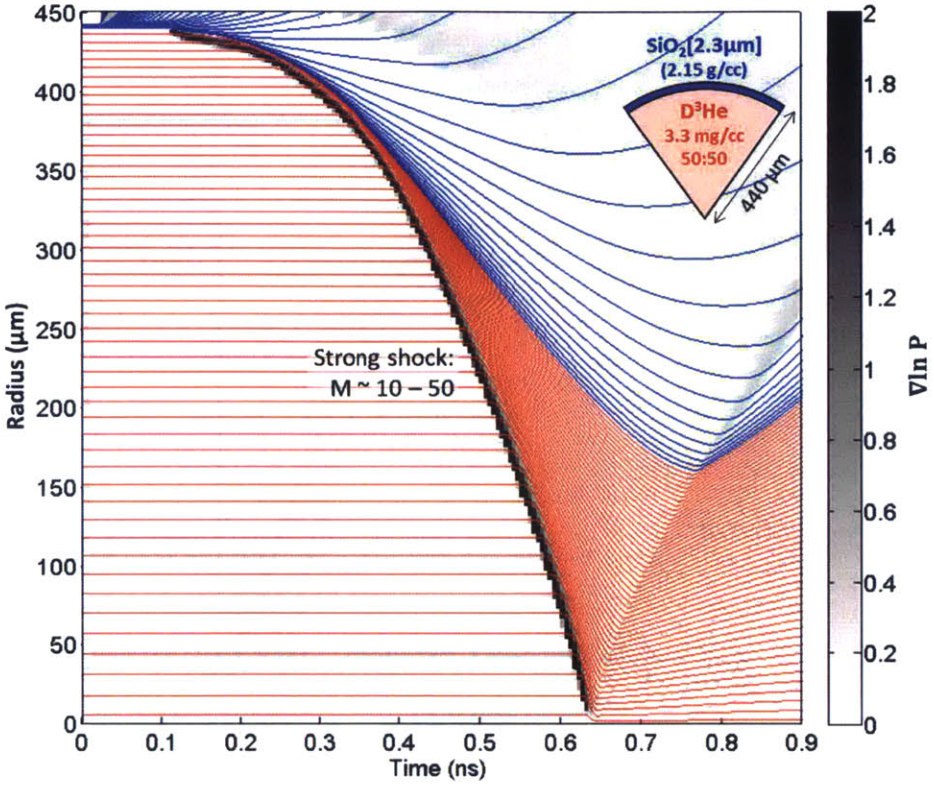

Figure 1.8. Lagrangian plot of a shock-driven implosion simulated using the 1D-radiation hydrodynamic code HYADES. The laser in the simulation was 14.6 kJ delivered in a 0.6 ns square pulse with a peak laser power of 23 TW and a laser absorption fraction of 57%. Trajectories of shell (blue) and fuel (red) zones are shown by lines. Strong shocks appear clearly in the local gradient in log pressure (grey scale). In this simulation, the shell burns through at ~0.32 ns (the time when the maximum shell density is lower than the maximum fuel density). Shortly thereafter, the shock breaks away from the fuel-shell interface. Because the shell has burned through, the imploding shell lacks sufficient mass to further compress the hotspot after reshock, and the plasma begins to rarefy.

up with the shock, sweeping up a thin layer of high-pressure fuel gas. The shock does not 'escape' from the imploding shell until halfway through the implosion, approximately when the shell runs out of material or *burns through*. In the example plotted in Figure 1.8, the shell burns through at approximately 0.32 ns. After burn-through, the density of the remaining shell plasma is reduced while continuing to match pressure with the adjacent fuel plasma. Once the temperature equalizes across the fuel-shell interface, both plasmas will be directly heated by the laser as long as it continues to deliver power.

Shock-driven ICF targets are useful for studies of ICF-relevant physics for several reasons. Firstly, thin-shell targets are relatively cheap and easy to manufacture compared to the more complex ignition designs. Secondly, shock-driven targets behave in a very '1D' manner: they are highly insensitive to asymmetries and instability growth.[26] Ablation front instabilities are limited by the high ablation velocity, and compression-phase instabilities are eliminated entirely. Thirdly, plasma ion temperatures on the order of 10 keV can be produced in the shock flash, generating substantial fusion yield for diagnosis. High yields have made shock-driven implosions valuable as a source of monoenergetic fusion particles for both diagnostic development[27,1,28,29] and physics studies

using charged particle radiography.[30–37] Finally and most importantly, shock-driven plasmas can be made to mimic the state of the ICF ignition design plasma prior to deceleration and compression, by selecting appropriate gas fill. An initial shock with a Mach number of $M \sim 10 - 50$ is driven in both cases. Comparison of Figures 1.7 and 1.8 shows that in both cases the single strong shock dominates the evolution of the central plasma until the reshock of the fuel-shell interface, after which point the shock-driven implosion simply falls apart. From a diagnosis standpoint, shock-driven plasmas provide a means of studying the physics relevant to the incipient hotspot plasma of an ICF target without having to contend with the much larger yields of nuclear particles and x-rays produced by compression burn.

In summary, shock-driven targets generally provide a means of studying the physics of plasmas with ~1–10 mg/cc densities and ~1–10 keV temperatures. Several shock-driven implosions are used in Chapter 2 as sources of monoenergetic fusion products for the development and calibration of new diagnostics and diagnostic methods. In Chapter 3, implosions such as those described here are used to study kinetic admixture of the fuel and shell in experiments with initially separated fusion fuels. Chapter 4 uses shock-driven implosions to study the plasma kinetic effects of species separation and thermal decoupling in multi-species ICF fuels.

A note on terminology: 'shock-driven' and 'exploding pushers'

Shock-driven implosions have a long history in the context of ICF. In experiments as early as the 1970s, thin-shell glass targets were volumetrically heated by laser-generated electrons or x-rays, causing the glass to explode in all directions. The inward-directed portion of the SiO_2 plasma produced by these *exploding pushers* would drive an implosion of the fuel contained within.[38] Exploding pushers were characterized by a fuel convergence ratio of 3 to 4 and insensitivity to asymmetry or instability growth, and were the first targets to produce thermonuclear neutrons.[39]

Shock-driven targets such as those described above and used in this thesis have frequently been referred to as 'exploding pushers,' as the targets appear identical to historical exploding pushers. This designation is misleading, however, as the physics of the shock-driven implosions used here are quite different. Ablation of the capsule wall drives the capsule implosion, but the capsule walls are sufficiently thin to burn through prior to the reshock of the fuel-shell interface and no subsequent compression occurs. Throughout this work and related papers the term 'exploding pushers' has been avoided in reference to shock-driven targets wherever possible. Notable exceptions include the polar direct-drive exploding pusher (ExplPush) and indirect-drive exploding pusher (IDEP) campaigns on the NIF, for which the term is used in the official campaign names.

1.1.4 ICF facilities

To experimentally achieve the conditions described in Section 1.1 has required the creation and development of high-powered laser technology to produce a drive with sufficient energy, symmetry, and repeatability. This section will provide a brief description of the history and status of experimental facilities for ICF research. The research contained in this thesis has been performed primarily on two of these facilities: the OMEGA laser system at the Laboratory for Laser Energetics (LLE) in Rochester, New York, and the National Ignition Facility (NIF) at Lawrence Livermore National Laboratory (LLNL) in Livermore, California. This section will therefore focus on the capabilities of these two facilities. For a more detailed background and history of experimental ICF, References [39] and [40] are highly recommended.

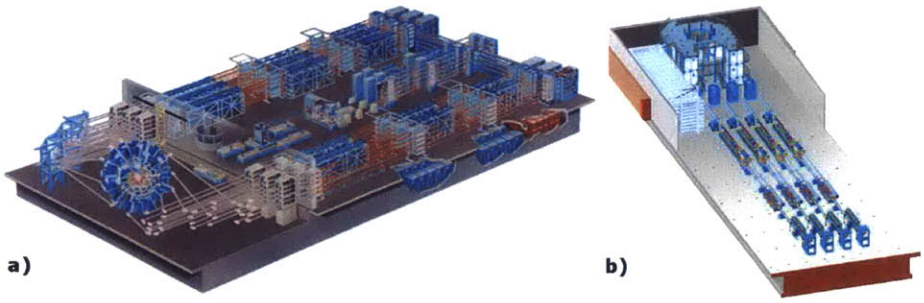

Figure 1.9. Schematic drawings of the laser facilities at the Laboratory for Laser Energetics (LLE) at the University of Rochester in Rochester, NY. a) The 60-beam OMEGA laser delivers 30 kJ of 351 nm laser light in approximately 1 ns. OMEGA is the primary facility for direct-drive ICF research, and has also been instrumental in developing indirect-drive ICF as well as HED physics research since 1995. Significant control over pulse shaping, energy, focusing, and pointing is available, as well as an extensive suite of diagnostics. b) The OMEGA-EP laser offers high-intensity and short-pulse capability. Four long-pulse beams can deliver approximately 4–6 kJ in 1 ns. Two of these beams can be operated in short-pulse mode, delivering 750 J in 10 ps. The two systems may be fired simultaneously in 'joint shot' mode, in which one EP beam is delivered to the OMEGA target chamber. (Images from `http://www.lle.rochester.edu/omega_facility`)

The OMEGA laser

The OMEGA laser was first activated in 1980 as a 24-beam Nd:phosphate-glass laser system, capable of outputting 12 TW of 1054 nm light ('1ω') in 50 ps and over 1.75 kJ total.[41] A 24-beam system was chosen to obtain geometric illumination uniformity of $\pm 10\%$ for a spherical target. By 1986, the system was upgraded to deliver 4 kJ of 1ω light in 1 ns or 2.5 kJ of frequency-converted 351 nm ('3ω') light in 0.7 ns.[42] As discussed briefly in Section 1.1, higher frequency light is absorbed more efficiently and closer to the ablation front, and is thus beneficial for improving absorption efficiency and reducing instability growth in laser-driven ICF applications.

Improved drive uniformity and increased total laser power were identified as the primary upgrades required to attain a goal of compressing a cryogenic DT-filled target to 200× liquid DT density. Two technologies that trade reduced beam coherence for improved uniformity are distributed phase plates (DPP)[43] and beam smoothing by spectral dispersion (SSD),[44] which were developed by LLE and implemented on the 24 OMEGA beams in 1987 and 1989, respectively. Improvement of the total drive energy to the 30 kJ which was predicted to be necessary to meet the compression goal required a full system upgrade.[40] To that end, the 24-beam OMEGA laser was decommissioned in December 1992 to begin construction of an upgraded design. The first target shot of the 60-beam OMEGA upgrade was completed in April of 1995.[45]

The modern 60-beam OMEGA system, shown in Figure 1.9a), is capable of delivering 30 kJ of UV (3ω) light to a target in 0.75 ns. This capability has been the primary resource for the study of direct-drive laser ICF. Since its inception, in excess of 20000 target shots have been performed at the OMEGA facility. OMEGA began direct-drive implosions of cryogenic targets with DT-ice layers in 2006, and by 2008 had demonstrated a compressed fuel density of over 500× the density of liquid deuterium. OMEGA held the record for ICF neutron production ($\sim 10^{14}$) until the NIF began cryogenic layered implosions in 2010. Although 30 kJ is insufficient to reach ignition using direct-drive, the cryogenic program on OMEGA aims to demonstrate hydrodynamically-equivalent performance to a NIF-scale 1.8 MJ igniting direct-drive implosion.[46]

A second laser facility, OMEGA-EP, shown in Figure 1.9b), was constructed side-by-side with

the 60-beam OMEGA system and completed in 2008. OMEGA-EP is capable of delivering four high-intensity beams to the EP target chamber, either in long-pulse (~1 ns) or short-pulse (~10 ps) mode. Alternatively the system can perform a 'joint shot' with the 60-beam OMEGA system, delivering one high-intensity beam to the OMEGA target chamber for short-pulse x-ray backlighting or studies of fast ignition, an alternate ignition approach.

Since 1996, experimental time on the OMEGA facility has been granted to HED physics researchers under the National Laser Users Facility (NLUF) program, funded by the Office of Inertial Fusion of the Department of Energy. This source of experimental time has fueled research in ICF and in related fields of fundamental science in high-energy-density regimes, as well as providing most of the experiments used in this thesis. OMEGA and OMEGA-EP provide flexibility of experimental design by allowing control over the timing, power, pointing, and shaping of individual beams. This flexibility has allowed the OMEGA facility to play a key role in the development of indirect-drive studies in preparation for experiments on the NIF; the exploration of alternate ignition designs, such as fast ignition, shock ignition, polar-direct-drive, and magneto-inertial fusion designs; the measurement of material equations-of-state in extreme pressure and density regimes; the study of astrophysical phenomena such as stellar- and big-bang-nucleosynthesis, plasma shocks and magnetic reconnection; and many more.

The system is designed to support a large and growing number of diagnostics, and to provide a unified platform for diagnostic development. Ten-inch manipulators (TIMs) provide a standardized interface for diagnostics fielded in the target chamber. Six TIMs in the OMEGA target chamber are positioned at various angles around the target and allow control over diagnostic positioning as well as shot-by-shot access to detectors as necessary. Many of the diagnostic techniques used in this thesis are discussed in Section 1.3. Several new diagnostics and diagnostic techniques have been developed using OMEGA experiments as part of this thesis: this work is discussed in Chapter 2.

An excellent summary of the history of the Laboratory for Laser Energetics from 1970 through 2010 is available in Reference [40].

The National Ignition Facility

Research in indirect-drive ICF was grounded in experiments and calculations of radiation (x-ray) driven implosions related to nuclear weapons tests. The conversion of laser light into a broad-band radiation source decouples to some extent the *driver* (e.g. the laser) from the implosion. Thus in the 1970's and 80's, data from underground testing could be directly applied to understanding laser-driven ICF (and heavy-ion driven ICF, when sufficiently intense ion beams become available). The rapid development of high-powered lasers produced a series of laser facilities during this time period, culminating in the ten-beam, 40 kJ Nova laser commissioned at LLNL in 1985. A wide variety of increasingly complex hohlraum and capsule designs were also investigated on these machines to evaluate the behavior and key parameters of indirect-drive ICF: conversion of laser light to thermal radiation, hydrodynamic instability growth and mix, and the production of energetic ('hot') electrons which can preheat the fuel and impede compression. These developments in experiment and theory indicated that marginal ignition and small energy gains would be accessible with a ~ 1–2 MJ laser, driving a hohlraum to 300 eV radiation temperature with implosion velocities of $\sim 4 \times 10^7$ cm/sec. The Department of Energy commissioned a conceptual design report in 1993 for the National Ignition Facility (NIF), a 2.0 MJ indirect-drive laser facility intended to demonstrate laboratory ignition of an indirect-drive ICF implosion.

The majority of indirect-drive research described above was carried out at Lawrence Livermore National Laboratory (LLNL) and Los Alamos National Laboratory (LANL) in a classified setting. Declassification of this work in 1994 led to John Lindl's comprehensive review paper of indirect-drive

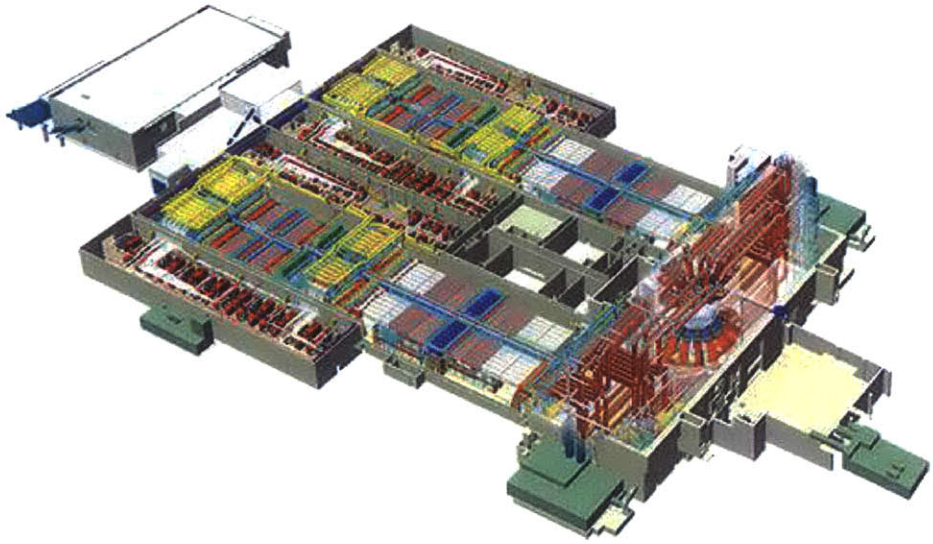

Figure 1.10. A schematic drawing of the National Ignition Facility (NIF) at Lawrence Livermore National Laboratory (LLNL). The NIF can deliver 2.0 MJ in 192 beams to the target chamber. High-contrast and high-precision pulse-shaping have been demonstrated, a necessary element to reach the NIF design goal of indirect-drive ICF ignition. (Image from `https://lasers.llnl.gov/about/what-is-nif`)

ICF (Reference [47]) and the subsequent book (Reference [39]), which also provided a description of the expected performance of the proposed NIF, shown in Figure 1.10. Construction of the NIF began at LLNL in 1997 and was completed in 2009, followed in 2010 by the first laser shot in excess of 1 MJ as well as the first integrated (i.e. including a cryogenic fuel layer) implosion.

The NIF is a 192-beam, 351 nm (frequency tripled) Nd:glass laser system. The beamlines are arranged for indirect-drive with a cylindrically-symmetric hohlraum oriented along the vertical axis. Ninety-six beamlines in each hemisphere are grouped into 24 'quads' with four beams each, which in turn enter the target chamber in four azimuthally-symmetric 'cones' at 23.5°, 30°, 44.5°, and 50° from the axis. The 'inner' cones (23.5°, 30°) are composed of four quads each, while the 'outer' cones (44.5°, 50°) are composed of eight quads each. This arrangement does not allow a true spherically-symmetric drive; however the beams can be individually repointed for non-symmetric 'Polar Direct Drive' (PDD) implosions. The target chamber has been designed such that spherically symmetric direct-drive is possible by reconfiguring 24 quads, should this arrangement be of interest in the future.

To date, the facility has demonstrated the capability of delivering 500 TW of laser power and 1.9 MJ of laser energy to a target. From 2010 to 2013, a series of implosions performed as part of the National Ignition Campaign (NIC) demonstrated orders of magnitude improvement in implosion performance, although ignition was not obtained. The parameter ITFX (Ignition Threshold Factor – eXperimental) was devised as an experimentally observable analog to the ICF Lawson criterion (Equation 1.7) based only on the measured nuclear yield and the ρR, and is defined as follows:[48]

$$\mathrm{ITFX} = \left(\frac{Y_{13-15\ \mathrm{MeV}}}{3e15}\right)\left(\frac{\mathrm{DSR}}{0.073}\right)^{2.3}. \tag{1.13}$$

Here the nuclear yield $Y_{13-15\ \mathrm{MeV}}$ is defined as the measured number of neutrons in the energy range 13–15 MeV, and the down-scattered ratio (DSR) is the ratio of the number of neutrons

scattered into the energy range 10–12 MeV to $Y_{13-15\ \mathrm{MeV}}$. DSR scales approximately linearly with the fuel ρR: DSR $\sim \rho R/(21\ \mathrm{g/cm^2})$, and is the fundamental measured quantity used to infer ρR in experiments. ITFX is defined such that an implosion with ITFX equal to unity has a 50% chance of igniting. An in-depth comparison of ITFX, the generalized Lawson criterion, and other proposed metrics for ICF is available in Reference [49].

From the first layered implosion (NIF shot N100929, ITFX = 0.0014)[e] to the best-performing NIC implosion (N120321, ITFX = 0.1), the ITFX increased by a factor of approximately 70. Subsequent 'high-foot' experiments with increased fuel adiabat (and therefore reduced hydrodynamic instability growth) have reached ITFX $\approx$ 0.4 and demonstrated more energy produced by fusion than was delivered to the fuel by the implosion.[50] Future work aims to demonstrate significant alpha heating and burn of the compressed fuel, through evolution of the successful implosion designs and better understanding and control of failure modes such as mix, implosion asymmetry, and unstagnated fuel flows.

The NIF's versatility and access to high intensities and high energies create opportunities for studying new regimes of fundamental physics. For example, experiments have demonstrated ramp compression of materials to 50 Mbar, for equation-of-state measurements comparable to the centers of gas giant planets.[51] NIF also allows studies of astrophysically-relevant plasmas such as collisionless shocks, nuclear science relevant to nucleosynthesis, and many more fundamental physics experiments. The introduction of petawatt, picosecond beams with the commissioning of NIF ARC in 2015 will enable many unique experiments, including Compton backlighting of high-density imploded capsules and fast ignition.

Understanding of the physics relevant to the HED plasmas produced by indirect-drive ICF depends on the design and implementation of cutting-edge diagnostic instruments. The design and implementation of a CVD-diamond high-voltage diode based nuclear bang-time diagnostic, as well as the upgrade of this diagnostic to measure shock- and compression-bang time on gas-filled hohlraum implosions, constitute a major component of this thesis and a significant contribution to ICF and HED science. The design, analysis methodology, and results of these diagnostics are described in Chapter 2. Development of a novel approach to interpreting secondary nuclear yield data from D_2-filled implosions to obtain information about fuel ρR, electron temperature, and mix has also been performed, and is described in Appendix D.

For more information on the current status of the NIF and the results of the ignition campaign, see Reference [52].

1.2 Hydrodynamics and Implosion Modeling

ICF implosions produce complex and rapidly evolving plasmas, featuring strong gradients in pressure, density and temperature. While certain aspects of these phenomena are accessible to analytical calculation, experiments are often too complicated to design or interpret by hand. For this reason physics simulations play a key role in the study of ICF. For the most part, these simulations follow an average-ion hydrodynamic framework, approximating the plasma as a fluid composed of one type of ion coupled to a fluid of electrons and evolving based on an equation of state.

The main results of this thesis explore experimental scenarios relevant to ICF in which these approximations break down. Hydrodynamic theory and its implementation in hydrodynamic simulations are briefly described in Section 1.2.1. Section 1.2.2 presents several ways in which the

[e]NIF shot numbers take the format NYYMMDD-00X-999, in which the first 6 digits after the N are set by the year, month, and date of the shot; the X is set by the order of this shot in that shot day sequence; and the 999 indicates a system shot, rather than a test. If unambiguous, the middle and last group of digits are removed.

approximations of hydrodynamics have been shown to break down in an ICF context, which will become important in subsequent chapters. In particular, the additional physics of interest discussed here will include ion diffusion and Knudsen-layer ion loss. An additional kinetic model regarding ion thermal decoupling was developed as part of this thesis, and is discussed in Chapter 4.

1.2.1 Hydrodynamic theory

Plasmas are gases of ions and electrons with sufficient energy to avoid recombination. A full dynamical treatment of a plasma would require knowing and calculating the sum total of electromagnetic, radiative, and collisional forces acting on all of the component particles – an incomprehensibly complex problem for the milligram-scale plasmas in an ICF implosion. The plasmas may instead be approximated as a fluid, as long as several limiting conditions are met. The mean-free-path of ions λ_i must be substantially shorter than the gradient scale lengths, and the collision rate of ions ν_{ij} must be substantially faster than the inverse of dynamical timescales. These conditions may be written as:

$$\lambda_i \ll \frac{F}{\nabla F} \ll L, \qquad \nu_i \gg \frac{\partial F/\partial t}{F} \gg \tau^{-1}, \tag{1.14}$$

for plasma conditions F (e.g. pressure, density, etc.), plasma size L, and plasma timescale τ. The two conditions in Equation 1.14 are related, as the mean-free-path is inversely proportional to the collision frequency, and is often defined simply as $\lambda_{jk} = v_{th,j}/\nu_{jk}$. The mean-free-path is more accurately calculated in an analogous way to the collision frequency, from the average rate of change in the momentum density of two colliding particle distributions. This calculation is presented in Appendix A.1 and results in the following expressions:

$$\nu_{jk} = \lambda_{jk}^{-1}\left(\frac{2T_i}{\pi m_r}\right)^{\frac{1}{2}} = \frac{8\sqrt{\pi}}{3\sqrt{2}}\left(\frac{e^2}{4\pi\epsilon_0}\right)^2\left(\frac{m_r}{m_j^2 T_i^3}\right)^{\frac{1}{2}} n_j \ln\Lambda. \tag{1.15}$$

Here the indexes (j,k) refer to colliding species with charge $eZ_{j,k}$ and mass $m_{j,k} \approx A_{j,k}m_p$, and the reduced mass $m_r \equiv (m_j m_k)/(m_j + m_k)$. In multi-species plasmas, a total collision frequency for a single species can be defined as a sum over collision rates with all species: $\nu_j = \sum_k \nu_{jk}$. The total mean-free-path is instead defined as an inverse sum: $\lambda_j^{-1} = (\sum_k \lambda_{jk})^{-1}$. The mass terms indicate that the ion-electron collision rate ν_{ie} is much slower than the ion-ion collision rate ($\nu_{ie} \lesssim \nu_{ii'}\sqrt{m_e/m_i} \approx \nu_{ii'}/43$), whereas the electron-ion collision rate ν_{ei} is much faster ($\nu_{ei} \gtrsim \nu_{ii'}\sqrt{m_i/m_e} \approx 43\nu_{ii'}$). The ions will drag the electrons around without losing or gaining significant momentum from them.

The thermalization rate is calculated as the collision rate for energy transfer, rather than momentum transfer. This rate differs from the collision rate for momentum transfer by a factor of $\nu_{jk,th} = \nu_{jk}2m_j/(m_j + m_k)$. This factor is unity for collisions between particles with identical masses, but scales as the mass ratio when $m_j \ll m_k$. Thus, while electrons lose their momentum to ions rapidly compared to the ion-ion collision rate, they retain their energy for much longer timescales. As a consequence, the electron temperature may not thermalize to the ion temperature during timescales of interest. This is especially true in the ICF context where the electrons absorb the energy from the lasers via inverse bremsstrahlung, and carry this energy to the ablation front where it is transferred to the ablating ions. To account for this, it is necessary to include separate electron and ion temperatures in the fluid theory used for ICF simulations.

If the conditions in Equation 1.14 are satisfied, then the individual particle dynamics do not matter on the experimental time- and length-scales, and the plasma behaves as a fluid with density ρ, pressure p, and internal energy e. Under these conditions, the conservation of mass, momentum,

and energy can be written generally as follows:

$$\frac{D\rho}{Dt} + \rho\nabla\cdot\vec{v} = 0, \tag{1.16}$$

$$\frac{D\vec{v}}{Dt} = -\frac{1}{\rho}\nabla p, \tag{1.17}$$

$$\frac{De}{Dt} + p\frac{D}{Dt}\left(\frac{1}{\rho}\right) = -\frac{1}{\rho}\nabla\cdot\vec{q} + \frac{1}{\rho}\mathcal{P} \tag{1.18}$$

where $D/Dt = (\partial/\partial t + \vec{v}\cdot\nabla)$ is the convective derivative, describing the total change of a local quantity in its reference frame; $\vec{q}$ is heat current; and $\mathcal{P}$ is external energy sources. In these equations, the plasma properties are shown on the left and source terms are shown on the right.

To solve these equations, $\vec{q}$ and $\mathcal{P}$ must be given in terms of the dynamical variables, and the relationship between pressure, density and temperature ('equation of state' or EOS) must be determined. In the limit of local heat conduction, the heat flux is given by $\vec{q} = -\chi(\rho, T)\nabla T$, where χ is the heat conductivity. Often the Spitzer form of heat conductivity is used, though in practice a 'flux limiter' is required to prevent unphysical heat conduction at strong gradients. In radiation-hydrodynamic simulations of ICF implosions, the energy source $\mathcal{P}$ can be calculated based on the absorption of laser light into the plasma via inverse bremsstrahlung. Such calculations have required detailed ray-tracing of the laser vector as it traverses the plasma and is bent by gradients in the local index of refraction. Finally, for fully ionized classical plasmas the ideal EOS ($p = nT$) may be used. However for compounds, high-density plasmas, warm-dense matter, and other complex states, an EOS lookup table based on a combination of theory and experimental measurements is often used.

Notably, the momentum equation as presented (Eqn. 1.17) lacks any force terms related to electromagnetism. This negligence of electromagnetic effects is common to most of the hydrodynamic codes used in ICF simulations today. Intuitively, electric and magnetic fields may be expected to play a significant role in the evolution of a plasma, since plasmas are composed of charged particles, conduct currents and transmit electromagnetic waves. In fact, experiments have demonstrated large electric fields at shock fronts,[33] large magnetic fields (produced by laser-produced plasmas) in hohlraums,[34] and magnetic fields around ablative RT instability spikes,[53] all scenarios which are highly relevant to ICF. The willingness to ignore electric fields probably arises from the fact that electron plasma frequencies are generally greatly in excess of 10^{13} Hz [i.e. $(0.1\text{ ps})^{-1}$] in ICF scenarios, which is orders of magnitude larger than dynamical timescales. This fact leads to expectation that electric fields are rapidly eliminated and quasineutrality of the plasma is a good assumption. Ignoring magnetic effects is likely a consequence of the fact that they cannot be modeled in 1D simulations. Since magnetic forces always accelerate perpendicular to the velocity (according to the Lorentz force: $F_B \propto \vec{v}\times\vec{B}$), they require at least two dimensions to operate. Magnetic forces simply cannot be captured in a spherically-symmetric scenario. Estimates of the plasma β, defined as the ratio of plasma pressure to magnetic pressure, evaluate how important the magnetic effects are to the evolution of the plasma. While in the study of RT-induced magnetic fields,[53] β was estimated to be much greater than 1 during the early stages observed and magnetic evolution did not significantly impact the hydrodynamic evolution, a study of laser-plasma production from a solid foil[54] determined that $\beta \sim 1$ and magnetic terms should be significant in their evolution. Two-dimensional simulations could capture some of the magnetic dynamics: for example, azimuthal magnetic fields and perpendicular currents could drive radial acceleration; however magnetic forces are fundamentally a 3D effect. Some recent work includes magnetohydrodynamic

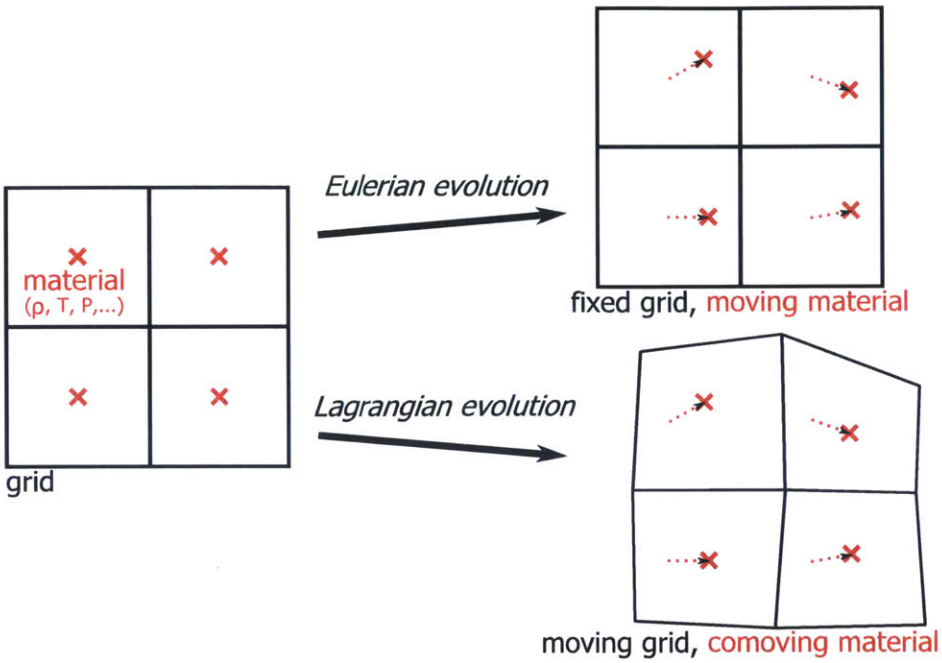

Figure 1.11. Cartoon of the Eulerian and Lagrangian formulations used in hydrodynamic simulations. The initial conditions include a grid (or mesh) defining the spatial coordinates and a description of the material properties at a number of points. The hydrodynamic equations describe the time evolution of these material properties. In the Eulerian framework (top right), the spatial grid does not change with time, and the mass elements move in relationship to the grid. The Eulerian framework has no mesh distortion, but interfaces between different materials are difficult to follow. In the Lagrangian framework (bottom right), the spatial grid is comoving with each mass unit, and mass does not flow across the grid boundaries. The Lagrangian framework intrinsically tracks interfaces, but in multiple dimensions the mesh can become severely distorted over time, requiring rezoning.

effects in multi-dimensional ICF simulations, for example using the 2D-DRACO code to explain radiography results demonstrating magnetic fields around the target stalk.[55]

The formulation in Eqns. 1.16-1.18 is referred to as the *Lagrange representation.* The use of the convective derivative throughout simplifies calculations of the change in the properties of a fundamental 'mass element.' In this formulation, position and velocity are treated as properties of a mass element, along with pressure, density, and temperature. Many radiation-hydrodynamic simulations use a Lagrangian framework, which to zeroth order is the simplest frame of reference in which to treat conservation of momentum and plasma composition. Lagrangian simulations also natively track the boundaries between different materials, such as the fuel and shell of an ICF implosion. The alternate definition, in which the reference frame is fixed in space and composition changes, is referred to as the *Eulerian representation.* The Eulerian formulation has an advantage in multi-dimensional simulations, as rotations of the fluid, which are allowed in more than one dimension, can evolve highly complex mass-element boundaries that become difficult for the Lagrangian framework to track. Figure 1.11 presents a comparison of the evolution of the simulation grid and materials under these two frameworks. In practice, an 'arbitrary Lagrangian-Eulerian' (ALE) framework is employed in modern multi-dimensional codes, in which both the grid and the material nodes may be transformed to obtain some of the computational benefits of both the Eulerian and Lagrangian formulations. The details of hydrodynamic simulation algorithms are beyond

Table 1.1. A summary of modern hydrodynamic simulation codes in common use in the fields of ICF and HEDP. All listed codes include planar, cylindrical, and spherical geometry, and simulate coupled ion and electron fluids and radiation fields; fluids have independent temperatures but not necessarily independent momentum transport. Reference numbers are provided in the Name column for more information, where available.

Name	Dimensions	Formulation	Additional Physics
HYADES[25]	1D	Lagrangian	–
LILAC (LLE)	1D	Lagrangian	3D ray-tracing, CBET
DRACO (LLE)[57]	2D,3D	Eulerian or ALE	3D ray-tracing, MHD
LASNEX (LLNL)	1D,2D	Lagrangian	diffusion
ARES (LLNL)	1D	Lagrangian	–
HYDRA (LLNL)[58]	2D,3D	ALE	3D ray-tracing, CBET, resistive MHD

the scope of this work, but information on the mathematical basis of ALE simulations may be found in Reference [56]. A summary of some modern hydrodynamic simulation codes used in ICF and their physical bases is presented in Table 1.1.

Hydrodynamic shocks

The presence of shocks in ICF implosions has been introduced previously, both for the compression of cryogenic fusion fuel in Sec. 1.1.2 and the discussion of shock-driven implosions in Sec. 1.1.3. A shock occurs in a fluid wherever a discontinuity in the pressure and density is allowed to propagate. The equations governing the properties of a hydrodynamic shock can be derived by establishing such a discontinuity, and enforcing the continuity equations (1.16-1.18) across the boundary. This exercise produces the *Rankine-Hugoniot jump conditions*, written here in the frame-of-reference of the shock:[11]

$$\rho_1 u_1 = \rho_2 u_2, \tag{1.19}$$

$$\rho_1 u_1^2 + p_1 = \rho_2 u_2^2 + p_2, \tag{1.20}$$

$$\rho_1 u_1 \left(e_1 + \frac{u_1^2}{2} + \frac{p_1}{\rho_1} \right) = \rho_2 u_2 \left(e_2 + \frac{u_2^2}{2} + \frac{p_2}{\rho_2} \right), \tag{1.21}$$

where ρ is density, u is fluid velocity, p is pressure, e is internal energy, and subscript 1 (2) indicates the fluid upstream (downstream) of the shock. These equations can be closed by assuming an ideal gas, for which $e = P/[\rho(\gamma - 1)]$. This leaves three equations in six unknowns (density, pressure, and fluid velocity on either side of the shock). Typically the fluid velocities are not of interest and are eliminated from the equations, resulting in the following two, equivalent representations:[11]

$$\frac{\rho_2}{\rho_1} = \frac{\frac{p_2}{p_1}(\gamma + 1) + (\gamma - 1)}{(\gamma + 1) + \frac{p_2}{p_1}(\gamma - 1)}, \tag{1.22}$$

$$\frac{p_2}{p_1} = \frac{\frac{\rho_2}{\rho_1}(\gamma + 1) - (\gamma - 1)}{(\gamma + 1) - \frac{\rho_2}{\rho_1}(\gamma - 1)}. \tag{1.23}$$

These equations describe the jump in density at the shock front in terms of the jump in pressure, or vice versa, and were used to plot the curve shown in Fig. 1.4.

The strength of the shock is most readily described in terms of the shock speed. Equations 1.19-1.21 are written in the frame-of-reference of the shock, but in the lab frame of an ICF implosion, $u_1 = 0$. Transforming into this reference frame, the shock speed u_{sh} can then be calculated as a function of the pressure or density jump at the shock front. In practice, the dimensionless Mach number M defined as the ratio of the shock speed to the upstream sound speed ($c_1 = \sqrt{\gamma p_1/\rho_1}$) is a valuable metric of shock strength. The jump equations can then be rewritten in terms of the Mach number:

$$\frac{\rho_2}{\rho_1} = \frac{(\gamma+1)M^2}{(\gamma-1)M^2+2}, \tag{1.24}$$

$$\frac{p_2}{p_1} = \frac{2\gamma M^2-(\gamma-1)}{(\gamma+1)}. \tag{1.25}$$

This form makes clear the behavior of the density and pressure jump in the limits of small and large Mach number. For strong shocks ($M \gg 1$), the pressure continues to increase as M^2, while the density approaches a limiting value, $(\gamma+1)/(\gamma-1)$, which equals 4 for an ideal gas. For weak shocks ($M \approx 1$), both the density and pressure jumps approach unity, as expected.

The equations presented above follow from the hydrodynamic equations, but only describe the fluid on either side of the shock. The structure of the shock itself is not treated directly. Shock structure is set on the scale of the mean-free-path of the shocked (downstream) ions. This is because the processes that compress the upstream fluid must happen on the length-scale of collisions between high-density and low-density ions. The structure of plasma shocks was first studied by Jaffrin and Probstein,[59] who predicted the shock width was a few times the ion mean-free-path λ_{ii} based on fluid theory. Subsequent theory and kinetic simulations have demonstrated that the kinetic streaming of ions into the low-density gas plays a strong role in the structure of shock front.[60] Kinetic simulations show that the shock front width in a plasma is on the order of $\lambda_{ii}\sqrt{m_i/m_e} \sim$ 40 to 60 times the ion mean-free-path.[61]

The shock-front structure is also made more complex by the electron fluid. Electrons in the shocked plasma are effectively free to stream into the unshocked plasma, because their mean-free-path is longer than that of the ions. The excess electron density in front of the ion shock establishes an electric field, which provides a restoring force. The electric potential jump at the shock front due to this effect has been shown to scale with the shocked electron temperature as $\Delta\Phi_{sh} \approx (T_e/e)\ln(\rho_2/\rho_1)$.[62] This effect has been used to explain the strong ($\sim 10^9$ V/m) electric fields that have been observed at shock fronts in ICF implosions.[63]

Because of the strong gradients at a shock front, a shock in a multiple-ion species plasma may also be expected to produce separation of ion species. Such ion species separation occurs via diffusive mechanisms, which will be discussed next.

1.2.2 Relevant extensions of hydrodynamic theory

In Section 1.2.1 the basic underlying formulation of hydrodynamics was presented. Kinetic extensions of hydrodynamic theory have been developed to address situations in which the ion-ion mean-free-path approaches the dynamic scale lengths of the experiment. This section presents two such extensions, ion diffusion and Knudsen-layer ion loss, which are relevant to the experiments discussed in this thesis because they affect the plasma composition and the fusion reactivity.

Ion diffusion

Ion diffusion describes the process through which the kinetic motion of individual particles transports them relative to the bulk flow of the surrounding plasma. In a collisional plasma, the scale length for directional particle travel before the path is randomized by scattering is the mean-free-path λ_i as defined in Equation 1.15 and Appendix A.1. Ion diffusion can be modeled as a random walk with a step length λ_i. Random walks are a well-known statistical problem for which the average distance of a walker from the starting point scales as $\sigma \propto \lambda\sqrt{N}$ for a step-size λ and N total steps. Since the average collision time is also known ($\tau_i = \nu_i^{-1}$), the diffusion length may also be written as a function of time: $\sigma \propto \lambda_i\sqrt{t/\tau_i}$. This discrete formulation is equivalent to the continuum expressions referred to as Fick's Laws:

$$\vec{J_i} = -D\nabla n_i, \tag{1.26}$$

$$\frac{\partial n_i}{\partial t} = D\nabla^2 n_i, \tag{1.27}$$

where n_i is the density of species i, and $\vec{J_i}$ is the diffusive flux of species i in units of $\mathrm{cm}^{-2}\ \mathrm{s}^{-1}$. Intuitively, the diffusion flux indicates the rate at which the diffusing quantity n_i moves, such that $\vec{J} = n_i v_{dif}$ for some diffusion speed v_{dif}. The diffusion coefficient D has units of cm^2/s, and in plasmas is calculated from Fokker-Planck kinetic theory. A formula for D is given in Reference [64] as follows:

$$D = 9\sqrt{\frac{\pi}{2}}\frac{\lambda_{De}^2\omega_{pe}N_{De}}{\ln\Lambda}, \tag{1.28}$$

where λ_{De} is the Debye length, $\omega_{pe} = (4\pi n_e e^2/m_e)^{1/2}$ is the electron plasma frequency, $N_{De} = (4\pi/3)n_e\lambda_{De}^3$ is the number of electrons in a Debye sphere (the 'plasma parameter'), and $\ln\Lambda$ is the Coulomb logarithm.

While in a uniform plasma individual particles are identical, diffusion governs the admixture and transport of non-uniform distributions of ions relative to the bulk flow. Typically, diffusion relaxes a concentration gradient toward uniformity: for example, in an ICF implosion, the initially sharp boundary between the fuel and the shell will mix via ion diffusion. However, strong gradients in pressure, electric potential, and temperature can also create and increase gradients in ion species fraction in a plasma with multiple ion species.[f] This process, sometimes referred to as 'species separation,' is also a diffusively-driven process, and is often distinguished by what type of gradient is causing the separation: barodiffusion for pressure gradients, electrodiffusion for electric-field gradients, and thermodiffusion for temperature gradients. The mass flux due to ion diffusion in a plasma composed of two ion species (1 and 2, where by convention 1 is the lighter ion species) can be generally written as follows (adapted from Reference [65]):

$$\vec{i_1} = -\rho D\left(\nabla c + k_p\nabla\log p_i + \frac{ek_E}{T_i}\nabla\Phi + k_T^{(i)}\nabla\log T_i + k_T^{(e)}\nabla\log T_e\right) = -\vec{i_2}. \tag{1.29}$$

Here the diffusive mass-flux for the light-ion species $\vec{i_1}$ is written in terms of gradients in the light-ion mass concentration $c = \rho_1/\rho$, the ion pressure p_i, the electric potential Φ, and the ion and electron temperatures $T_{i,e}$. The coefficients $k_p, k_E, k_T^{(i)}$ and $k_T^{(e)}$ are generally functions of the

[f] More generally, each of these terms has an impact on the local chemical potential of the plasma. Diffusive mass flux arises from the relaxation of chemical potential gradients.

ion mass concentration as well as the ion masses and charges. In addition, the thermodiffusion coefficients depend on the detailed physics of collisions that must be calculated kinetically. The derivation of these coefficients is the subject of Reference [65] and several preceding works.[64,66,67]

The formulation of ion diffusion in Equation 1.29 is explicit and predictive, but is only valid for diffusion in a two-species plasma. The conservation of mass flux in the comoving frame implied by the condition $\vec{i_1} + \vec{i_2} = 0$ can be directly extended to three species.[g] However there is not an obviously self-consistent way to mathematically extend the diffusion coefficients to more than two species. Both the thermal force between two species and the dynamic friction between two species are affected by the presence of additional species. A more general, n-species formulation would have to be fully derived from the individual momentum equations, which has not been done.[68]

Given a formula for the ion diffusion mass flux such as Equation 1.29, it can be discretized and incorporated in a hydrodynamic simulation to redistribute ion species density. In the Lagrangian formulation where units of mass are followed, the expected mass flux at each zone boundary can be calculated by evaluating the gradients and coefficients at the boundary. The mass flux into and out of each zone is then adjusted prior to the next timestep. Ion diffusion models have been incorporated into some of the codes listed in Table 1.1, including ARES and LASNEX. The form presented in Equation 1.29 is relatively new, and has not at the time of this writing been incorporated into hydrodynamic simulations. Comparable formulations similar to those developed by Zel'dovich and Raizer[69] and Landau and Lifshitz[70] have been incorporated into the simulations.[71] As has been noted, such formulations are only technically applicable for the number of species for which they are derived, although in the interest of generality they have been applied to whatever species are simulated. A flux-limited version has been developed as one of several approximate or "reduced" ion kinetic (RIK) models in hydrodynamic simulations by Nels Hoffman.[72] This diffusion model includes a scalar multiplier to provide arbitrary control over the magnitude of the effect in simulations, as the discussion over appropriate diffusion coefficients is an area of active development.

In multi-dimensional simulations, the plasma must be occasionally rezoned to prevent complex distortion of the mesh. Rezoning algorithms average the material from multiple zones into a new zone with simpler geometry. Near an interface, rezoning can cause artificial 'diffusion' by mixing various ion species. This diffusion is entirely numerical in nature and is not based on any physical formulation. Users should be cautious not to ascribe undue physical significance to these effects.

Knudsen-layer ion loss

Assuming the scale size of an ICF experiment is given by L, ions within a mean free path λ_i of the boundary may be expected to escape the experiment. This effect is quantified by the *Knudsen number* $N_k = (\lambda_i / L)$, named after Danish physicist Martin Knudsen who studied the vapor layer that develops near a liquid/gas boundary.

Even in plasmas with small Knudsen numbers $N_k \ll 1$, ion loss can be expected to play an important role. The thermal mean-free-path, which is described in Eqn. 1.15, increases with the temperature squared. While that formula is averaged over the thermal distribution, more generally the mean-free-path of an individual particle also scales with the particle's energy squared:

$$\lambda_i(\epsilon) = \lambda_i(T_i) \left(\frac{\epsilon}{T_i} \right)^2 . \tag{1.30}$$

Thermal distributions are characterized by a Maxwell-Boltzmann distribution of the plasma

[g]This condition derives from the distinction between diffusive mass flux and flow velocity. Diffusion is defined in the comoving frame; any total mass flux is captured in the fluid dynamics.

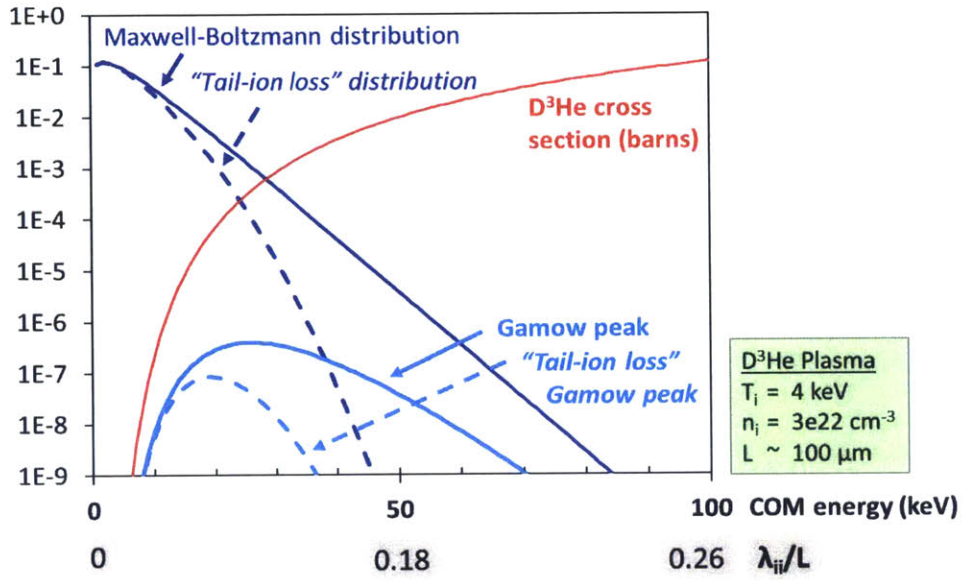

Figure 1.12. The ion distribution (blue) as a function of ion kinetic energy in a plasma with an ion temperature of 4 keV, a density of 3×10^{22} cm^{-3}, and a scale length $L \sim 100$ μm. The standard Maxwell-Boltzmann thermal distribution (solid) is modified by the effect of Knudsen-layer tail-ion loss (dashed, following Reference [73]). Although L is much longer than the thermal ion-ion mean-free-paths ($\lambda_{ii,th} \sim 4$ μm), the mean-free-path λ_{ii} increases with the ion energy squared so higher energy ions can more readily escape. The distribution function is multiplied by the D^{3}He-fusion cross section (red) to obtain the distribution of fusing ions, known as the Gamow peak (cyan). For the thermal distribution, the largest number of fusion reactions occur at a 26 keV center-of-mass energy ($6.5 \times T_i$). The modified tail-ion loss distribution has a dramatically reduced area under the Gamow peak (cyan dashed), which reduces the effective fusion reactivity by a factor of 10, and moves the Gamow peak maximum energy to 19 keV ($4.75 \times T_i$).

ions. The particle distribution is described as follows:

$$f(v, n, T) = n \left(\frac{m}{2\pi T}\right)^{3/2} \exp\left(-\frac{mv^2}{2T}\right) d^3v. \tag{1.31}$$

The implication of Eqns. 1.30 and 1.31 is that the mean-free-path of the bulk ions may be small enough that they are collisionally confined, while the ions on the high-energy tail of the Maxwellian distribution are comparable to the plasma scale lengths. This effect, referred to as *Knudsen layer ion loss*, can lead to the loss of tail ions and the distortion or truncation of the local Maxwellian distribution.

The loss of tail ions from the fuel is not necessarily a significant mechanism for energy or mass loss from the local plasma over short timescales and for small Knudsen numbers. However this distortion can have a disproportionate impact on the fusion reactivity of the plasma. As discussed in Section 1.1.1, the rapid increase in the fusion cross-section with the collisional center-of-mass energy implies that the mean energy of fusing particles in a thermal plasma (e.g. the *Gamow peak energy*, ϵ_G) is normally several times the plasma ion temperature. The loss of tail ions thus directly inhibits the fusion reactivity of the plasma even for plasmas with small N_k. A representative calculation of this effect in a shock-driven D^{3}He plasma is shown in Figure 1.12.

This effect was identified by A.G. Petschek and D.B. Henderson in the 1970s[74] and the im-

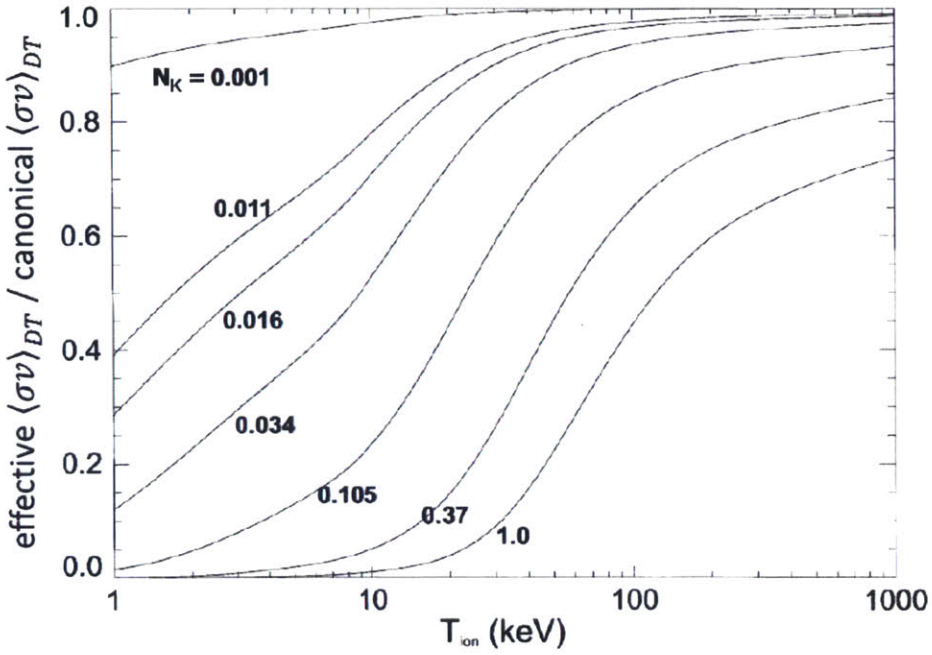

Figure 1.13. Effective D-T fusion reactivity relative to its canonical value as a function of ion temperature and Knudsen number ($N_K = \lambda_i/L$). Ions with energy several times the thermal energy dominate fusion processes. Because the mean-free-path of ions scales with their energy squared, substantial reactivity reduction can occur for Knudsen numbers on the order of a few percent. Figure adapted from Reference [73].

pact of Knudsen number on the effective fusion reactivity was quantified recently by Kim Molvig and colleagues.[73] A modified Knudsen number-dependent distribution function was derived for a spherical geometry. As shown in Figure 1.13, at temperatures of relevance to fusion even Knudsen numbers as low as $N_k = 0.01$ can have a significant impact on the reactivity. This effect has been incorporated into hydrodynamic simulations by Nels Hoffman as one of a set of approximate or "reduced" ion kinetic models (RIK).[72] The RIK simulations are applied to model the experiments in this thesis.

Both ion diffusion and Knudsen-layer ion loss occur when the ion-ion mean free path λ_i is smaller than but approaching the scale size of the experiment. In this sense they are *transitional* kinetic effects, evident in plasmas where the bulk behaves hydrodynamically. If the collision time (the inverse of the collision rate described in Eqn. 1.15) is long relative to dynamical timescales, the plasma becomes *fully* kinetic. In this regime, the hydrodynamic equations do not adequately describe even the bulk plasma evolution. One such fully kinetic effect is ion thermal decoupling, which was developed as part of this thesis and is discussed in Chapter 4. Several fully kinetic codes are beginning to be applied to ICF-relevant conditions; these simulations solve the Vlasov-Fokker-Planck equation to evaluate the particle distributions directly[75,76] or use a particle-in-cell (PIC) approach.[61] Initial results are promising, however the computationally intensive nature of such simulations has limited the scope of their application.

1.3 Diagnostic Techniques for ICF and HED Plasmas

The experiments and diagnostics developed and presented in this thesis build upon previous work in the fields of HED plasma physics and ICF. This section describes several of the diagnostics used in this work, and presents their history and operational principles. The diagnostics and techniques presented here will be used throughout this thesis, and form the basis for the new diagnostic developments which are presented in Chapter 2.

Several nuclear diagnostics recording both neutrons and charged particles have been instrumental in successfully performing the experimental work described in this thesis. The fusion reactions listed in Equation 1.2 produce nearly monoenergetic charged and neutral particles, many of which escape the experiment. Measurements of these particles can provide valuable information about both the plasma that generated them and the environments they encountered on their way to the detector.

This section begins by discussing what information can be obtained from nuclear spectra, and then describes specific diagnostic techniques to obtain these spectra and histories. Most of the charged particle diagnostics discussed here are based on the solid-state nuclear track detector CR-39. The properties of CR-39 are discussed first, followed by its application in the Charged Particle Spectrometers (CPS1 and CPS2) at OMEGA, the Wedge Range-Filters (WRF) at OMEGA and the NIF, and the Proton Core Imaging System (PCIS) at OMEGA. Next the information contained in time-resolved measurements of nuclear emission are discussed. Scintillator-based nuclear spectral and timing diagnostics are described, including the neutron Time-of-Flight (nTOF) diagnostics at OMEGA and NIF and the neutron- and proton-temporal diagnostics (NTD and PTD) at OMEGA. Lastly, the use of chemical vapor deposition (CVD) diamond wafers as a high-voltage diode for measurements of ionizing radiation are introduced, as this technology forms the basis for the particle Time-of-Flight (PTOF) diagnostic described in Chapter 2.

1.3.1 Information contained in the fusion-product spectra

The fusion reactions presented in Equation 1.2 indicate the nominal kinetic energies of the fusion products, which depend on the Q values of the reactions and the relative masses of the products. More specifically, these values are calculated using the energy and momentum balance of the reaction: for the fusion of two particles (1,2) generating two products (3,4), the energy of one of the products in the center-of-mass frame is given by $E_3' = (Q + K)m_3/(m_3 + m_4)$, where $K = m_{r,12}v_{r,12}^2/2$ is the kinetic energy of the reactants in the center-of-mass frame. The relative velocity is $\vec{v}_{r,ij} = (\vec{v}_i - \vec{v}_j)$, and primes designate the center-of-mass frame. However the energy observed by the diagnostic instruments must be calculated in the lab frame. Assuming the reaction's center-of-mass velocity is given by $\vec{V}_{COM}$, the total velocity of the product in the lab frame is $\vec{v}_3 = \vec{V}_{COM} + \vec{v}_r' m_4/(m_3 + m_4)$. Neglecting relativistic effects, the energy of this product in the lab frame is then:

$$E_3 = \frac{1}{2}m_3 v_3^2 = \frac{1}{2}m_3 V_{COM}^2 + \frac{m_4}{m_3 + m_4}(Q + K) + V_{COM}\cos\theta\left[\frac{2m_3 m_4}{m_3 + m_4}(Q + K)\right]^{\frac{1}{2}}. \quad (1.32)$$

The angle between the center-of-mass velocity and the relative particle velocity has been defined such that $\vec{V}_{COM} \cdot \vec{v}_r = V_{COM} v_r \cos\theta$. In plasmas, the reactant particles will have energy a few times the thermal energy, and $K < 100$ keV which is negligible compared to $Q \sim 10$ MeV. Similarly, the thermal average center-of-mass energy represented by the first term on the right-hand side is typically negligible. However the final term represents a non-negligible correction to observed

energy. An approximate simplified formula is as follows:

$$E_3 \approx \frac{Qm_4}{m_3+m_4} + V_{COM}\cos\theta\left[\frac{2Qm_3m_4}{m_3+m_4}\right]^{\frac{1}{2}}. \tag{1.33}$$

To determine the observed fusion spectra, the formula in Equation 1.32 must be averaged over the distributions of fusing particles. In thermal plasmas the angular term has no preferred direction and the energy of individual products can be either boosted or reduced by this correction. The net result is a broadening of the total spectrum, sometimes referred to as *Doppler broadening.* The amount of spectral broadening was first calculated by H. Brysk in Reference [17]. By taking the 2nd spectral moment of Equation 1.32, Brysk demonstrated that the spectral distribution is approximately a Gaussian in energy space with width $\sigma_3^2 = 2m_3T_i\langle E_3\rangle/(m_3+m_4)$. Here, T_i is the ion temperature of the fusing plasma, and $\langle E_3\rangle$ is the mean product energy in the lab frame (to first order, $\langle E_3\rangle \approx Qm_4/(m_3+m_4)$).

By measuring the fusion spectra, we can therefore learn about not only the nuclear yield, but also the ion temperature of the fusing plasma. For a sense of scale, consider the D-D reaction, which produces a neutron and a ^{3}He ion and has $Q \approx 3.27$ MeV. The mean neutron energy is 2.45 MeV, and the thermal broadening of the spectral peak is $\sigma \approx \sqrt{T_i/\text{keV}} \times 35$ keV. This translates into spectral full-width at half maximum (FWHM $= \sigma\sqrt{8\ln(2)}$) of FWHM $\approx \sqrt{T_i/\text{keV}} \times 82$ keV. Spectral widths on this scale can be measured with existing technology, which is described below. Relativistic corrections to the mean energy, spectral width, and spectral skew of the fusion products was calculated by L. Ballabio, et al. in Reference [77], which is used for measurements of the ion temperature throughout this work.

As fusion products leave the implosion, scattering and interaction with electromagnetic fields change their energy. Charged particles in particular are susceptible to ranging in plasmas, as they lose energy to Coulomb collisions with other charged particles. Energy straggling from these collisions will broaden the spectrum if the particles are downshifted by a significant fraction of their birth energy. In many experiments, evolution of the ρR with time also introduces a time-dependent downshift that tends to dominate the thermal broadening of the spectrum. Since the birth energy is known a priori to high accuracy,[h] the energy downshift of fusion products can be used to infer the areal density (ρR) of the implosion. This approach has been used on both OMEGA and NIF for measurements of the total areal density at bang-time,[78,79] and is viable up to areal densities of ~ 300 mg/cm^2.

Neutrons interact much less strongly than charged particles since they only scatter via nuclear interactions. In general, most neutrons will escape an ICF implosion without scattering. However in high-areal density implosions, measurements of the downscattered neutron spectrum can provide information on the areal density of the implosion at burn. The fuel and the ablator materials have different characteristic cross-sections for neutron scattering as a function of angle, and so information about both features may be obtained. This principle has been implemented on both OMEGA and the NIF using the Magnetic Recoil Spectrometer (MRS).[16]

Shock-driven implosions have little areal density at peak compression ($\rho R \lesssim 1$ mg/cc), and so energy downshifts in these implosions are often negligible. Due to capsule charging, upshifts of the emitted fusion products on the order of ~0.5 MeV are often observed if bang-time occurs while the laser is still on.[80] In charged particle radiography experiments, fusion products from a shock-driven backlighter transit a plasma of interest and are recorded. The energy downshift in the plasma of

[h] A small upshift in the birth energy ($\sim$ 10's of keV) is also produced by the thermal kinetic energy of the plasma, which is represented by the terms including K and V_{COM}^2 in Equation 1.32. Ballabio, et al. characterizes this upshift in Reference [77], and it is included in all spectral modeling in this thesis.

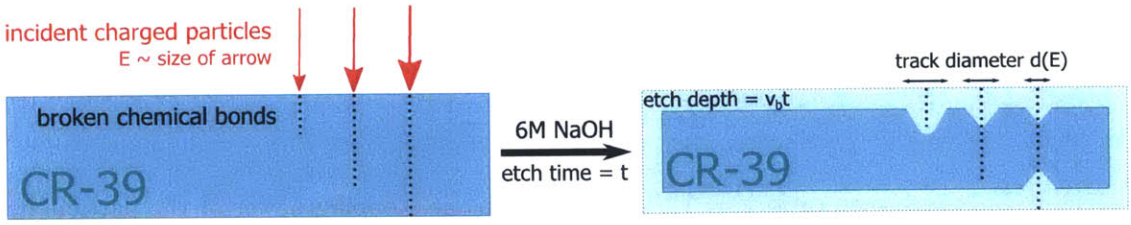

Figure 1.14. Schematic of charged particle detection using the solid-state nuclear track detector CR-39. Incident charged particles leave trails of broken chemical bonds in the plastic. When etched in 6-molar sodium hydroxide (NaOH), the etch rate along the trails (V_t) is faster than the bulk etch rate of the plastic (V_b), forming conical pits with central angle set by $\sin\theta = V_b/V_t$. The diameter of these tracks depends on the bulk etch rate and the bulk-to-track etch rate ratio, as described in Equation 1.34. Since the etch rate ratio is a function of particle stopping power, the track diameter is a function of incident particle energy for a given species of charged particle. Particles that transit the CR-39 can form tracks on both sides.

interest may then be measured.

Certain of the fusion reactions in Equation 1.2 produce high-energy particles that are themselves fusion reactants. In particular, the D-D fusion reaction produces both a 1.01 MeV triton and an 0.82 MeV helium-3 ion. As these particles transit and slow down in the deuterium fuel, they have an opportunity to undergo fusion with field deuterons. These are referred to as *secondary fusion reactions*, and will be discussed in more detail in Appendix D where an analysis method for determining fuel ρR, T_e, and/or mix using multiple secondary yields is developed. In brief, the number of secondary reactions scales with the primary fusion yield and the areal density of deuterium in the implosion. If the plasma is dense enough that the reactants are ranged out, then the secondary yield saturates at a value dependent on the stopping power of the plasma. The center-of-mass velocity of secondary reactions is much higher than that of thermal reactions, so the typical spectrum of secondary products is several MeV wide.[81]

1.3.2 Detecting charged particles with CR-39

CR-39 is a transparent, rigid plastic used extensively as a solid-state nuclear track detector for charged particle measurements in ICF and HED experiments. The chemical structure of CR-39 is $C_{12}O_7H_{18}$, with a density of 1.30 g/cm^3. CR-39 is typically manufactured in sheets of either 1 or 1.5 mm thick and laser cut to appropriate shapes for a variety of applications. The CR-39 used in this work was manufactured by Track Analysis Systems, Ltd.[82]

A schematic of the method of detecting charged particles using CR-39 is shown in Figure 1.14. When charged particles with energy on the order of MeV strike the CR-39, they slow and stop in the plastic primarily through collisions with electrons. These collisions break chemical bonds along the path of the incident particle. Liberated electrons can cascade and deposit the released energy more broadly. When exposed to sodium hydroxide (NaOH), the bulk of the plastic is removed slowly, but the trails of broken chemical bonds are removed much more rapidly.[83] This combination generates conical pits or 'tracks' where the energetic charged particle was incident, with diameters on the order of 10 microns, which are readily visible under a microscope.

The diameter of the resulting track depends sensitively on the track- and bulk-etch rates of the plastic (V_t and V_b, respectively), and on the amount of time for which it was etched. Assuming

normally incident particles, the diameter of a track may be estimated as:[84]

$$D = 2V_b t\sqrt{\frac{V_t/V_b - 1}{V_t/V_b + 1}}. \tag{1.34}$$

The track-to-bulk etch-rate ratio $V = V_t/V_b$ depends on the stopping power of the particle in the plastic. In principle this means that the track etch rate changes along the path of a single track. In practice, the range of high-energy particles in the CR-39 is often much larger than the amount of plastic removed by standard etching ($\sim$ 10 μm), so changes in the stopping power are ignored. An empirical formula for the scaling of etch rate ratio with stopping power is as follows:

$$V = \frac{V_t}{V_b} = 1 + k\left(\frac{dE/dx_{\text{elec}}}{[\text{keV}/\mu\text{m}]}\right)^n, \tag{1.35}$$

where k and n are free parameters and the electronic stopping power dE/dx_{elec} is evaluated at the surface in units of keV/μm. Typically k = 0.002 and n = 1.9 are good values for CR-39 etched in 6-molar NaOH at 80° Celsius, as has been done for all data in this thesis.[85]

The implication of Equations 1.34 and 1.35 is that both different particle species and different particle energies can be distinguished by track diameter. The variation of track diameter with energy is captured in a diameter-vs-energy or "D vs E" curve, which has been calibrated for protons in the range 1–9 MeV.[86] This curve allows direct spectroscopy of particles observed using CR-39, although the accuracy of this technique is limited due to piece-to-piece variation, changes in the calibration due to environmental effects such as exposure to vacuum for long periods of time,[36] or exposure to x-rays.[87] Instead, CR-39 is typically used as the detector component in spectrometer instruments which analyze the energy of incident particles using other means.

CR-39 has several additional benefits for its use as a nuclear track detector in ICF applications. It is 100% quantum efficient for the detection of protons in the energy range 0.5–5 MeV, and for other charged particles in a comparable energy range. This makes it an exceptional image plate for charged particle radiography and fusion burn profile imaging diagnostics. CR-39 is also sensitive to neutrons, with an efficiency of 1×10^{-4} and 6×10^{-5} for DD-neutrons and DT-neutrons, respectively.[88] Moreover, CR-39 is relatively cheap to obtain and easy to handle, being insensitive to light and most solvents.

Because of the 100% quantum efficiency of CR-39 to charged particles, the dynamic range of a CR-39 detector is limited on the upper end by the overlap of charged particle tracks. The fraction of overlapping tracks χ is approximately equal to four times the track density η multiplied by the average track area a,[89] implying that 10% of tracks are overlapped when $\eta = \chi/4a = 0.025/a$. Measurable tracks typically must have a diameter greater than approximately 2 μm, with 10 μm being preferred, so track overlap becomes a danger for fluences in excess of 3×10^4 tracks/cm^2 and unavoidable for fluences in excess of 8×10^5 tracks/cm^2. In such situations, careful processing of the data with low etch times is required to avoid data loss. Simulation[89] and experimental[29,90] studies have explored several methods of significantly increasing the dynamic range of CR-39 based detectors.

1.3.3 Charged particle spectrometers

The charged particle spectrometers used in this thesis were first implemented on OMEGA, and are described in Reference [27]. Two different technologies for high-resolution charged particle spectroscopy are used: magnetic deflection and range filtering.

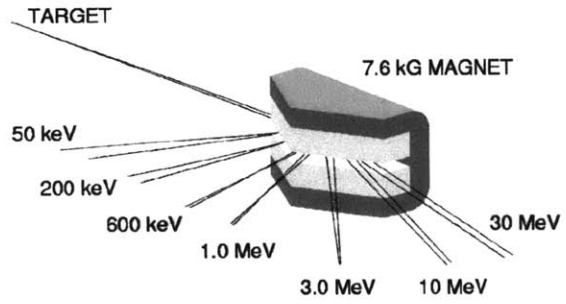

Figure 1.15. Conceptual design of the OMEGA CPS. Incident charged particles (protons shown) are deflected by a permanent dipole magnet. For a given particle type, the radius of curvature of the trajectory in the magnetic field is proportional to the square-root of the particle energy. The magnet was designed to focus 3.0 MeV protons generated at target chamber center onto the detection plane; other detected particles are not perfectly focussed at the detectors and are recorded with an instrumental line-broadening as described in Appendix B. The image was first presented in Reference [85].

The Charged Particle Spectrometers (CPS1 and 2) installed on OMEGA use a dipole magnetic field to deflect particles onto an array of CR-39, as shown schematically in Figure 1.15. The radius of curvature of the particles in the dipole field is derived from the Lorentz force as $R_{gyro} = p/qB \propto \sqrt{AE}/ZB$, for a particle with momentum p, charge $q = Ze$, mass A and magnetic field B.[i] Each location in the detection plane corresponds to a particular R_{gyro} and thus to a particular energy for a particle with given mass and charge. Particles with equal values of (AE/Z^2) will be deflected to the same location: for example, protons (A=1, Z=1) and alpha particles (4,2) will both be deflected to the same location for the same incident energy, while deuterons (2,1) at that same location will have half the energy. The different sizes of tracks produced by these particles in CR-39 can be used to distinguish between them. Another commonly used technique to distinguish between incident species is filtering of the CR-39 to transmit only the lighter, more penetrating particles.

The effective sensitivity of the CPS instruments to charged particles is set by the size of the entrance apertures to the magnets. Both CPSs use a rectangular aperture that is 15 mm long in the direction perpendicular to the bending plane. Parallel to the bending plane, apertures can be selected with a width from 0.1 to 10 mm to vary the single-shot dynamic range of the CPS instruments. CPS1 holds the aperture outside the target chamber wall, 235 cm from target chamber center (TCC), and records between 2×10^{-6} and 2×10^{-8} of the particles produced, depending on the aperture size. The CPS2 aperture is inserted to 100 cm from TCC and transmits a larger fraction of the particles produced (between 10^{-5} and 10^{-7}). Increasing the aperture width allows more particles to be detected, but also increases the instrumental line broadening of the system. The magneto-optical properties of the magnet were designed to focus 3 MeV protons generated at TCC onto the detector plane; other detected particles are not perfectly focused on the detectors and are recorded with an instrumental broadening dependent on the aperture width. The effect of this broadening on a measured Gaussian signal was calculated to facilitate more accurate spectral line-width measurements using CPS data: this analysis and its results are presented in Appendix B. For more information on the CPS systems, see References [85, 27].

The Magnetic Recoil Spectrometer (MRS), which is primarily a neutron spectrometer,[91] can also be used as a sensitive charged particle spectrometer if the neutron scattering foil is removed so that particles can directly enter the magnet aperture. This system has a comparatively high efficiency due to a large magnet aperture (22 cm^2, efficiency $\sim 3 \times 10^{-5}$) and combined with its focusing properties an energy resolution of about ~ 0.15 MeV is obtained for 14.7 MeV protons.

The Wedge-Range-Filter (WRF) compact proton spectrometers use ranging in a solid filter

[i]Including the relativistic momentum, the gyro-radius is found to scale proportionally to $R_{gyro} \propto \sqrt{AE(1 + E/2mc^2)}/ZB$. The correction term is never larger than 0.4% for the particles studied here.

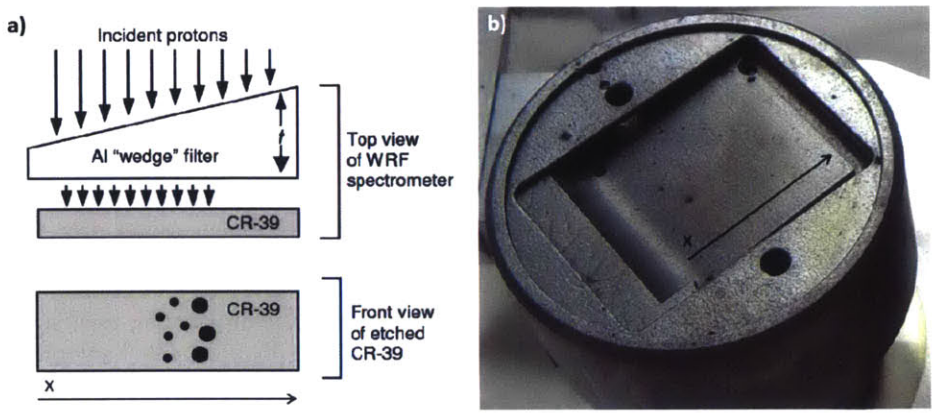

Figure 1.16. a) Conceptual design of the compact Wedge-Range-Filter (WRF) proton spectrometers. Protons are ranged through a wedge-shaped aluminum filter before being detected by a CR-39 detector. The fraction of the incident proton spectrum that penetrates the filter varies with filter thickness (t) as a function of the position (x). The energy and fluence of detected particles on the CR-39 can then be analyzed as a function of location and be used to reconstruct the incident proton spectrum. Figure taken from Reference [27]. b) A photograph of a WRF assembly as fielded on OMEGA. The diameter of the circular assembly is 5 cm.

rather than magnetic fields to evaluate the proton spectrum, as depicted in Figure 1.16. An incident proton spectrum transits a wedge-shaped filter made of aluminum or zirconium. The transmitted proton spectrum varies as a function of location and is measured by a piece of CR-39. The incident spectrum can be reconstructed using the observed particle fluences and track diameters as a function of location on the CR-39, and the WRF response function. Each WRF is individually calibrated by exposure to protons of known energy and line-width on the MIT Linear Electrostatic Ion Accelerator (LEIA)[92] to determine its characteristic thickness and slope. Currently, protons in the range 4 to 20 MeV can be measured with an energy uncertainty of ±60 keV. Typical WRFs introduce instrumental broadening of $\sigma \sim 170$ keV to the 14.7 MeV D^3He-proton line. A description of the analysis algorithm and recent upgrades to the precision and uncertainty of WRF proton spectral measurements is presented in Reference [93].

Due to their compactness, many WRFs may be fielded at various positions in the target chamber on a single implosion. On OMEGA, up to seven WRF modules may be fielded on a single TIM, though commonly only three or one are fielded per TIM per shot. A single WRF may be inserted to 10.5 cm from the implosion, such that the maximum collection efficiency is $\sim 10^{-3}$ and very low-yield implosions may be studied. On the NIF, up to four WRF modules may be fielded on both the (90,78) equatorial DIM and the (0,0) polar DIM. Fielding multiple modules on a single shot reduces statistical uncertainty, protects against noisy or compromised CR-39, and allows studies of anisotropy in the recorded proton energy.

1.3.4 Charged particle imaging

Imaging of the fusion product emission region can provide valuable, detailed information regarding the profiles of temperature and density in the plasma during burn. Pinhole imaging of nuclear products is practical in ICF only for implosions with very high yields. To achieve sufficiently high image resolution, pinholes must be substantially smaller than the hotspot size, which is typically on the order of 100 μm or smaller. This dramatically limits the collection efficiency for practical imaging systems: a pinhole imager on OMEGA would collect on the order of only one out of $\sim 10^8$

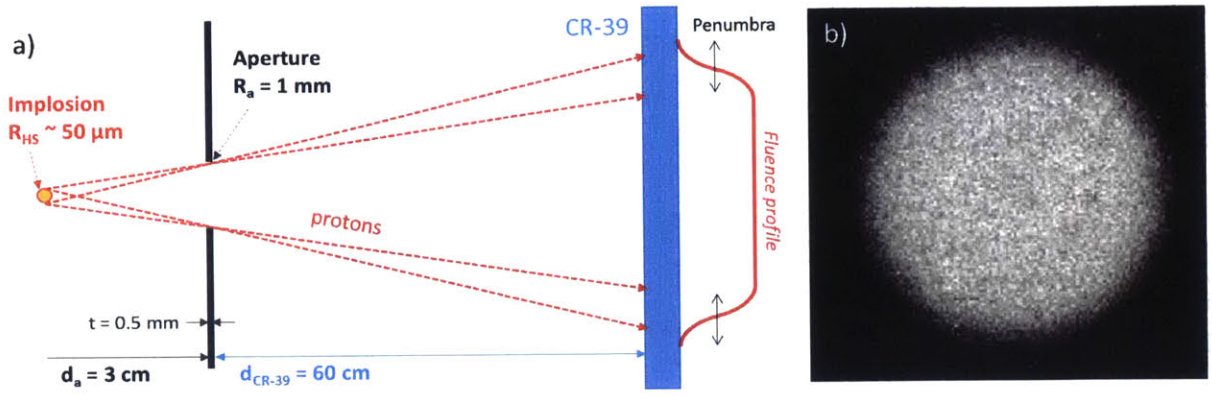

Figure 1.17. a) A schematic depiction of penumbral imaging of charged nuclear fusion products using the Proton Core Imaging System (PCIS) on OMEGA. Fusion particles produced in the implosion transit the aperture and are detected using CR-39. In the penumbra of the recorded image, the edge of the aperture occludes progressively more of the burn region as the radius in the image plane increases. The radial profile of the penumbral image can be analyzed to determine the profile of nuclear burn. b) An image of PCIS data acquired on an OMEGA implosion. Light regions indicate greater proton fluence. This figure is adapted from Reference [94].

fusion particles.

Penumbral imaging using the Proton Core Imaging System (PCIS) on OMEGA[94] provides good spatial resolution with much better efficiency than pinhole imaging. A schematic for how the PCIS operates is shown in Figure 1.17. Fusion particles are produced in the core of the implosion and transit a circular aperture, which has a radius R_a much larger than the hotspot radius R_{HS}. These particles are recorded using a piece of CR-39 located far behind the aperture. An image of the aperture is projected onto the image plane as a circle of particles with radius $R_a M_r$, where $M_r = (d_{\text{CR-39}} + d_a)/d_a$ is the radiographic magnification of the system.[j] On the edge of the signal, the burn region is partially occluded by the edge of the aperture such that larger radii in the signal plane observe less of the burn volume. The radial profile of the penumbral part of the image in the signal plane is therefore an integration of the surface-brightness profile of the burn in one dimension. Analysis of the data can recreate the radial profile of the burn.

The two-dimensional surface brightness of the burn distribution can be directly reconstructed from the penumbral image, as is discussed in Reference [94], and this method is used to study asymmetries in the burn distribution. When imaging spherically symmetric implosions, the angular information in the recorded image may be neglected, and the recorded image can be averaged into a radial image lineout with improved particle statistics. In this case, a radial burn profile model is forward-fit to the image lineout to determine the shape and size of the burn region. A standard form for this model is provided in Reference [95] and uses a radial profile described by a family of exponential functions:

[j]The pinhole magnification of the system is related to the radiographic magnification as follows: $M_p \equiv d_{\text{CR-39}}/d_a = M_r - 1$.

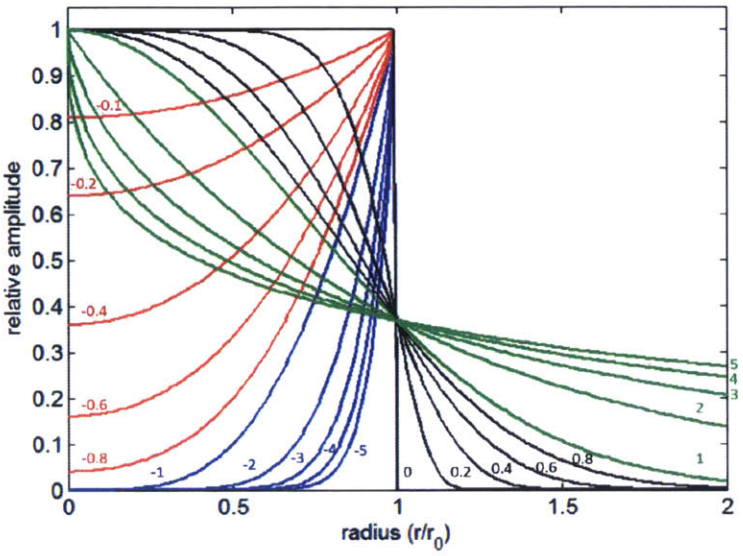

Figure 1.18. Relative amplitude versus radius for the models of burn radius $S(r,[S_0,r_0,p])$ defined in Equation 1.36. Amplitudes are normalized to S_0 and radii are normalized to the radius scale length r_0. Curves are labeled with the value of the peakedness (p) and are color coded: $-5 < p \leq -1$ (blue), $-1 < p < 0$ (red), $0 \leq p < 1$ (black), and $1 \leq p < 5$ (green). PCIS penumbral imaging data is numerically fit using these models to evaluate the radial burn profile.

$$S(r,[S_0,r_0,p]) = \begin{cases} S_0 \exp\left[(r/r_0)^{2/p}\right], & p > 0 \\ S_0\left(2-(1-p)\exp\left[-\log(1-p)(r/r_0)^2\right]\right)^2 (r \leq r_0), & 0 > p > -1 \\ S_0\left(2-2\exp\left[-\log(2)(r/r_0)^2\right]\right)^{-2p} (r \leq r_0), & -1 > p \end{cases} \tag{1.36}$$

$$B(r,[S_0,r_0,p]) = \int_{-\infty}^{\infty} S\left(\sqrt{r^2-z^2}\right) dz. \tag{1.37}$$

Here, S describes the radial emission profile in units of Y/cm^3, and B is the surface-brightness profile produced by S when integrated along the axis of imaging, z. Both S and B are uniquely determined by a set of three parameters: the amplitude S_0, the radius of burn r_0, and the shape parameter or 'peakedness' p. Values of p greater than zero correspond to radial emission profiles that are peaked at the origin, while values of p less than zero correspond to 'hollow' emission profiles, which in this formalism peak at r_0. Examples of the profile shapes defined by this model are shown in Figure 1.18. The penumbral profile is determined from the amount of surface-brightness 'seen' as a function of radius in the imaging plane. The formula for the radial profile in the image plane is

$$\left.\frac{dN}{dR}\right|_{R=M_rR_a+M_px} = -\frac{P_c(x)}{4\pi M_p(d_a+d_{\text{CR-39}})^2}, \tag{1.38}$$

$$P_c(x,[S_0,r_0,p]) = M_rR_a\int_{-\pi}^{\pi} B\left(\sqrt{x^2+2R_c(R_c+x)(1-cos\theta)}\right) cos\theta d\theta, \tag{1.39}$$

where $R_c = R_aM_r/M_p$, and $x = (R - M_rR_a)/M_p$ is the projection of R into the imaging plane. The amplitude S_0 is readily removed from all integrals, however there is no general analytical form for the integrals in B and P as a function of the parameters r_0 and p. These integrals must be evaluated numerically and fit to the data.

In practice, the radius containing 50% of the emitted yield (r_{50}) is a more natural parameter to describe the size of the burn region than the e-folding radius (r_0). In experimental studies, best-fits of r_0 and p to the data are found to be substantially covariant. In contrast, r_{50} is narrowly defined

by the observed data, and is non-covariant with the peakedness p. No deep theoretical explanation of this fact has yet been derived, but it is likely related to the fact that the measured quantity most directly related to size of the burning region is the full-width at half maximum of dN/dR. When reporting results from PCIS studies the shape parameters (r_{50}, p) are used.

The effective collection efficiency for penumbral imaging includes all particles in the penumbral region of the image. In the geometry discussed above and shown in Fig. 1.17, the penumbra has an area of approximately $A_p = (2\pi R_a M_r)(2R_{HS}M_p)$, and collects on average half of the emitted yield in this region. The collection efficiency, defined as the number of observed particles divided by the total yield, is then $f_{PCIS} = A_p/8\pi(d_a + d_{\text{CR-39}})^2 = 0.5(M_p/M_r)(R_a R_{HS}/d_a^2)$. For typical values on the OMEGA PCIS (d_a = 3 cm, R_a = 1 mm, $R_{HS} \sim$ 50 μm, $M_p = M_r - 1 = 20$), the collection efficiency is on the order of $\sim 10^{-5}$, which is three orders of magnitude better than the estimate for pinhole imaging.

Since the particles used in the imaging are charged, transient electric fields on the PCIS aperture can have an impact on the data. The large electron and x-ray fluences from the target can charge up the aperture prior to bang-time. The electric forces on the charged particles as they transit the aperture deflect them slightly, producing a characteristic pattern in the center of the recorded image, which would otherwise be uniform. This effect has been investigated numerically as part of this thesis, and is described in Appendix C. When both DD-protons and D^3He-protons are recorded along a single PCIS line-of-sight, the difference in deflection of the two species can be used to correct for this distortion.

1.3.5 Reaction timing measurements

The rate of nuclear production is governed by the evolution of the density and temperature profiles of the fuel, as described by Equation 1.4. Typically in an ICF implosion, nuclear production occurs only for a brief period around peak convergence, with a FWHM on the order of 100 ps. The time of peak production is referred to as *bang time*. The nuclear bang time (or times, if both shock- and compression-bang are recorded) provides a valuable point of reference for simulations of the implosions, and are affected by the laser absorption and efficiency of the drive. If the reaction history can be resolved, models of the plasma evolution during burn can be tested more specifically.

Details of calculating the bang-time from an observed nuclear source are developed in Chapter 2 in support of the particle Time-of-Flight (PTOF) diagnostic which was developed for OMEGA and the NIF as part of this thesis. In brief, detectors positioned close to the implosion are required for high-precision reaction history measurements, to avoid being dominated by Doppler broadening. Figure 1.19 shows the effects of Doppler broadening on a burn-history measurement. The spectral broadening discussed above produces a temporal broadening at a given distance from the source, since the time-of-flight $t \approx d/\sqrt{2E/m}$. The Doppler broadening can be calculated from this formula using error analysis, resulting in:

$$\sigma_{Doppler} \approx \frac{dt}{dE}\sigma_E = \frac{d}{\sqrt{2E/m}}\frac{\sigma_E}{2E}. \tag{1.40}$$

where $\sigma_{Doppler}$ is the standard deviation of the particle time-of-flight to the detector and σ_E is the standard deviation of the particle energy. The Doppler broadening and the reaction history width (σ_T) add in quadrature to give the total width of the neutron signal at the detector, $\sigma_{total} = \sqrt{\sigma_T^2 + \sigma_{Doppler}^2}$. In general a good reaction history measurement will require that Doppler broadening does not dominate the total signal width. Assuming DD-neutrons with a Gaussian spec-

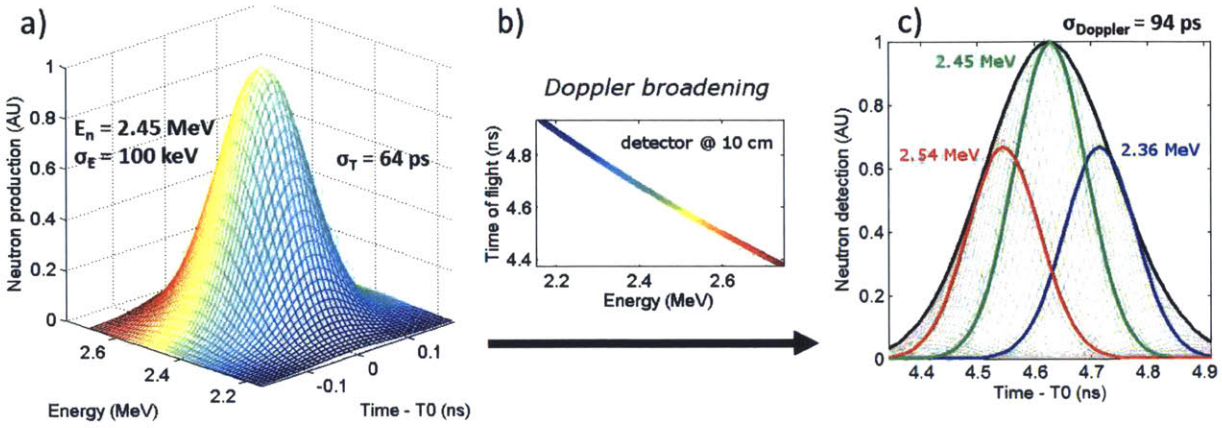

Figure 1.19. A calculation of the effects of Doppler broadening on measurements of the reaction history. a) A neutron source is generated by the fuel, with a distribution in both time and energy. The DD-neutron source shown here has a Gaussian distribution with a width of $\sigma_E = 100$ keV about a mean energy of 2.45 MeV, and a temporal Gaussian distribution with a width $\sigma_T = 64$ ps (FWHM = 150 ps). Color indicates neutron energy, with blue less energetic and red more energetic. b) The time-of-flight for this source to the detector at 10 cm has a distribution dependent on energy. c) Incorporating the temporal and spectral broadening, a total source function of neutrons arriving at the detector is generated. Higher-energy neutrons (red) arrive sooner and lower-energy neutrons (blue) arrive later, introducing additional temporal broadening. The temporal width σ_T and the thermal width $\sigma_{Doppler}$ add in quadrature to give the total broadening, σ_{total}.

tral width $\sigma_E = 100$ keV are measured,[k] to assure the temporal Doppler broadening is less than 100 ps requires that the detector be located within 10.6 cm of the target. Higher energy particles are more forgiving, since $\sigma_{Doppler} \propto E^{-3/2}$, but in general close detectors are necessary. Measurements neglecting reaction history and recording only the average bang-time are more robust, but still must be close to the implosion to avoid being dominated by uncertainty in the particle energy. Time-resolving detectors far away from the implosion are more successfully used by assuming a bang-time and using time-of-flight to evaluate a spectrum, rather than the other way around.

Reaction history measurements require time-resolved detectors with fast response times. In particular the rise-time of the detector response must be comparable to or faster than the desired temporal resolution. Theoretically, the fall-time of the detector response does not need to be fast compared to the measured source: in the limit of infinite fall-time, the detector behaves as an integrator, and the fluence rate may be determined by taking the time derivative of the detector signal. In practice, rapid signal fall-off is valuable for subsequent time-resolved measurements of large and small signals, such as down-scattered DT-neutrons on the tail of the primary DT-neutron peak. To measure an average bang-time the instrument rise-time need not be shorter than the burn duration: a sufficiently high time-resolution of the detector signal is the only requirement. However, accuracy can be lost if the rise-time is substantially longer than the burn duration, so a detector with a rapid response is still desired.

Scintillators are commonly used in nuclear diagnostics for time-resolved measurements. The incident nuclear particles deposit energy in the scintillator, which re-emits some of this energy as light. The scintillator light is detected by a photomultiplier tube (PMT) or photodiode (PD). The neutron time-of-flight (nTOF) diagnostic suite at OMEGA and the NIF use liquid-xylene and bibenzyl crystal scintillators,[96] with fall-times of approximately 2 ns.[97] The BC422 scintillator is

[k] This would be generated by an ion temperature of $T_i \approx 8.16$ keV.

used for the neutron and proton temporal diagnostics (NTD and PTD) at OMEGA.[98,99] In these instruments, the emitted light is imaged by a series of lenses onto a streak camera. BC422 nominally has a < 20 ps rise time and 1 ns fall time, rapid enough for burn-history measurements using these diagnostics.

Synthetic diamond wafers made using the chemical vapor deposition (CVD) technique have also been used as photoconducting diodes for time-resolved nuclear and x-ray measurements.[100] When bombarded with ionizing radiation, the electrons in the diamond are excited into the conduction band. These electrons and the accompanying holes flow as a current driven by a high-voltage bias, and are detected as a current impulse. Diamond has a large band-gap (5 eV), which improves the rejection of background from optical radiation. The rise- and fall-time of these detectors depends on the electrical and geometrical properties of the diamond and the bias voltage, but can be obtained with sub-ns rise-times. More information on the properties of CVD-diamond detectors will be presented in Chapter 2, which includes the development of a CVD-diamond based particle time-of-flight (PTOF) bang-time detector for OMEGA and the NIF, as well as an upgrade of this diagnostic (MagPTOF).

1.4 Thesis Overview

This introduction has presented the history and theoretical basis for ICF and HED plasma physics. The hydrodynamic theory underpinning simulations of ICF experiments was motivated and described in brief, including a description of shock dynamics and some proposed extensions in scenarios where the assumptions of hydrodynamics begin to break down and kinetic physics becomes relevant. Experimental platforms and diagnostic instruments relevant to the work contained herein have been described.

The remainder of this thesis presents original work in the fields of ICF and HED physics. Except where noted, all of the work presented in the remainder of this thesis was performed by the author during the course of his research. Chapter 2 presents several diagnostics and diagnostic techniques developed as part of this work for use on OMEGA and the NIF. The Particle Time-of-Flight diagnostic (PTOF), a CVD-diamond based bang-time detector, was developed on OMEGA to measure the bang time using D^3He-protons and DD-neutrons on the NIF, and has successfully measured bang-time on over 60 NIF implosions. To measure the shock-bang time in hohlraum implosions with large x-ray backgrounds, an upgrade (MagPTOF) was developed and is being implemented. (A new analysis technique for the secondary fusion products was also developed, using both secondary D^3He-protons and DT-neutrons from D_2-filled implosions to constrain the fuel ρR, electron temperature, and mix levels; this work is discussed in Appendix D.) Chapter 3 presents the results of implosions of thin deuterated plastic shells filled with pure ^3He on the OMEGA laser system to study kinetic mix at the fuel shell interface. These experiments produced D^3He-proton yields at levels congruent with total volumetric mixture of the fusion reactants, despite the fact that these experiments are resistant to hydrodynamic instabilities. The results are ascribed to significant ion diffusive mixing of the fuel and shell plasmas after shell burn-through. Chapter 4 presents the results of D^3He-gas filled shock-driven implosions on the OMEGA laser system to study kinetic plasma dynamics in strongly-shocked plasmas. The experiments demonstrate anomalous trends in DD- and D^3He-fusion yields as well as in the burn-averaged ion temperatures for implosions with low initial gas density. These results are ascribed to two multiple-ion kinetic effects in the plasma: thermal decoupling and species separation of the D and ^3He ions. Chapter 5 concludes with a summary of the results presented in this thesis.

1.5 References

1. H. G. Rinderknecht, M. G. Johnson, A. B. Zylstra *et al.*, "A novel particle time of flight diagnostic for measurements of shock- and compression-bang times in D^3He and DT implosions at the NIF," Review of Scientific Instruments, **83**(10), 10D902 (2012).
2. H. G. Rinderknecht, H. Sio, J. A. Frenje *et al.*, "A magnetic particle time-of-flight (MagPTOF) diagnostic for measurements of shock- and compression-bang time at the NIF (invited)," Review of Scientific Instruments, **85**(11), 11D901 (2014).
3. H. G. Rinderknecht, H. Sio, C. K. Li *et al.*, "First Observations of Nonhydrodynamic Mix at the Fuel-Shell Interface in Shock-Driven Inertial Confinement Implosions," Physical Review Letters, **112**, 135001 (2014).
4. H. G. Rinderknecht, H. Sio, C. K. Li *et al.*, "Kinetic mix mechanisms in shock-driven inertial confinement fusion implosions," Physics of Plasmas, **21**(5), 056311 (2014).
5. H. G. Rinderknecht, M. J. Rosenberg, C. K. Li *et al.*, "Ion thermal decoupling and species separation in shock-driven implosions," Physical Review Letters, **114**, 025001 (2015).
6. A. Einstein, "Zur elektrodynamik bewegter körper," Annalen der Physik, **322**(10), 891 (1905).
7. A. S. Eddington, "The internal constitution of the stars," The Observatory, **43**, 341 (1920).
8. R. Atkinson and F. Houtermans, "Zur frage der aufbaumglichkeit der elemente in sternen," Zeitschrift fr Physik, **54**(9-10), 656 (1929).
9. H. A. Bethe, "Energy production in stars," Physical Review, **55**, 434 (1939).
10. G. Audi, A. Wapstra and C. Thibault, "The ame2003 atomic mass evaluation: (ii). tables, graphs and references," Nuclear Physics A, **729**(1), 337 (2003), the 2003 {NUBASE} and Atomic Mass Evaluations.
11. S. Atzeni and J. Meyer-Ter-Vehn, *The Physics of Inertial Fusion: Beam Plasma Interaction, Hydrodynamics, Hot Dense Matter*, International Series of Monographs on Physics, (Oxford University Press, 2004).
12. ENDF/B-VII.0 Library, see `http://www.nndc.bnl.gov/`.
13. H.-S. Bosch and G. M. Hale, "Improved formulas for fusion cross-sections and thermal reactivities," Nuclear Fusion, **32**(4), 611 (1992).
14. J. D. Lawson, "Some criteria for a power producing thermonuclear reactor," Proceedings of the Physical Society. Section B, **70**(1), 6 (1957).
15. R. Betti, P. Y. Chang, B. K. Spears *et al.*, "Thermonuclear ignition in inertial confinement fusion and comparison with magnetic confinement," Physics of Plasmas, **17**(5), 058102 (2010).
16. J. A. Frenje, D. T. Casey, C. K. Li *et al.*, "Probing high areal-density cryogenic deuterium-tritium implosions using downscattered neutron spectra measured by the magnetic recoil spectrometer," Physics of Plasmas, **17**(5), 056311 (2010).
17. H. Brysk, "Fusion neutron energies and spectra," Plasma Physics, **15**, 611 (1973).
18. J. Nuckolls, L. Wood, A. Thiessen *et al.*, "Laser compression of matter to super-high densities: Thermonuclear (ctr) applications," Nature, **239**, 139 (1972).
19. S. W. Haan, J. D. Lindl, D. A. Callahan *et al.*, "Point design targets, specifications, and requirements for the 2010 ignition campaign on the National Ignition Facility," Physics of Plasmas, **18**, 051001 (2011).
20. S. E. Bodner, "Rayleigh-Taylor Instability and Laser-Pellet Fusion," Physical Review Letters, **33**(13), 761 (1974).
21. V. N. Goncharov, "Theory of the Ablative Richtmyer-Meshkov Instability," Physical Review Letters, **82**, 2091 (1999).
22. Y. Aglitskiy, A. L. Velikovich, M. Karasik *et al.*, "Direct Observation of Mass Oscillations Due to Ablative Richtmyer-Meshkov Instability in Plastic Targets," Physical Review Letters, **87**, 265001 (2001).
23. K. O. Mikaelian, "Oblique shocks and the combined Rayleigh-Taylor, Kelvin-Helmholtz, and Richtmyer-Meshkov instabilities," Physics of Fluids, **6**(6), 1943 (1994).
24. General Atomics, see `https://fusion.gat.com/global/IFTRole`.
25. J. T. Larsen and S. M. Lane, "HYADES - A plasma hydrodynamics code for dense plasma studies," Journal of Quantitative Spectroscopy and Radiative Transfer, **51**, 179 (1994).

26. C. Bayer, M. Bernard, D. Billon *et al.*, "Laser implosion of microballoons: study of the transition from exploding-pusher to ablative regime," Nuclear Fusion, **24**(5), 573 (1984).
27. F. H. Séguin, J. A. Frenje, C. K. Li *et al.*, "Spectrometry of charged particles from inertial-confinement-fusion plasmas," Review of Scientific Instruments, **74**(2), 975 (2003).
28. D. T. Casey, J. A. Frenje, M. Gatu Johnson *et al.*, "Measuring the absolute deuterium-tritium neutron yield using the magnetic recoil spectrometer at OMEGA and the NIF," Review of Scientific Instruments, **83**(10), 10D912 (2012).
29. M. J. Rosenberg, F. H. Séguin, C. J. Waugh *et al.*, "Empirical assessment of the detection efficiency of CR-39 at high proton fluence and a compact, proton detector for high-fluence applications," Review of Scientific Instruments, **85**(4), 043302 (2014).
30. C. K. Li, F. H. Séguin, J. A. Frenje *et al.*, "Measuring E and B fields in laser-produced plasmas with monoenergetic proton radiography," Physical Review Letters, **97**(13), 135003 (2006).
31. C. K. Li, F. H. Séguin, J. A. Frenje *et al.*, "Monoenergetic proton backlighter for measuring E and B fields and for radiographing implosions and high-energy density plasmas (invited)," Review of Scientific Instruments, **77**(10), 10E725 (2006).
32. J. R. Rygg, F. H. Séguin, C. K. Li *et al.*, "Proton radiography of inertial fusion implosions," Science, **319**(5867), 1223 (2008).
33. C. K. Li, F. H. Séguin, J. R. Rygg *et al.*, "Monoenergetic-Proton-Radiography Measurements of Implosion Dynamics in Direct-Drive Inertial-Confinement Fusion," Physical Review Letters, **100**(22), 225001 (2008).
34. C. K. Li, F. H. Séguin, J. A. Frenje *et al.*, "Observations of Electromagnetic Fields and Plasma Flow in Hohlraums with Proton Radiography," Physical Review Letters, **102**(20), 205001 (2009).
35. C. K. Li, F. H. Séguin, J. A. Frenje *et al.*, "Charged-particle probing of x-ray-driven inertial-fusion implosions," Science, **327**(5970), 1231 (2010).
36. M. J.-E. Manuel, A. B. Zylstra, H. G. Rinderknecht *et al.*, "Source characterization and modeling development for monoenergetic-proton radiography experiments on OMEGA," Review of Scientific Instruments, **83**(6), 063506 (2012).
37. C. K. Li, D. D. Ryutov, S. X. Hu *et al.*, "Structure and Dynamics of Colliding Plasma Jets," Physical Review Letters, **111**, 235003 (2013).
38. M. D. Rosen and J. H. Nuckolls, "Exploding pusher performance - A theoretical model," Physics of Fluids, **22**(7), 1393 (1979).
39. J. D. Lindl, *Inertial Confinement Fusion: The quest for ignition and energy gain using indirect drive*, Aip-Press Series, (American Institute Qf Physics, 1998).
40. "Highlights of the History of the University of Rochesters Laboratory for Laser Energetics," online (2011), LLE Document No. DOE/NA/28302-992.
41. J. Bunkenberg, J. Boles, D. Brown *et al.*, "The omega high-power phosphate-glass system: Design and performance," Quantum Electronics, IEEE Journal of, **17**(9), 1620 (1981).
42. M. Richardson, P. McKenty, F. Marshall *et al.*, "Ablatively-Driven Targets Imploded with the 24 UV Beam Omega System," in H. Hora and G. Miley, (editors) "Laser Interaction and Related Plasma Phenomena," pages 421–448, (Springer US, 1986).
43. "OMEGA phase conversion with distributed phase plates," LLE Review Quarterly Report, **33**, 1 (1987), LLE Document No. DOE/DP40200-65.
44. S. Skupsky, R. W. Short, T. Kessler *et al.*, "Improved laser-beam uniformity using the angular dispersion of frequency-modulated light," Journal of Applied Physics, **66**(8), 3456 (1989).
45. T. R. Boehly, D. L. Brown, R. S. Craxton *et al.*, "Initial performance results of the OMEGA laser system," Optics Communications, **133**(1-6), 495 (1997).
46. T. C. Sangster, V. N. Goncharov, R. Betti *et al.*, "Improving cryogenic deuterium–tritium implosion performance on OMEGA," Physics of Plasmas, **20**(5), 056317 (2013).
47. J. Lindl, "Development of the indirect-drive approach to inertial confinement fusion and the target physics basis for ignition and gain," Physics of Plasmas, **2**(11), 3933 (1995).
48. M. J. Edwards, P. K. Patel, J. D. Lindl *et al.*, "Progress towards ignition on the National Ignition Facility," Physics of Plasmas, **20**(7), 070501 (2013).

49. B. K. Spears, S. Glenzer, M. J. Edwards *et al.*, "Performance metrics for inertial confinement fusion implosions: Aspects of the technical framework for measuring progress in the National Ignition Campaign," Physics of Plasmas, **19**(5), 056316 (2012).
50. O. A. Hurricane, D. A. Callahan, D. T. Casey *et al.*, "Fuel gain exceeding unity in an inertially confined fusion implosion," Nature, **506**(7488), 343 (2014).
51. R. F. Smith, J. H. Eggert, R. Jeanloz *et al.*, "Ramp compression of diamond to five terapascals," Nature, **511**(7509), 330 (2014).
52. J. Lindl, O. Landen, J. Edwards *et al.*, "Review of the National Ignition Campaign 2009-2012," Physics of Plasmas, **21**(2), 020501 (2014).
53. M. J.-E. Manuel, C. K. Li, F. H. Séguin *et al.*, "First Measurements of Rayleigh-Taylor-Induced Magnetic Fields in Laser-Produced Plasmas," Physical Review Letters, **108**, 255006 (2012).
54. M. Rosenberg, *Studies of Ion Kinetic Effects in Shock-Driven Inertial Confinement Fusion Implosions at OMEGA and the NIF and Magnetic Reconnection Using Laser-Produced Plasmas at OMEGA*, Ph.D. thesis, Massachusetts Institute of Technology (2014).
55. I. V. Igumenshchev, A. B. Zylstra, C. K. Li *et al.*, "Self-generated magnetic fields in direct-drive implosion experiments," Physics of Plasmas, **21**(6), 062707 (2014).
56. J. Donea, A. Huerta, J.-P. Ponthot *et al.*, *Arbitrary Lagrangian-Eulerian Methods*, volume 1, chapter 14, (John Wiley & Sons, Ltd., 2004).
57. D. Keller, T. Collins, J. A. Delletrez *et al.*, "DRACO — A New Multidimensional Hydrocode," Bull. Am. Phys. Soc. 44, 37 (1999).
58. M. M. Marinak, G. D. Kerbel, N. A. Gentile *et al.*, "Three-dimensional HYDRA simulations of National Ignition Facility targets," Physics of Plasmas, **8**(5), 2275 (2001).
59. M. Y. Jaffrin and R. F. Probstein, "Structure of a plasma shock wave," Physics of Fluids, **7**(10), 1658 (1964).
60. F. Vidal, J. P. Matte, M. Casanova *et al.*, "Ion kinetic simulations of the formation and propagation of a planar collisional shock wave in a plasma," Physics of Fluids B: Plasma Physics (1989-1993), **5**(9), 3182 (1993).
61. C. Bellei, H. Rinderknecht, A. Zylstra *et al.*, "Species separation and kinetic effects in collisional plasma shocks," Physics of Plasmas, **21**(5), 056310 (2014).
62. P. A. Amendt, J. L. Milovich, S. C. Wilks *et al.*, "Electric field and ionization-gradient effects on inertial-confinement-fusion implosions," Plasma Physics and Controlled Fusion, **51**(12), 124048 (2009).
63. C. K. Li, F. H. Séguin, J. A. Frenje *et al.*, "Proton radiography of dynamic electric and magnetic fields in laser-produced high-energy-density plasmas," Physics of Plasmas, **16**(5), 056304 (2009).
64. P. Amendt, O. Landen, H. Robey *et al.*, "Plasma Barodiffusion in Inertial-Confinement-Fusion Implosions: Application to Observed Yield Anomalies in Thermonuclear Fuel Mixtures," Physical Reviev Letters, **105**, 115005 (2010).
65. G. Kagan and X.-Z. Tang, "Thermo-diffusion in inertially confined plasmas," Physics Letters A, **378**(21), 1531 (2014).
66. P. Amendt, S. C. Wilks, C. Bellei *et al.*, "The potential role of electric fields and plasma barodiffusion on the inertial confinement fusion database," Physics of Plasmas, **18**(5), 056308 (2011).
67. G. Kagan and X.-Z. Tang, "Electro-diffusion in a plasma with two ion species," Physics of Plasmas, **19**(8), 082709 (2012).
68. Private communication with G. Kagan.
69. Y. B. Zel'dovich and Y. P. Raizer, *Physics of Shock Waves and High-Temperature Hydrodynamic Phenomena*, Dover Books on Physics, (Dover Publications, 2002).
70. L. Landau and E. Lifshitz, *Fluid Mechanics*, v. 6, (Elsevier Science, 1959).
71. Private communication with J. Greenough.
72. N. M. Hoffman, G. B. Zimmerman, K. Molvig *et al.*, "Reduced models for the ion-kinetic regime in inertial-confinement-fusion capsule implosions," Physics of Plasmas (to be submitted).
73. K. Molvig, N. M. Hoffman, B. J. Albright *et al.*, "Knudsen Layer Reduction of Fusion Reactivity," Physical Review Letters, **109**, 095001 (2012).
74. A. Petschek and D. Henderson, "Influence of high-energy ion loss on DT reaction rate in laser fusion pellets," Nuclear Fusion, **19**(12), 1678 (1979).

75. A. Inglebert, B. Canaud and O. Larroche, "Species separation and modification of neutron diagnostics in inertial-confinement fusion," EPL (Europhysics Letters), **107**(6), 65003 (2014).
76. B. E. Peigney, O. Larroche and V. Tikhonchuk, "Ion kinetic effects on the ignition and burn of inertial confinement fusion targets: A multi-scale approach," Physics of Plasmas, **21**(12), 122709 (2014).
77. L. Ballabio, J. Källne and G. Gorini, "Relativistic calculation of fusion product spectra for thermonuclear plasmas," Nuclear Fusion, **38**(11), 1723 (1998).
78. V. A. Smalyuk, P. B. Radha, J. A. Delettrez *et al.*, "Time-Resolved Areal-Density Measurements with Proton Spectroscopy in Spherical Implosions," Physical Review Letters, **90**, 135002 (2003).
79. A. B. Zylstra, J. A. Frenje, F. H. Séguin *et al.*, "The effect of shock dynamics on compressibility of ignition-scale National Ignition Facility implosions," Physics of Plasmas, **21**(11), 112701 (2014).
80. D. G. Hicks, C. K. Li, F. H. Séguin *et al.*, "Charged-particle acceleration and energy loss in laser-produced plasmas," Physics of Plasmas, **7**(12), 5106 (2000).
81. F. H. Séguin, C. K. Li, J. A. Frenje *et al.*, "Using secondary-proton spectra to study the compression and symmetry of deuterium-filled capsules at OMEGA," Physics of Plasmas, **9**(6), 2725 (2002).
82. Track Analysis Systems Ltd, see `http://www.tasl.co.uk/`.
83. B. G. Cartwright, E. K. Shirk and P. B. Price, "A nuclear-track-recording polymer of unique sensitivity and resolution," Nuclear Instruments and Methods, **153**(2-3), 457 (1978).
84. G. Somogyi, "Development of etched nuclear tracks," Nuclear Instruments and Methods, **173**(1), 21 (1980).
85. D. Hicks, *Charged-Particle Spectroscopy: A New Window on Inertial Confinement Fusion*, Ph.D. thesis, Massachusetts Institute of Technology (1999).
86. N. Sinenian, M. J. Rosenberg, M. Manuel *et al.*, "The response of CR-39 nuclear track detector to 1-9 MeV protons," Review of Scientific Instruments, **82**(10), 103303 (2011).
87. J. Rojas-Herrera, H. G. Rinderknecht, A. B. Zylstra *et al.*, "Impact of x-ray dose on the response of CR-39 to 1-5.5 MeV alphas," Review of Scientific Instruments (submitted).
88. J. A. Frenje, C. K. Li, F. H. Séguin *et al.*, "Absolute measurements of neutron yields from DD and DT implosions at the OMEGA laser facility using CR-39 track detectors," Review of Scientific Instruments, **73**(7), 2597 (2002).
89. A. Zylstra, J. Frenje, F. Séguin *et al.*, "A new model to account for track overlap in CR-39 data," Nuclear Instruments and Methods in Physics Research Section A: Accelerators, Spectrometers, Detectors and Associated Equipment, **681**(0), 84 (2012).
90. H. Sio, F. H. Séguin, J. A. Frenje *et al.*, "A technique for extending by 10^3 the dynamic range of compact proton spectrometers for diagnosing ICF implosions on the National Ignition Facility and OMEGA," Review of Scientific Instruments, **85**(11), 11E119 (2014).
91. J. A. Frenje, D. T. Casey, C. K. Li *et al.*, "First measurements of the absolute neutron spectrum using the magnetic recoil spectrometer at OMEGA (invited)," Review of Scientific Instruments, **79**(10), 10E502 (2008).
92. N. Sinenian, M. J.-E. Manuel, A. B. Zylstra *et al.*, "Upgrade of the MIT Linear Electrostatic Ion Accelerator (LEIA) for nuclear diagnostics development for Omega, Z and the NIF," Review of Scientific Instruments, **83**(4), 043502 (2012).
93. F. H. Séguin, N. Sinenian, M. Rosenberg *et al.*, "Advances in compact proton spectrometers for inertial-confinement fusion and plasma nuclear science," Review of Scientific Instruments, **83**(10), 10D908 (2012).
94. F. H. Séguin, J. L. DeCiantis, J. A. Frenje *et al.*, "D^3He-proton emission imaging for inertial-confinement-fusion experiments (invited)," Review of Scientific Instruments, **75**(10), 3520 (2004).
95. F. H. Séguin, J. L. DeCiantis, J. A. Frenje *et al.*, "Measured dependence of nuclear burn region size on implosion parameters in inertial confinement fusion experiments," Physics of Plasmas, **13**(8), 082704 (2006).
96. V. Y. Glebov, C. Forrest, J. P. Knauer *et al.*, "Testing a new NIF neutron time-of-flight detector with a bibenzyl scintillator on OMEGA," Review of Scientific Instruments, **83**(10), 10D309 (2012).
97. R. Hatarik, L. A. Bernstein, J. A. Caggiano *et al.*, "Characterizing time decay of bibenzyl scintillator using time correlated single photon counting," Review of Scientific Instruments, **83**(10), 10D911 (2012).
98. R. A. Lerche, D. W. Phillion and G. L. Tietbohl, "25 ps neutron detector for measuring ICF-target burn history," Review of Scientific Instruments, **66**(1), 933 (1995).
99. J. A. Frenje, C. K. Li, F. H. Séguin *et al.*, "Measuring shock-bang timing and ρR evolution of D^3He implosions at OMEGA," Physics of Plasmas, **11**(5), 2798 (2004).
100. L. S. Pan, P. Pianetta, D. R. Kania *et al.*, "Electrical Transport Properties of Undoped CVD Diamond Films," Science, **255**(5046), 830 (1992).

2

Development of Nuclear Bang-Time Diagnostics for OMEGA and the NIF

Nuclear bang-times, and more generally the nuclear reaction histories, are implosion metrics that are commonly used to diagnose ICF experiments. The bang-times, which are defined as the times of peak nuclear production, provide a readily observable and brief timing reference near the end of the implosion, and are sensitive to, for example, the efficiency and evolution of the laser power absorption. For this reason the bang-times (including the *x-ray bang-time*, the time of peak x-ray self-emission from the hotspot plasma) are the most commonly referenced benchmarks to demonstrate the validity of ICF simulations. Burn histories provide additional information on the detailed time evolution of the plasma temperature and density during nuclear production. Nuclear bang-times are also critical in charged-particle radiography studies, where the timing of the sample images must be known. For these reasons, the development and improvement of timing diagnostics is of great and continued interest in ICF and HED research. A number of nuclear bang-time and burn-history diagnostics currently in use on OMEGA were introduced in Section 1.3.5.

The design, development, implementation, and analysis of data from a particle time-of-flight (PTOF) bang-time detector on the NIF constitutes a major component of this thesis. This detector is uniquely capable of measuring bang-times using various nuclear products, including DT-neutrons, DD-neutrons, TT-neutrons, and D^3He-protons. Bang-times have been measured on implosions that produced DD-neutron yields as low as 3×10^{10} and DT-neutron yields approaching 10^{15}. Of particular interest, and the primary motivation behind its implementation, is PTOF's ability to record both the shock- and compression-bang times in NIF implosions with D^3He-gas fill, using D^3He-protons and DD-neutrons, respectively. While several methods of recording the shock-bang time have been attempted, only the D^3He-proton measurement by PTOF has to date measured this valuable observable.

During the operation of PTOF it was found that the x-ray background generated by gas-filled hohlraum implosions on the NIF dominates the PTOF signal, requiring substantial shielding that interfered with the D^3He-proton measurement. An upgrade to the PTOF diagnostic to provide robust shock- and compression-bang time measurements in such gas-filled hohlraum implosions was designed as part of this thesis. This upgrade, called MagPTOF, includes a magnet to deflect the D^3He-protons around substantial x-ray shielding and onto the detector. The proton and neutron signals are predicted to be well-resolved in this system, and the signal-to-background ratio is expected to be increased by a factor of 1000. The MagPTOF is currently being implemented on the NIF and is expected to be ready for shots in May of 2015.

This chapter describes the design, calibration, implementation, and data analysis procedure of PTOF; presents the primary research results obtained using PTOF; and describes the design for

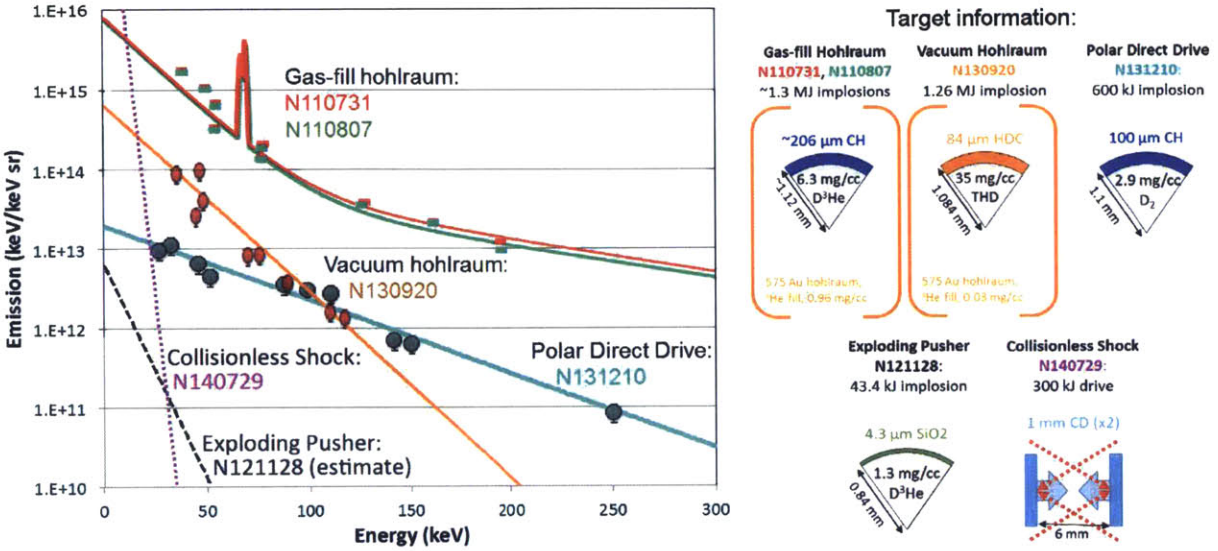

Figure 2.1. X-ray emission spectra measured on several types of implosions at the NIF. Measurements (points) were recorded by the FFLEX diagnostic, and the obtained spectra are fitted with one- or two-temperature radiation model described in Equation 2.1 (solid lines).[1] The energy and temperature fits to the spectra are as follows, in (kJ, keV): Gas-filled hohlraum N110807 (73,18) + (0.66, 105); Vacuum hohlraum N130920 (6.1, 18.4); Polar direct-drive N131210 (2.7, 47). An estimate of the core bremsstrahlung x-ray emission from the exploding pusher implosion N121128 (black dashed line) and a fit to the low-energy x-ray spectrum measured by the HGXD diagnostic on the collisionless shock experiment N140729 (magenta dotted line) are also shown for comparison. Gas-filled hohlraum implosions generate x-ray spectra that are generally hotter and orders of magnitude more intense than other target implosions. Target information for each of the shot types is indicated on the right. FFLEX data courtesy of Matthias Hohenberger, LLNL.

the MagPTOF upgrade. Section 2.1 presents an overview of the bang-time measurement capability at the NIF and motivates the need for the PTOF diagnostic. Section 2.2 describes the PTOF as implemented on both OMEGA and NIF, and Section 2.4 presents the results of calibration studies of the PTOF detectors. Section 2.3 introduces the analysis procedure used for PTOF data, and Section 2.5 presents several interesting results obtained to date with this diagnostic. The MagPTOF upgrade is motivated and described in Section 2.6.

2.1 Challenges of Diagnosing Nuclear Bang Time at the NIF

The implementation of timing diagnostic techniques at the NIF has involved a great deal of ingenuity. Indirect-drive, which is the principal experimental configuration for the NIF, generates more intense x-rays from the hohlraum than direct-drive, and these x-rays act as a background for the bang-time measurements. Figure 2.1 compares the measured hot x-ray spectra from two NIF shots, one indirect-drive with a gas-filled hohlraum, and the second polar-direct-drive. This data was recorded by the filter-fluorescer diagnostic system (FFLEX).[1] The spectra are generally modeled as a sum of thermal distributions, for which each distribution is described as:

$$I_\gamma = \frac{e}{4\pi}(5\times 10^{11})\frac{Z^*}{79}E_\gamma \exp\left[-\frac{h\nu}{T_\gamma}\right], \tag{2.1}$$

where I_γ is the spectral intensity in units of keV/(keV sr),[a] $Z^* = \langle Z^2 \rangle / \langle Z \rangle$ is the average atomic number of the target creating the radiation field, E_γ is the total energy in the distribution in Joules, and T_γ is the temperature of the distribution. The most intense radiation fields are generated by gas-filled hohlraums, which can output ~20 kJ of x-rays in an 18 keV exponentially decreasing distribution. In contrast, even the most successful implosions produce less than 23 kJ carried by DT-neutrons (equivalent to a yield of $\sim 10^{16}$); typical DD-neutron (Yield $\sim 10^{11}$) and D^3He-proton ($\sim 10^8$) signals from NIF implosions contain only 40 and 0.2 milliJoules of energy, respectively, smaller than the x-ray background by a factor of a million or more. In summary, bang-time diagnostics require excellent shielding, time-resolved signal discrimination, high sensitivity to the species of interest relative to background, or a combination of all three.

Through the use of filters and temporal discrimination, x-ray framing cameras (such as hGXI, GXD, and HGXD, to name a few) and streak cameras (such as DISC) have been highly successful at imaging the x-ray emission history. The SPIDER is a streak camera-based x-ray burn-history diagnostic that is routinely used to measure x-ray emission history with a ±10 ps accuracy and ±30 ps absolute timing accuracy.[2] A dedicated south-pole x-ray bang-time diagnostic (SPBT) discriminates the core emission by selecting monochromatic x-rays from the background with curved Bragg-reflection lenses.[3] Since x-rays travel at the speed of light, the time history of signals are not distorted by travel and timing diagnostics can be fielded as far from the implosion as necessary to accommodate the equipment, as long as the signal is sufficiently bright.

Unlike x-ray signals, nuclear emission histories suffer from Doppler broadening, which requires the diagnostics to be positioned comparatively close to the target, as discussed in Section 1.3.5. The scintillators used in the NTD and PTD diagnostics on OMEGA are sensitive to the indirect-drive x-ray background. Sufficient shielding to eliminate this x-ray background also blocks the transport of charged particles to the scintillator, eliminating the possibility of a charged-particle bang-time measurement in indirect-drive implosions. Attempts have been made to measure the proton bang-time in OMEGA hohlraum implosions that are scaled down in size to generate a comparable radiation temperature to that observed at the NIF. So far, this has not been successful: the background radiation from the hohlraum nevertheless swamps the signal.

CVD-diamond detectors have been used for neutron measurements at OMEGA and the NIF, as an alternative to scintillator/photodiode detectors. Polycrystalline diamond made by the chemical vapor deposition (CVD) method is a photoconducting material, with a density of 3.5 g/cc and a band-gap of 5.5 eV.[4] The principal of operation is depicted in Figure 2.2. A wafer of CVD diamond is biased with a large voltage, generating a planar electric field within the material. Incident energetic particles or photons excite electrons into the conduction band, either directly by collisions (charged particles), photoabsorption and scattering (photons), or indirectly by nuclear scattering (neutrons). Each excited electron also leaves a 'hole' in the valence band, which can move as a virtual positive electron. The population of excited electrons falls off exponentially with time; the timescale is defined as the carrier lifetime $\tau \sim 1$ ns. While excited, the electron and hole are exposed to the bias voltage and flow through the diamond as a current with a voltage-dependent velocity $v = \mu(E)E$, where the mobility μ is on the order of 1000 cm^2/V sec and E is the electric field. (This scaling typically holds up to a saturation velocity.) Electrons and holes that escape the detector into the circuit produce a time-dependent current impulse, which can be measured using a fast oscilloscope.

CVD-diamond detectors have been studied since the early 1990's,[5] and made rapid progress in terms of improved collection depth, $d = \mu\tau E$.[6] The average excitation energy per electron-hole pair in CVD-diamond has been measured to be 13 eV,[4] so each incident charged fusion particle will

[a]The steradian (sr) is the unit of solid angle.

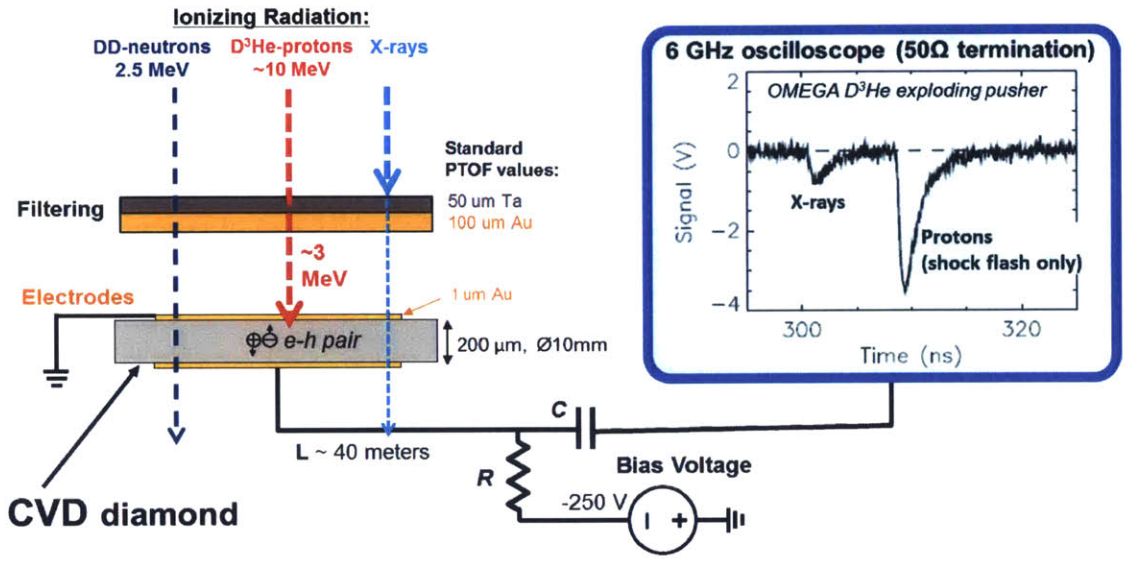

Figure 2.2. A schematic illustrating the principle of operation for CVD-diamond-based radiation and charged-particle detectors. A CVD-diamond wafer is biased with high voltage, producing a strong electric field in the bulk diamond. Ionizing radiation is incident on a CVD-diamond wafer after transiting a filter stack. The radiation excites electrons into the diamond's 5.5 eV conduction band, generating electron-hole pairs. Once excited, these charge carriers are pushed by the electric field, producing a current impulse. A capacitor transmits the high-frequency component of the current impulse, which is then recorded by a fast oscilloscope. The values shown for the filtering composition and thickness, wafer thickness, cable length, and bias voltage are typical for NIF experiments. Data is shown from an OMEGA D^3He-gas filled shock-driven implosion on June 10th, 2010 (shot 58364). This data was recorded with a 1 mm thick CVD-diamond biased at 1500 V, filtered with 100 µm Al + 100 µm Ta, and positioned 50 cm from the target.

excite a large number of carriers. CVD-diamond has a high resistivity ($\sim 10^{12}$ Ω cm) producing minimal leakage currents, and a high breakdown voltage ($\sim 10^7$ V/cm) allowing very high biases with associated improvements in sensitivity and response time. It is also radiation hard in the sense that detectors can withstand large doses of radiation without changing properties.[7] Importantly, CVD-diamond can operate in vacuum, allowing simple implementation within the target chamber. Several CVD-diamond neutron time-of-flight (nTOF) detectors were developed at OMEGA.[8] The CVD-diamond based NTOF-4M-BT diagnostic was implemented on the NIF at 4.5 meters from the implosion, with the goal of measuring DT-neutron bang-time.[9] NTOF-4M-BT had a demonstrated timing accuracy of better than $\pm$ 50 ps for DT-neutrons, and operated for yields between 10^{12} and 10^{16}.[10] However, it was not sensitive enough to record DD-neutron or charged-particle bang-times, and is no longer operational.

One alternative to nuclear measurements is the measurement of the high-energy nuclear gamma rays that are produced by most fusion reactions. For example, deuterium-tritium fusion generates a 16.75 MeV gamma ray with a branching ratio of approximately 4×10^{-5}. The Gamma Reaction History (GRH) diagnostic measures these gamma rays using Cherenkov radiation from Compton-scattered electrons.[11] This method has very good background discrimination, since the Cherenkov radiation mechanism selects for signals in excess of a threshold of 3.5 MeV in the GRH design. However due to the low branching ratio and position at 6 meters from the target, this instrument is limited to DT-fusion measurements at yields above 10^{14} neutrons.[12] On OMEGA, the equivalent Gas Cherenkov Detectors (GCDs) are inserted close to the implosion in TIMs and can thus collect much larger fractions of the generated fusion gammas,[13] however such a reentrant system has not

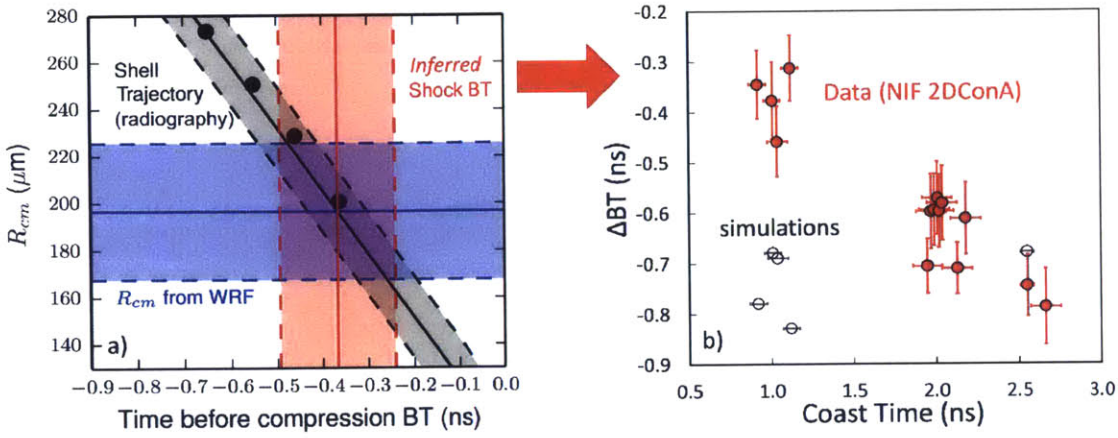

Figure 2.3. a) Measured implosion trajectory (black points) and fit to the data with $\pm 1\sigma$ uncertainty (black bar) from a 2D-radiograph of a low-adiabat surrogate NIF implosion using the ConA platform.[15,16] The WRF-measured proton spectra are used to infer the radius of the shell at shock-bang time (blue); by combining these datasets, an estimate of the shock-bang time can be inferred (red). b) The inferred (compression − shock) ΔBT from the combined WRF and radiography data on several low-adiabat surrogate NIF implosions (red), plotted as a function of the "coast time" (the amount of time between when the laser turns off and compression-bang time). The simulated values for several implosions (black circles) show a clear discrepancy with the measured data points, providing evidence that the shock-bang time is not well understood in low-adiabat implosions. This figure is adapted from work by Alex Zylstra.[17]

been implemented on NIF. To measure the D^3He-gammas (16.66 MeV, with a branching ratio of 1.25×10^{-4})[14] from a NIF-typical D^3He shock-yield on the order of 10^8 protons, the current GRH converter would have to be fielded 2 cm from the implosion, which is an impractical solution.

2.1.1 Measurements of the shock-bang time

The shock-bang time has been a particularly elusive quantity of interest since the beginning of the NIC. As discussed in Section 1.1.2 and shown in Figure 1.7, the four weak shocks that compress the cryogenic fuel combine into a strong shock with Mach number of $M \sim 10$–50 in the central DT-vapor. The shock represents the first information about the drive that reaches the center of the implosion. The time when the shock rebounds from the center of the implosion is a valuable metric of shock timing that can be used to benchmark models of shock propagation in the experiment. When the rebounding shock strikes the imploding cryogenic fuel, the deceleration phase begins and the hotspot starts to form and compress, culminating in stagnation and peak nuclear production. The relative timing of the shock- and compression-bang times, defined as $\Delta BT \equiv (BT_{compr} - BT_{shock})$, is thus a sensitive metric for the physics of compression and hotspot formation. A direct measurement of the shock-bang time and of ΔBT will provide valuable new constraints on the 1D physics of the shock propagation and shell deceleration, improving the understanding of the in-flight conditions of the fuel and shell.

Hydrodynamic simulations of ignition-scale implosions indicate that ΔBT is insensitive to changes in the experimental parameters. However, experimental evidence seems to suggest that ΔBT may be changing by as much as 50%, as shown in Figure 2.3.[17] As described in Section 1.3.1, compact WRF proton spectrometers have been used to measure the proton spectrum from which the total ρR is inferred at shock-bang time in low-adiabat ignition-scale surrogate implosions filled with D^3He gas. In this analysis, a radius of the shell at shock-bang time is determined. In Ref-

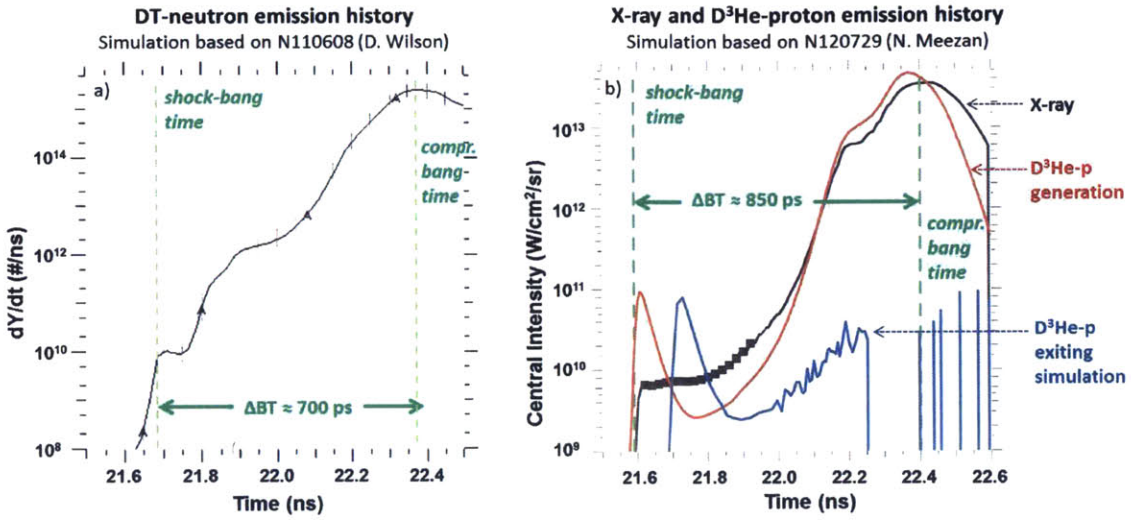

Figure 2.4. Simulated DT-neutron, x-ray, and D^3He-proton emission history from NIF implosions. a) Simulated DT-neutron emission for NIF cryogenic implosion N110608. The simulation was provided by Doug Wilson. The shock-bang appears as a ~100 ps plateau in the DT-neutron emission rate, approximately 700 ps prior to peak emission. The contrast between the neutron emission rate at shock-bang and the peak emission rate is 2×10^5. b) Simulated x-ray and proton emission for NIF D^3He-gas filled surrogate implosion N120729. The simulation was provided by Nathan Meezan. The shock-bang appears in the x-ray emission history (black) as a ~200 ps plateau, approximately 850 ps before peak emission. The emission rate at shock-bang is approximately 5000× lower than at peak emission. A clear spike in the D^3He-proton production is observed at shock-bang time (red). The rate of D^3He proton production at shock-yield is a factor of 500 less than the peak production rate; however the increasing density of the implosion with time prevents compression-yield protons from escaping. In the history of D^3He-protons exiting the simulation (blue), the shock-yield is the dominant feature.

erence [17], this radius is compared to the shell trajectory as measured by time-resolved x-ray radiographs of the implosion using the 'Convergent Ablator' (ConA) platform[15,16] to infer a rough shock-bang time. This data show that the ΔBT varies from 0.4 to 0.8 ns, as a function of the "coast time," which is the time difference between the end of the laser impulse and compression-bang time. This variation is not reproduced in the simulations, which anticipate ΔBT to be constant. Since these shifts are not reproduced in the simulations, they suggest that the timing of the shock collapse at the center of the implosion and of the subsequent onset of the deceleration phase are not well understood in these ignition-scale implosions. This discrepancy supports the need for an independent measurement of the shock-bang time and ΔBT, to confirm the result, perform a more precise and systematic study of this discrepancy between data and simulations, and strongly constrain models of shock-propagation and deceleration-phase dynamics.

The shock-bang is a notoriously difficult event to diagnose using either nuclear or x-ray emission from ignition-scale experiments on the NIF. Signatures of the shock-bang in DT-neutron, x-ray, and D^3He-proton emission history are presented in Figure 2.4, as inferred from a simulation by Doug Wilson of a cryogenic NIF implosion N110608. At shock convergence, the DT-neutron emission rate plateaus at 10^{10} ns^{-1} for a duration of about 100 ps. This is followed by a monotonic, approximately exponential increase in the emission rate until peak nuclear production (compression-bang time), 700 ps after shock-bang. The emission rate at shock-bang is more than five orders of magnitude less than that at compression-bang time, making this signature exceptionally hard to diagnose. Assuming the burn-averaged ion temperature is 5 keV, Doppler broadening of the main peak will

overwhelm the shock-bang signal for any detector further than 40 cm from the implosion, while closer detectors would have to contend with increased x-ray background and detector saturation issues due to high neutron fluxes. In 2011, attempts to design a CVD-diamond-based diagnostic to measure the neutron shock-bang signature were unsuccessful due to these challenges.

The x-ray and proton emission rates shown in Figure 2.4 were post-processed from a 1D-HYDRA simulation by Nathan Meezan, for an ignition-surrogate NIF Symmetry Capsule (SymCap) implosion N120729. The x-ray shock-bang signature presents similar difficulties to the DT-neutron signature. In this simulation the shock-bang appears as a plateau in the x-ray emission history with a duration of approximately 200 ps, before the emission ramps up to peak intensity at compression-bang time, 850 ps later. The x-ray shock-bang intensity is a factor of 5000× less than the peak emission intensity. While this signature is more accessible than the DT-neutron shock-bang due to improved contrast and the lack of Doppler broadening, attempts to measure the x-ray shock-bang time and duration using streak cameras (DISC) have been generally unsuccessful due to background.

Unlike the DT-neutron and x-ray shock-bang signatures, the D^3He-proton emission at shock-bang forms a well-defined peak. This peak has been measured by WRF spectrometers on over 80 surrogate D^3He-gas filled NIF shots since 2010.[17] Importantly, although the D^3He-protons generated during the shock-bang are a factor of $\sim$ 1000 fewer than the number generated during compression burn, the increase in ρR with time prevents the compression-generated protons from escaping the implosion. For this reason, the D^3He-protons produced during the shock-burn are the dominant proton emission feature, making the D^3He-proton channel the most advantageous signal for measuring the shock-bang time. Admittedly, this signal is measurable only in surrogate D^3He-gas filled implosions, and cannot be directly observed in implosions with cryogenic-DT layers. However, the surrogacy of such implosions to cryogenic implosions has been repeatedly demonstrated,[18,15] and experimental results from these studies are valuable in their own right for studying implosion physics and testing models of the implosion dynamics.

Alternative proposals for measuring the shock-bang time have included a direct measurement of the pressure history at the center of the target, measured by looking at the velocity of a reflective material placed at the target center via reflectometry through a reentrant cone. This method makes use of the velocity interferometer system for any reflector (VISAR) which has been used for many shock-timing experiments on the NIF,[19] and could in principle provide the shock-convergence time in a cryogenically layered implosion. However this type of 'keyhole' experiment is effectively a one-off: the shock-bang time measurement dominates the experimental design, so shock-bang time cannot be measured systematically for a wide-range of conditions and compared to other observables. As such, the D^3He-proton channel is by far the most promising shock-bang signature for systematic studies of the shock-bang time and compression-shock ΔBT. This measurement was the primary motivation for the design and implementation of the PTOF diagnostic.

2.2 Design and implementation of the Particle Time-of-Flight diagnostic

A particle time-of-flight (PTOF) diagnostic has been implemented to measure neutron and proton bang times at both OMEGA and the NIF. This versatile diagnostic is designed to operate at low yields, providing the only measurement of both DD-neutrons and D^3He-protons in surrogate D^3He-gas filled implosions at the NIF.

The PTOF detector is a circular, synthetic diamond wafer made by the chemical vapor deposition (CVD) technique that is biased along its axis. Incident high-energy particles excite

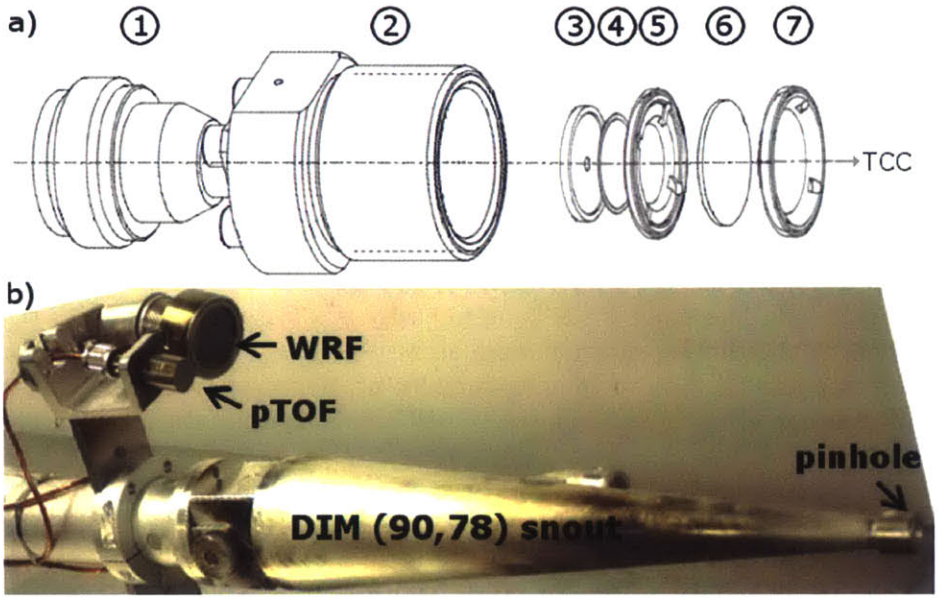

Figure 2.5. The PTOF detector as fielded on the NIF. a) The PTOF detector consists of: 1. N-type connector with biased central pin; 2. brass housing; 3. ceramic insulator; 4. 10 mm diameter CVD-diamond wafer with electrodes (standard thickness is 200 μm); 5. grounding ring aperture (8 mm ID); 6. internal filtering, configurable up to 1 mm thick; and 7. filter retaining ring. Optional external filtering in the form of 1 or 2 cm thick tungsten slugs can be screwed onto the outside of the brass housing. The detector housing (all components except the diamond wafer) is identical to that used in SPBT and was designed by A. Macphee.[3] b) The PTOF detector, shown here with 2 cm W external filtering, is fielded on DIM (90,78). The mounting hardware holds the detector at a fixed position relative to the pinhole of the primary x-ray diagnostic; depending on which snout hardware is used and the insertion depth, PTOF is held 42 to 52 cm from target chamber center (TCC). Up to four cling-on diagnostics may be fielded on a single DIM; PTOF is routinely fielded alongside three WRF modules. The mounting hardware was designed by NIF engineering.

electron-hole pairs in the diamond volume, a fraction of which are swept out by the bias field as a time-dependent current and recorded on an oscilloscope as a time-dependent voltage as shown schematically in Figure 2.2. The CVD-diamonds used are optical-quality, 200 μm thick samples with a diameter of 10 mm. The samples were acquired from Diamond Materials, GmbH,[20] and were further processed at Lawrence Livermore National Laboratory, where electrodes were deposited on the front and rear surfaces. The 1 μm thick, 9 mm diameter Au electrodes were deposited on top of an intermediate 200 Å Ti wetting layer. The diamonds are housed inside a brass assembly depicted in Figure 2.5. A rear electrode pin biases the sample, which is grounded to the housing by a ring-shaped front aperture. The aperture leaves 64% of the detector surface exposed. In front of the aperture, the housing has room for up to 1 mm of filtering material to act as x-ray shielding, which is held in place by a retaining ring. The outside of the housing is threaded, providing an easy mechanism to mount the diagnostic. These threads have also been used to attach additional x-ray shielding to the detector.

On the NIF, the PTOF diagnostic is fielded as a 'cling-on' diagnostic on a Diagnostic Instrument Manipulator (DIM)[21] located at (θ=90, ϕ=78) in the NIF chamber. The mounting hardware positions up to four such diagnostics at a fixed location relative to the pinhole of the primary x-ray diagnostic fielded in the DIM. Because of this arrangement, PTOF has no independent alignment and rides along on the primary diagnostic in DIM (90,78). Depending on the particular snout

hardware used and the insertion depth for the DIM on-shot, the PTOF detector distance to target chamber center (TCC) is between 42 and 52 cm. The detector typically fielded side-by-side with a compact WRF proton spectrometer, though solid radiochemistry (SRC) diagnostics have also been designed to fit on the 4-position hardware. At 50 cm from TCC, PTOF is the closest nuclear bang-time diagnostic to the implosion. Figure 2.5 shows a snout assembly with PTOF.

The standard bias for the NIF PTOF is -250 V. This value was set by the presence of several SMA connectors in the biased portion of the cable chain, which are generally not rated to biases higher than ~300 V. The PTOF cable chain underwent an overhaul in the fall of 2013, during which all biased connectors in the cable chain were replaced with N-Type connectors, which will nominally hold biases up to 1500 V. However, the PTOF has not been tested to higher voltages to date, and continues to operate at the 'standard' value. Calibration testing on OMEGA was performed at a variety of voltages, as will be discussed in Section 2.4.

The present and historical cable chains of the PTOF detector on the NIF are shown in Figure 2.6. Signals generated in the CVD diamond are transmitted from DIM (90,78) to the NIF mezzanine through 95 feet of low-loss LMR-400 cable. Currently, the connectivity of the PTOF cable chain from the bias-T to the PTOF detector is verified by time-domain reflectometry (TDR) prior to every shot. Until the cable upgrade in October 2013, the signal was first recorded on an FTD10000 7 GHz transient digitizer,[22] then attenuated and split before it was recorded on two channels on a Tektronix DPO70604B digital oscilloscope.[23] Since the cable upgrade, the operator may choose to record the signal on the FTD10000 and on one channel of the Tektronix digitizer, or on two channels of the digitizer only. The FTD10000's ability to withstand large input voltages allows this two-scope configuration to record signal amplitudes between 1 mV and 250 V on a single shot. A fiducial impulse signal sourced from the master laser oscillator provides a precise timing reference for both oscilloscopes with respect to the firing of the NIF laser. X-ray impulses are used to evaluate the absolute cross-timing between the fiducial impulse and the NIF laser at TCC, as well as to provide an impulse response function for the system. Details on the calibration of the PTOF system will be discussed in Section 2.4. In brief, the impulse response of the PTOF system has been shown to have a rise time of approximately 0.37 ns and a fall time of 1.44 ns. As discussed in Section 1.3.5, this is rapid enough for precise evaluation of bang-times to better than ± 0.1 ns, but does not have a fast enough rise time to measure the reaction history, unless it is unusually long ($\geq$300 ps).

An example of the raw data recorded by the NIF PTOF system is shown in Figure 2.7. This shot shows x-ray, D^3He-protons, and DD-neutrons. Interestingly, on this shot PTOF recorded D^3He-protons from both shock- and compression, which is clear from the characteristic double bump. The method of analysis for data acquired from this system is presented next.

2.3 Method for analyzing PTOF data

The PTOF data is a voltage impulse produced by the detector, affected by the cable system and measured on an oscilloscope. By measuring the response of the detector, cable and scope system to an impulse of ionizing radiation, we can connect the measured voltage to a *source function* that actually drives the detector. We assume that an infinitely rapid (delta-function) impulse of any type of ionizing radiation to the detector would produce the same impulse response, except for the absolute magnitude. This assumption is justified by the idea that any ionizing radiation will simply excite electron-hole pairs, which is measured. The detector is transparent to both neutrons and x-rays, so they are expected to deposit their energy volumetrically. Protons and charged particles deposit their energy differently as a function of depth in the diamond, and so in principle the

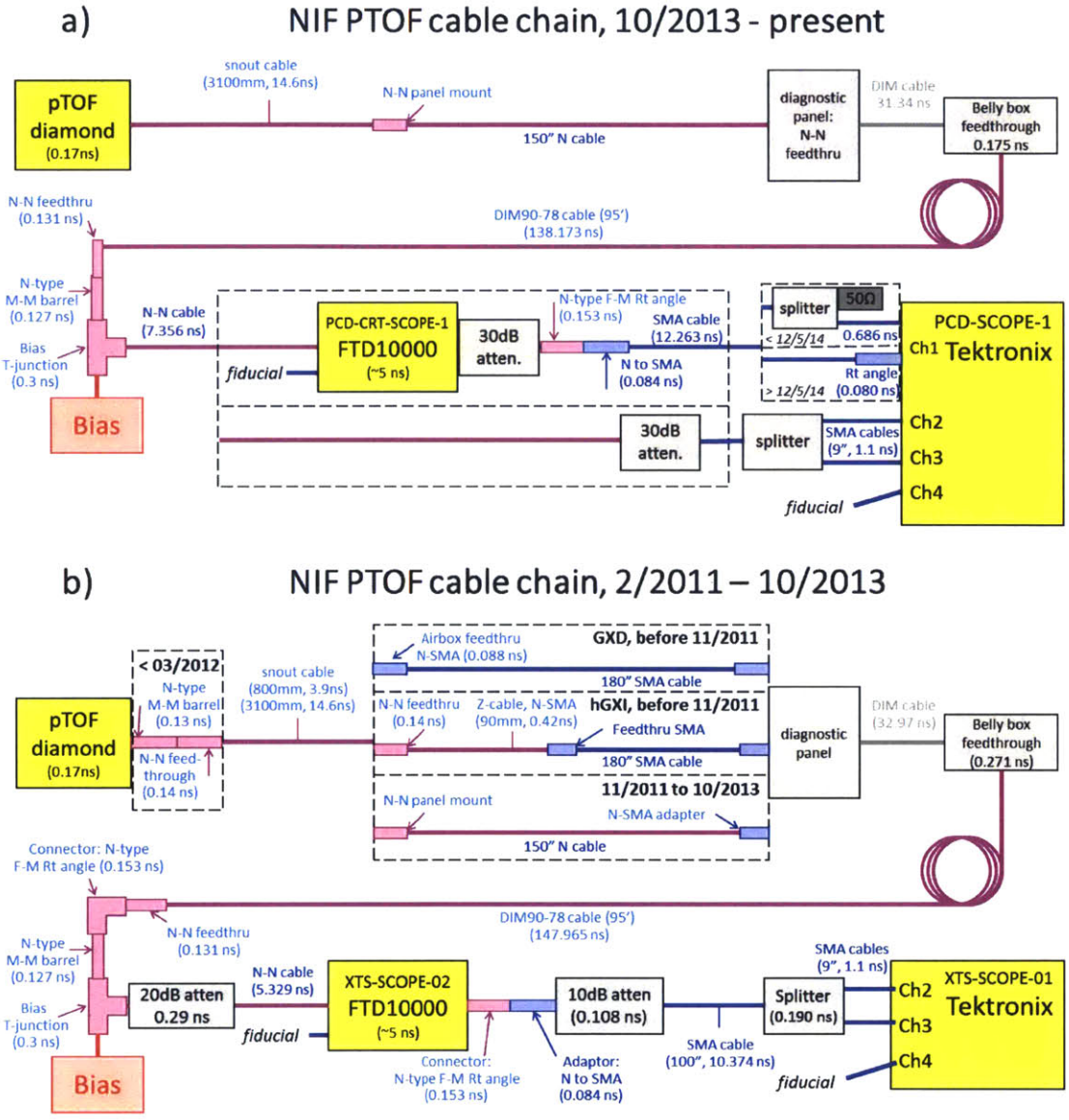

Figure 2.6. A schematic of the PTOF cable chain as fielded on the NIF, including approximate timings for each component. a) The setup installed in October 2013, which is current as of this writing. b) The historical PTOF cable chains since the first PTOF shots in 2011. Note that originally, the cables inserted into the target chamber were not uniform, and varied with diagnostics. This was corrected in November 2011. The hardware holding the PTOF was also simplified in March 2012. In both cases, attenuator locations and values are not permanent and are altered from shot to shot; values shown are typical. The cable chain was designed and is maintained by NIF engineering.

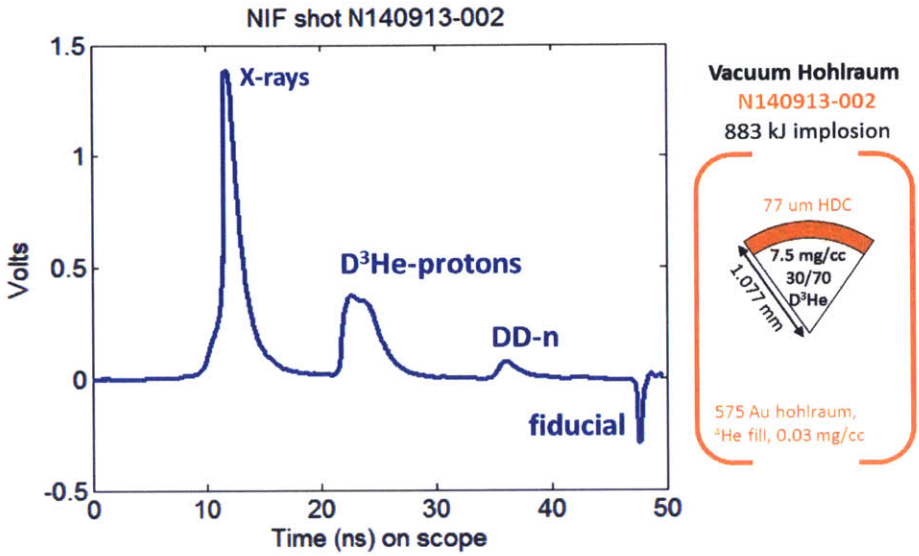

Figure 2.7. An example of raw PTOF data recorded on NIF shot N140913-002. On this near vacuum hohlraum implosion, PTOF observed x-rays, D^3He-protons, and DD-neutrons. The timing fiducial appears at 48 ns on the trace. On this particular shot both shock- and some compression-burn protons were observed, producing a double peak. The DD-neutron compression yield and D^3He-proton shock yield were 2.7×10^{11} and $\sim 2 \times 10^8$, respectively. The PTOF parameters were as follows: detector 200H, filters 25 μm Ta + 100 μm Au, snout cable #01. Target data is on the right-hand side.

impulse response might differ for these particles. To zeroth order, such variations are ignored here, and there is no evidence from the operation of the PTOF system that such effects are important. In general, the PTOF signal is assumed to be a convolution of the source function and the detector impulse response function (IRF).

The source function for nuclear particles striking the detector is most generally calculated from the temporal and spectral nuclear production history, $d^2Y/dt\ dE$, which I will call the *emission function*, $\mathrm{Em}(t, E)$. A depiction of the emission function and its relationship to observed spectra, inferred burn history, and the observed particle source function is shown in Figure 2.8. In particular, the burn history and emitted spectrum are calculated from this function as:

$$\frac{dY}{dt} = \int \mathrm{Em}(t, E) dE, \tag{2.2}$$

$$\frac{dY}{dE} = \int \mathrm{Em}(t, E) dt. \tag{2.3}$$

The simplest case is that in which the energy and time dependence of the emission function are not covariant. In this case, the emission function can be separated into a time dependant and an energy dependant part: $\mathrm{Em}(t, E) = (dY/dE)(dY/dt)$. Each of these parts may then be treated as an independent function, usually a Gaussian distribution with a respective spectral width σ_E and temporal width σ_t, as is shown in Figure 1.19:

$$\mathrm{Em}_{sep}(t, E) = \mathrm{Em}_E(E)\,\mathrm{Em}_t(t) = \frac{Y}{2\pi\sigma_E\sigma_t} \exp\left[-\frac{(E - E_0)^2}{2\sigma_E^2}\right] \exp\left[-\frac{(t - t_0)^2}{2\sigma_t^2}\right]. \tag{2.4}$$

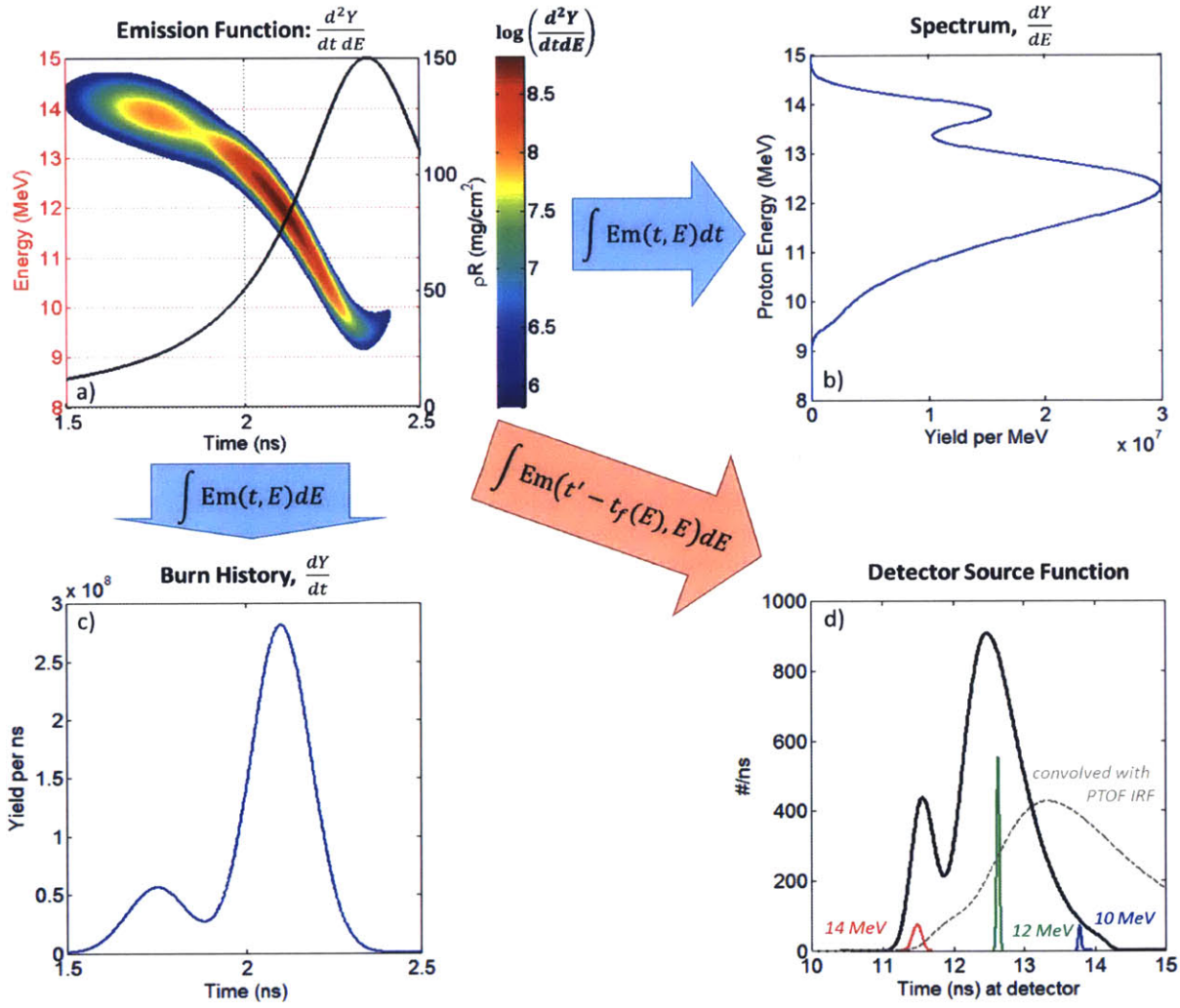

Figure 2.8. An example of the (a) fusion emission function Em(t,E), and its relationship to the (b) emitted spectrum, (c) burn history and (d) the source function for a time-resolved diagnostic. Em(t,E) is equal to $d^2Y/dtdE$ (color map, shown as log_{10}[Em]) and is determined by the temperature and density of the fusing plasma, with the emitted energy reduced by the total areal density (ρR, black line). Integrating the emission function over time gives the emitted particle spectrum, and over energy gives the (emitted) burn history. The integral that produces the source function is given in Equation 2.6. Only the measured spectra and source functions are directly observed, and the emission function and the emitted burn history must be inferred from them. The values in this plot were selected to match the data observed in OMEGA implosions by J. Frenje, et al.[24] In (d), the arriving packets of 14, 12, and 10 MeV protons are shown to highlight the effects of doppler broadening and ρR evolution on the source function (black). The convolution of the source function with a nominal PTOF impulse response is also shown (grey dashed).

However this is not generally true. For example, the shock yield in surrogate D^3He-gas filled NIF implosions occurs at or near peak velocity of the imploding fuel, and ρR evolution rather than thermal broadening dominates the recorded spectra. This is clear especially in scenarios where some protons from the beginning of the compression burn are recorded, as in the PTOF data shown in Figure 2.7. However for compression-bang and for neutrons, which are not scattered or downshifted substantially by the fuel whenever they are emitted, the assumption of separability is reasonable. Special cases in which the ρR evolution must be taken into account for D^3He-proton data will be addressed later.

The source function for particles hitting the detector at a distance from TCC d can be calculated directly from the emission function by way of the *time-of-flight equation*, $t_f = d/c\beta(E)$. Here, c is the speed of light and β is the relativistic velocity:[b]

$$\beta(E) = \sqrt{\frac{(E + mc^2)^2 - m^2c^4}{(E + mc^2)^2}}. \tag{2.5}$$

Each particle emitted at time t with energy E arrives at the detector at a time $t' = t + t_f(d, E)$. Thus the source function is uniquely defined in terms of the emission function and the detector distance as:

$$\mathfrak{S}(d, t') = \int \mathrm{Em}\left(t' - t_f(d, E), E\right) \left(\frac{A_d}{4\pi d^2}\right) S_d(E) dE. \tag{2.6}$$

Here, A_{det} is the active area of the detector, and S_d is the sensitivity of the detector to the particle as a function of energy. Assuming that the detector sensitivity is approximately a constant with energy S_{d0}, the time integral of the source function is then $\int \mathfrak{S} dt = Y S_{d0} A_d / 4\pi d^2$.

Even in the specific case of separable Gaussian emission functions in time and energy given in Equation 2.4, it is difficult to analytically evaluate the source function. In practice, the simplest method is to numerically integrate a presumed emission function, with a time resolution equal to or higher than the recorded data. This procedure is used to generate the source function for particles hitting the PTOF detector. Assuming a separable Gaussian emission function, the source function for the spectral component as a function of time in the detection plane t' is determined as

$$\mathfrak{S}_E(t') = \mathrm{Em}_E\left(E(t_f)\right) \left[\frac{(E(t_f)^2 + 2mc^2 E(t_f))^{3/2}}{dmc}\right] \delta\left(t' - t_f\right). \tag{2.7}$$

The term in square brackets is the Jacobian $\partial E / \partial t_f$, which is included to preserve the area of the integrand when converting from energy-space to time-space, and δ is the Dirac delta function, which enforces an assumption that all particles were emitted at $t = 0$. This spectral source function is then convolved with the burn history. A procedure which is more generally applicable when the spectral- and time-emission histories are coupled is to calculate the incidence history for each particle energy at the detector plane [$\mathrm{Em}\left(t' - t_f(E_0), E_0\right)$ for each E_0] and then sum these separate histories. The latter procedure requires an interpolation for each spectral bin, while the former requires one interpolation and a convolution.

The assumed spectrum for this process depends on the type of particle being measured. For D^3He-protons, the emitted spectrum is measured directly by WRF spectrometers. This data can

[b]For DT-neutrons, the most energetic particle that is routinely measured, the relativistic correction is ~1% in velocity, which translates into 0.1 ns: larger than the uncertainties for some experiments. Even for DD-neutrons, the correction is ~46 ps, sufficiently large to care about.

Table 2.1. Bulk velocity energy shift coefficients C_{bulk} for several commonly measured species. These coefficients are used to calculate the mean energy shift of fusion products ($\Delta E/E$) due to flow velocity of the fusing plasma (V_{COM}) using the equation provided, where θ is the angle between the detector line-of-sight and the direction of flow.

Species	C_{bulk}
DD-n	0.00923
D^3He-p	0.00377
DT-n	0.00385

$$\frac{\Delta E}{E} \approx C_{\text{bulk}} \cos\theta \left(\frac{V_{COM}}{[100\ \mu\text{m/ns}]} \right)$$

be directly used to generate the proton source function for PTOF.[c] For DD-neutron signals, no spectrum is measured. However the birth spectra of fusion products from a thermal plasma was calculated with relativistic corrections by Ballabio, et al. up to the third spectral moment.[25] The mean energy is weakly dependent on the ion temperature, and the spectral width is proportional to $\sigma \propto \sqrt{T_i}$, as discussed in Section 1.3.1. The ion temperature that is independently measured by the nTOF diagnostics is used to determine the anticipated spectrum and source function for DD- and DT-neutrons. Since PTOF has too slow of a rise to measure the burn history, it is generally insensitive to the Doppler broadening: an ion temperature of 3 keV will introduce Doppler broadening of ~300 ps at the PTOF detector, comparable to the rise time. However it is important to take corrections to the mean energy into account.

Recent nuclear diagnostic data suggest that significant non-stagnated flows exist in NIF implosions.[26] Such flows would have a direct impact on the observed spectra of fusion products[d] and therefore potentially on the time-of-flight. The relevant equation for this effect is Equation 1.32, which presents the particle energy as a function of collisional center-of-mass velocity. In Section 1.3.1, this formula was Maxwellian-averaged to determine the spectral broadening due to ion temperature. Because of symmetry, the mean energy was unaffected to 1st order. However assuming there is residual velocity in the fuel, this will break the symmetry and shift the mean energy by

$$\frac{\Delta E_3}{E_3} \equiv \frac{E_3(V_{COM})}{E_3} - 1 \approx V_{COM} \cos\theta \left[\frac{2m_3(m_3+m_4)}{m_4(Q+K)} \right]^{\frac{1}{2}}. \tag{2.8}$$

Typical residual flow velocities are on the order of 100 μm/ns. For DT-neutrons (Q = 17.6 MeV, $m_3 = 1$, $m_4 = 4$), this flow velocity shifts the neutron energy by up to ± 0.38% and the time-of-flight by only ±18 ps, which is negligible. For DD-neutrons (Q = 3.27 MeV, $m_3 = 1$, $m_4 = 3$), this flow velocity shifts the neutron energy by a similarly small ± 0.92%, however the effect on the time-of-flight is significant at ±106 ps. Ultimately, this effect may need to be considered when analyzing DD-neutron data. A simplified formula for calculating the mean energy shift due bulk fuel velocity for DD-neutrons, D^3He-protons, and DT-neutrons is provided in Table 2.1

Following the above procedure, a source function is established with two variables: the time of peak emission ('bang-time') and the amplitude of the source, which is proportional to yield. By convolving the source function with the instrument response function, a model of the PTOF data is produced. The convolution of the two functions is defined mathematically as $M(t) = (\mathfrak{S} * \text{IRF}) = \int \mathfrak{S}(t')\text{IRF}(t-t')dt'$. Convolution is commutative, associative, and distributive. Note that, for

[c] Using the WRF spectrum to calculate a proton source function is imperfect because the WRF is a time-integrated diagnostic. Because the time evolution of the ρR dominates the width of the proton spectrum, the high-energy protons are emitted at the beginning of the shock-bang and the low-energy protons at the end. This effect introduces broadening to the source function of approximately half the burn width, which is typically < 100 ps and is negligible.

[d] Indeed, this is how they were inferred: from changes in the observed neutron energy for different lines of sight.

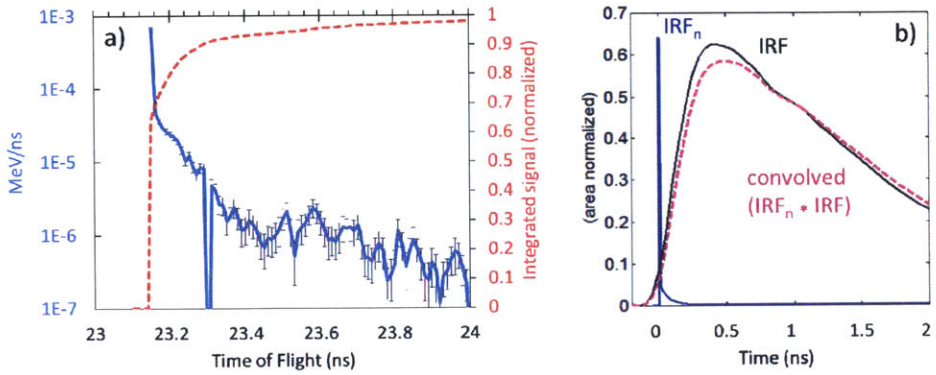

Figure 2.9. a) DD-neutron energy deposition rate (blue) and cumulative deposition (red) in the PTOF detector modeled by a Monte-Carlo neutron transport simulation including 2 cm tungsten shielding. 64% of the energy is deposited within 10 ps of the nominal time-of-flight ($t_0 = 23.15$ ns); 29% is deposited in an exponential tail with a time constant of 71 ps, and the remaining 6% energy is deposited more than 300 ps after t_0. b) An additional impulse response for DD-neutron signals with 2 cm W shielding was evaluated from the simulation (blue, shown here $\times 0.01$). When convolved with the PTOF instrument IRF (black) the combined IRF shape is slightly changed (magenta), with the rise-time slower by approximately the IRF$_n$ falloff time.

a delta-function source, the model signal $M(t)$ is simply equal to the impulse response function; similarly, for a delta-function impulse response, the model signal is equal to the source function.

Modifications to the source function that occur at or near the detector may be best included in the analysis as additional impulse responses to be convolved with the source function. For example, the PTOF is often fielded with a 2 cm tungsten x-ray shield, which scatters some of the incident DD-neutrons. Monte Carlo simulations of 2.45 MeV neutron transport using the code MCNP5[27] showed that 64% of the total energy deposited by neutrons in the PTOF diamond was deposited within 10 ps of the nominal time-of-flight, but the remaining energy was deposited in a decaying tail with a time constant of 70 ps, as shown in Figure 2.9. This response is most simply included by assuming that each neutron has an additional impulse response function (IRF$_n$). In reality, the apparent impulse response is probabilistic and averages over many individual neutrons, both scattered and unscattered. However, a measurable PTOF signal requires over a thousand neutrons to interact with the detector, so a probabilistic approach is sufficient. Since convolution is associative, this additional impulse response may simply be convolved into the model signal as $M(t) = \mathfrak{S} * (\mathrm{IRF} * \mathrm{IRF}_n)$.

The model signal is forward-fit to the recorded PTOF data: for a given set of the two variables, the model and data are compared by evaluating the sum of the squared difference between them. The amplitude and bang-time are then varied until an optimal fit is found. The goodness of the fit is defined by the size of the *chi-squared* parameter:

$$\chi^2 = \sum_i^N \frac{[x_i - M(x_i)]^2}{\sigma_i^2}, \tag{2.9}$$

where x_i are the measured data, $M(x_i)$ are the modeled data, and σ_i are the expected uncertainty in each datapoint. The uncertainties are typically taken as the noise floor for the scope channel in question.[e] A good fit requires that the average difference between the data and the model is no

[e] In principle, statistical noise would also be included; however the 'smearing out' of the signal by the IRF makes

Table 2.2. Typical error budget for the PTOF-measured bang times using DT-neutrons, DD-neutrons and D^3He-protons, and for the ΔBT between measurements of shock- and compression-bang time using D^3He-protons and DD-neutrons, respectively. D^3He-protons are assumed to be ranged down to ~10 MeV. Time units are picoseconds.

Source of uncertainty	Uncertainty			Timing Uncertainty (ps)			
	DT-n	DD-n	D^3He-p	DT-n	DD-n	D^3He-p	ΔBT
Crosstiming to laser system				±15			
Detector IRF (in situ)				±25			±35
Forward Fit (S/N = 10)				±18			±25
Cable repeatability shot-to-shot				±5			
Nominal detector distance	±0.5 mm			±10	±23	±12	±12
DIM positioning accuracy	±1 mm			±19	±46	±23	±23
Mean energy†	±11 keV	±5 keV	±140 keV	±4	±23	±79	±82
Total:				±41	±66	±90	±96

† Fuel velocity ±20km/s

greater than the uncertainties, and so is defined as $\chi^2 \approx N - k$, where N is the number of data points and k is the number of variables,[f] or as it is usually written: $\chi^2_{reduced} \equiv \chi^2/(N-k) \approx 1$. The region of acceptable fits is usually defined as fits with $\chi^2 - \min\chi^2 \leq 1$. This condition is used to establish the 1-σ error bars in the fit parameters, by finding the most extreme values of each parameter for which the condition still holds.[g]

In the event that the minimum reduced chi-squared is not equal or close to unity, there are several possible explanations. First, the uncertainties σ_i of the measurement may be incorrect. In this scenario the uncertainty is either larger or smaller than expected, resulting in a minimum χ^2_{red} that is smaller or larger than 1. One approach is to rescale the uncertainty to enforce the condition $\min\chi^2_{red} = 1$, and then use the rescaled χ^2 values to evaluate the uncertainty of the inferred parameters. This leads to the error bar condition $\chi^2 - \min\chi^2 \leq \min\chi^2_{red}$. Obviously care should be taken to ensure the new measurement uncertainty values are realistic. Second, the model itself could be wrong, either due to an incorrect source function or IRF. In this case, the model must be reconsidered.

The details of the total uncertainty in the inferred bang-time vary from shot to shot, but typical values are presented in Table 2.2 Both systematic and random uncertainties are included. The timing uncertainty due to detector distance and particle energy uncertainties follow from standard error analysis, for example $\sigma_{E,t} = (dt_f/dE)\sigma_E$. The total uncertainty for a given product equals the root-mean-square sum of all individual timing uncertainties. The dominant uncertainty for D^3He-protons is the mean energy, which is inferred from WRF spectrometers fielded on the same DIM. The absolute uncertainty of this measurement is greater than the WRF calibration uncertainty of ±60 ps because the WRFs measure the proton energy along a different line-of-sight from the PTOF. The observed variation in mean proton energy as measured by different WRFs fielded on the same DIM is ±140 keV, which translates into a proton time-of-flight uncertainty of ±79 ps. Since the neutron energy is relatively well known, the dominant uncertainty for DD-neutrons is the uncertainty in detector distance to the target. The detector location is fixed relative to the x-ray

it difficult to evaluate that contribution, while the fact that many particles are typically measured makes the effect negligible.

[f]The number of variables is subtracted because the fitting process will match some piece of data ideally, regardless of the uncertainties. Some sources use N - k - 1; since $N \gg k$, this choice does not make a significant difference.

[g]The procedures described here are standard statistical procedure for data analysis. An excellent introduction for experimental researches is presented by P. Scott.[28]

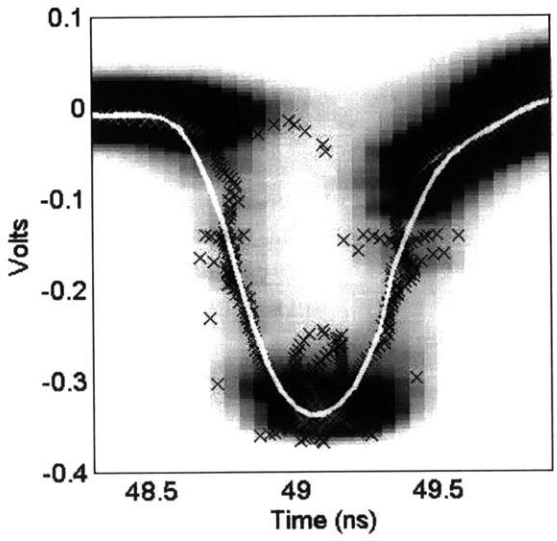

Figure 2.10. The timing fiducial image recorded on the PTOF FTD10000 transient digitizer. The depletion of signal brightness for rapidly changing signals makes the auto-analysis, which is based on finding the centroid in pixel columns, ineffective. The left, right, and bottom of the peak are processed separately by sampling with lineouts at 0°, 45°, 90°, and 135°. A set of probable points (x) is evaluated from the centroids of objects in these lineouts, and a smoothing spline (white line) is fit to the total set of probable points. The weights and parameters of the fit were fine-tuned to get a consistent result, with a timing accuracy of ±15 ps. This sample is from N131108; color scale is truncated to show detail.

diagnostic pinhole on the DIM (90,78) snout, and the nominal distance from the detector to TCC is calculated from the engineering drawings. This method was shown to produce the same result as CAD models of the diagnostic hardware to within ±0.5 mm. The magnification of the primary (90,78) x-ray imaging data can be analyzed to determine the insertion depth of the pinhole, and therefore the on-shot location of the PTOF detector. Typically this procedure can determine the radial position of the detector with an accuracy of ± 1 mm. When inferring the ΔBT, several of the systematic uncertainties are eliminated (such as absolute cross-timing and cable timing) or reduced (such as distance uncertainty). However, the evaluation of ΔBT includes fitting and energy uncertainties from both particles, and is therefore not better known than the absolute bang-times. The total typical uncertainty for all nuclear bang-times are typically better than ± 100 ps.

2.4 PTOF calibration studies

Three aspects of the PTOF system have been calibrated extensively: timing, impulse response, and detector sensitivity. Additionally, the relative sensitivity of the PTOF detectors to the signals of interest and the x-ray background has been studied in NIF experiments to establish the optimum shielding.

2.4.1 PTOF cross-timing and IRF calibration

The cross-timing of the scope traces to the laser system is established using a timing shot, in which an 88 ps full-width at half maximum (FWHM) laser impulse is used to drive a thin gold or silver foil at TCC. This generates a short x-ray burst which is detected by the PTOF system as an impulse. The resulting PTOF signal is used for precise cross-timing of the fiducial impulses to the laser timing at TCC. Uncertainty in the time-dependent spectral emission of the targets on such timing shots introduces a slight systematic uncertainty in the cross-timing. The absolute PTOF fiducial cross-timing is estimated to be approximately ±15 ps.

Accurate and repeatable identification of the fiducial impulse on the FTD10000 is highly important for transferring this timing reference from shot to shot. Figure 2.10 shows a recorded image of the fiducial impulse. The instrument uses the incident voltage to sweep an electron beam onto

a phosphor screen, which is subsequently recorded and digitized. Extremely rapid impulses such as the fiducial impulse cause a reduction in image intensity, such that the standard digitization method of finding the centroid of intensity for each column of pixels does not capture the rise and fall accurately. To determine an accurate shape for the fiducial, three sub-images are generated containing the rising and falling edges and the peak of the fiducial. These images are then sampled by lineouts taken at a variety of angles (typically: vertical, horizontal, and at either 45° or 135°, whichever is more perpendicular to the impulse slope). Features in the lineouts are isolated and used to calculate a set of probable points in the curve. Finally, a smoothing spline fit to all recorded probable points accurately reproduces the impulse shape. In principle, this method can be applied to the entire trace, but in practice most scenarios feature only slowly-varying traces and the standard analysis is acceptable. The fit to the fiducial peak is processed following the method of Lerche, et al.:[29] the half-maximum points on the rising and falling edges are interpolated from the data, and the midpoint taken to establish the time. This method can establish the absolute arrival time of a Gaussian impulse to better than 10% of the step size, or $\sim \pm 5$ ps in this application.

As is presented in Figure 2.6, the cable chain has been modified repeatedly over the course of PTOF operations. Each change to the cable chain will shift the signal transit time to the oscilloscopes, and therefore change the absolute timing calibration of the system. These changes must be accounted for to maintain the calibration from shot to shot. The most common change is the snout cable, which is installed and removed on each shot during standard PTOF operations. Fifteen, 3100 mm snout cables have been fabricated, calibrated, and are currently available for use in PTOF operations.[h] The min-max variation in the signal transit time through the cables is 123 ps, and must be accounted for in analyzing the bang-time. The 150-inch cable is typically installed for a particular DIM instrument (e.g GXD, hGXI), and is occasionally changed as well. Currently there are six instances of this part, with a min-max timing variation of 45 ps. The diagnostic panel, DIM cable, belly-box feedthrough, and facility cable (95') were modified once, during the cable upgrade in October 2013, during which the entire cable chain was simplified and standardized. In the mezzanine, hardware is generally not modified, with the exception that attenuators can be interposed in the cable chain both before and after the FTD10000 scope and before the Tektronix oscilloscope. The attenuators used are absolutely timed and typically have single transit times on the order of 100–300 ps.

To keep track of the current state of the cable chain, determine the difference in total cable chain transit time between the current shot and a timing shot, and calculate the appropriate adjustment to the absolute timing, a Cable Chain Management System (CCMS) was programmed using MATLAB.[30] This system maintains and updates a database of the components installed on each shot, and can output a transit time shift between two shots of interest. Only the snout cable is updated routinely; less frequently-modified components must be updated in the database manually. The CCMS is integrated into the first module of the analysis program, which parses the data and adjusts it for absolute timing. The resulting corrected trace is then passed to the second module for bang-time analysis.

X-ray impulses also are used to establish the impulse response of the PTOF system. The IRF is critical to the analysis of PTOF data, as was discussed in Section 2.3. The data collected from two x-ray impulse shots is shown in Figure 2.11. On x-ray impulse shot N110531, the PTOF recorded an IRF characterized by a 1.70 ns FWHM. A model frequently used for impulses of this shape is a

[h]Eight, 800 mm 'short' snout cables were fabricated and remain in the system, although they are not currently used. Only two of these were ever used on NIF shots.

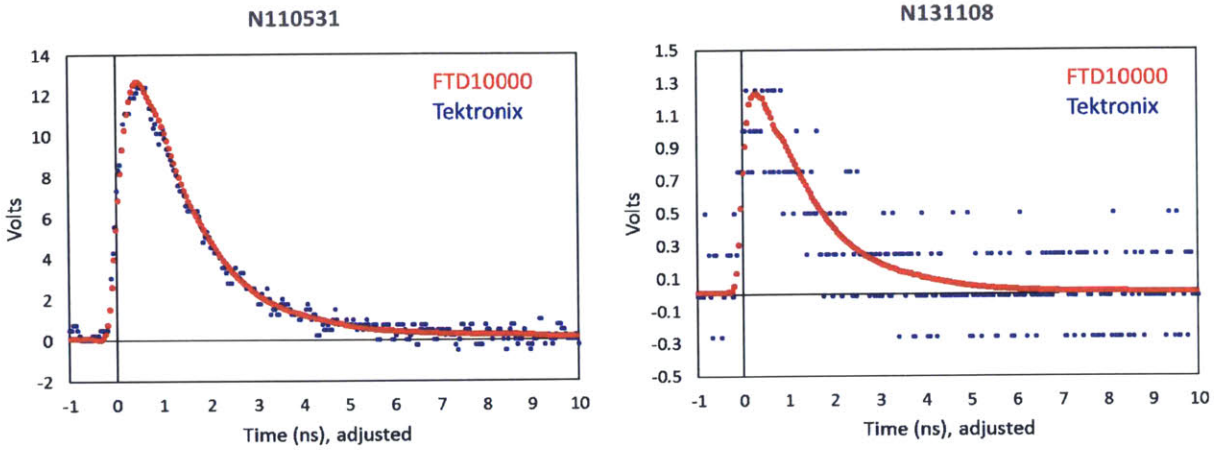

Figure 2.11. PTOF traces from two x-ray impulse shots at the NIF. N110531 was an 88 ps, 5.4 kJ impulse onto a gold target; N131108 was an 88 ps, 9.75 kJ impulse onto a gold disc. IRFs were derived from this data for use in the analysis of the PTOF data recorded on implosions. A standard rise-time of 370 ps and fall-time of 1.44 ns were inferred from N110531, and 300 ps and 1.3 ns from N131108. The change in rise and fall time between these two impulses is likely due to changes in the PTOF cable chain.

product of exponentials:

$$\mathrm{IRF}(t, \tau_{rise}, \tau_{fall}) = (t \geq t_0)\left(1 - \exp\left[-\frac{t - t_0}{\tau_{rise}}\right]\right)\exp\left[-\frac{t - t_0}{\tau_{fall}}\right]\left(\frac{\tau_{rise} + \tau_{fall}}{\tau_{fall}^2}\right), \tag{2.10}$$

where τ_{rise}, τ_{fall} are the characteristic rise and fall times. The final term normalizes the integral such that $\int \mathrm{IRF} dt = 1$. Using this model, the rise- and fall-times of the PTOF IRF were measured to be 370 ps and 1.44 ns on the N110531 timing shot, with a FWHM of 1.61 ns. Slightly shorter characteristic times, 300 ps rise, 1.30 ns fall, and 1.52 ns FWHM, were measured on the N131108 timing shot, after the cable upgrade. The change may be due to the removal of connectors and overall simplification of the cable chain.

2.4.2 PTOF calibration to D^3He-protons, DD-neutrons, and DT-neutrons

Several PTOF detectors have been fielded on diagnostic development implosions at OMEGA to determine their characteristic sensitivity to various nuclear products of interest. On OMEGA, the PTOF detectors are mounted in a TIM such that the detector could be positioned at various distances to TCC. The approximate setup of detectors fielded on the NIF was replicated: the PTOF cable chain consisted of 12' RG142 cable, 38 m of LMR400 cable, a bias T (Picosecond model 5531), and 2.5 m of LMR300 cable, before being split into three channels and recorded on a Tektronix DPO70604B digitizer (6 GHz). Up to three detectors were fielded in different TIMs on a single shot for the calibration studies. The majority of the calibration studies were performed during a half-day of OMEGA shots on November 2nd, 2010, and during shot operations on May 24th through 26th, 2011. Calibrations for detector sensitivity to D^3He-protons, DD-neutrons, and DT-neutrons were recorded for CVD-diamonds ranging from 100 to 1000 μm thick, with bias voltages ranging from -250 to -1500 V.

Typical calibration data from a D_2-filled, shock-driven implosion is shown in Figure 2.12. The typical sensitivity of the standard PTOF detector, a 200 μm thick diamond wafer biased at -

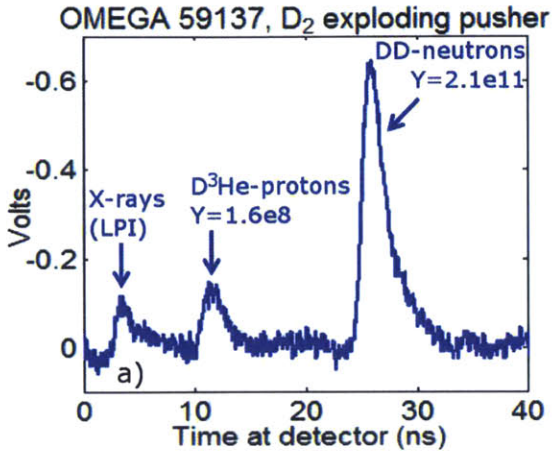

Figure 2.12. PTOF calibration results from a shock-driven D_2-gas filled implosion on OMEGA, showing signals from x-rays, DD-neutrons, and secondary D^3He-protons. This type of data was used to determine the PTOF sensitivity to DD-neutrons; D^3He- and DT-gas filled implosions were also used to determine the PTOF sensitivity to D^3He-protons and DT-neutrons, respectively. This signal was recorded using a 1000 μm thick detector biased at 500 V, filtered with 100 μm Al + 100 μm Ta, and positioned 50 cm from TCC.

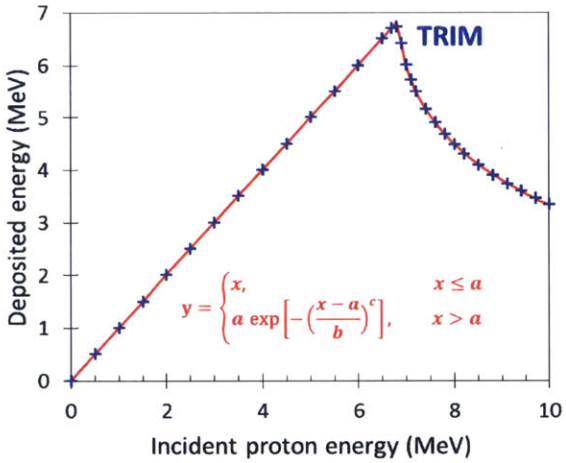

Figure 2.13. Energy deposition in a 200 μm thick CVD-diamond wafer as a function of proton energy, simulated using the ion transport code TRIM (blue points).[31] A parametrized model (red) matches the data well with the following values: a = 6.869 ± 0.005 MeV, b = 5.782 ± 0.077 MeV, c = 0.524 ± 0.007.

250 V, was determined to be 2.0×10^{-8} V ns per incident 2.45-MeV neutron, 5.4×10^{-8} V ns per incident 14.1-MeV neutron, and 7.3×10^{-5} V ns per incident 11.4-MeV proton. The selection of PTOF diamonds have demonstrated a range of sensitivity that varies by a factor of 0.5–4× around these values. Further results of calibration experiments and related PTOF tests may be found in Appendix G.

The D^3He protons were ranged down to 11.4 MeV using 100 μm Al and 100 μm Ta filters. Such protons transit 200 μm of diamond, and therefore will not deposit all of their energy in the detector. It is expected that the maximum sensitivity of a given detector as a function of proton energy would correspond with the energy of a proton with a range equal to the thickness of the detector. For the standard 200 μm wafer, this corresponds to a proton energy of about 6.9 MeV. Below this energy, the proton is fully stopped in the wafer and thus deposits less energy in the detector; above this energy, the proton escapes the detector with some remaining energy. The TRIM ion transport code[31] was used to calculate the energy deposited in a 200 μm CVD-diamond by protons as a function of incident proton energy, as shown in Figure 2.13. To first order, the detector sensitivity is expected to scale as the amount of deposited energy.

The relative sensitivity of a detector to protons and to neutrons was found to vary as a function of the detector thickness. Figure 2.14 shows results from the calibration of detectors between 100 and 1000 μm thick. As discussed previously, protons deposit their energy as a function of location

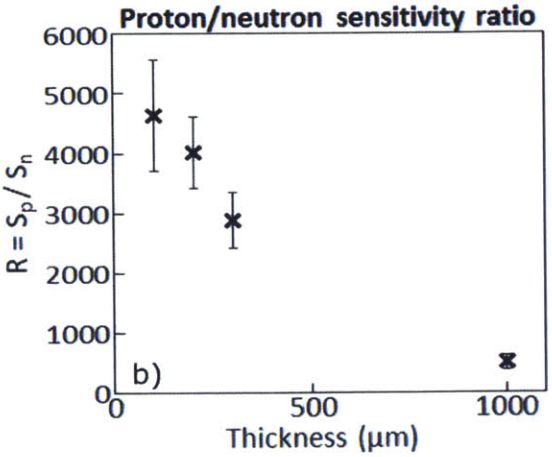

Figure 2.14. PTOF detector sensitivity to ~ 11-MeV protons relative to 2.45-MeV neutrons was studied as a function of detector thickness. Thinner detectors are observed to have higher relative proton sensitivity. This data was recorded using shock-driven implosions on the OMEGA laser facility. Detectors were filtered with 100 μm Al + 100 μm Ta and biased at 500 V.

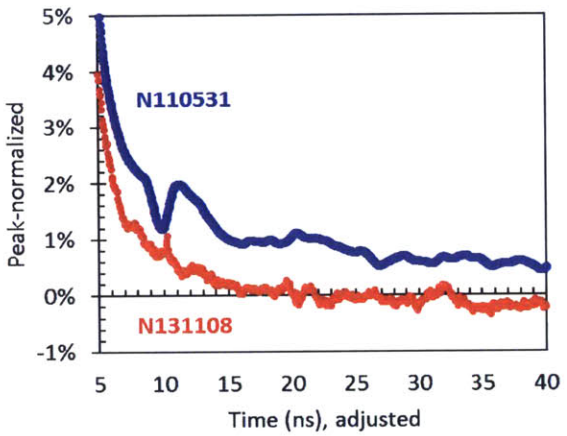

Figure 2.15. A zoomed-in view of the tails of PTOF traces recorded on NIF impulse shots, showing features on the order of ~1% of the peak. N110531 (blue) was recorded using the original 800 mm ('short') snout cables, while N131108 (red) was recorded with the 3100 mm ('long') snout cables. The reflection associated with the connector at the end of the short cable is clearly seen at 10 ns, and is eliminated by using the long cable. The slight negative trend on the tail of the IRF is caused by recharging of the detector bias after the impulse, which occurs on a relatively long (~μs) timescale.

within the diamond. In contrast, x-rays and neutrons both deposit energy volumetrically, because the characteristic ρR for scattering is much greater than the thickness of the detector. The range in diamond of the 11 MeV protons used in this study was approximately 470 μm; additional detector thickness would be expected to increase neutron and x-ray sensitivity, but not proton sensitivity. Because of the volumetric deposition process, x-ray and neutron sensitivity are expected to scale similarly. The 200 μm detectors were selected for PTOF in order to optimize the proton signal relative to x-ray background.

2.4.3 Characterization of PTOF x-ray background

The level of x-ray background in the PTOF data has been a point of concern, as such backgrounds can dominate the DD-neutron and D^3He-proton signals of interest if the detector is not properly shielded. D^3He protons and DD-neutrons arrive at the detector approximately 10 and 20 ns after the x-ray impulse, respectively, giving the detector roughly 7 and 14 e-folding times to recover. However at the ~5% level, the tail of the impulse response function does not follow a pure exponential falloff, and is instead dominated by bumps associated with reflections at imperfectly impedance-matched connections. Many of these connections are reinstalled from shot to shot, and so cannot be accurately characterized even in principle. For this reason, the original 3.9 ns snout cables were replaced with 14.6 ns cables in December 2011. The 'long' snout cables delay reflections by twice

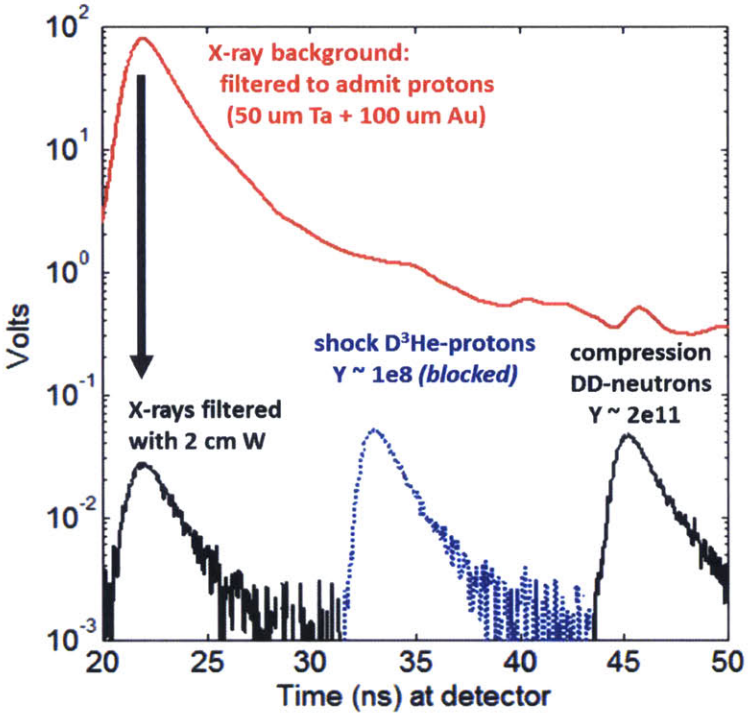

Figure 2.16. Synthetic PTOF x-ray and particle signals from a NIF gas-filled hohlraum implosion of a surrogate D^3He-gas-filled target. When the detector is filtered to admit protons (red, with 50 μm Ta + 100 μm Au), the signal is dominated by hohlraum x-rays with a peak on the order of 100 V. The expected scale of the D^3He-proton signal is shown (blue) for comparison. With 2 cm tungsten shielding (black), the x-rays are reduced by three orders of magnitude enabling the measurement of the DD-neutrons, but protons are blocked. X-ray levels are based on those observed on shot N110807.

the crossing time (~29.2 ns), and out of the region of interest. Figure 2.15 compares the tails of impulse responses recorded using these two cables, showing that the characteristic reflection feature is eliminated from the region of interest by using the long cables. That being said, several assorted noisy features persist on the order of a few tenths of a percent of the peak. To prevent interference of these features with the data, the ratio of signal peak voltage to x-ray peak voltage must be no less than 0.01, and preferably in the range 0.1 to 1.

A strong x-ray signal could also alter the effective IRF of the detector for a subsequent, smaller signal arriving on its tail. L. Dauffy, et al. studied this effect in Reference [32] using a 250 μm thick CVD diamond biased at +250 V, which was irradiated to produce a saturated signal with a peak voltage greater than 10% of the bias followed by a second signal either 5, 10, or 20 ns later. The 5 ns delayed signals demonstrated an altered IRF, while the 10 and 20 ns delayed signals demonstrated the linear IRF, indicating that the detector had recovered between 5 and 10 ns after the saturating impulse. While this study is encouraging with regard to the PTOF data, for which the DD-neutron signals arrive ~ 20 ns after the x-rays, future double-pulse studies are encouraged to demonstrate the effect of multiple subsequent impulses on the PTOF IRF.

Gas-filled hohlraum implosions at the NIF produce the largest observed x-ray backgrounds as shown in Figure 2.1, primarily generated by laser-plasma interactions (LPI). A comparison of the relative signal levels between hohlraum x-rays, compression DD-neutrons, and shock D^3He-protons for various amounts of detector filtering is shown in Figure 2.16. In initial experiments with the PTOF detector on such gas-filled hohlraum implosions, the x-ray background dominated the signal trace, producing peaks in excess of 100 V. Given the calibrated sensitivity to protons of $\sim 7\times10^{-5}$ V ns/proton and the typically observed D^3He-proton shock yield on the order of 10^8, the expected proton signal was 0.1 V, three orders of magnitude less than the x-ray peak. Compounding the difficulty of picking out a small signal from the noisy tail of the x-ray signal, the signals produced

by the x-ray sources were a substantial fraction of the bias voltage. Such a large signal distorts the impulse response of the detector. This can be understood by considering that the charge carriers produced in the CVD-diamond dynamically screen out the bias field within the diamond volume. As electron-hole pairs are swept out, the effective field within the diamond is reduced, which in turn decreases the drift velocity for the remaining charge carriers. As a rule of thumb, the sensitivity of the detector becomes nonlinear for signals in excess of 10% of the bias voltage. An approach to taking this effect into account was proposed by D. Kania,[33] in which the signal is scaled according to the bias voltage V_b:

$$V'(t) = \frac{V(t)}{1 - \frac{V(t)}{V_b}}. \tag{2.11}$$

While such a scaling is useful for understanding the observed x-ray signals, it does not help recover the particle signals from the x-ray tail.

To reduce the magnitude of the direct x-ray signal to the required level for accurate measurements of the particle species of interest, a high-Z filter with an areal density of several tens of g/cm^2 is required. The PTOF on the NIF may be fielded with 1 or 2 cm of tungsten attached to the housing as shielding. Such a filter reduces the x-ray background to the order of 100 mV, allowing robust measurements of the DD-neutron signals. However, any D^{3}He protons are blocked from reaching the detector. For this reason, the upgrade to the PTOF is currently being implemented. This upgrade, entitled MagPTOF, includes a permanent dipole magnet to deflect shock-bang protons around the tungsten x-ray shielding and onto the detector, and is discussed in Section 2.6.

To optimize the PTOF data collected on each shot, it is important to select the correct level of filtering. To this end, a predictive model for the x-ray peak signal as a function of detector filtering was created using MATLAB.[30] An x-ray spectral intensity model is taken from a fit to the measured FFLEX data from a comparable shot. The transmission of this spectrum through the filters is calculated:

$$I_T(E_\gamma) = I_0(E_\gamma) \exp\left[-\left(\frac{\mu_{en}}{\rho}(E_\gamma)\right)\rho x\right], \tag{2.12}$$

where E_γ is the photon energy, I_0 the incident x-ray spectrum in units of keV/(keV sr), (μ_{en}/ρ) are the photon-energy dependent x-ray mass attenuation coefficients of the filter material with units of cm^2/g,[34] ρ is the mass density of the filter and x the thickness of the filter. This transmitted spectrum is absorbed in the CVD-diamond by Compton scattering,[i] in which a photon with energy E_γ transfers an approximate average energy of $E_\gamma^2/(E_\gamma + m_e c^2)$ to an electron.[j] An additional signal due to the K- and L-shell fluorescence of the gold electrodes is calculated as well. The energy deposited in the detector for a given photon energy is multiplied by the transmitted spectrum and the solid angle of the detector, and integrated to obtain the total deposited photon energy. An example of these calculations for two filter choices and the x-ray spectrum recorded on N140712 is shown in Figure 2.17. Assuming an average of 16 eV is required to generate an electron-hole pair, the total charge created by the x-ray source is calculated.

This technique was calibrated using the measured FFLEX spectrum from a NIF shot with a recorded PTOF x-ray signal (N110807), from which it was determined that the effective signal produced by the PTOF system was 2.6 V ns per nC of generated charge. Dividing this value by the 50 Ω impedance of the system, the calibration suggests that the PTOF system collects about 5% of the produced charge. The calibration value can be used directly to convert the simulated

[i]Due to the hardness of the filtered spectrum, photoabsorption in the diamond contributes less than 10% to the signal.

[j]This approximation is valid to within 20% for all values of E_γ, and approaches the correct values in the asymptotic limits $E_\gamma \ll m_e c^2$ and $E_\gamma \gg m_e c^2$.

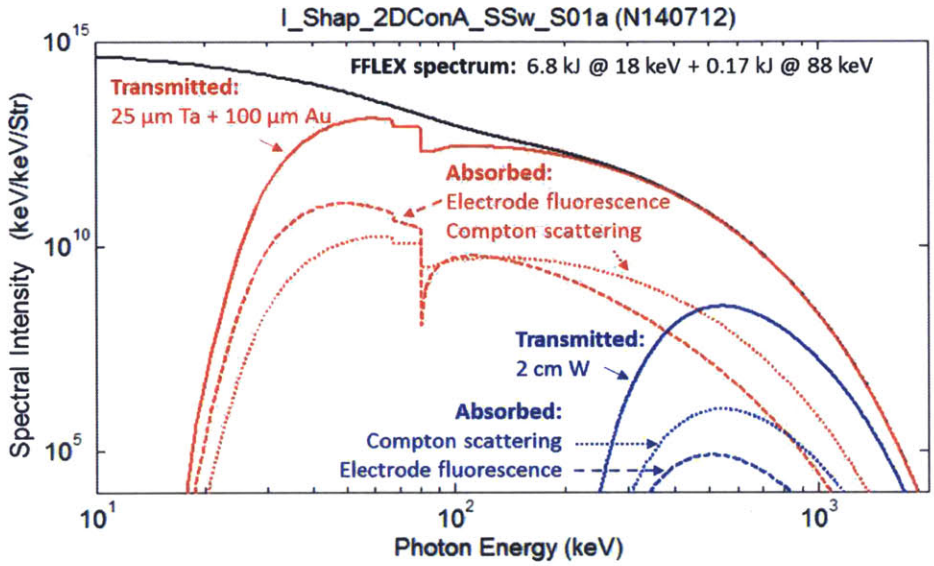

Figure 2.17. Transmitted and absorbed x-ray spectra calculated for the PTOF detector shielded by different filters. The measured x-ray spectrum (black) from N140712, a 2-temperature distribution with 6.8 kJ in 18 keV and 0.17 kJ in 88 keV, is degraded by the filters: 25 μm Ta + 100 μm Au (red) or 2 cm W (blue). The energy deposited in the CVD diamond by the transmitted x-rays is through Compton scattering (dotted) or via fluorescence in the gold electrodes (dashed). The predicted x-ray signals for these two filters are 36.2 V ns (red) and 0.003 V ns (blue).

energy deposition in the detector for a given filtering and x-ray spectrum into the expected size of the x-ray peak. This procedure has been used to select filtering for a wide range of shots, including x-ray timing impulses, polar-direct-drive implosions, and implosions in near-vacuum hohlraums, and generally predicts the size of the x-ray peak to within a factor of 2.

2.5 Overview of results from the PTOF on NIF

To date, PTOF has recorded data on over 140 NIF shots, including 33 cryogenic DT/THD implosions, 13 exploding pushers, 13 polar direct-drive (PDD) implosions, and over 60 D^3He- or D_2-gas filled surrogate shots. This section will highlight interesting PTOF data obtained at the NIF between 2011 and the present. These results were acquired and analyzed as part of this research, in support of a wide range of shot operations at the NIF facility.

2.5.1 Cryogenic DT and THD implosions

PTOF has participated on many of the NIF cryogenic implosions as a DT-neutron bang-time diagnostic, including the first 50:50 D:T cryogenic layer shot, N110608. An example of data recorded on a cryogenic implosion is shown in Figure 2.18. The high neutron yields, ranging from high 10^{13} up to above 10^{15}, drive the PTOF detector into the regime of non-linear operation, as discussed in Section 2.4.3. However, accurate bang-times were recorded by fitting to the rising edge of the signal, implementing the Kania scaling (Equation 2.11), and allowing the rise- and fall-times of the impulse response function to vary to match the data. Additionally, as yields increased, a peak associated with photons generated by an inelastic (n, γ) reaction in the gold hohlraum was observed. This

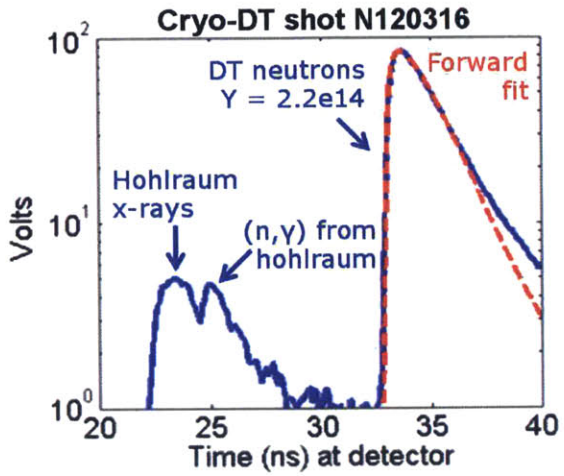

Figure 2.18. PTOF data recorded on a cryogenic DT-layered implosion (N120316). Signals from x-rays and DT-neutrons are observed, as well as photons from (n,γ) reactions in the hohlraum. The distortion of the impulse response due to high signal voltages can be seen in the discrepancy between the signal (blue) and the best fit to the DT-neutron peak (red) in the tail. Detector filtering was 1 mm Ta.

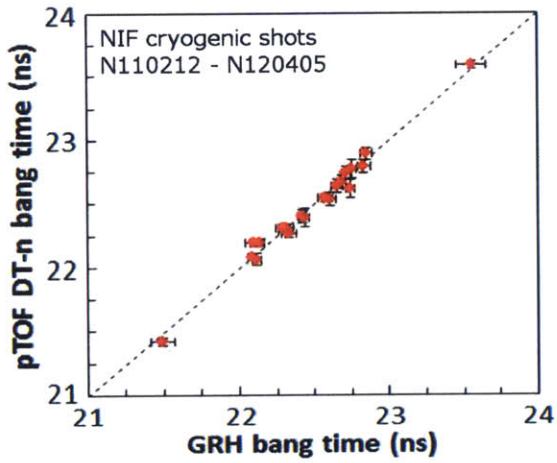

Figure 2.19. A comparison of the DT-neutron bang-times measured by PTOF and DT-gamma bang-times measured by GRH on cryogenic shots in 2011–2012. The two diagnostics agree to within experimental uncertainties ($\chi^2_{reduced} = 0.64$).

feature will allow highly accurate bang-times to be recorded on indirect-drive implosions with even higher neutron yields, as the DT-neutron signal becomes unusably nonlinear.

On cryogenic implosions from 2011 to 2012, PTOF-measured DT-neutron bang times agreed with the DT-γ bang-time measured by GRH[11] to within experimental uncertainties. This result provides confidence that the PTOF calibration and analysis procedures described in this chapter result in an accurate measurement of the nuclear bang-time. Fig 2.19 shows PTOF vs GRH-measured nuclear bang-times.

2.5.2 Exploding pushers

Exploding pushers, or thin-glass shock-driven implosions as discussed in Section 1.1.3, are used at the NIF for diagnostic development. PTOF has measured bang-time on several exploding pushers filled with DT, D_2, or D^3He. An example of data from a D^3He-gas filled exploding pusher, the shot N121128 shown in Figure 2.20, is remarkable for its high quality: the fit of the source function folded with the IRF to the data is perfect to within experimental uncertainties. This implosion produced a highly uniform D^3He-proton spectrum, as measured by four WRFs on the polar DIM and three on the equator and by the MRS in charged-particle mode. This implosion provides a proof-of-concept for the development of a monoenergetic D^3He-proton backlighter on the NIF,

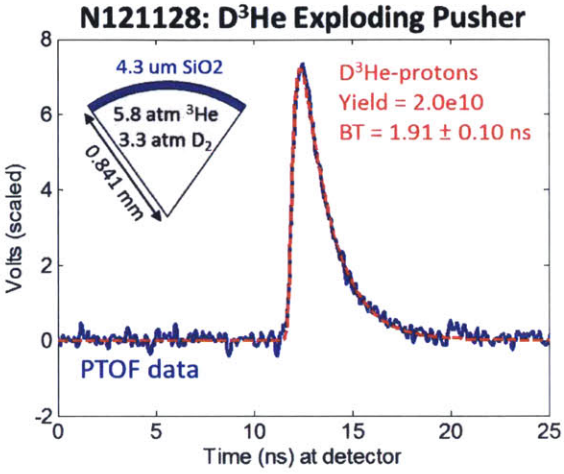

Figure 2.20. PTOF data from D^3He Exploding Pusher implosion N121128. A 4.3 μm thick glass shell filled with D^3He was imploded with a 192-beam, 43.3 kJ laser pulse with a 1 ns rise and 350 ps flat-top. PTOF recorded a D^3He-proton bang-time of 1.9±0.1 ns, approximately 0.2 ns prior to x-ray bang-time measured by SPBT and in good agreement with the pre-shot simulation. The WRFs recorded an isotropic Gaussian proton spectrum with mean energy 14.47±0.06 MeV and yield of $(2.04\pm0.07)\times10^{10}$. This implosion is discussed along with other NIF exploding pushers by M. Rosenberg.[35]

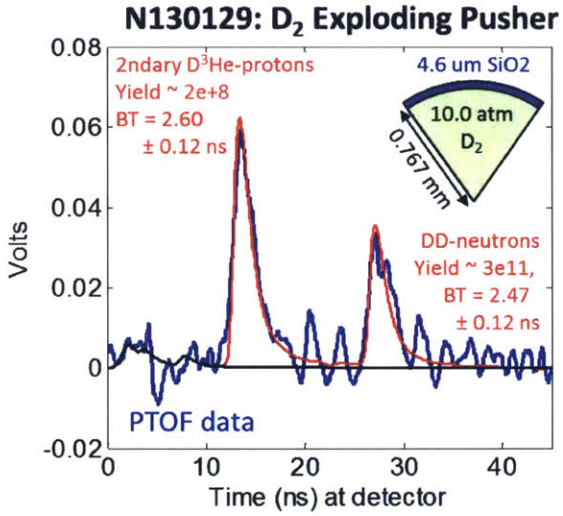

Figure 2.21. PTOF data from D_2 exploding pusher implosion N130129. A 4.6 μm thick glass shell filled with D_2 gas was imploded with a 192-beam, 51.4 kJ laser pulse with a duration of 1.4 ns. PTOF recorded for the first time both the primary DD-neutrons and the secondary D^3He-protons on a single implosion, obtaining a bang-time from each. The measured bang-times are in agreement with each other and with the simulated values. The ratio of measured secondary proton to primary neutron yields was used to infer an approximate fuel ρR of 5 mg/cm^2. This implosion is discussed along with other NIF exploding pushers by M. Rosenberg.[35]

which can be used for quantitative proton radiography studies. In such experiments the PTOF will be essential for recording the sample time for the experiment.

For the D_2-gas filled exploding pusher N130129, PTOF was again fielded in proton mode and recorded for the first time both primary DD-neutrons and secondary D^3He-protons from a single NIF implosion. The PTOF data from this experiment is shown in Figure 2.21. The recorded bang-times are in agreement with each other and with the simulated bang-times. Since the yields of DD-neutrons and D^3He-protons on this implosion are comparable to those observed from compression- and shock-yield in ignition surrogate D^3He-gas filled implosions, this data shows promise for the measurement of both shock- and compression-bang time on a single implosion. The relative primary and secondary yields were used to calculate a fuel ρR of ~5 mg/cm^2.

The good agreement between the PTOF data and the simulations on these and similar implosions verified that the energy coupling was captured well in the simulations and was not the source of an observed underperformance in the nuclear yields. The degraded nuclear performance in the exploding pushers was explained as the emergence of ion kinetic effects, specifically Knudsen-layer tail ion loss as discussed in Section 1.2.2.[35]

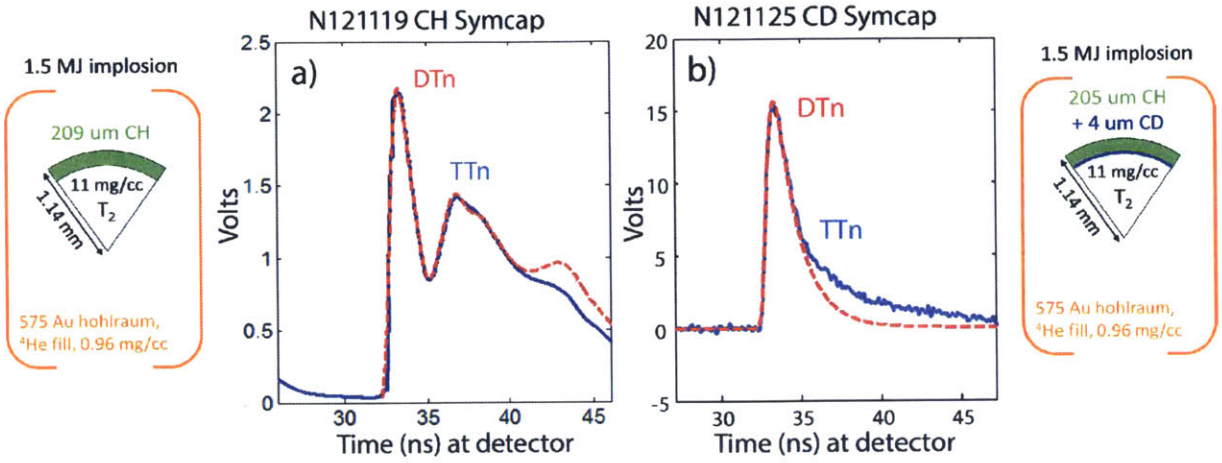

Figure 2.22. PTOF data (blue) from two CD Symcap hydrodynamic mix experiments in which capsules made of a) pure CH (N121119) or b) including an inner layer of deuterated plastic (N121125) were filled with pure tritium gas and imploded using indirect drive. Fits to the PTOF data (red dashed) were used to infer bang-time for DT-neutrons (both shots) and TT-neutrons (a only). In the CH experiment (a), DT-neutrons are produced from ¡0.15% deuterium contamination in the tritium gas, whereas in the CD-layer experiment (b) DT-neutrons are predominantly produced by regions where fuel and shell are turbulently mixed. TT-neutrons are also observed in both experiments. In (a) the TT-neutron yield was large enough to fit the data and obtain a TT-n bang-time. Only the rising edge of the TT-n signal is used, as the modelled signal shape disagrees with the observed data later in time. The bang-time inferred from TT-neutrons and DT-neutrons agree to within uncertainties. Figure is adapted from Casey, et al., Reference [36].

2.5.3 Hydrodynamic mix experiments

High-mode hydrodynamic instability growth can lead to mix of the shell material into the fuel, which is a primary concern for ICF research as described in Section 1.1.2. This effect was studied directly at the NIF using a nuclear tracer method in the CD Symcap campaign. CH capsules were prepared with a 4 μm layer of deuterated plastic (CD) recessed at various distances from the inner surface of the shell, filled with pure T_2 gas, and imploded in an indirect-drive geometry.[36] In these experiments, DT-neutrons can only be produced in regions of the implosion that have undergone atomic mix of the CD layer and the T_2 fuel. A CH capsule without a CD layer was imploded to establish a baseline of neutrons produced by D_2 contamination in the T_2 fuel. These experiments demonstrated that most of the mix that occurs in NIF indirect-drive implosions is from the innermost 2 μm of the shell.

On these implosions, PTOF recorded both the 14.1 MeV DT-neutrons and the TT-neutrons, as shown in Figure 2.22. The T-T fusion reaction produces an alpha particle and two neutrons. Because the reaction outputs three particles rather than two, the energy of the products is not constrained to a single value by kinematics, and a broad spectrum of neutrons is created with energies up to 9.44 MeV. A model of the TT-neutron spectrum is shown in Figure 2.23. Since the energy of neutrons produced covers a wide range, the sensitivity of the PTOF detector as a function of neutron energy must be taken into account. The neutron sensitivity as a function of energy shown here and used in the analysis was calculated by Tom Phillips using MCNP,[27] and is also shown in Figure 2.23.

Due to inaccuracies in the model, a good fit is not obtained for the entire TT-n spectra to the data. However in data with clear TT-neutron signal, such as the null experiment shown in Figure 2.22a), the TT-n bang-time was inferred in two ways: by fitting just the rising edge and first

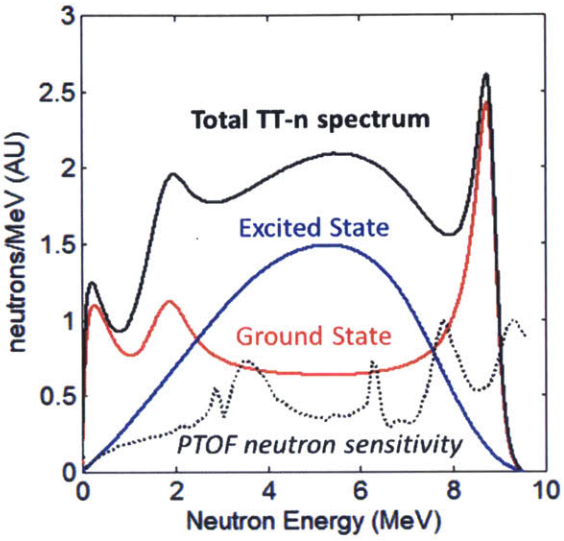

Figure 2.23. Model spectrum for neutrons produced by the T-T fusion reaction, as calculated by Dan Sayre using R-matrix modeling. The relative scale of the ground state (red) and excited state (blue) reactions was fit to OMEGA data. Spectra were provided by M. Gatu Johnson. The PTOF sensitivity as a function of neutron energy is also shown (black dotted), which was calculated by Tom Phillips using Monte Carlo modeling of neutron transport in CVD diamond.

peak of the TT-n signal, and by locating the time when the TT-n signal begins to rise and identifying this with the most energetic neutrons. The bang-time inferred using both of these methods agree with each other, and with the DT-neutron inferred bang-times, as expected since both are produced in the gas-fill of the CH implosion. On CD-layered experiments such as Figure 2.22b), the TT-neutron signal was observed but was not generally usable for a bang-time measurement, due to the lack of a distinct peak.

2.5.4 Polar Direct Drive (PDD)

PTOF has provided the only nuclear bang-time measurement for the PDD series at the NIF. Ten PDD implosions have been performed since December 2013, on which PTOF has recorded DD-neutron compression-bang time for all but one.[k] These implosions also provided the first measurement of both primary DD-neutron and secondary D^3He-proton-bang time on a single implosion, as shown in Figure 2.24. When both measurements were obtained, the primary- and secondary-bang times were in agreement to within uncertainties, as expected.

The measurement of the DD-neutrons and secondary D^3He-protons on a single shot is possible because of the comparatively low x-ray background produced by PDD implosions, as shown previously in Figure 2.1. A comparison of the x-ray background recorded on several PDD shots is shown in Figure 2.25. These four shots produced very reproducible x-ray backgrounds, using a laser energy in the range 605–760 kJ and a peak power in the range 123–176 TW, and in fact it was the shot with the largest x-ray background on which both the primary and secondary fusion products were measured. The secondary fusion bang-time provides a valuable confirmation of the primary bang-time on these implosions, and it is recommended that the diagnostic be run in this mode for the PDD implosions as long as the x-ray backgrounds remain similarly low.

2.5.5 HDC ablator implosions in Near Vacuum Hohlraums (NVH)

PTOF has recorded for the first time both the shock- and compression-bang time in a single implosion using D^3He-p and DD-n, respectively, from a HDC target imploded in a near vacuum

[k] An electrical failure of the PTOF diamond prevented data collection on N140228-004.

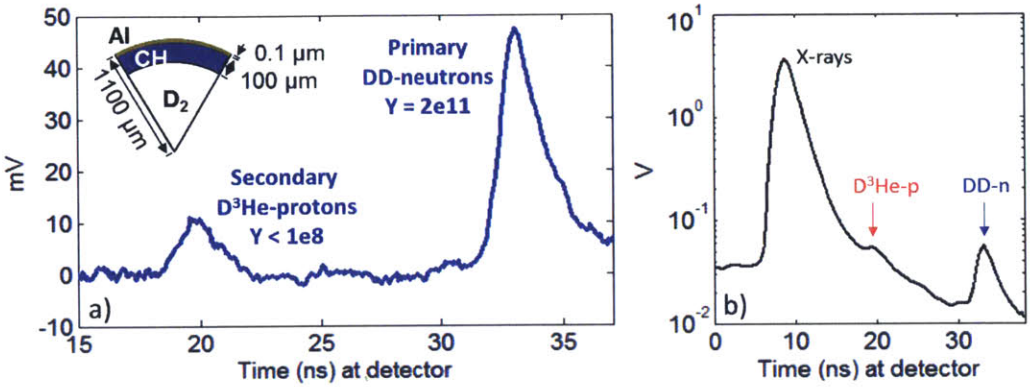

Figure 2.24. a) Background subtracted PTOF signal trace from NIF PDD implosion N140306-003 (blue), on which PTOF measured both primary DD-neutrons (Yield = 2×10^{11}) and secondary D^3He-protons (Yield < 10^8). Due to the low x-ray fluence on PDD implosions, PTOF could be fielded with reduced high-Z filtering, enabling measurement of D^3He-protons. This measurement shows promise for the shock- and compression-bang time measurements using the MagPTOF detector, which will have comparable nuclear yields to those recorded here. b) The raw PTOF trace from this shot (black) showing the 3.6 V x-ray peak followed by the D^3He-proton and DD-neutron peaks.

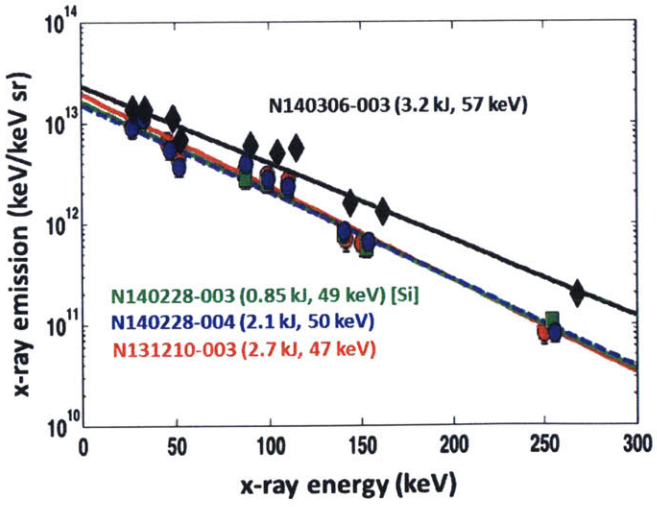

Figure 2.25. X-ray emission spectra measured on several PDD implosions on the NIF. Measurements (points) were recorded by the FFLEX diagnostic. The measurements were fit (lines) using a 1-temperature exponential decay described by Equation 2.1; the fit parameters (energy and temperature) are given for each shot. X-ray intensity is sufficiently low to field the PTOF in proton mode: on shot N140306-003, PTOF recorded both DD-neutron and secondary D^3He-proton signals following a 3.6 V x-ray peak, as shown in Figure 2.24.

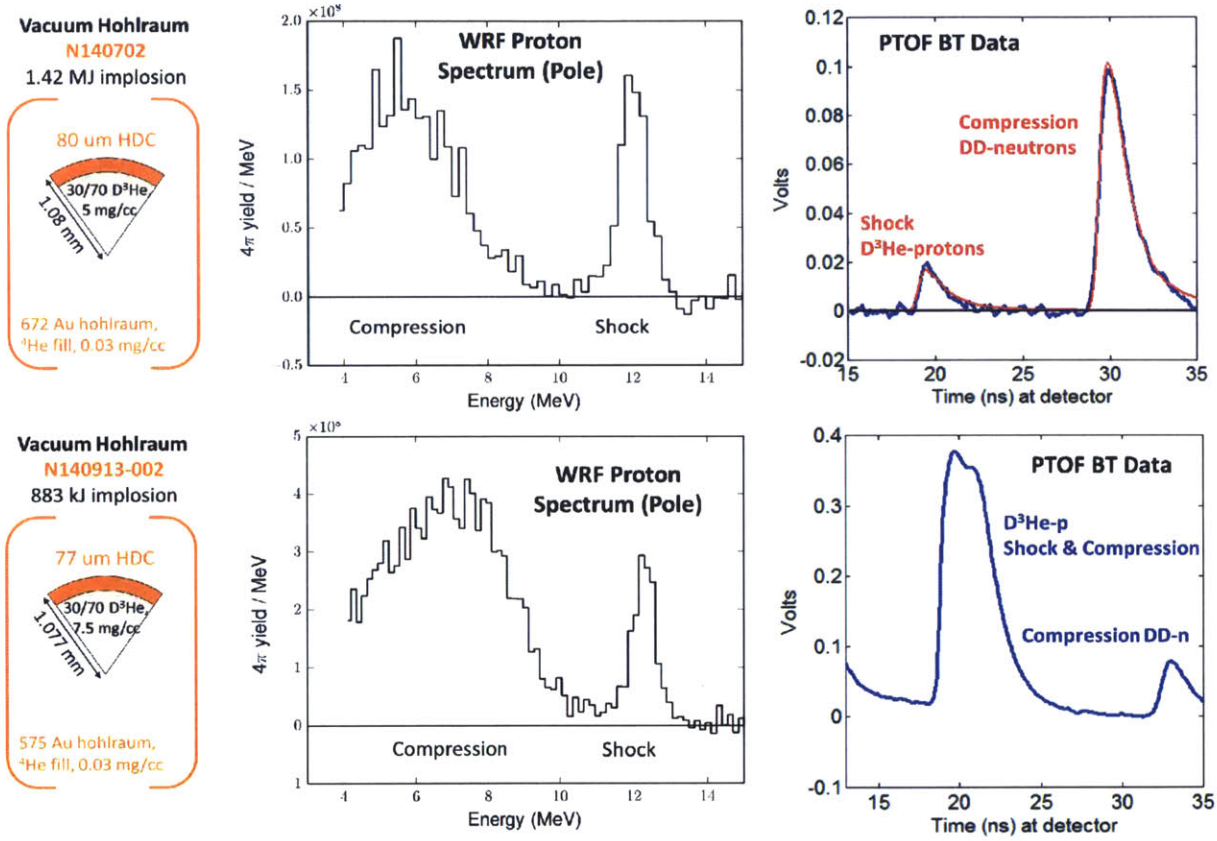

Figure 2.26. PTOF and WRF data recorded on implosions of D^3He-gas filled high-density carbon (HDC) targets in near-vacuum hohlraums (NVH). For both shot N140702 and N140913-002, a clear shock- and compression-proton signal is seen in the WRF spectrum, and both D^3He-protons and DD-neutrons are observed in the PTOF data. For N140702, the PTOF filtering of [50 μm Ta + 100 μm Au] and a thick band on the hohlraum only transmitted the most energetic protons to the detector. A ΔBT of 0.9 ± 0.1 ns was inferred. For N140913-002, a combination of thinner filtering ([25 μm Ta + 100 μm Au]) and reduced hohlraum material along the line-of-sight allowed the entire shock-bang peak and part of the compression peak to reach the PTOF, resulting in a characteristic 'double bump' feature. A ΔBT of 0.63 ± 0.1 ns was inferred. In both experiments, the measured ΔBT were in reasonable agreement with post-shot simulations, which stands in contrast to the results from low-adiabat implosions (see Figure 2.3).

hohlraum (NVH). The NVH platform includes a hohlraum gas fill of 0.03 mg/cc ^{4}He, compared to the standard hohlraum fill of 1.6 mg/cc ^{4}He. This dramatically reduces the production of hot electrons by LPI and therefore the x-ray background production, as shown in Figure 2.1. As for the PDD implosions, the low background allows PTOF to be fielded with filters that transmit D^{3}He-protons. The data from two such implosions is shown in Figure 2.26.

In the first implosion (N140702), the proton ranging in the capsule (measured to have a ρR of ~85 and ~280 mg/cm^2 at shock- and compression-bang time, respectively), the hohlraum wall, and the PTOF filtering of 50 μm Ta + 100 μm Au, transmitted only the highest-energy protons to the PTOF detector, with an effective sensitivity of ~5%. The shock-bang time, compression-bang time, and ΔBT were inferred to be 8.82±0.1 ns, 9.74±0.07 ns, and 0.9±0.1 ns, respectively, in reasonable agreement with post-shot simulations. The highest-energy protons are systematically emitted early in the shock-bang, due to ρR evolution with time. For this reason, the actual shock-bang time may be corrected to be later than the reported value by no more than half the burn width (~75 ps).

In the second implosion (N140913-002), a slightly lower ρR (~75 and ~250 mg/cm^2 at shock- and compression-bang time, respectively), a different hohlraum geometry and reduced PTOF filtering of 25 μm Ta + 100 μm Au allowed substantially more of the proton spectrum to reach the PTOF detector. Because of this, both a shock- and compression-emitted proton signal are observed. By fitting to only the shock component, a shock-bang time of 8.27±0.07 ns was inferred, while the DD-neutron peak was used to infer a compression-bang time of 7.64±0.1 ns. These values and the inferred ΔBT of 0.63±0.1 ns were in good agreement with post-shot simulations.

The agreement between the PTOF-measured ΔBT and the simulated values for the NVH implosions stands in contrast to the results for low-adiabat ignition surrogate implosions, for which there is evidence that ΔBT disagrees with the simulated value on some experiments (see Figure 2.3). This difference is possibly due to kinetic plasma effects during the shock-phase of the low-adiabat implosions, which are not present in the high-adiabat NVH implosions. Future work will continue to investigate the trend of ΔBT with laser and target parameters. Shot N140913-002 was the first in a "mini-campaign" of sub-scale (<1 MJ of laser energy) HDC implosions in near-vacuum hohlraums, with the goal of measuring both the shock- and compression-ρR and bang-times. These measurements will provide a direct measurement of how the ρR asymmetry varies from shock- to compression-bang time, as well as a test of the shock properties.

2.6 Design of the Magnetic PTOF upgrade for the NIF

As discussed in Section 2.1.1, measurement of the shock-bang time in NIF indirect-drive implosions is a difficult but important problem. PTOF has demonstrated a simultaneous measurement of both shock- and compression-bang time, using the D^{3}He-protons and DD-neutrons respectively, from near-vacuum hohlraum implosions (see Sec. 2.5.5). However on standard gas-filled implosions, additional x-ray shielding is required and the D^{3}He-protons are blocked. An upgrade to the PTOF diagnostic has been designed to provide shock- and compression-bang time measurements regardless of x-ray background. By including a small dipole magnet, the Magnetic PTOF (MagPTOF) will deflect protons around the shielding and onto the detector, allowing for simultaneous measurements of D^{3}He-protons and DD-neutrons produced at shock-burn and compression-burn, respectively.

2.6.1 MagPTOF design

The MagPTOF diagnostic represents a significant upgrade to the existing PTOF diagnostic on the NIF, and includes four main components, depicted schematically in Figure 2.27. The MagPTOF detector, cables, bias, and oscilloscope systems are identical to the existing PTOF system, which

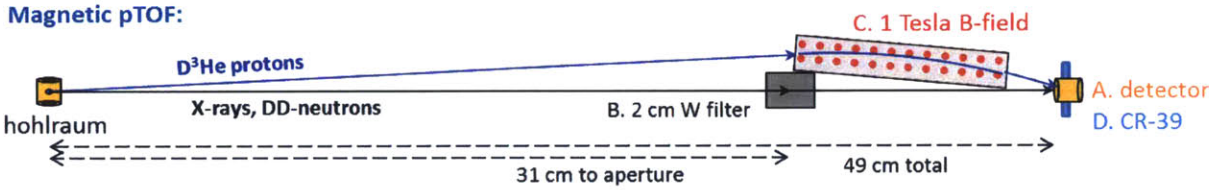

Figure 2.27. A schematic of the MagPTOF diagnostic on the NIF. The diagnostic includes four main components: A) CVD-diamond detector; B) x-ray shielding (tungsten, configurable in units of 1 cm up to 4 cm) to shield the detector from hohlraum x-ray background; C) a permanent dipole magnet with a 1 tesla peak field strength, to deflect protons around the shielding and onto the detector; and D) optional annular piece of CR-39 around the CVD-diamond, to confirm proton fluence and energy on each shot. The MagPTOF detector, cables, and electronics are identical to the existing ones for the PTOF.

is described in detail above and in Reference [37]. The detector, nominally positioned 49 cm from the implosion, detects protons between 6 and 16 MeV. X-ray shielding made of tungsten cylinders protects the detector from direct x-ray fluence from the hohlraum. This shielding may be configured in units of 1 cm up to a maximum of 4 cm, depending on the predicted level of x-ray background. A permanent dipole magnet with a peak field of approximately 1 T deflects protons around the shielding and onto the detector. Lastly, an annular piece of CR-39 nuclear track detector (see Section 1.3.2 and Reference [38]) can be positioned around the PTOF detector to confirm proton fluence and energy on the CVD diamond after each experiment.

An engineering design for the diagnostic that meets NIF requirements has been completed. The MagPTOF assembly shown in Fig. 2.28a) maintains the relative alignment of the magnet, x-ray shielding, and detector. The housing is made of aluminum to reduce weight; surfaces facing target chamber center are covered with stainless steel for ablation resistance and debris shielding. This assembly weighs approximately 5.4 lbs. Like the PTOF diagnostic, the MagPTOF assembly is fielded on the diagnostic instrument manipulator (DIM)[21] installed on the NIF target chamber at the angular position ($\theta = 90°, \phi = 78°$), as shown in Fig. 2.28b). The MagPTOF mounting bracket replaces the upper half of the previous 4-position PTOF/WRF mounting bracket with an alternate design to support the added weight of the MagPTOF assembly. The center of the magnet aperture is positioned 13.6 degrees above the equator of the NIF target chamber, matching the polar angle of the neighboring WRF. For cylindrically symmetric hohlraum designs, the protons incident on both MagPTOF and WRF will be ranged through identical hohlraum profiles, and proton spectra will be identical along both lines of sight. Since the evaluation of shock-bang time from the MagPTOF proton data requires precise knowledge of the average proton energy, matching the WRF polar line-of-sight reduces the uncertainty in the measurement. The location of the adjacent upper WRF in the target chamber is maintained from the previous 4-position design. The hardware holding the two WRFs below the equator is unchanged.

2.6.2 Magnet optimization

D^3He-protons emitted from NIF hohlraum implosions typically have an average energy in the range 8–12 MeV, accounting for energy downshift in both the imploding capsule and the hohlraum wall. A magnet has been optimized for the MagPTOF system, such that protons in this energy range will be reliably deflected onto the CVD-diamond detector without requiring active controls or detailed knowledge of the proton spectrum prior to the experiment.

The deflecting magnet, a permanent dipole manufactured by Dexter Magnetic Technologies,[39] is composed of $Nd_2Fe_{14}B$, with a density of 7.4 g/cc, and is sheathed in vacuum-tight autenistic

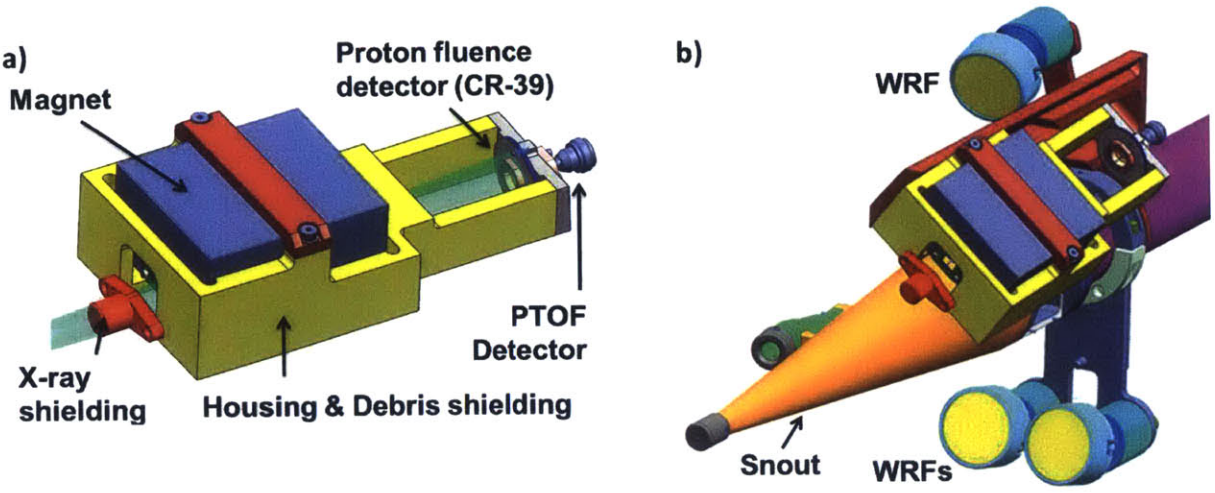

Figure 2.28. Three dimensional models of the MagPTOF engineering design. a) The x-ray shielding (red cylinder), aperture and magnet (purple), detector (gold), and annular CR-39 (blue) are held in relative alignment by an aluminum housing (yellow). Target chamber center (TCC)-facing components will be sheathed in stainless steel for ablation resistance and debris protection. The point-projection shadow of the shielding from TCC (green transparent) has a radius in the detector plane of ~3× the detector's active radius. b) The MagPTOF is attached to the NIF DIM (90,78) snout with a stainless-steel mounting arm (red), alongside a WRF spectrometer (blue). Engineering drawing by J. Magoon, Laboratory for Laser Energetics.

stainless steel to prevent outgassing of the glue compound into the NIF target chamber. The magnet has a pole gap of 1.5 cm, a pole depth of 2 cm, and is 8 cm long. The aperture in front of the magnet is positioned 31 cm from the implosion, subtending a solid angle fraction of 1.08×10^{-4}.

The magnetic field, which has a peak strength of 1 tesla, deflects incident protons away from the magnet's yoke into the region behind the x-ray shielding. The radius of curvature for a charged particle in a magnetic field is $R_{gyro} = p/qB$, where p is the particle momentum, q its charge and B the magnetic field strength. For a 10 MeV proton traveling through the MagPTOF magnet, the peak radius of curvature will be approximately 50.9 cm. This proton's path will be deflected by approximately 9 degrees after transiting the magnet. To maximize the path length of the protons in the magnetic field, the body of the magnet is rotated 4 degrees in the bending plane. This rotation balances the entrance and exit angles for ~10 MeV protons arriving at the magnet from TCC, and also introduces a weak focusing of protons in the bending plane.

A series of proton trajectory calculations were performed by Dexter Magnetic Technologies using the geometry and modeled field of the magnet described in Section 2.6.1. In the nominal geometry, the detector records protons generated at TCC with energy in the range 6 to 16 MeV, as shown in Figure 2.29. The effective solid angle fraction of the detector is above the nominal detector solid angle fraction of 1.7×10^{-5} for protons in the energy range 8 to 16 MeV, and is approximately 1.8×10^{-5} for 10 MeV protons. A slight focusing effect arises from a combination of focusing in the cross-field direction and defocusing in the parallel-field direction. The gradient of the dipole field along the depth of the pole gap was found to focus incoming protons along the cross-field axis by a factor of 33%. In addition, fringe fields at the apertures of the magnet were found to defocus incoming protons along the field axis, also by a factor of 33%. As the shape of the magnet aperture is 1.4 cm in the cross-field direction compared to 1 cm in the parallel-field direction, the magnet has a net focusing effect, enhancing the effective solid angle of the detector

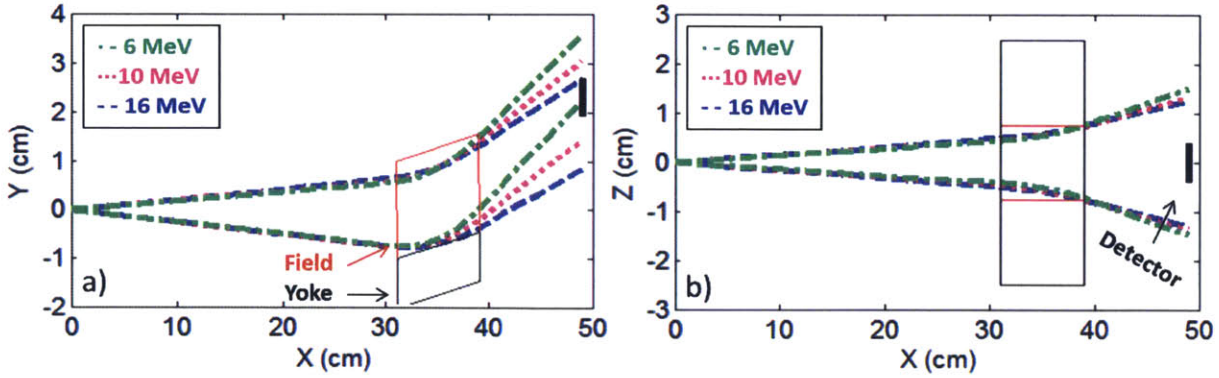

Figure 2.29. a) Calculated proton trajectories for the MagPTOF system projected to the bending plane (x,y). b) Calculated trajectories projected perpendicular to the bending plane (x,z). Protons with energy 6, 10, and 16 MeV (green dot-dashed, magenta dotted, and blue dashed, respectively) were launched from the origin and transported through the dipole magnetic field (red) to the detector plane (black). The effective solid angle fraction of the detector was found to be above 1.7×10^{-5} for protons in the energy range 8–16 MeV. Trajectory calculations were performed by Dexter Magnetic Technologies.

by about 10%.

An important design consideration for the magnet is to minimize the effect of misalignment on the proton signal level. As the diagnostic is mounted onto the side of x-ray diagnostic snouts fielded on DIM (90,78), the system is not independently pointed and must be designed to function correctly with any DIM instruments. In practice, nominal insertion depth of the existing PTOF diagnostic has varied by ±1 cm, depending on the DIM instrument installed. With the magnet line-of-sight nominally aligned to 13.6° above the equator, this insertion depth variation translates into approximately $\pm0.4°$ of misalignment in the bending plane (dispersion direction).

To evaluate the effect of mispointing the MagPTOF, proton trajectory calculations were also made for proton launch points moved by ±1 cm both in the bending-plane and perpendicular to the bending plane, corresponding to a $\pm1.6°$ angular mispointing. Figure 2.30 shows the results of this study, which indicate that the design robustly transports protons to the detector with an effective solid angle fraction of $\sim 1.6 \times 10^{-5}$ or higher for misalignment of $\pm1.6°$ in all directions, well beyond the expected alignment uncertainty.

Temporal broadening of the proton signal due to increased path-lengths in the system was also examined, and the results for 10 MeV protons are shown in Figure 2.31. For all proton energies studied, this magnet design introduced a temporal broadening of less than $\pm$ 7 ps, well below other timing uncertainties. For comparison, typical proton spectra measured in D^3He gas-filled implosions at the NIF display a FWHM of ~1 MeV. This spectral width corresponds to a time-of-flight broadening of approximately 500 ps, which dominates the temporal width of the proton source function and renders the temporal broadening due to the magnet negligible.

The advantages of a focusing magnet for increasing the proton signal were considered. However such a magnet would have more stringent alignment requirements and would require better a priori knowledge of the incident proton spectrum. The expected proton signals with a non-focusing magnet are sufficient for making the desired measurement.

2.6.3 Signals and background

The primary goal of this upgrade is to minimize background due to x-rays from the implosion while measuring the D^3He-proton signal from the shock-burn. Based on D^3He-proton signals observed

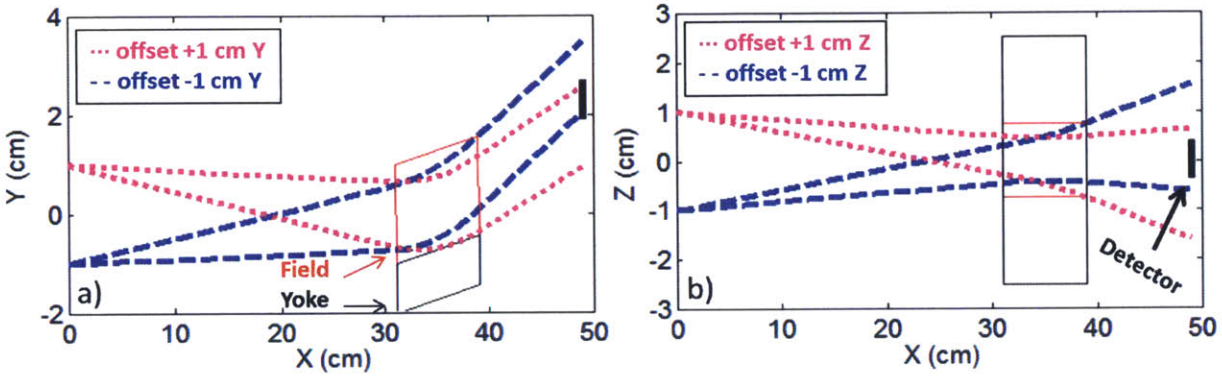

Figure 2.30. Calculated 10 MeV proton trajectories for the MagPTOF system when the proton source location is offset by +1 cm (magenta dotted) and -1 cm (blue dashed) relative to the origin a) in the bending plane (x,y) and b) perpendicular to the bending plane (x,z). The protons were transported through the dipole magnetic field (black, red) to the detector (black). The MagPTOF system was found to be tolerant to offsets of this size, which translate to ± 1.6° misalignment of the detector line-of-sight. Trajectory calculations were performed by Dexter Magnetic Technologies.

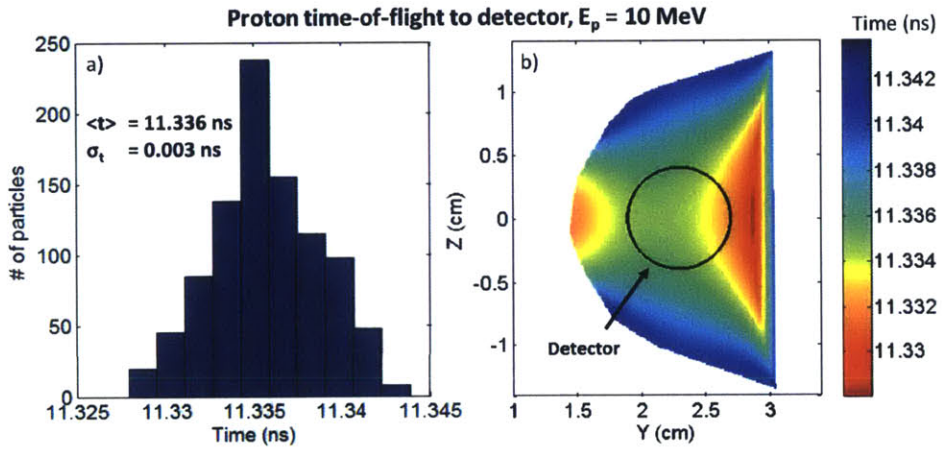

Figure 2.31. a) Calculated time-of-flight distribution for 10 MeV protons transiting the modeled magnetic field to the detector. The temporal broadening caused by the magnet is negligible (σ = 3 ps for 10 MeV protons, <7 ps for 6 to 16 MeV protons). b) Time-of-Flight map for the 10 MeV protons at the detector plane. Particles within the black circle are detected. Trajectory calculations were performed by Dexter Magnetic Technologies.

Table 2.3. Summary of the estimated background levels for MagPTOF from a variety of sources

Source of background	Estimated Background
Nd K-shell fluorescence	110 mV (no filters at detector)
	7 mV (w/ filters at detector)
X-ray scatter from mounting bracket	14 mV
direct x-rays	5 mV
e- scattered from W	<1 mV
Total	130 mV (no filters at detector)
	27 mV (w/ filters at detector)

using the PTOF on NIF and OMEGA and the effective solid angle of MagPTOF, the expected MagPTOF signal level for a typical shock D^3He-proton yield of 1×10^8 is approximately 50 mV, as shown in Figure 2.16. Because the x-ray background sources and the proton signal are separated by approximately 10 ns due to time-of-flight, which is several times the impulse response falloff time (~1.3 ns), the detector has time to recover from x-rays prior to observing the protons. However, for a robust proton measurement, the peak x-ray background should be comparable to or smaller than the signals of interest. Possible background sources with the MagPTOF conceptual design have been thoroughly reviewed, including direct x-ray signal from the hohlraum, x-ray fluorescence in the magnet, shielding, and mounting hardware, and photo- and Compton-scattered electrons from the tungsten shielding.

X-ray-induced fluorescence in the magnet was found to be the most significant source of background. Although the magnet is composed primarily of iron, the primary source of fluorescent background is expected to be the neodymium due to the higher-energy x-rays produced (E_{line} = 43.6 keV, compared to 7.1 keV for iron) and the comparatively large probability of fluorescence (P_{fluor} = 92.2%, compared to ~ 34% for iron).[40] The neodymium fluoresced photons with an energy of 43.6 keV have a mean free path in the magnet material of $\lambda = 270$ μm, defining the volume of magnet material that can produce fluorescent background for the detector.

The number of photons incident on the magnet with energy high enough to stimulate fluorescence depends on the x-ray spectrum observed, as:

$$N = \int_{E_{line}}^{\infty} \frac{S(E)}{E} \exp\left[-(\mu/\rho)_{\mathrm{Nd}} w_{\mathrm{Nd}} \rho_{mag} x_1\right] \Omega_1 dE, \tag{2.13}$$

where S(E) is the spectrum of x-rays produced in the experiment in units of keV/(keV sr); $(\mu/\rho)_{\mathrm{Nd}}$ is the x-ray mass attenuation coefficient of neodymium[34] and $w_{\mathrm{Nd}} = 0.267$ is the mass fraction of neodymium in the magnet; ρ_{mag} is the density of the magnet; x_1 is the depth in the magnet from which fluorescent photons can escape; and Ω_1 is the solid angle of the inside magnet surface. For the geometry of the MagPTOF system, $\Omega_1 \approx 9 \times 10^{-4}$ sr. If we assume that fluorescent photons from a depth of λ are able to escape and strike the detector, then from the geometry discussed in Section 2.6.1, $x_1 \approx 2.6\lambda = 566.8$ μm.

The energy absorbed in the detector via neodymium K-shell fluorescence in the magnet is estimated conservatively as:

$$E_{abs} = N P_{fluor} E_{line} (\Omega_2/4\pi) P_{abs} f_{abs}, \tag{2.14}$$

where P_{abs} is the probability of photon absorption by the detector; $\Omega_2 \approx 1.6 \times 10^{-2}$ sr is the solid angle of the magnet inner surface relative to the detector; and f_{abs} is the fraction of the photon

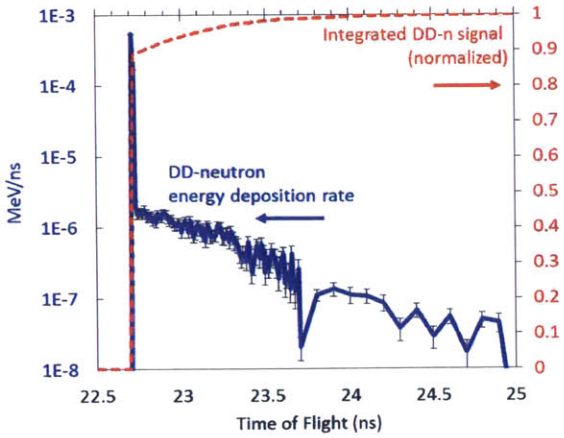

Figure 2.32. Simulated energy deposition rate by DD-neutrons in the MagPTOF detector versus time (blue points). The Monte Carlo N-Particle Transport code MCNP5 was used for this calculation. The integrated neutron signal (red dashed line) reaches 89% of the total neutron signal within 20 ps of the expected arrival time for 2.45 MeV DD-neutrons, confirming that the scattered neutrons will not significantly perturb the DD-neutron measurement. The model incorporates the detector, 2 cm tungsten shielding, magnet, and MagPTOF housing in a simplified geometry.

energy absorbed in the detector. For Nd-fluorescence photons, the dominant absorption process in the detector is incoherent Compton scattering, but the average fraction of energy deposited by this process is only $f_{abs} = E_{line}/(M_e + E_{line}) \approx 8\%$. Because of this, the energy absorbed through Compton scattering and photoelectric absorption are comparable, and the product $P_{abs} f_{abs} \approx 0.2\%$.

Numerically integrating over the measured spectrum S(E) from a typical shot with a peak laser power of 420 TW,[1] and scaling this model to the x-ray peaks observed by the existing PTOF as described in Section 2.4.3, a background peak amplitude of 110 mV is expected, comparable to the expected proton signal. If necessary, this background may be further reduced by including additional filtering at the detector: the current standard proton filtering of 50 μm Ta + 100 μm Au would reduce fluorescent x-rays striking the detector by a factor of 15.

Other sources of background were also evaluated. The direct x-ray spectrum is dramatically reduced by the tungsten shield and produces only 5 mV of background. X-ray scattering from the detector mounting bracket, which has been found to be a significant source of background for the existing PTOF diagnostic when fielded with 2 cm tungsten shielding (~300 mV), is expected to produce 14 mV for MagPTOF as much less of the detector mounting bracket is directly exposed to TCC. Photo- and Compton-scattered electrons from the rear surface of the tungsten shielding are expected to produce a background of less than 1 mV. Other sources of background, such as x-ray fluorescence in the neighboring DIM hardware and neutron-induced fluorescence, have not been reviewed in detail, but simple estimates indicate they are negligible compared to the neutron and proton signals and the effects considered here. Complete modeling of the DIM hardware using GEANT4, a multi-physics Monte-Carlo particle transport code, will be used to validate these estimates in the future. A summary of estimated contributions to the MagPTOF background may be found in Table 2.3. These estimates are comparable to or less than the expected proton signals, allowing a robust measurement of D^3He-proton bang-time.

While the PTOF diagnostic has routinely measured compression-bang time using 2.45 MeV DD-neutrons, the additional mass of the magnet and shielding will scatter neutrons and change the detector's effective sensitivity and impulse response. The tungsten x-ray shielding has a single-scattering depth of approximately 2.5 cm for the DD-neutrons. For the default 2 cm shielding, it is estimated that the fraction of unscattered neutrons reaching the detector will be ~46% of the initial neutron fluence. The neutrons are scattered over a solid angle fraction of approximately 0.1, with an average scattering angle of ~30°.When the PTOF detector is shielded by 2 cm tungsten, the detector is positioned only about 7 mm from the rear surface of the shielding – less than the detector diameter. Many of the scattered neutrons therefore still hit the detector, producing the ~70 ps tail seen in the DD-neutron impulse response (Figure 2.9). However because of the ~18 cm

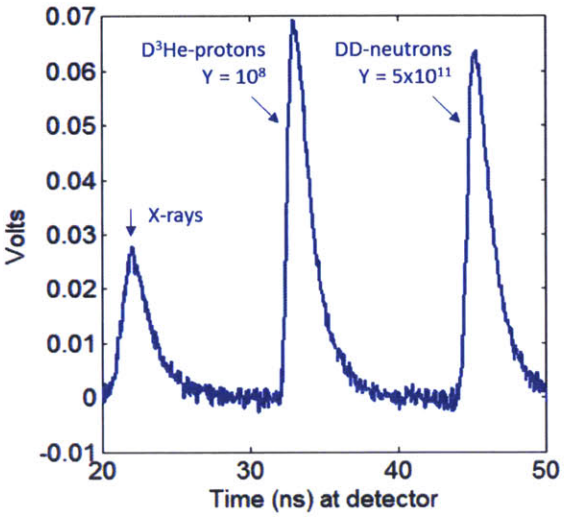

Figure 2.33. Predicted signals and background for the MagPTOF system (blue) for a NIF implosion with an ion temperature of 3 keV demonstrate a clear record of both fusion species of interest, distinct from the x-ray background. This model includes standard additional filtering on the detector (50 μm Ta + 100 μm Au), 10% focusing of the protons, and 54% neutron loss due to scattering in the tungsten shield, as well as a 1 mV noise floor associated with the recording system. Compared to the signal recorded by the existing PTOF diagnostic filtered to admit D^3He-protons as shown in Figure 2.16, the MagPTOF upgrade reduces the background by over three orders of magnitude.

gap between the shielding and the detector in the MagPTOF geometry, the detector occupies a solid angle fraction of approximately 0.0002 with respect to the shielding and nearly all (> 99%) of the neutrons scattered in the tungsten shielding will be deflected sufficiently to miss the detector. For this reason the neutrons scattered in the shielding are effectively lost to the measurement.

The substantial mass in the MagPTOF housing and magnet will also scatter DD-neutrons onto the detector. These scattered neutrons will have longer path-lengths and reduced energy relative to the direct unscattered neutrons, resulting in a delayed arrival time at the detector. To evaluate the impact of such scattering on the observed neutron signal, a model of neutron scattering in MagPTOF was developed using the particle Monte-Carlo transport code MCNP5.[27] Neutron energy deposition in the detector was simulated as a function of time for a simplified version of the MagPTOF geometry including magnet, housing bracket, 2 cm tungsten shielding, and detector. In these simulations, 95% of the neutrons passing through the detector were unscattered. The scattered neutrons appear as a tail on the time-resolved neutron energy deposition in the detector, as shown in Figure 2.32. These scattered neutrons contribute only 11% of the total energy deposited by all neutrons. Due to the small amplitude of this signal tail, the analysis procedure for the DD-neutron signal peak as described in Section 2.3 will not be substantially impacted. The simulated MagPTOF DD-neutron impulse response will be convolved into the DD-neutron source function when fitting to MagPTOF data, as the 2 cm W impulse response is for PTOF data.

Based on these estimates of proton and neutron signals and x-ray background, a typical MagPTOF trace was simulated, as shown in Figure 2.33. This predicted signal is for a typical gas-filled hohlraum implosion with D^3He gas-filled target, producing a D^3He-proton yield of 1×10^8 and a DD-neutron yield of 5×10^{11}. Notably, the peak expected x-ray background has been reduced by over 3 orders of magnitude from the background in PTOF data when the diagnostic is filtered to admit D^3He protons, as shown in Figure 2.16. Such data will readily provide robust measurements of both the shock- and compression-bang times using the D^3He-proton and DD-neutron signals, respectively.

Since the detector, cables, signal recording system, and analysis procedure are all carried over from the PTOF diagnostic, the timing uncertainty budget for the MagPTOF upgrade is nearly identical to that for PTOF. The temporal broadening introduced by the magnet has been included in the error budget shown in Table 2.2, and is negligible compared to other considerations. The dominant uncertainty in the proton time-of-flight is the uncertainty in the proton energy, which is

measured by the neighboring WRF with a typical uncertainty of ±140 keV.

2.6.4 Timeframe for MagPTOF implementation

Initial conceptualization of the MagPTOF concept began in January 2012. The first magnet designs were created by Chun Li of Dexter Magnetic Technologies[39] and were used to validate the MagPTOF concept. Initial calculations of the x-ray background in the MagPTOF concept were performed in collaboration with J. Ryan Rygg, the on-site responsible scientist (RS) for the MagPTOF at LLNL, in February 2012. Between February and April, an initial set of engineering requirements for the MagPTOF upgrade was developed with Todd Clancy of LLNL. While funding was sought, development of the magnet with Dexter continued. A working draft design for the MagPTOF magnet, shielding and detector geometry was developed, and particle trajectory calculations were performed to verify the viability of the project.

A discussion in January 2013 reviewed the engineering requirements and laid the groundwork for a three-way collaboration between MIT, LLE, and LLNL to design, fabricate, and implement the MagPTOF upgrade. The magnet design was developed during spring and summer 2013. A stakeholders meeting in September 2013 defined the personnel responsible for the project: in addition to me, Johan Frenje and Hong Sio at MIT were responsible for the physics design; Jason Magoon, Milt Shoup III and Craig Sangster at LLE for the engineering design and fabrication; and Shannon Ayers and Chris Bailey at LLNL for the integration and operational design of the diagnostic. The initial engineering design was completed by January 2014, delayed somewhat by the need to determine a solution to support the mass of the magnet within seismic safety standards. The design passed review by several LLNL review boards: TaLIS on January 29th, Configuration Control Board (CCB5) on February 3rd, and a Preliminary Design Review was conducted successfully on February 13th. Several additional DIM (90,78) diagnostic snouts were identified to require MagPTOF compatibility, and were incorporated into the design. A revision of the magnet was required to reduce the fringe fields to meet the NIF requirement of less than 1 gauss at 20 cm. Three magnets were ordered in June 2014: a primary and backup magnet to be cleaned, assembled and shipped to LLNL for use, and a third to be retained at MIT for additional testing on the MIT Linear Electrostatic Ion Accelerator (LEIA).[41] The magnets required a slight redesign to reduce weight by changing the sheathing to aluminum, which delayed the delivery until the end of October. The Final Design Review was held on August 28th. The tungsten x-ray shielding was redesigned from that shown in Figure 2.28, to eliminate a slight occlusion of the entrance aperture. The MagPTOF components began fabrication at LLE in October 2014. The expected date for shot readiness on the NIF is three months after the receipt of the magnets, in March 2015.

2.7 Summary

In conclusion, the nuclear bang-time is an important observable for understanding the dynamics of ICF implosions. In particular, the shock-bang time, which occurs when the first shock reaches and rebounds from the center of the implosion, can put strong constraints on the modeling of the shock and implosion dynamics. The shock-bang is notoriously difficult to measure via the neutron or x-ray channels in ignition-scale experiments on the NIF, but is accessible using D^3He-protons due to the much stronger dependence of the D^3He reactivity on temperature.

To record the D^3He-proton shock-bang time, a nuclear bang-time diagnostic based on the particle time-of-flight (PTOF) technique was designed and implemented on both the OMEGA Laser Facility and the NIF. The detector is a CVD-diamond high-voltage photoconducting diode biased at -250 V and held approximately 50 cm from the implosion. Incident high-energy neutrons and

protons generate electron-hole pairs in the diamond volume, which are swept out by the bias field and observed as a voltage impulse. The signal is recorded on a digitizer along with a timing fiducial that is absolutely timed to the NIF laser using an x-ray impulse shot. A model of the fusion-product emission spectrum and history is evolved by time-of-flight to generate a model of the particle source function hitting the detector. This source is convolved with the measured IRF and forward-fit to the recorded data to determine the nuclear bang-time.

The PTOF system measures nuclear bang-times to better than ± 100 ps using DD- or DT-neutrons and D^3He-protons. The IRF was measured using an x-ray impulse and was found to have a rise-time of 0.3 ns and a fall-time of 1.3 ns. The 200 μm thick, 10 mm diameter wafers were calibrated on the OMEGA laser facility and found to have a sensitivity of 2×10^{-8} V ns/DD-neutron, 5×10^{-8} V ns/DT-neutron, and 7×10^{-5} V ns/D^3He-proton. The relative detector sensitivity to protons and neutrons was found to vary as a function of detector thickness: thinner detectors were observed to have a higher sensitivity to protons relative to neutrons. The PTOF has measured nuclear bang-times on over 140 NIF implosions, including the first measurements of both shock- and compression-bang time on a single implosion using D^3He-protons and DD-neutrons, respectively. The large x-ray backgrounds produced by gas-filled hohlraum implosions were found to drive the PTOF detector into a non-linear regime of operation and interfere with the measurement of particle signals. To eliminate this background, a 2 cm tungsten shield was introduced to protect the detector and allow measurement of the DD-neutron compression-bang time. However, the D^3He-proton signal was blocked by this additional shielding.

To overcome this limitation, the MagPTOF diagnostic has been designed for the NIF to simultaneously measure shock- and compression-bang time in D^3He gas-filled hohlraum implosions. This upgrade of the PTOF diagnostic incorporates a thick tungsten filter to shield the detector from high-energy x-rays generated by the hohlraum, and a magnet to deflect shock-generated D^3He-protons around the shielding and onto the CVD-diamond detector. Background from x-rays is estimated to be substantially smaller than the signals of interest. Neutron scattering in the shielding and magnet has been simulated, and the results indicate that this background does not impact the ability to measure compression-bang time using DD-neutrons. This diagnostic capability will provide the first measurements of shock- and compression-bang time in surrogate D^3He-gas filled implosions in gas-filled hohlraums at the NIF, which will mutually reinforce the proton spectral measurements of the ρR at shock-burn, and thereby provide a significant new constraint on modeling of the implosion dynamics.

2.8 References

1. J. W. McDonald, R. L. Kauffman, J. R. Celeste *et al.*, "Filter-fluorescer diagnostic system for the National Ignition Facility," Review of Scientific Instruments, **75**(10), 3753 (2004).
2. S. F. Khan, P. M. Bell, D. K. Bradley *et al.*, "Measuring x-ray burn history with the Streaked Polar Instrumentation for Diagnosing Energetic Radiation (SPIDER) at the National Ignition Facility (NIF)," SPIE Proceedings, **8505**, 850505 (2012).
3. D. H. Edgell, D. K. Bradley, E. J. Bond *et al.*, "South pole bang-time diagnostic on the National Ignition Facility (invited)," Review of Scientific Instruments, **83**(10), 10E119 (2012).
4. D. Kania, M. Landstrass, M. Plano *et al.*, "Diamond radiation detectors," Diamond and Related Materials, **2**(5-7), 1012 (1993), diamond 1992.
5. L. S. Pan, P. Pianetta, D. R. Kania *et al.*, "Electrical Transport Properties of Undoped CVD Diamond Films," Science, **255**(5046), 830 (1992).
6. S. Han, "New developments in photoconductive detectors (invited)," Review of Scientific Instruments, **68**(1), 647 (1997).

7. W. Adam, E. Berdermann, P. Bergonzo *et al.*, "Pulse height distribution and radiation tolerance of CVD diamond detectors," Nuclear Instruments and Methods in Physics Research Section A: Accelerators, Spectrometers, Detectors and Associated Equipment, **447**(1-2), 244 (2000).
8. G. J. Schmid, R. Griffith, N. Izumi *et al.*, "CVD diamond as a high bandwidth neutron detector for inertial confinement fusion diagnostics," Review of Scientific Instruments, **74**(3), 1828 (2003).
9. J. M. McNaney, "NTOF-4M-BT: a primer and short history of the detector (October 2013)," Technical Report LLNL-TR-646418, Lawrence Livermore National Laboratory (2013).
10. V. Y. Glebov, T. C. Sangster, C. Stoeckl *et al.*, "The National Ignition Facility neutron time-of-flight system and its initial performance (invited)," Review of Scientific Instruments, **81**(10), 10D325 (2010).
11. R. M. Malone, B. C. Cox, S. C. Evans *et al.*, "Design and construction of a Gamma reaction history diagnostic for the National Ignition Facility," Journal of Physics: Conference Series, **244**(3), 032052 (2010).
12. Private Communication with H. Herrmann.
13. R. R. Berggren, S. E. Caldwell, J. R. Faulkner *et al.*, "Gamma-ray-based fusion burn measurements," Review of Scientific Instruments, **72**(1), 873 (2001).
14. F. E. Cecil, D. M. Cole, R. Philbin *et al.*, "Reaction ^{2}H(^{3}He, γ)^{5}Li at center-of-mass energies between 25 and 60 keV," Physical Review C, **32**, 690 (1985).
15. D. G. Hicks, N. B. Meezan, E. L. Dewald *et al.*, "Implosion dynamics measurements at the National Ignition Facility," Physics of Plasmas, **19**(12), 122702 (2012).
16. J. R. Rygg, O. S. Jones, J. E. Field *et al.*, "2D X-Ray Radiography of Imploding Capsules at the National Ignition Facility," Physical Review Letters, **112**, 195001 (2014).
17. A. B. Zylstra, J. A. Frenje, F. H. Séguin *et al.*, "The effect of shock dynamics on compressibility of ignition-scale National Ignition Facility implosions," Physics of Plasmas, **21**(11), 112701 (2014).
18. G. A. Kyrala, J. L. Kline, S. Dixit *et al.*, "Symmetry tuning for ignition capsules via the symcap technique," Physics of Plasmas, **18**(5), 056307 (2011).
19. H. F. Robey, P. M. Celliers, J. L. Kline *et al.*, "Precision Shock Tuning on the National Ignition Facility," Physical Review Letters, **108**, 215004 (2012).
20. Diamond Materials, GmbH., see `http://www.diamond-materials.com/`.
21. W. J. Hibbard, M. D. Landon, M. D. Vergino *et al.*, "Design of the National Ignition Facility diagnostic instrument manipulator," Review of Scientific Instruments, **72**(1), 530 (2001).
22. Greenfield Technology, see `http://www.greenfieldtechnology.com/`.
23. Tektronix, see `http://www.tek.com/`.
24. J. A. Frenje, C. K. Li, F. H. Séguin *et al.*, "Measuring shock-bang timing and ρR evolution of D^{3}He implosions at OMEGA," Physics of Plasmas, **11**(5), 2798 (2004).
25. L. Ballabio, J. Källne and G. Gorini, "Relativistic calculation of fusion product spectra for thermonuclear plasmas," Nuclear Fusion, **38**(11), 1723 (1998).
26. B. K. Spears, M. J. Edwards, S. Hatchett *et al.*, "Mode 1 drive asymmetry in inertial confinement fusion implosions on the National Ignition Facility," Physics of Plasmas, **21**(4), 042702 (2014).
27. Monte Carlo N-Particle (MCNP) Transport Code, see `https://mcnp.lanl.gov/`.
28. P. Scott, "Chi-Square: Testing for Goodness of Fit," see `http://physics.ucsc.edu/~drip/133.html` (2000), Intermediate Lab Manual, Chapter 4.
29. R. A. Lerche, B. P. Golick, J. P. Holder *et al.*, "Algorithm for precision subsample timing between Gaussian-like pulses," Review of Scientific Instruments, **81**(10), 10E121 (2010).
30. MATLAB, see `http://www.matlab.com`.
31. J.F. Ziegler and J. P. Biersack, "SRIM-2013: Stopping and Range of Ions in Matter," see `http://www.srim.org/index.htm`.
32. L.S. Dauffy, R.A. Lerche, G.J. Schmid *et al.*, "Recovery of CVD diamond detectors using laser double pulses," J. Phys. IV France, **133**, 951 (2006).
33. D. R. Kania, "Radiation-induced conductivity: High-speed detection of x rays and neutrons," Laser and Particle Beams, **9**, 91 (1991).

34. J. Hubbell and S. Seltzer, "Tables of X-Ray Mass Attenuation Coefficients and Mass Energy-Absorption Coefficients from 1 keV to 20 MeV for Elements Z = 1 to 92 and 48 Additional Substances of Dosimetric Interest," see `http://www.nist.gov/pml/data/xraycoef/index.cfm` (2013).

35. M. J. Rosenberg, A. B. Zylstra, F. H. Seguin *et al.*, "Investigation of Ion Kinetic Effects in Direct-Drive Exploding-Pusher Implosions at the NIF," Physics of Plasmas (submitted).

36. D. T. Casey, V. A. Smalyuk, R. E. Tipton *et al.*, "Development of the CD Symcap platform to study gas-shell mix in implosions at the National Ignition Facility," Physics of Plasmas, **21**(9), 092705 (2014).

37. H. G. Rinderknecht, M. G. Johnson, A. B. Zylstra *et al.*, "A novel particle time of flight diagnostic for measurements of shock- and compression-bang times in D^3He and DT implosions at the NIF," Review of Scientific Instruments, **83**(10), 10D902 (2012).

38. N. Sinenian, M. J. Rosenberg, M. Manuel *et al.*, "The response of CR-39 nuclear track detector to 1-9 MeV protons," Review of Scientific Instruments, **82**(10), 103303 (2011).

39. Dexter Magnetic Technologies, see `http://www.dextermag.com`.

40. M. Chadwick, M. Herman, P. Obložinský *et al.*, "ENDF/B-VII.1 nuclear data for science and technology: Cross sections, covariances, fission product yields and decay data," Nuclear Data Sheets, **112**(12), 2887 (2011), special Issue on ENDF/B-VII.1 Library.

41. N. Sinenian, M. J.-E. Manuel, A. B. Zylstra *et al.*, "Upgrade of the MIT Linear Electrostatic Ion Accelerator (LEIA) for nuclear diagnostics development for Omega, Z and the NIF," Review of Scientific Instruments, **83**(4), 043502 (2012).

3

Studies of Kinetic Fuel-Shell Mix using Shock-Driven Implosions

3.1 Introduction

As discussed in Chapter 1, hydrodynamic mix is a major concern for inertial confinement fusion studies. Mix of non-hydrogenic materials into the fuel is severely detrimental to the final pressure of the fuel assembly, since these contaminants enhance the energy loss pathways of bremsstrahlung and line-radiation.[1] The study of mix has concentrated almost entirely on the growth of hydrodynamic instabilities in accelerating frames, such as Rayleigh-Taylor, Kelvin-Helmholtz and Richtmyer-Meshkov instability growth at the ablation front[2,3] and during deceleration.[4,5] Instabilities at material interfaces of the target have been studied as a seed for deceleration phase growth.[6,7] It is presumed that when these instabilities reach the non-linear stage, they begin to drive turbulent mixture of the fluids down to the atomic scale. Non-hydrodynamic ('kinetic') mechanisms, which occur when the mean free path of the shell ions into the fuel becomes comparable to the experimental scale lengths, have not been previously studied in the ICF context.

Thick deuterated plastic (CD) shells filled with either ^{3}He[8,9] or tritium gas[10–13] have previously been used to study hydrodynamic mix mechanisms during the compression phase of ablatively-driven implosions. D^{3}He- or DT-fusion reactions in such experiments are only expected to occur in regions where fuel and shell material have been atomically mixed. Experiments on OMEGA have shown that the shock yield from such ablatively-driven implosions is below the measurement threshold, from which it is inferred that negligible fuel-shell mix occurs prior to the shock bang-time.[8,9] This finding was in agreement with the expectations from hydrodynamic mix models, which predict that fuel-shell mix only occurs after the rebounding shock has struck the incoming shell, during the deceleration phase when hydrodynamic instability growth is substantial.

Based in part on these previous findings, the expectation for thin-shell, shock-driven experiments such as were introduced in Section 1.1.3 was that fuel-shell mix at shock-bang time would be minimal. The low convergence and rapid total ablation (or 'burn-through') of the shell in the shock-driven implosions imply negligible growth of hydrodynamic instabilities prior to peak nuclear production, and therefore negligible turbulent mix, as was observed in the shock-phase of the thick-CD implosions. In particular, for thin-CD shell targets filled with pure ^{3}He, the shock yield of D^{3}He-protons was expected to be small. However in this work the opposite was observed, as shown in Figure 3.1. The yield of D^{3}He-protons from pure ^{3}He-filled targets was essentially identical to the yield from targets filled with a 50:50 D:^{3}He mixture and imploded with identical laser conditions. This result is strong evidence that significant fuel-shell mix occurs in these experiments prior to shock bang, in spite of their hydrodynamic stability. The lack of hydrodynamic mix mechanisms in

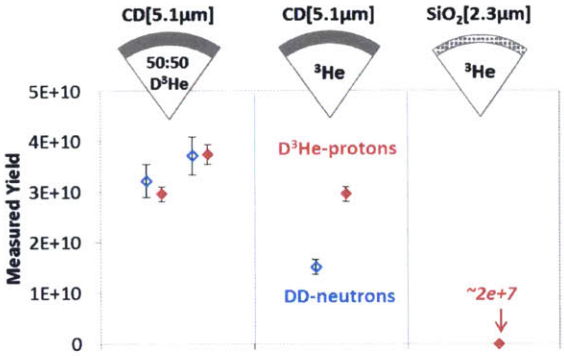

Figure 3.1. Yields of D^3He-protons (solid red) recorded from 30 kJ implosions of deuterated plastic shells (ρ = 1.1 g/cc, D:C = 1.4) filled with a 50:50 D^3He mixture are comparable in magnitude to implosions of the same shells filled with pure ^3He. Implosions of glass shells filled with ^3He produce yields 3 orders of magnitude lower, ruling out D_2-gas contamination of the targets as an explanation for this result. The observed D^3He-p yields require shell-deuterium mix into the ^3He fuel to be of order 10% the initial ^3He gas density.

these implosions isolates kinetic processes as an explanation for the large nuclear yields observed.

This chapter presents a series of shock-driven thin-CD implosions, which demonstrate a significant kinetic mechanism for fuel-shell mix. Hydrodynamic instability growth is shown to be negligible prior to the deceleration phase, which means that a non-hydrodynamic mix mechanism must be invoked to explain the data. Ion diffusion is proposed as one plausible explanation of these results, by generating a mix layer near the fuel-shell interface prior to shock-bang time. Other kinetic effects, such as shock acceleration of light ions in the shell, may also play an important role, and such mechanisms are studied here as possible contributing factors.

The impact of the kinetic processes examined herein, in particular shock acceleration, on hot-spot ignition designs is under investigation. Recent ignition designs include four shocks, which are timed to coalesce near the inside surface of the DT-ice layer, generating a single strong shock that traverses the fill gas.[14] Kinetic fuel-shell mixing associated with shock traversal of the fuel-shell interface may occur in ignition experiments.[15] Between shock coalescence and the compression phase, the central plasmas of ignition targets are comparable to those produced in shock-driven implosions: the central DT-vapor is low-density (ρ = 0.3 mg/cc) and strongly shocked (M $\sim$ 10–50), comparable to the kinetic mix experiments discussed here (ρ = 0.49 mg/cc, M $\gg$ 10). Kinetic physics in the strongly-shocked gas is a subject of active investigation, as such processes may modify the initial conditions for compression, influencing the evolution of ignition targets later in time.

This chapter is organized as follows: Section 3.2 describes the design of these experiments. The results of the experiments are described in Section 3.3. Section 3.4 demonstrates in detail that hydrodynamic mode growth was small in these experiments, and cannot explain the observed trends in the data. Section 3.5 proposes ion diffusion as a likely candidate for explaining the observed trends. Section 3.6 investigates and rules out several additional kinetic effects which may have caused the high levels of mix observed. The results are summarized in Section 3.7.

3.2 Experimental Design

Spherical capsules 860 μm in diameter and made of 5.1 μm-thick deuterated plastic (CD) were acquired from General Atomics.[16] The CD used in these capsules had a D:C ratio of 1.4, and a density of 1.1 g/cc. The capsules were filled with mixtures of deuterium and ^3He gas and imploded by the 60-beam OMEGA laser. Initial experiments were performed on March 7th, 2012, and used a 1 ns square laser pulse delivering 30 kJ of laser energy. Six targets were imploded on this shot day: two each filled with pure deuterium, 50:50 D^3He, and pure ^3He. The gas fill of all targets had a mass density of 0.499 mg/cc, with a max-min variation of 0.010 mg/cc. To attain the full 30 kJ energy, beam smoothing by spectral dispersion (SSD) was not used on these initial implosions.[17] On August 2nd, 2012, two additional pure ^3He-gas filled targets with identical shells and gas fills to

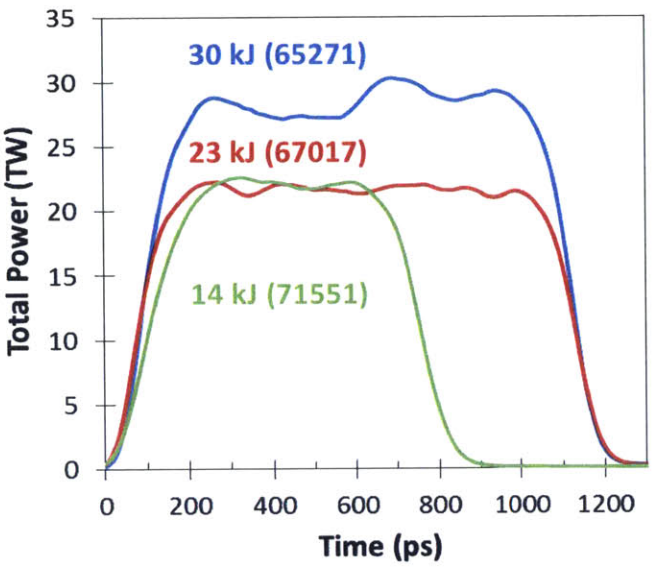

Figure 3.2. Three laser pulse shapes were used in the thin-CD experimental campaign; an example of each is shown. Square impulses with 1 ns FWHM duration (SG1018) were used in the March 7th, 2012 (shot 65271, blue) and August 2nd, 2012 (shot 67017, red) experiments, delivering ~30 kJ and ~23 kJ of total laser energy, respectively. Square impulses with 0.6 ns FWHM duration (SG06vA01) were used on the November 21st, 2013 experiments (shot 71551, green); the total energy of ~14 kJ was selected to match the peak power of the 23 kJ experiments.

the previous shots were imploded using 23 kJ in a 1 ns square pulse with full SSD beam smoothing. Finally, on November 21st, 2013, five more implosions (two filled with 50:50 D^3He and three filled with pure ^3He) were performed, all with equal initial mass density but using 14.2 kJ energy in an 0.6 ns square pulse. This energy was chosen to maintain a constant peak power with the August 2012 implosions. Distributed phase plates were used in all cases to generate a fourth-order super-Gaussian (SG4) beam profile.[18] A summary of the shot parameters for this series is given in Table 3.1, and a comparison of the laser pulse shapes used is shown in Figure 3.2.

The expected evolution of these implosions is shown in Figure 3.3, which presents a simulation of the above conditions using the 1D-radiation-hydrodynamic code HYADES.[19a] A predicted x-ray preheat of the CD-shell to 20 eV was included in these simulations, which has the effect of causing the CD material to blow down by ~20 μm prior to shock breakout at ~250 ps. As discussed in Section 1.1.3, these thin-shelled, shock-driven capsules produce nuclear yield, called "shock yield," primarily from heating of the fuel by the shock during its rebound from the center of the implosion at approximately 0.7 ns. In thick-shelled implosions with substantial remaining shell mass, shock-bang is immediately followed by the deceleration phase and compression of the fuel. The remaining shell material can significantly compress the fuel and generate a second period of nuclear yield production, termed "compression yield." However in these experiments, the CD-shell has burned through prior to deceleration at approximately 0.5 ns, and the remaining CD plasma density is roughly comparable to the fuel plasma density. The effects of this can be seen in the trajectory of the fuel-shell interface after the shock rebound, when the remaining mass is too small to significantly compress and heat the fuel. Little compression yield is expected.

Maintaining constant mass density for the different initial gas fills is beneficial for several reasons. The rate of hydrodynamic instability growth is governed by the Atwood number $\mathcal{A}$, defined as follows:

$$\mathcal{A} = \frac{\rho_1 - \rho_2}{\rho_1 + \rho_2}, \tag{3.1}$$

where the densities $\rho_{1,2}$ are taken on either side of a material interface and material 1 is denser,

[a]The HYADES simulations used throughout this thesis were provided by Alex Zylstra. Extensive post-processing routines were developed as part of this work to examine the simulated plasma and extract the relevant diagnostic information for comparison to the measured data.

Table 3.1. Shot information for kinetic mix studies using implosions of deuterated plastic (CD) shells filled with mixtures of D and ^{3}He on the OMEGA laser.

Shot Information		Capsules		Initial gas fill		Laser Information		
Shot #	Fill Type	OD (μm)	wall (μm)	ρ_0 (mg/cc)	f_D	Energy (kJ)	Absorption %	Pulse Shape
65266	D_2	858.2	5.10	0.497	1.0	29.54		SG1018
65269	D^3He	861.0	5.00	0.498	0.50	29.48		SG1018
65271	^3He	876.2	5.10	0.502	0.0	29.07		SG1018
65273	D_2	866.0	5.00	0.496	1.0	29.53		SG1018
65275	D^3He	856.2	5.10	0.506	0.51	29.27		SG1018
65278	^3He	877.2	5.10	0.498	0.0	29.46		SG1018
	average	865.8±9.07	5.07±0.05	0.5±0		29.39±0.19		
67015	^3He	877.3	5.14	0.502	0.0	22.85	41%	SG1018
67017	^3He	877.6	5.08	0.493	0.0	22.76	41%	SG1018
	average	870.86±9.56	5.08±0.05	0.5±0		26.77±3.62	41%	
71536	D^3He	871.1	5.22	0.485	0.5	13.93	55%	SG06vA01
71537	^3He	876.8	5.14	0.491	0	14.10	53%	SG06vA01
71547	^3He	869.5	5.16	0.481	0	14.50	51%	SG06vA01
71549	D^3He	873.7	5.31	0.498	0.5	14.45	52%	SG06vA01
71551	^3He	880.9	4.95	0.488	0	14.31	53%	SG06vA01
	average	874.37±4.58	5.16±0.13	0.49±0.01		14.26±0.24	53±1%	

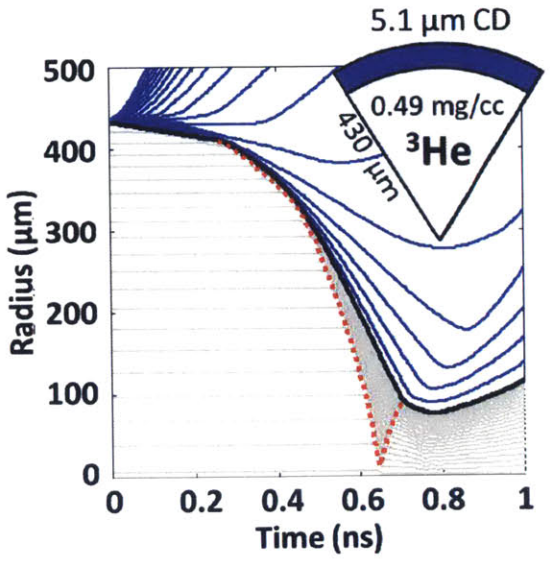

Figure 3.3. Lagrangian mass element profiles simulated for a 30 kJ implosion of a 5.1 micron CD shell (blue) filled with 0.49 mg/cc pure ^{3}He (grey). The 1D-radiation-hydrodynamic code HYADES was used for this simulation. The inward trajectory of the fuel-shell interface (black) is interrupted by the rebounding shock (red dotted), initiating a brief deceleration phase. Shock burn occurs when the rebounding shock locally heats and compresses the fuel to fusion-relevant conditions.

by convention. By maintaining the same initial gas density as the deuterium fraction is varied, the Atwood number at the fuel shell interface is the same for all implosions, and the hydrodynamic growth will also be the same. If the plasma is sufficiently collisional that the ions and electrons are equilibrated throughout the implosion, this condition also produces plasmas with equivalent equations of state for any D:^{3}He ratio,[20] such that the experiments will evolve similarly when subjected to the same pressure source from the laser.[b] This condition is referred to as *hydroequivalence*. Because both D and ^{3}He atoms have the same ratio of total particle number to mass [(1+Z)/A = 1], the ideal equation of state [$P = (1 + Z)\rho_i T/Am_p$] also remains unchanged for D^{3}He mixtures with equal initial mass density. For the strongly-shocked implosions used in this work, the electrons and ions are in general not equilibrated to each other, and so the equation of state is not strictly identical as f_D is varied. The effects of this will be discussed in more detail in Chapter 4.

3.3 Experimental Results

The nuclear yields of 14.7 MeV protons from the D-^{3}He fusion reaction were measured using multiple Wedge Range-Filter (WRF) proton spectrometers and the Charged Particle Spectrometers (CPS1 and CPS2).[21] D^{3}He-proton yields above 10^{10} were produced by capsules containing 50:50 D^{3}He mixtures and containing pure ^{3}He. Yields of 2.45 MeV neutrons from the D-D fusion reaction were measured using the neutron Time-of-Flight (nTOF) diagnostic suite,[22] and also exceeded 10^{10} in all experiments. Nuclear bang-times were recorded using the Neutron Temporal Diagnostic (NTD)[23] and Proton Temporal Diagnostic (PTD)[24] introduced in Section 1.3.5. A laser absorption fraction of 41% ± 1% in the 23 kJ implosions and 53% ± 1% in the 14 kJ implosions was recorded by full aperture backscatter stations (FABS).[25] The recorded bang time and absorption fraction were used to constrain the 1D simulations of these implosions.

[b] Radiation from the core scales as Z^2 and will therefore increase with ^{3}He fraction. However 1D radiation hydrodynamics simulations indicate this is a small effect: yields are predicted by 1D-HYADES simulations to scale as the expected hydroequivalent scaling to within 10%.

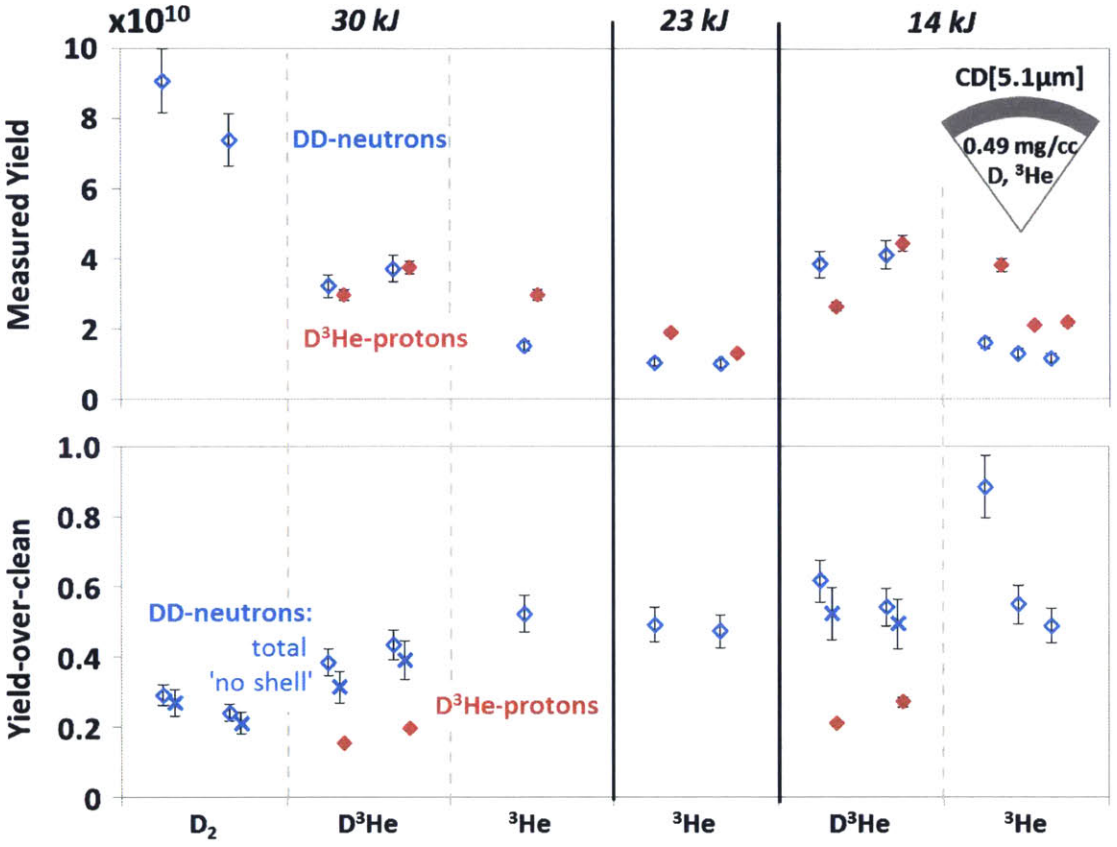

Figure 3.4. a) Nuclear yields of D^3He-protons (solid diamonds, red) and DD-neutrons (open diamonds, blue) from implosions of deuterated plastic shells filled with hydroequivalent mixtures of D_2, D^3He or ^3He gas. Experiments were performed on three shot days: 30 kJ (1 ns square) on March 7th, 2012; 23 kJ (1 ns square) on August 2nd, 2012; and 14 kJ (0.6 ns square) on November 21st, 2013. Experiments performed at 30, 23, and 14 kJ showed similar levels of mix as inferred from D^3He-proton yields. b) Yield-over-clean (YOC) compared to 1D-HYADES simulations. DD-neutron YOC is shown for both total yield (open diamonds, blue) and corrected to remove the shell yield contribution (x, blue). The correction assumes that the experimental shell yield is the same for all experiments with the same laser power, as in the simulations.

3.3.1 Yields

The recorded yields are presented in Figure 3.4a, and the ratio of observed yield to expected yields from 1D HYADES simulations ('yield-over-clean' or YOC) is presented in Figure 3.4b. In all CD-shell experiments, the DD-neutron yield is on the order of 10^{10}. This is in reasonable agreement with 1D-simulations, which predict nuclear yield of approximately 2–3 $\times$ 10^{10} from the CD shell in addition to yield from the fuel. D^3He-proton yields are measured above 10^{10} for both pure ^3He- and D^3He-filled targets. The YOC is shown both including and excluding the CD-shell DD-neutron yield, assuming that the shell yield is the same in all experiments with the same laser energy, and is equal to the total neutron yield from the pure ^3He-filled experiments. Both DD-neutron and D^3He-proton YOC values are comparable to those reported for thin-glass exploding pushers filled with similar levels of 50:50 D^3He fuel.[26] The neutron yield from the shell appears to be somewhat better modeled (YOC = 50%) than yield from the gas (YOC = 20–40%). The experiments imploding identical targets with a shorter 0.6 ns laser impulse, which had the same peak power as the 23 kJ

implosions, produced comparable yields. The 14 kJ implosions had slightly higher YOCs for DD-neutrons than the 23 kJ implosions. Since the 23 kJ and 14 kJ experiments only diverge after the laser turns off at ~0.6 ns, this finding suggests that the late-time laser energy is simulated to increase the yields, but in practice does not. This is consistent with the measured laser absorption fractions for the two sets of experiments shown in Table 3.1, which indicate that the late-time laser energy is not efficiently absorbed. One ^{3}He-filled, 14 kJ implosion was an outlier, producing a DD-neutron YOC of ~90% and substantially more D^{3}He-proton yield than the nominally identical implosions. As we will see, this implosion was also an outlier in terms of the burn-averaged ion temperature. The reasons for this behavior are not evident from the other shot data.

Mixing of the shell and fuel mass is the best candidate for explaining the D^{3}He-proton yield observations. Contamination of the ^{3}He gas with deuterium has been ruled out as a cause for this observation, as the gas source of ^{3}He was determined to contain 1.4 parts atomic D per 10^4 atomic ^{3}He by mass spectroscopy. A ^{3}He-filled glass target with similar initial shell ρR was imploded as a control experiment, and produced D^{3}He-proton shock yield three orders of magnitude lower than was observed from the CD-shell experiments, as shown on the right of Figure 3.1. From this experiment it is estimated that the as-shot deuterium contamination in the ^{3}He gas is approximately 2 parts in 10^4. This value includes all other possible sources of contamination between the ^{3}He source bottle and the as-shot target. Permeation of ^{3}He gas into the CD shell prior to the shot is also ruled out as a cause for this observation. Assuming the shell maintains a ^{3}He gas partial-pressure equal to the gas fill pressure, the D:^{3}He ratio in the shell is 425:1. Including this value in 1D-radiation-hydrodynamic simulations produces yields approximately two orders of magnitude below those observed.

Analytical yield models

The observed D^{3}He-proton and DD-neutron yields were used to estimate how much deuterium would have to enter the pure ^{3}He fuel prior to burn to produce these results. Following Eqn 1.4, the nuclear yields scale as:

$$Y_{DD-n} = \int (n_D^2/2)\langle\sigma v\rangle_{DD} dV dt, \tag{3.2}$$

$$Y_{D^3He-p} = \int n_D n_{^3He} \langle\sigma v\rangle_{D^3He} dV dt. \tag{3.3}$$

Assuming that the evolution of density and temperature profiles is to zeroth order identical in both the 50:50 D:^{3}He and pure ^{3}He case, the yield is proportional primarily to the number density of the reactant ions. If the mix is uniformly distributed, the mixed deuterium number density in the pure ^{3}He fuel (n'_D) can be estimated as

$$n'_D = \left(\frac{n_{^3He,0.5}}{n_{^3He,1}}\right) n_{D,0.5} = 0.36 \times n_{^3He,1}, \tag{3.4}$$

where the subscript number indicates the initial atomic ^{3}He ion fraction in the gas. Using the initial gas-fill mass density of 0.499 mg/cc, n'_D is calculated to be approximately 3.6×10^{19} cm^{-3}. This value corresponds to the inner 47 nm of initial CD material being uniformly mixed throughout the ^{3}He fuel. As this density is sufficiently high to perturb the hydrodynamic evolution of the plasma, the calculation is approximate; however it is instructive to note the large amount of deuterium mix that is required to explain the observations. The DD-neutron yield produced by this level of

mixed deuterium follows from similar scalings as 0.36 times the DD-neutron yield from the fuel in the 50:50 experiment, which is consistent with observations. However in both experiments, the CD plasma is expected to produce a neutron yield on the order of 10^{10} DD-neutrons when it is reshocked.

Note that this simple calculation implicitly assumes that mix does not occur in the D^3He-filled implosion. This assumption is valid under the ion diffusive mix mechanism, as will be shown later. Including in these calculations the effect of uniform mix on both D^3He and pure ^3He implosions produces an even larger mix requirement: $n'_D = 0.9\ n_{3He,1}$, which is inconsistent with the observed DD-neutron yields.

The application of more well-developed analytical models of yield production as a function of mix and deuterium fraction to the data was attempted, but was unsuccessful. The hydroequivalence of the different fills suggests that the evolution of temperature and mass-density profiles of each experiment are nearly the same to zeroth order. The species densities n_i in Equation 3.3 may be rewritten in terms of mass density ρ, which is identical for all experiments, and the deuterium number fraction f_D, as follows:

$$\begin{aligned} n_D &= \rho f_D / m_p (3 - f_D), \\ n_{^3He} &= \rho (1 - f_D) / m_p (3 - f_D). \end{aligned} \tag{3.5}$$

Assuming f_D does not evolve within an implosion, it may be removed from the integral, and a scaling of yield versus f_D derived for the initial gas. The yield from the deuterium in the initial gas fill is expected to follow this hydroequivalent scaling: $Y_{DD}(f_D) = Y_{DD}(f_D = 1)\ 4f_D^2/(3 - f_D)^2$.[20] The DD-neutron production by the shell plasma should be approximately constant.

Attempts to constrain a model of the different yield-producing regions to the data recorded on March 7th, 2012 based on the dual assumptions of fuel hydroequivalence and perturbative deuterium mix into the fuel did not converge to a consistent solution. A model for the DD-neutron yields was developed by assuming that the yield from the CD-shell is equal in all experiments, the yield from the fuel scales as n_D^2, and the initially-hydroequivalent fuels were perturbed by an equal amount of shell-deuterium mix in all experiments. The deuterium density is modeled as $n_D \rightarrow n_D + n_{mix} = (\rho/m_p)\,[f_D/(3 - f_D) + f_{mix}/2]$, producing a yield model:

$$Y_{tot} = Y_{gas} + Y_{shell} = Y_{DD-clean} \left[\frac{2 f_D}{3 - f_D} + f_{mix} \right]^2 + Y_{shell}. \tag{3.6}$$

This model has three variables: shell yield Y_{shell}, fuel yield from a 'clean' D_2 implosion $Y_{DD-clean}$, and mix fraction f_{mix}. Using the DD-neutron data from the 30 kJ implosions presented in Fig. 3.4 (for which $f_D = 0$, 0.5, and 1) to solve this system of equations, the model does not converge to a reasonable solution: the shell yield is required to be consistent with 0, while mix generates the majority of yield for all deuterium fractions. Such a strongly-mixed scenario violates the condition of hydroequivalence. Additionally, this scenario is inconsistent with burn-average ion temperature data (Figure 3.5): the temperatures from the pure ^3He implosions are in good agreement with the simulations which predict shell-yield only, whereas a higher burn-average temperature would be expected if volumetrically-mixed deuterium were dominant.

One source of this inconsistency is apparent in the DD-neutron yield-over-clean for the fuel shown in Fig. 3.4, which is less in the pure D_2 implosions (25%) than in the 50:50 implosions (35%). The pure deuterium fuel appears to be underperforming, in terms of both DD-neutron yield and temperature, compared to the 50:50 D^3He fuel. Such non-hydroequivalent performance has been observed in the compression yield of ablatively-driven D^3He targets, but with the opposite trend, such that 50:50 D^3He-filled implosions underperformed relative to hydroequivalent D_2 fills.[20]

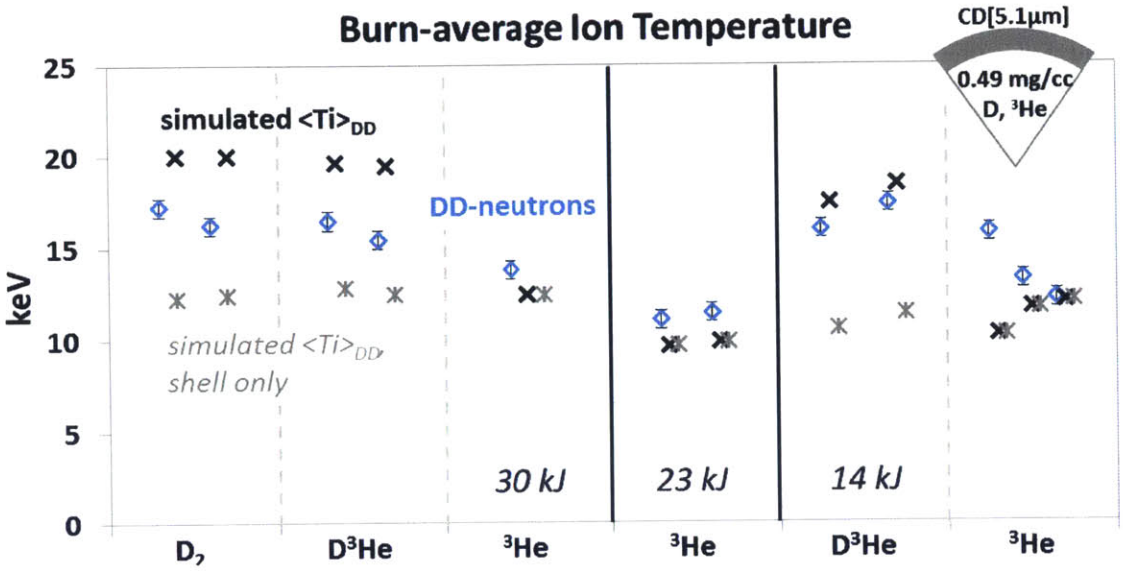

Figure 3.5. Nuclear burn-averaged temperatures recorded from the spectral line width of the measured DD-neutrons (open diamonds, blue). DD-neutron burn-averaged ion temperatures predicted from 1D-HYADES simulations are shown for the total experiment (x, black) and for the shell only (stars, grey). NTOF instrument analysis provided by Vladimir Glebov, LLE.

One possible explanation is that kinetic effects dominate the evolution of these implosions prior to and during burn, such that models based on hydrodynamic equivalence are inappropriate for explaining the yield trends even in the D_2 and 50:50 D^3He cases.

In summary, the assumption of hydrodynamic yield performance in these implosions is likely to be invalidated by the kinetic nature of the plasmas. Much better agreement with the observed yield and temperature trends is produced by simulations including reduced ion kinetic models, as will be discussed in Section 3.6.

3.3.2 Burn-averaged ion temperatures

Burn-averaged ion temperatures were inferred from the Doppler-broadened line width of DD-neutrons for all experiments, as shown in Figure 3.5. For the 1 ns square pulse implosions (30 and 23 kJ, shown on the left of the figure), the measured temperatures agree well with simulations for the pure ^{3}He-filled experiments, and fall between the simulated shell-only and simulated total burn-average ion temperature for the implosions with D_2 fill. As with the yields, there is better agreement between measured and simulated temperatures for experiments where the yield is produced primarily in the CD plasma. Both of these results are possibly due to the lower burn temperatures and higher average-Z in the remaining shell material, which produces $\sim 20\times$ shorter ion-ion mean-free-paths during burn as compared to the hot, low-Z fuel. The hydrodynamic equations assume short mean-free-paths relative to zone size, and are therefore more valid during burn in the shell than in the fuel.

The 0.6 ns laser impulse implosions (14 kJ, on the right of the figure), which have the same peak power as the 23 kJ implosions, appear to produce burn-averaged ion temperatures similar to the 1D-simulations for D^3He-gas fill, suggesting that the fuel is better modeled than for the implosions with more laser energy. This is similar to the result discussed previously that the 14 kJ implosions produced yields in better agreement with the simulations. We can infer that the fuel behaves

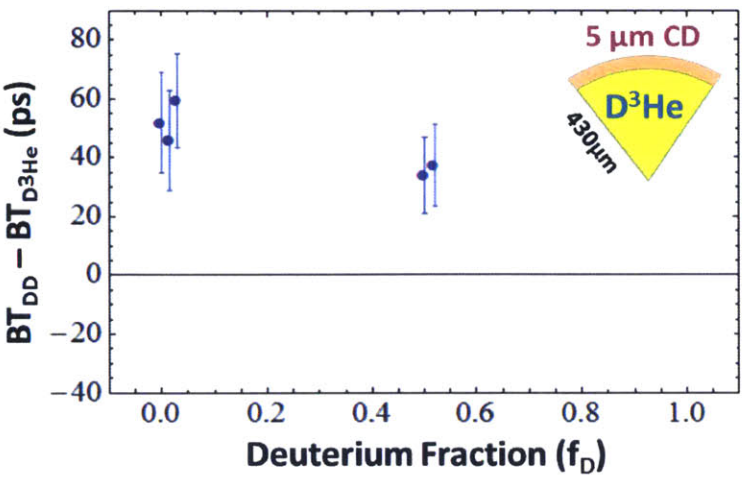

Figure 3.6. Comparison of DD-neutron and D^3He-proton bang-times in implosions of thin-CD targets filled with various mixtures of deuterium and ^3He. Positive values indicate DD-neutron bang-time occurred after D^3He-proton bang-time. Points are slightly offset in f_D for legibility. Statistical uncertainties are shown. Cross-timing uncertainties were reduced to $\sim \pm 15$ ps by recording both nuclear products on a single streak-camera diagnostic (multiPTD). Instrument analysis performed by Hong Sio.

in a more hydrodynamic manor in these implosions. The observed DD-neutron burn-averaged temperatures are higher in the pure-^3He implosions compared to the 1D-simulations, especially in the outlier experiment. This is consistent with the mix of shell deuterium into the central gas, where the plasma ion temperature is expected to be hotter than in the shell.

3.3.3 Burn histories

The burn histories of D^3He-protons and DD-neutrons were recorded using the Particle Temporal Diagnostic (PTD)[24] and Neutron Temporal Diagnostic (NTD),[23] which were introduced in Section 1.3.5. In the 30 kJ experiments, NTD measured a DD-neutron bang-time of 780±50 ps on the first implosion only (#65266, pure D_2-gas fill), and the D^3He-proton bang-time was not recorded.[c] A DD-neutron bang-time was recorded on both of the 23 kJ experiments (#67015 and #67017, both ^3He-gas fill), which agreed with each other to within uncertainties and had an average value of 845±50 ps. The ~10% delay with the reduced laser energy agreed well with the expectation from simulations. D^3He-proton bang-times were again not recorded on this shot day, due to a malfunction in PTD. For the 14 kJ implosions, both DD-neutron and D^3He-proton bang-times were recorded. The DD-neutron bang-times were in agreement with those measured on the 23 kJ implosions to within the standard cross-timing uncertainty to the laser of ±50 ps. The measured bang-times and burn-durations are summarized in Table 3.2.

The D^3He-proton bang-times were measured to occur earlier than the DD-neutron bang-time by 40–50 ps, as shown in Figure 3.6. This comparison was obtained with high relative precision ($\sim \pm 15$ ps) by modifying the PTD nose cone to record both DD-neutron and D^3He-proton signals on a single instrument. The PTD scintillator was split into two optically separated parts, both of which are imaged by the streak camera. One half is shielded from D^3He-protons and provides a neutron signal; the other is exposed to the protons and provides the proton signal. This *multiPTD* was conceptualized as part of this work and is being developed by Hong Sio.

The relative bang-time data in Figure 3.6 suggest that the bang-time differential is slightly larger for the pure ^3He-gas fill ($f_D = 0$), compared to the 50:50 D^3He fill ($f_D = 0.5$). This possible

[c]These experiments were shot on March 7th, 2012 as OMEGA-only implosions interleaved with joint OMEGA-EP shots. After the first implosion, NTD was configured to measure the x-rays from the EP beam firing for the remainder of the shot day. PTD must be fielded in TIM5, which is directly opposite the incident EP beam and was required for a radiochromic film diagnostic.

Table 3.2. Bang-times (BT) and burn-durations (full-width at half-maximum, or FWHM) recorded on thin-CD implosions by NTD and PTD. All time values have units of picoseconds. Standard cross-timing uncertainties in the bang-time for these two instruments are ±50 ps; random uncertainties from shot to shot are ~ ±10 ps. NTD analysis courtesy of Christian Stoeckl, LLE; PTD analysis courtesy of Hong Sio.

Shot Information		Laser Information		DD-neutrons		D^3He-protons	
Shot #	Fill Type	Energy (kJ)	Pulse	BT	FWHM	BT	FWHM
65266	D_2	30	1 ns	780	180	–	–
67015	^3He	23	1 ns	855	185	–	–
67017	^3He	23	1 ns	835	185	–	–
			average	845±14	185		
71536	D^3He	14	0.6 ns	815	142	769	112
71537	^3He	14	0.6 ns	828	133	747	119
71547	^3He	14	0.6 ns	826	137	770	119
71549	D^3He	14	0.6 ns	794	145	748	117
71551	^3He	14	0.6 ns	830	144	754	137
			average	819±15	140±5	758±11	121±9

trend agrees with expectations. Assuming uniform mix of shell deuterium into the ^3He fuel, the bang-time of D^3He-protons will not change between the two cases. Based on the yield results shown in Figure 3.4, it appears that the total DD-neutron yield is dominated by the shell in the pure ^3He case, compared to the 50:50 case. The reduction in DD-neutron yield when the gas-fill is changed from 50:50 D^3He to pure ^3He implies that the neutron yield from the gas is significantly reduced, and the shell is dominant in the latter case. (The shell will generate approximately the same amount of DD-neutrons, regardless of the capsule gas fill.) Since the yield production follows the shock wave, the central plasma is expected to burn earlier than the shell. This implies that the DD-neutron bang-time will be slightly later for pure ^3He. This behavior is observed both in the absolute DD-neutron bang-times shown in Table 3.2, and in the relative bang-times shown in Figure 3.6. Higher-precision measurements are under development and will confirm this trend in future implosions.

3.3.4 Nuclear imaging

Nuclear burn profiles of DD-protons and D^3He-protons were recorded on the 14 kJ (0.6 ns) implosions using the PCIS instrument introduced in Section 1.3.4. The PCIS instrument was fielded in TIM 2, with the aperture positioned 2.95 cm from TCC and the CR-39 positioned 59 cm behind the aperture. Two pieces of CR-39 were fielded to record both DD-protons and D^3He-protons along the same line of sight. The front piece of CR-39 was filtered with 12.5 μm Al + 7.5 μm Ta, while the rear piece was filtered with either 200 or 162.5 μm Al, depending on the thickness of the front piece. The best fits of the burn profile model described by Equation 1.36 to the penumbral images recorded on one of the ^3He-gas filled implosions are shown in Figure 3.7. The measured profiles are centrally peaked, indicating that deuterium from the shell has penetrated deeply into the ^3He fuel. The fits are parametrized by the radius containing 50% of the yield (r_{50}) and the peakedness of the profile (p); the inferred values of these parameters for all the recorded data are shown in Figure 3.8. The results of 1D-HYADES simulations are shown in the plots. In the simulations, trace ^3He was included in the CD shell, which provides the 1D-simulated D^3He-proton burn for the pure ^3He-gas fill.

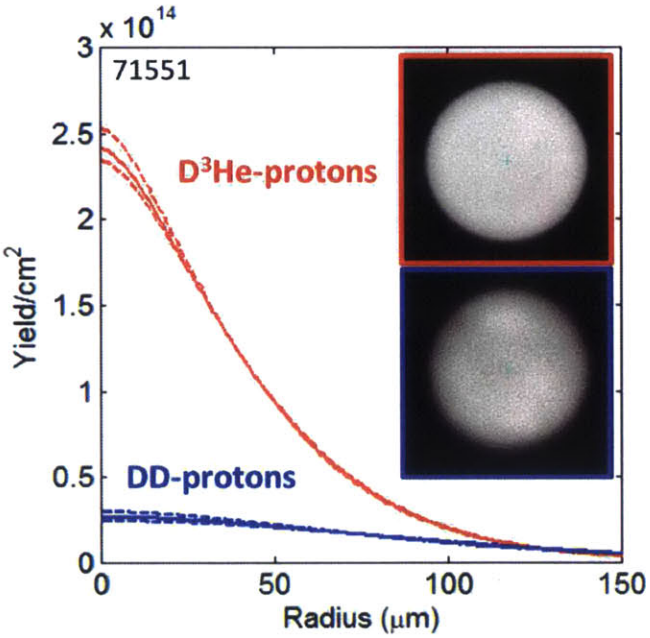

Figure 3.7. Inferred surface brightness profiles for D^3He-protons (red) and DD-protons (blue) for OMEGA shot 71551 (Om131121), which imploded a ^3He-gas filled CD shell using 14.6 kJ of laser energy in an 0.6 ns square impulse. The best fit (solid) and $\pm 1\sigma$ uncertainty region (dashed) had model parameters of $(r_{50},p) = (74.0 \pm 0.8,\ 1.71 \pm 0.07)$ for the D^3He protons and $(131 \pm 5,\ 1.22 \pm 0.18)$ for the DD-protons. Both profiles are centrally peaked. (inset) The recorded aperture images for D^3He-protons (top) and DD-protons (bottom).

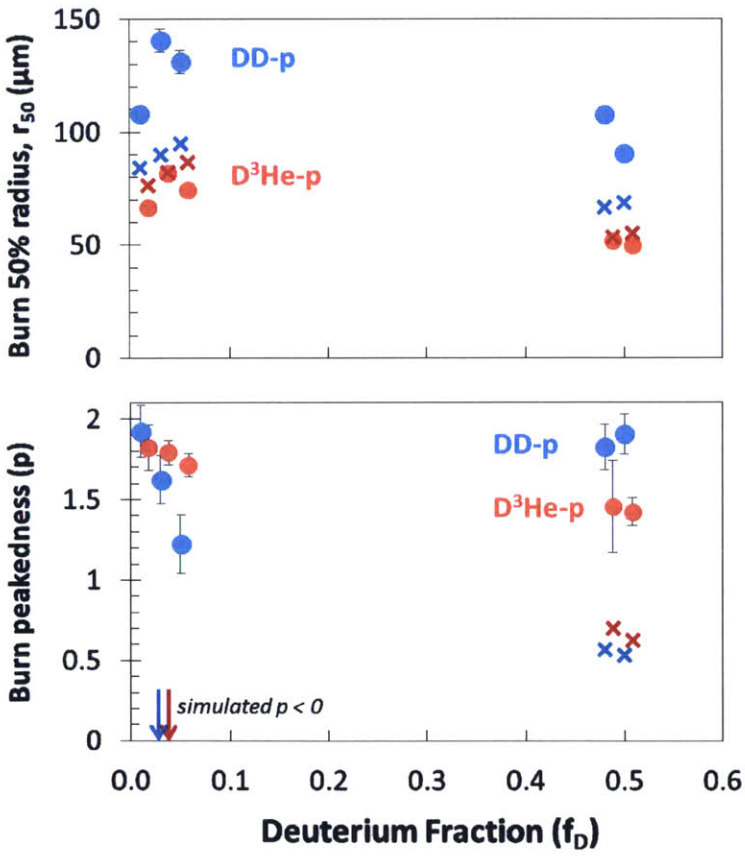

Figure 3.8. Measured (points) and simulated (x) burn profile parameters for DD-protons (blue) and D^3He-protons (red) from thin-CD implosions: (top) 50% burn radius, and (bottom) peakedness of the burn profile. Data were inferred from penumbral nuclear images recorded using the PCIS instrument. Points have been spread out in f_D for clarity, and uncertainties are comparable to the size of the point where not shown. Note that pure ^3He simulations included isobaric trace ^3He in the CD shell to produce a diagnostic signature. The burn radii for D^3He-protons appears to be in good agreement with the simulations, while the DD-neutron burn radii are significantly larger. Comparing the shape, the data are centrally peaked ($p > 1$) for all cases, whereas the simulations are flatter ($p \sim 0.7$) for $f_D = 0.5$ and have a hollow profile ($p < 0$, not shown) for $f_D = 0$.

Two features stand out in the data. Firstly, the profiles are observed to be centrally peaked ($p > 1$) for both species and all experiments. This is in dramatic contrast to the simulations, which predict flatter burns for the 50:50 D^3He fill ($p \sim 0.75$) and hollow burn profiles for the pure ^3He fill ($p < 0$, not shown in the graph). The centrally-peaked profiles strongly indicate that deuterium has mixed deeply into the pure ^3He fuel prior to burn. Secondly, the absolute size of the D^3He-proton burn region is well-modeled by the simulations, while the DD-proton burn region is measured to be a factor of 2× larger than the simulations. This result is somewhat unexpected, as most of the DD-neutron yield is expected to be produced by the shell. This is possible evidence of undercompression of the capsule, or underperformance of the fusion production at smaller radii.

3.3.5 Time-resolved x-ray imaging

An x-ray framing camera (XRFC1) was used to obtain time-resolved images of x-ray emission from the 23 and 14 kJ implosions.[27] This system has four independently-timed strips, each of which consists of a gold-coated photocathode which produces electrons when struck by x-rays, a microchannel plate (MCP), and a phosphor which is connected to either a film pack or a CCD camera by fiberoptics. When each strip is triggered, a voltage impulse (~1 kV) travels across that strip in approximately 200 ps. The electrons produced by the photocathode when the voltage impulse passes are accelerated through the MCP and excite the phosphor, the emission of which is recorded. Several pinholes positioned between the photocathode and TCC image the emission of the target onto the strips, which then provide a time-resolved record of x-ray emission.

An example of the XRFC data recorded on shot #71547 is shown in Figure 3.9. For these studies, a 4x4 pinhole array was used, projecting four images onto each strip, and the camera imaged the implosion with a magnification of 6. Each individual pinhole had a diameter of 10 μm. The images were filtered by 4 mils of beryllium, which limits the incident x-ray photon energy to greater than ~2 keV.[28] In the figure, the trigger time of the strips increases from top to bottom, and on each individual strip time increases from left to right. The relative timing of the strips is controlled by the operator, and can be changed from shot to shot: here, strips 2, 3 and 4 were delayed by 250, 500, and 700 ps relative to strip 1, respectively. The images on a single strip are separated by approximately 60 ps.

Several notable features stand out in this data. The first image on strip 1 is dim and increases in brightness from left to right: this image captures the laser turning on. A circular shell structure is clearly seen in the emission until the middle of strip 3, although it becomes increasingly blurry beginning on strip 2. This blurriness is related to the burn-through of the shell, which is predicted to occur around 500 ps. Near the end of strip 3, the shell limb disappears: this is around shock bang-time, and is likely due to increased self-emission from the hot core. On strip 4, the implosion reaches peak compression and begins to expand. The images remain highly circular throughout the implosion, and no asymmetric features are seen near peak compression. This stands in contrast to x-ray self-emission data recorded on high-convergence, compressively-driven implosions, which indicate highly 2D shapes, as well as blobs of bright emission which suggest chunks of cold shell material penetrating into the hotspot. The mounting stalk can be seen as a feature in the lower left quadrant of the images. While the stalk is clearly visible, it does not appear to significantly perturb the circularity of the implosion: no 'jet' features are observed.

The radius of the limb in each image was analyzed to quantify the trajectory and symmetry of the implosion. An outside contour at close to maximum brightness was found, and then fit using Legendre polynomials up to second-order modes to obtain the radius. An example of the resulting trajectory is shown in Figure 3.10, analyzed from the raw data shown in Figure 3.9. The data shown is typical of the series: no clear difference was observed between D_2- and D^3He-gas

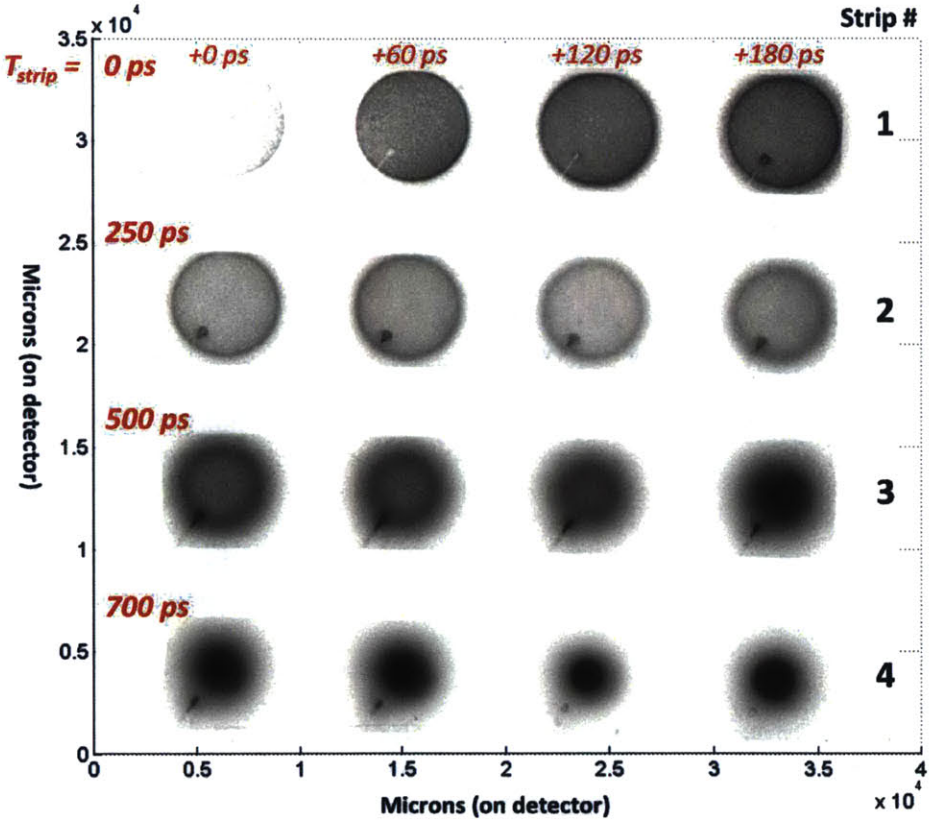

Figure 3.9. Example of x-ray framing camera (XRFC) images from OMEGA shot #71547, a thin-CD implosion filled with pure ^{3}He gas. Time increases from left to right and top to bottom. The timing of each strip, and the relative timing of each image within the strip, is shown in red. Interesting features include: the laser turning on in strip 1, image 1; the circular limb of the imploding shell, which disappears or is overwhelmed by core emission in strip 3, image 4; and the fill tube in the lower-left quadrant of each image. Axes units are in microns, at the detector: the camera was set up with a magnification of 6x.

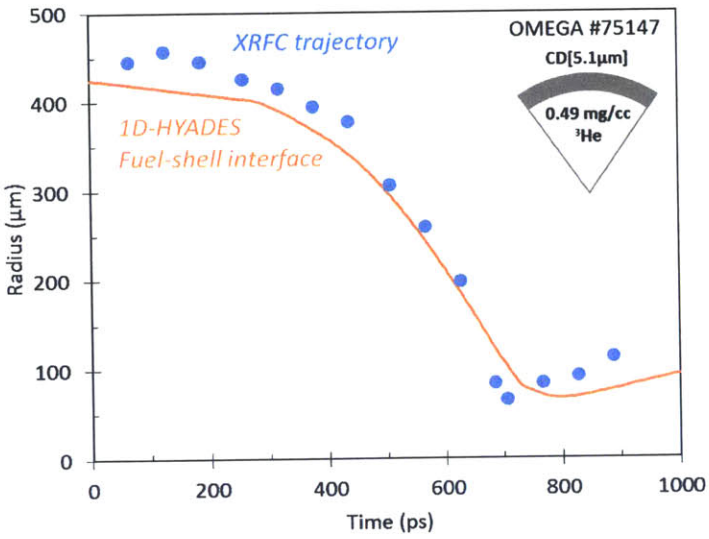

Figure 3.10. Trajectory analysis from the XRFC data recorded on OMEGA shot #71547 and shown in Figure 3.9. Legendre polynomials up to mode 2 were fit to the limb contour to obtain the radius in each image (blue points). For comparison, the 1D-HYADES simulated radius of the fuel-shell interface is shown (orange).

filled implosions. This trajectory is compared to the simulated trajectory of the fuel-shell interface from 1D-HYADES simulations of the implosion. While this is not a one-to-one comparison, it is nevertheless instructive. For most of the implosion, the peak x-ray emission should come from outside the fuel-shell interface, as is observed. Around 500 ps, the radius of peak emission comes much closer to the fuel-shell interface. This seems reasonable, as the shell is expected to have burned through at this point, so the densest CD plasma will be at the interface. Finally, near shock-bang time the emission radius appears to be smaller than the fuel-shell interface. Shock rebound will enhance the density and temperature in the core, which will boost core x-ray production. Furthermore, significant 1D-mixing of the fuel and shell near shock bang-time, which was inferred from the nuclear data, would lead to enhanced emission at smaller radii. The fact that the images at this time do not have a clear limb is also suggestive of substantial mix, as the carbon-rich parts of the plasma are expected to be the strongest emitters. This analysis also confirms the spherical nature of the implosions: at no point during the implosions does the 2nd Legendre mode exceed 5% of the radius, and is typically within the measurement uncertainty of symmetrical.

In summary, the x-ray framing camera images recorded on these implosions demonstrate that the implosions evolve in a highly 1D-manner, and may provide additional evidence for significant mix of the fuel and shell prior to shock bang-time. In future experiments it might be beneficial to include a tracer layer by doping the inner surface of the shell with trace amounts of a high-Z element. The line emission from this dopant could be used to track the fuel-shell interface directly, and the brightness of emission would provide an independent measurement of mix. Ongoing work by M. Rosenberg, et al. to study the relationship between x-ray images and fusion product emission images will also provide valuable insight into the core structure of the implosion.[29]

3.4 Models of Hydrodynamic Instability Growth

The impact of hydrodynamic instabilities – including Rayleigh-Taylor (RT) instability and Richtmyer-Meshkov instability at the fuel-shell interface – on these implosions has been shown to be negligible. Hydrodynamic growth principally occurs in the ablation front, where it is seeded by capsule surface

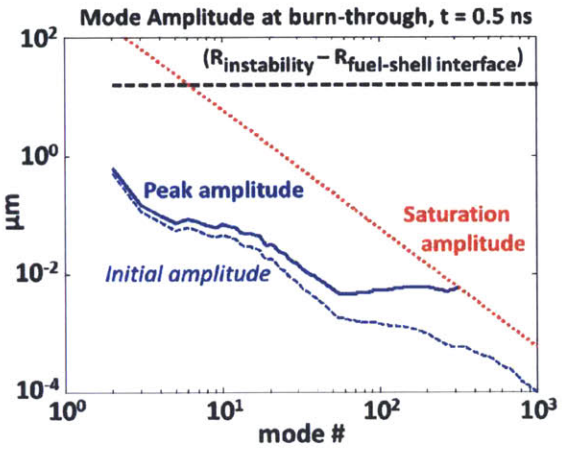

Figure 3.11. The expected amplitude of perturbations at the ablation front at shell burn-through (t $\approx$ 0.5 ns) as estimated from 1D-simulations. Atomic-force microscopy measurements of the capsule roughness were used for initial amplitudes (blue dashed). At burn-through, all non-saturated modes (blue solid) are at least an order of magnitude smaller than the distance between the region of peak instability and the fuel-shell interface (black dashed). Modes above $\ell \sim 300$ reach the saturation amplitude (red dotted).

roughness and laser imprint, and during the deceleration phase. This section addresses and rules out instability growth during both of these periods as a driver of the significant fuel-shell mix observed in these experiments, using analytical arguments and 1D- and 2D-hydrodynamic simulations.

3.4.1 Ablation front mode growth

The RT instability growth at the ablation front early in time, which is seeded by initial capsule surface roughness, was studied and found not to significantly impact the implosions. Initial surface mode amplitudes were measured by Atomic-Force Microscopy (AFM). The RMS peak amplitude of the initial surface roughness is 0.56 μm, including modes $\ell = 2$ to 1000. This value is dominated by low-order modes: the RMS amplitude is reduced to 0.15 μm for modes $\ell > 5$. Simulated 1D profiles were used to determine the time-dependent Atwood number $\mathcal{A} = (\rho_h - \rho_l)/(\rho_h + \rho_l)$ and local acceleration a. For each timestep in these simulations, the unstable region was identified using the general instability condition $\nabla P \cdot \nabla \rho < 0$,[30] and the maximum growth rate for each mode $\gamma(t, \ell) = \sqrt{\mathcal{A}(t)a(t)k(\ell)}$ was determined, where k(ℓ) is the wavenumber of the mode.[d] Using the measured power spectrum and simulated peak growth rate at each time step, the expected amplitude at time t for modes up to 1000 was estimated as the initial amplitude multiplied by the growth factor $\prod_0^t \exp[\gamma(t_i)\Delta t_i]$. The peak mode amplitudes at burn-through are shown in Figure 3.11, at which time they reach a maximum RMS value of 0.69 μm. Modes above $\ell \approx 300$ have exceeded the regime of linear growth as defined by the Haan saturation criterion.[31] Assuming full atomic fuel-shell mixing, this amplitude is an order of magnitude smaller than the approximately 10 μm mix layer that will be shown to be necessary to explain the data. Central to this discussion is that this treatment overestimates the expected growth, as it does not account for the stabilizing effect of the ablation velocity.[4]

The shock breakout through the fuel-shell interface does not drive significant amounts of mix due to the Richtmyer-Meshkov (RM) instability. The RM instability grows linearly with time as $\eta_0(1 + k(\Delta v)\mathcal{A}t)$, where η_0 is the seed amplitude, k the wavenumber, Δv the change in velocity due to the shock, and $\mathcal{A}$ the Atwood number defined in Equation 3.1.[32] Initial roughness of the inner surface is less than or equal to the roughness of the outside of the capsule,[33] which was measured using Atomic Force Microscopy (AFM) and had an RMS amplitude less than 0.6 microns.

[d] This is the classical RT growth rate. In the ablation front, the RT growth rate also includes the effect of a finite density gradient, which reduces the growth rate of short wavelength modes, and the effect of ablation velocity, which reduces the growth rate for all modes and can fully stabilize the instability for short wavelengths.[30] By not including these stabilizing terms, this analysis provides an upper bound on the expected instability growth.

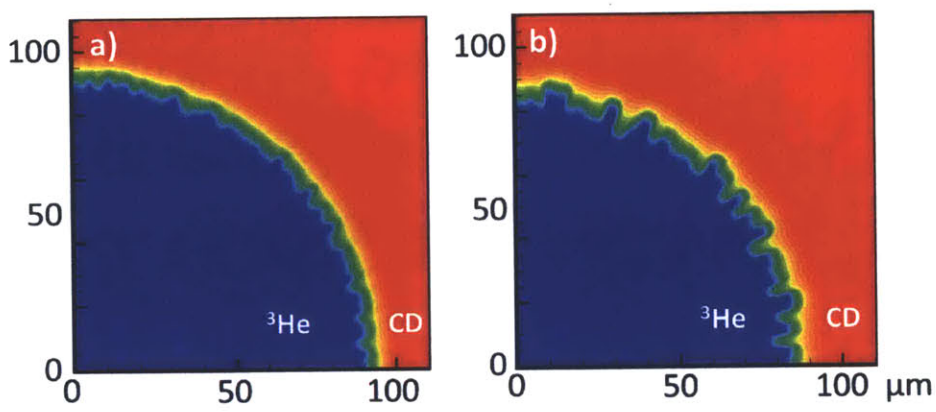

Figure 3.12. Atomic distribution of CD and ^{3}He from 2-dimensional, multi-mode DRACO simulations a) when the rebounding shock strikes the fuel-shell interface and b) near peak compression. Blue indicates pure ^{3}He; red, pure CD. Simulations show negligible development of perturbation modes prior to reshock of the fuel-shell interface, and little growth thereafter. The maximum penetration depth of shell material into the gas is approximately 10 μm, or approximately 15% of the fall-line depth. Simulations courtesy of Jacques Delettrez, LLE.

Evaluating the expected peak amplitude of RM growth by shock bang-time in this experiment, the RMS peak amplitude is less than 1 micron, which is insufficient to reproduce the observed yields assuming full atomic mix. Additionally, the shock breakout is immediately followed by a period of strong inward acceleration, which will further stabilize RM growth.[6]

3.4.2 2D DRACO simulations

To investigate the growth of hydrodynamic modes in detail, multi-mode 2D-DRACO simulations[34,35] were performed as shown in Figure 3.12. In these simulations, which explored modes up to $\ell = 150$ and included the effect of laser imprint, instability growth at the fuel-shell interface was negligible through shock rebound. In addition to the discussion above, the large ablation velocity (approximately 10 μm/ns) likely stabilizes the growth of ablation-front instability. After the shell burns through at 0.5 ns, no steep gradients remain where the Atwood number is large and the ablation-front instability growth is truncated.

During the deceleration phase of the 2D-DRACO simulations, instabilities grew to a spike penetration distance of approximately 10 μm (see Figure 3.12b), which is less than 15% of the minimum shell radius. A useful reference value for the penetration distance is the "fall line," defined as the projection of the fuel-shell interface location if it were to continue imploding at its peak velocity rather than decelerate. A simulation of the fall-line and fuel-shell interface position versus time is shown in Figure 3.13a. In a hydrodynamic model of the implosion, the fall-line represents the farthest that shell material can penetrate into the gas at any given time.[36,37] A physics-based mix model describing penetration of shell material to a fraction of the fall-line depth was employed, assuming full atomic mixing of shell and fuel in the mix region.[38] This fall-line analysis is unable to recreate the observed yields. Comparing the <15% penetration fraction observed in 2D-DRACO simulations to the fall-line analysis as shown in Figure 3.13b, the D^{3}He-proton yields predicted by these hydrodynamic methods are approximately an order of magnitude lower than observed.

This inability to generate the observed yields even when positing a worst possible case of hydrodynamic mix stems from the fact that in these experiments, hydrodynamic mix is introduced

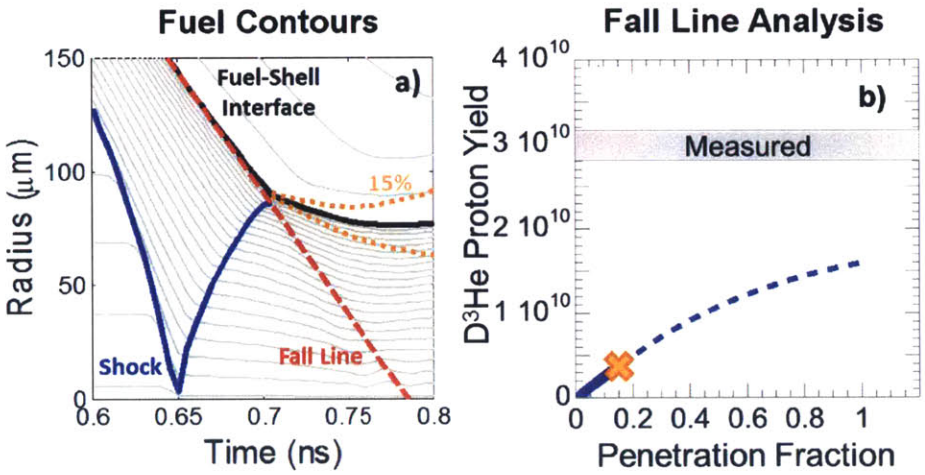

Figure 3.13. a) Lagrangian mass-element trajectories from a 1D simulation of these experiments. The fall-line (red dashed), a tangent projection of the fuel-shell interface (black solid) at peak velocity, represents the furthest distance hydrodynamic shell mix could penetrate into the gas. b) A fall-line mix model, in which hydrodynamic mix penetrates to a fraction of the fall-line distance from the fuel-shell interface ('penetration fraction'), was unable to reproduce the observed D^3He-proton yields, even in the physically unreasonable worst-case scenario of penetration fraction = 1. Multi-mode 2D-hydrodynamic simulations of these experiments (Figure 3.12) predict a penetration fraction of 15% [a) orange dotted line, b) orange x], corresponding to roughly an order of magnitude less yield than was observed. Fall-line yield analysis in b) courtesy of Peter Amendt, LLNL.

only during the deceleration phase, after peak shock burn. To generate the high values of yield observed, the mix must be established prior to shock burn. This temporal selection makes such shock-driven implosions an excellent testbed for physics impacting ICF implosions prior to the deceleration phase.

3.5 Ion Diffusion

It has been shown that hydrodynamic growth processes are insufficient to explain the observed yields in these experiments, which implies that another mechanism or mechanisms for mix must be dominant. Ion diffusion provides one driving mechanism for atomic mix at the fuel shell interface in these experiments that is sufficiently strong to generate the observed yields.

The fuel-shell interface introduces a boundary in partial pressure, such that it is entropically favorable for deuterium, carbon, and ^{3}He ions to diffuse across it. As introduced in Section 1.2.2, classical atomic diffusion will occur at this boundary at a rate governed by the ion species concentration gradient: $j_k = -D\nabla n_k$, where D is the classical diffusion coefficient:[39]

$$D = (\langle Z \rangle + 1)\, k_B T / \langle A \rangle \nu_{kl}, \tag{3.7}$$

$\langle Z \rangle$ and $\langle A \rangle$ are the local average charge state and ion mass, and ν_{kl} is the collision frequency of ion species k with all species $l \neq k$. For classical (concentration gradient-driven) diffusion, the diffusion coefficient scales as $T^{5/2} n^{-1}$. At the fuel-shell interface, shell material is predicted to be cold (30 eV) and dense (10^{22} cm^{-3}), implying a small diffusion coefficient ($D \sim 8$ μm^2/ns, calculated for shell deuterium in ^{3}He) prior to shell burn-through, which occurs at approximately 0.5 ns in these experiments. After shell burn-through the temperature at the fuel-shell interface

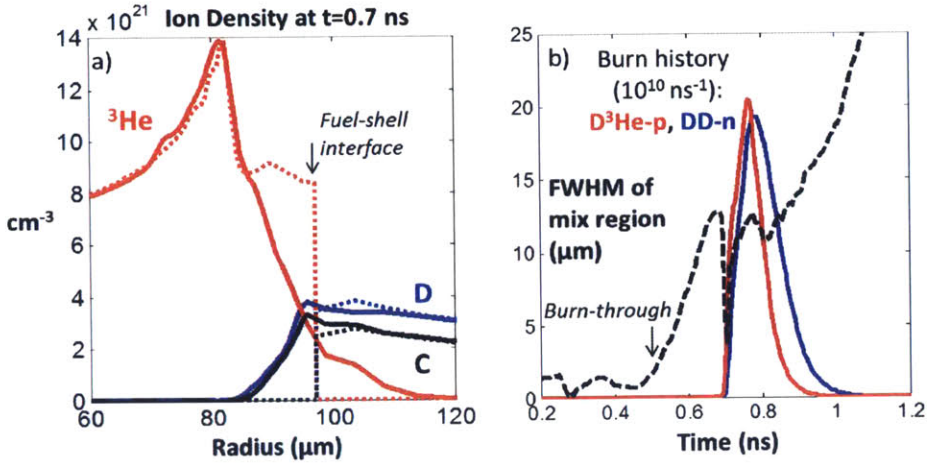

Figure 3.14. a) Ion density profiles from 1D simulations of a thin CD experiment, just prior to the rebounding shock passing through the fuel-shell interface. Dotted curves show the raw hydrodynamic output with no diffusion; solid curves show the same simulation post-processed with a classical ion diffusion model. The D^3He-proton yield generated from the ion-diffusive mix layer is within a factor of 2 of the observed yield. b) Full-width at half-maximum of the mix region (black dashed) and nuclear burn rate for DD-n (blue) and D^3He-p (red) as a function of time in the post-processed ion-diffusion simulation. The thickness of the mix region rapidly increases after shell burn-through (0.5 ns), exceeding 10 μm just prior to shock burn (0.7 ns).

increases rapidly to ~1 keV while the density drops to a few 10^{21} cm^{-3}, driving much more rapid diffusion: D reaches $\sim 4 \times 10^4$ $\mu m^2/ns$ in the ~200 ps before shock burn, with a time-averaged value of $\sim 4 \times 10^3$ $\mu m^2/ns$. Using the solution for Fick's law in a planar slab as an approximation to the spherical case, the depth of the mix layer grows as $\sqrt{4Dt}$, and the depth of deuterium mix into the ^3He is expected to be on the order of tens of microns.

Simulations of the experiments performed with the 1D-radiation-hydrodynamics code HYADES[19] were post-processed using this formalism to determine the impact of classical atomic diffusion on ion density profiles. The ion density flux at each zone boundary was calculated while conserving ion number globally; the pressure and temperature profiles were not modified. Ion flux at each timestep was limited to 10% of the ions in the source zone to prevent numerical instability. Figure 3.14 shows that by shock bang-time, a mix layer with a full-width at half maximum in excess of 10 μm is expected to develop at the fuel shell interface. The simulated yield from this mix layer is approximately 70% of the observed values. The total amount of mixed deuterium in this simulation is 15% of the total ^3He, within a factor of a few of the earlier estimate in Equation 3.4.

The effect of ion diffusive mix is predicted to be much less significant for implosions filled with 50:50 D^3He, for which simulated DD-neutron and D^3He-proton yields vary by less than 5% when the ion-diffusion post-processing is applied. After shell burn-through the deuterium density is comparable in the 50:50 D^3He fuel and the remaining CD plasma, so the partial pressure gradient driving deuterium diffusion vanishes. This finding supports the assumption that mix is negligible in the D^3He implosion which was used to estimate the approximate amount of deuterium mix.

In plasmas with multiple ion species, the diffusion rate will also include terms associated with gradients in pressure, temperature, and electric potential.[39,40] These sources may further enhance atomic mix as shocks traverse the fuel shell interface. A 1D radiation-hydrodynamic simulation incorporating an integrated ion-diffusion model based on the formulation of R.W. Schunk in Reference [41], which includes pressure and electron-pressure gradient terms, was used to simulate the 30 kJ, ^3He-filled experiments. This model generated D^3He proton yields approximately 2× the

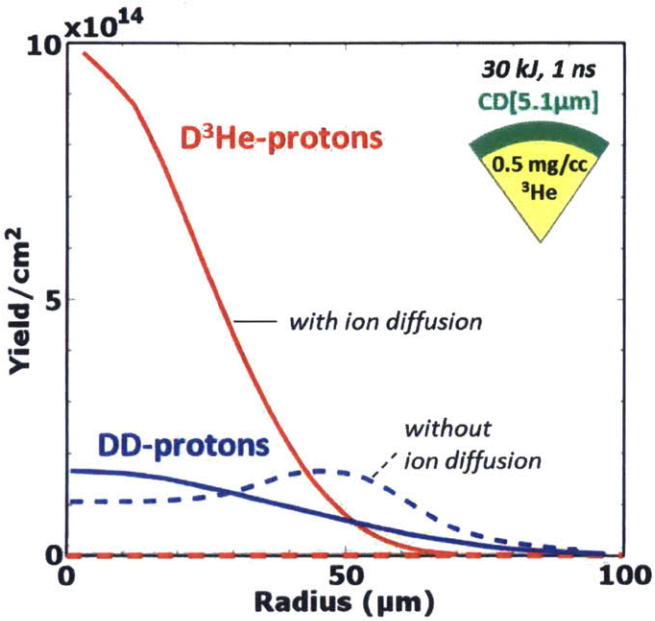

Figure 3.15. Simulated surface brightness profiles for D^3He-protons (red) and DD-protons (blue) based on OMEGA shot 65278 (Om120307), which imploded a ^3He-gas filled CD shell using 30 kJ of laser energy in an 0.6 ns square impulse. Simulations performed without an ion diffusion model (dashed) produce a 'hollow' profile that is peaked off-axis. Simulations performed including an ion diffusion model (solid) produce centrally peaked profiles for both reactants, in agreement with the data shown in Figure 3.7. Simulations courtesy of Peter Amendt.

Table 3.3. Parameters for the Reduced Ion Kinetic (RIK) simulations, calibrated to a subset ("4-shot") and the entire set ("8-shot") of results from thin-glass implosions performed on March 14th, 2013, spanning the pressure range for the initial gas fill of the thin-CD experiments.

	f_{ls}	f_e	f_{Knu}	f_{idifm}	f_{icndm}	f_{mix}
4-shot	0.63	0.06	0.1	0.3	2	0
8-shot	0.63	0.06	0.1	0.1	4	0

observed yields. Using the same code to simulate a 20-μm thick CD shell under the same laser and gas fill conditions resulted in negligible mix at shock burn and a D^3He-proton shock yield four orders of magnitude smaller than the thin CD shell case. Since the thick CD shell does not burn through during the implosion, the fuel-shell interface remains cold and dense: the average diffusion coefficient of shell deuterium into the ^3He is estimated to be $D \sim 5$ μm^2/ns over the 1.6 ns prior to shock burn. This value is three orders of magnitude smaller than the value in the thin-shell case, and the estimated depth of the mix layer generated by diffusion is ten times smaller. Ion diffusion therefore provides an explanation for the high shock yields in these experiments that is consistent with the observed lack of mix at shock yield in thick-shelled experiments.[9]

Surface brightness profiles from the 1D-radiation hydrodynamic simulations run both with and without an integrated ion diffusion model are shown in Figure 3.15. The clean simulations predict a 'hollow' profile that is peaked off-axis, which is inconsistent with the measured data shown in Figure 3.7. The simulations including an ion diffusion model produce centrally peaked surface brightness profiles, in agreement with the measured data and supporting the hypothesis that ion diffusion transports deuterons deep into the core of these implosion.

Table 3.4. Comparison of observed yields and temperatures (Obs) with 1D fluid-based simulations including Reduced Ion Kinetic (RIK) models, and the same simulation code with the kinetic models turned off (clean). For the RIK simulations, two sets of model calibration parameters were applied and the results were averaged; the uncertainty indicates the variation between the two sets of parameters. The particular experiments simulated were the 30 kJ implosions 65273 (f_D=1), 65275 (f_D=0.5), and 65278 (f_D=0). RIK simulations provided by Nels Hoffman, LANL.

f_D	DD-neutrons ($\times 10^{10}$)			D^3He-protons ($\times 10^{10}$)			$\langle T_i \rangle_{DD}$ (keV)		
	Obs	RIK	clean	Obs	RIK	clean	Obs	RIK	clean
1.0	7.4±0.7	10±4	34	—	—	—	16.3±0.5	14.6±1.0	17.8
0.5	3.7±0.4	3.0±0.5	6.9	3.8±0.2	2.7±0.1	10	15.5±0.5	13.2±0.7	16.1
0.0	1.5±0.2	1.1±0.1	2.2	3.0±0.2	1.8±0.4	10^{-4}	13.8±0.5	11.7±0.6	12.8

3.5.1 Reduced Ion Kinetic modeling

A simulation technique incorporating reduced ion-kinetic (RIK) models in a 1D fluid-based radiation-hydrodynamic code was applied to the 1 ns implosion experiments.[e] The RIK simulation method was developed by Nels Hoffman, LANL, who also provided the simulated results shown here. The RIK models represent the effects of kinetic transport of ion mass (ion diffusion) and energy (ion thermal conduction), as well as the reduction in fusion reactivity due to loss of energetic Maxwellian-tail ions (Knudsen-layer depletion).[42,43] Each of the three kinetic models includes a single free parameter: f_{idifm}, f_{icndm}, and f_{Knu}, respectively. Including also the laser absorption fraction (f_{ls}), electron flux limiter (f_e), and a 1D-model of turbulent (i.e. hydrodynamic) mixing (f_{mix}), the full model has six free parameters. These model parameters were calibrated to a subset (four shots) and the entire set (eight shots) of thin glass-shell D^3He implosion data recorded in OMEGA implosions on March 14th, 2013, as described in Reference [26], resulting in the parameters shown in Table 3.3. These calibration implosions had a comparable initial gas density to the implosions discussed here. It is worth noting that no non-zero level of the turbulent mixing parameter f_{mix} was consistent with the trends in the data: this parameter was set to 0 in both the 'four-shot' and the 'eight-shot' calibration models. Both calibrations were applied to simulations of the thin-CD implosions discussed here, and the average and variance of these results is presented in Table 3.4, along with the observed values for those shots. The RIK models capture the trends of the observed yields and ion temperatures much more accurately than the clean simulations (Figs. 3.4 and 3.5), and produced 60% of the observed D^3He-proton yield for the pure ^3He implosion (#65278).

The effects of each of the three RIK models on the simulations is presented in Figure 3.16, which shows the measured data plotted as a function of deuterium fraction in the fuel, compared to simulations run with the three RIK models turned on sequentially. The 'four-shot' calibrated parameters were used for this study. Of the three RIK models, only the ion diffusion model introduces the ion mass transport necessary for generating significant D^3He-proton yield from a pure ^3He implosion. With the ion kinetic parameters turned off (the 'clean' simulation in Fig. 3.16), the D^3He-proton yield from the pure ^3He implosion dropped to $\sim 10^6$.[f] Including ion diffusion in the simulations, the trend of the data is captured for both D^3He-protons and DD-neutrons. It is noteworthy that in addition to reproducing the observed high D^3He-proton yields for pure ^3He fuels ($f_D = 0$), the ion diffusion model also reproduces the observed low DD-neutron yields for pure deuterium fuels ($f_D = 1$). These features strongly support the ion diffusive explanation of

[e]These simulations used artificial viscosity, and did not include a physical viscosity model.

[f]The D^3He-proton yield produced in this case is from in-flight reactions of 0.8 MeV ^3He produced by DD-fusion with plasma deuterons in the CD plasma.

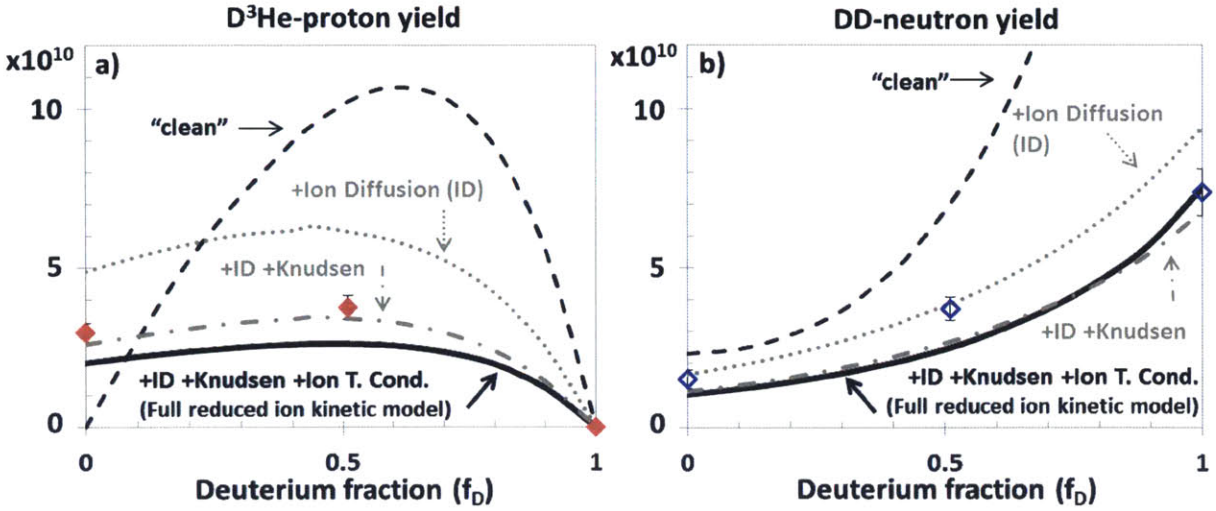

Figure 3.16. Measured a) D^3He-proton (red points) and b) DD-neutron (blue points) yields as a function of deuterium fraction and ^3He fraction ($f_D = 1 - f_{^3He}$), compared to a simulation including Reduced Ion Kinetic (RIK) models (thick line) and 'clean' simulations (thin dashed). The RIK simulation shown was calibrated to four D^3He-filled thin-glass implosions with comparable fuel density. The individual effects of the three RIK models (ion diffusion, Knudsen reactivity reduction by tail-ion loss, and ion thermal conduction) are evaluated by turning the models on one at a time. Ion diffusion (grey dotted) recaptures the observed trends in the data; Knudsen tail-ion loss (grey dot-dash) brings the simulated yields closer to the measured yields. Ion thermal conduction has a smaller effect in these simulations, compared to the other two models. RIK simulations provided by Nels Hoffman, LANL.

the observed data. Knudsen-layer reactivity reduction and ion thermal conduction both reduce the yields, better capturing the absolute yields measured; reactivity reduction is predicted to be the stronger of these two effects.

These findings indicate that ion diffusion, a kinetic plasma effect, plays an important role in these experiments, and imply that such effects must be considered in plasma systems containing comparable temperatures, densities, and gradients. In ignition experiments, the fuel-shell interface remains at low temperature and high density throughout the implosion, and ion diffusion is not expected to significantly contribute to fuel-shell mix. However the initial shock in the central gas of ignition targets generates temperatures and densities comparable to those in exploding pusher implosions. Modifications to the shock profile due to differential ion species diffusion could result in changes to the fuel adiabat and alter the initial conditions for compression and burn.[44] Diffusion and other kinetic effects may also affect the transfer of mass from the cold DT fuel into the hotspot during compression. However ion diffusion has not previously been studied in high-energy-density experiments. The results of these experiments will contribute to the calibration of ion diffusion models, such as the RIK models discussed above, to further explore the impact of such effects on ignition experiments.

3.6 Alternative Kinetic Explanations

It has been shown that a non-hydrodynamic mechanism is required to explain the results of these experiments, and ion diffusion has been proposed as one possible explanation. Between shell burn-through ($\sim$ 500 ps) and shock bang time ($\sim$ 700 ps), the temperature of the plasma at the fuel-shell

interface increases by over a factor of 10 while the density drops, increasing the rate of diffusion dramatically. In simulations including a model of ion diffusion, an approximately 10 μm wide mix region forms prior to shock bang time, which upon reshock generates yields comparable to those observed. However, the initial promise of this ion diffusion model does not rule out the possibility that other kinetic mechanisms may play an important role in these experiments. Several other kinetic mechanisms have been investigated to determine which are possible contributors to the observed results.

Shock acceleration of deuterons

A mechanism mediated by electric fields at the shock front has been investigated as a possible contributor to the enhanced D^3He-proton yield observed in these experiments. Strong electric fields in the shock front[45] will accelerate a population of fast, directional deuterons ahead of the shock. This shock reflection mechanism is similar to the shock unloading or vaporization at a material-gas interface in weak-shock scenarios,[46] and has been studied previously in simulated collisionless[47,48] and collisional shocks.[49] Recently, fully-kinetic simulations of shocks breaking out across fuel-shell interfaces have shown that, in some cases, this mechanism is capable of introducing significant mix of light shell ions into the fuel.[15]

Strong local electric fields E(x) on the order of 10^9 V/m have been observed near shock fronts in ICF implosions using proton deflectometry.[50,45] These fields generate an electric potential barrier:

$$\Phi = -\int_0^x E\,(x)\,dx, \tag{3.8}$$

which will reflect deuterons lacking sufficient kinetic energy to surmount it. Electron diffusion across the shock front is expected to dominate electric field generation in these experiments, producing potentials on the order of the post-shock electron temperature, $\Phi \approx T_e/e$.[51] The electron pressure gradient will be used in these calculations to infer local electric field $E(x) = -\nabla P_e/n_e e$, for comparison of the appropriate scale for Φ, although it is approximately an order of magnitude weaker than the expected source from electron diffusion. This difference is a consequence of the shock not being in a steady state due to continuing laser drive.

The fraction of deuterons accelerated is most readily assessed in the reference frame of the shock front. In this frame, inflowing deuterons have velocity $v_x = (\vec{u}_{shock} + \vec{v}_{th})|_x$. Reflected deuterons will satisfy the condition $0 < v_x < \sqrt{2Ze\Phi/m}$, or translating back into the lab frame, $-u_{shock} < v_x < \sqrt{2Ze\Phi/m} - u_{shock}$. Integrating the distribution function over this range of velocities gives the fraction of deuterons that will be accelerated by the shock. For a Maxwell-Boltzmann distribution, this is given by:

$$f_{acc} = \frac{1}{2}\left[\mathrm{Erf}\left(\frac{\sqrt{2Ze\Phi/m} - u_{shock}}{v_{th}}\right) - \mathrm{Erf}\left(-\frac{u_{shock}}{v_{th}}\right)\right], \tag{3.9}$$

where $v_{th} = \sqrt{2T/m}$ is the thermal velocity of deuterons upstream of the shock front. The accelerated fraction is plotted in Figure 3.17, as a function of u_{sh} and $\sqrt{Ze\Phi}$ appropriately normalized to v_{th}. For a given v_{th} and $u_{sh} \gg v_{sh}$, the accelerated fraction is maximized when $Ze\Phi = 2mu_{shock}^2$, and falls off rapidly for $Ze\Phi < mu_{shock}^2/2$. In general the accelerated fraction will be larger when v_{th} is small compared to the terms in the numerator, though the maximum accelerated fraction is above 80% when v_{th} equals the shock velocity.

It is important to note that this formalism neglects collisions of the reflected deuterons within the shock front. Such collisions have been shown to inhibit reflection of deuterons with short mean-

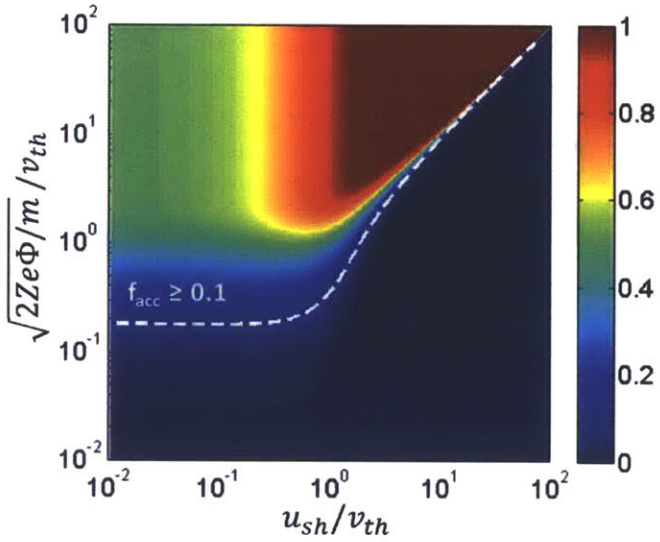

Figure 3.17. The fraction of accelerated ions (color scale) as a function of shock speed u_{sh} and the electric potential limiting speed $\sqrt{2Ze\Phi/m}$, normalized to the thermal velocity v_{th}. Substantial acceleration ($f_{acc} \gtrsim 10\%$, shown in the figure as the region above white dashed line) requires the electric potential limiting speed to be greater than ~18% of the thermal velocity, but less than the shock speed.

free-paths, reducing the reflected fraction.[15] However the large gradients present at the shock front and the dynamic nature of the reflection effect complicate a full collisional estimate. This derivation provides an upper bound for the reflected population, and a worst-case scenario in terms of the expected mix.

Figure 3.18 shows the plasma ∇P_e-induced electric potential near the time of shock breakout (270 ps) as calculated from 1D HYADES simulations. At this time, $u_{shock} \approx 115$ μm/ns, $\Phi_{\nabla Pe} \approx 0.1$ kV, $\Phi_{Te} \approx 1.6$ kV. The CD plasma in front of the shock is not fully ionized, with $T_e = T_i \approx 30$ eV, $\langle Z \rangle = 1.5$, and ion density on the order of 10^{21} cm^{-3}.[g] Applying Equation 3.9 to this plasma determines that 36% of the pre-shock deuterons are expected to be accelerated by the potential $\Phi_{\nabla Pe}$, as shown in Figure 3.18. If the potential scales with the much stronger Φ_{Te} as is expected, then 99% of the pre-shock deuterons will be accelerated by this process.

Shock-accelerated deuterons within a mean-free-path of the fuel-shell interface will stream into the ^{3}He gas. Using a model for scattering in strongly-coupled plasmas,[52] the mean-free-path λ_{MFP} for deuterons traveling at $2u_{shock}$ through the plasma conditions described above is approximately 3 μm. The expected number of deuterons kinetically mixed into the ^{3}He gas is calculated to be $f_{acc} n_D \left(4\pi R^2\right) \lambda_{MFP} \approx 3 \times 10^{15}$, assuming 99% reflection. This is approximately 10% the number of ^{3}He atoms in the fuel.

The mean-free-path for these reflected deuterons in the unshocked ^{3}He plasma is approximately 3 microns. This value is similar to the mean-free-path in the CD plasma because the ^{3}He is pre-compressed by the blowdown of preheated CD material. Once inside the ^{3}He, the deuterons will thermalize and move with the fluid throughout the implosion and burn. Artificially introducing 3×10^{15} deuterons into the outermost 3 microns of the ^{3}He fuel in the simulations produces of order 10^{10} D^{3}He-protons, comparable to what is observed. This behavior would be expected to produce D^{3}He-proton yield in a narrow spherical-shell region near the fuel-shell interface. Such a 'hollow' burn profile would produce a PCIS signature with $p < 0$, which is ruled out by the burn profile data shown in Figure 3.8. It is worth noting, however, that the shock will continue reflecting deuterons as it passes through the fuel. In the latter scenario, the shock may carry a population of 'surfing' deuterons much deeper into the fuel. If some or all of these deuterons later thermalize

[g] Recall that this model includes the predicted effect of x-ray preheat of the CD, which both heats the inner CD layer and causes it to 'blow down' by 20 μm prior to shock breakout.

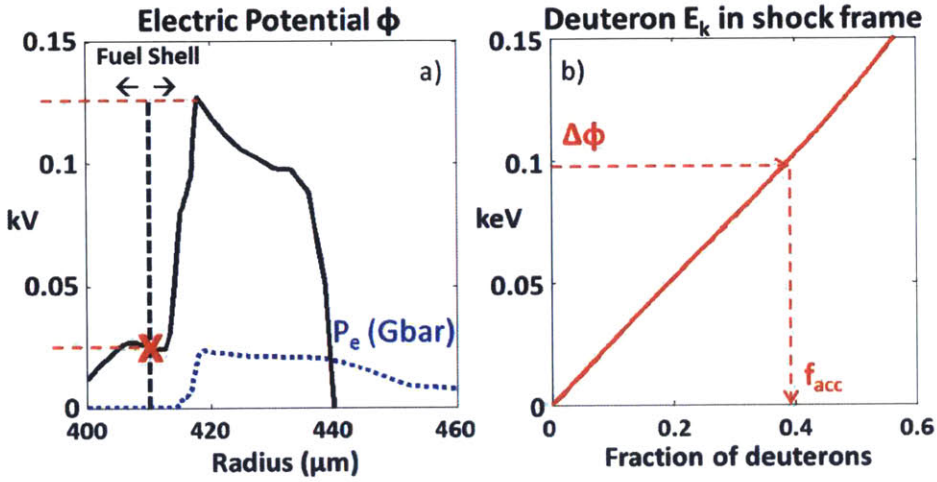

Figure 3.18. a) Radial lineout of electric potential $\Phi_{\nabla P_e}$ inferred from 1D-radiation-hydrodynamic simulations, near shock-breakout from the shell into the ^{3}He fuel (t = 270 ps). The plasma in front of the shock (red x) has T $\sim$ 30 eV and $n_i \sim 10^{21}$. b) The fraction of deuterons in front of the shock below a given kinetic energy in the shock frame. Comparing this curve to the potential jump at the shock front (dashed red line) shows that a large fraction of deuterons (>30%) will be reflected by the shock and launched into the ^{3}He fuel at approximately twice the shock velocity.

volumetrically in the fuel, they will provide a uniform atomic mix background for fusion production at shock bang-time, and a centrally-peaked burn profile, as observed. Since this result can also be produced by sufficiently strong ion diffusion, the current data cannot distinguish between these two scenarios. Future experiments can be designed to have the same laser history through shock breakout (~300 ps), to preserve the behavior of deuteron shock acceleration into the fuel, and then to truncate the laser at shell burn-through (~500 ps), to avoid volumetric ion diffusion. In this scenario, 'surfing' deuterium shock-accelerated mix would present a signature of volumetric burn, and would be measurably different from the weak ion diffusion mechanism, which would present a signature of hollow burn.

Baro-,[39] electro-,[53] and thermo-diffusion[40] at the shock front have recently been studied as a mechanism driving species separation in mixed plasmas. In a CD plasma which has not been fully ionized, pressure, electric-field, and thermal terms are all expected to push deuterium ahead of the shock.[40] If deuterium is pushed ahead of the shock front by these diffusion mechanisms, they would increase the population of deuterium available for acceleration and mixture at the fuel-shell interface.

An upper bound for the amount of shock accelerated deuterium has been calculated to be comparable to the value required to explain the data. Further theory and kinetic simulations are required to estimate how much the accelerated deuteron fraction is reduced from this prediction due to collisionality in the shock front, and to understand the extent to which this mechanism occurs in ignition experiments. However it is clear from these calculations that the strong electric field at the shock front can significantly modify the shock dynamics in these implosions and must be considered.

Beam-target fusion

Another mechanism which has been proposed to account for this data is beam-target fusion, wherein a population of directed ions encounters a plasma containing a reactant species. Several mechanisms

may create such a non-thermal population of radially-streaming ions in these experiments, including shock acceleration as discussed in Section 3.6, insufficient thermalization times for the shocked fuel, and loss of confinement for ions on the thermal high-energy tail due to long mean-free-paths.[42] It will be shown that none of these beam-target mechanisms are expected to produce significant fusion yield in these experiments.

Shock Acceleration The shock acceleration mechanism described previously has been shown to generate a population of deuterons streaming into the ^{3}He fuel. However this population is not sufficiently energetic to generate significant beam-target fusion. In any beam-target scenario, the fusion probability depends very strongly on the velocity of this directional population. The center of mass energy E_{CM} of the collision between ions 1 and 2 is $E_{CM} = E_1 m_2 / (m_1 + m_2) \propto v_1^2$ if species 2 is at rest, and the D-^{3}He fusion cross section is roughly proportional to E_{CM}^3 for $E_{CM} < 150$ keV.[54] At twice the shock velocity, the streaming deuterons carry a kinetic energy of only 0.14 keV; and the collisional center-of-mass energy for these deuterons on static ^{3}He is $E_{CM} = 0.6 E_D \approx 0.08$ keV. This energy is low enough that it is unlikely that any of the accelerated deuterons will fuse with a ^{3}He ion at this stage.

Reflection of ^{3}He ions by the rebounding shock after shock convergence will produce a population of much more energetic ions, as the shock strength and shock velocity increase significantly with spherical convergence. However, the shock acceleration mechanism is less efficient at shock rebound than at shock breakout. The electric field strength due to the electron pressure gradient and electron temperature sources are roughly comparable at shock rebound ($\sim$ 1 keV). The electric field is not magnified by shock convergence, because electron-ion thermal equilibration is on the order of 10 ns at shock rebound, which is long compared to dynamical timescales: for example, the fusion burn duration was measured to have a full-width at half maximum of 180 ps. The shock thermal energy is not transferred efficiently to the electrons and electron temperature remains in the range 3–5 keV. On the basis of Equation 3.9, it is expected that the fraction of shock-accelerated ^{3}He ions is less than 1%.

An approximate fusion yield for this reflected population was calculated based on 1D HYADES simulations. Profiles of density, temperature, and plasma flow velocity in the CD shell and a model of plasma stopping power[55] were used to determine the energy as a function of distance for a ^{3}He ion with known initial energy escaping the implosion. The collisional center-of-mass energy of the ^{3}He ion with thermal deuterons was calculated for each zone, taking into account the background plasma flow, and a parametrized D-^{3}He fusion cross-section model[54] was used to determine the total fusion probability. Assuming 1% of ^{3}He ions are reflected at the shock front and travel at twice the rebound shock velocity, the beam-target fusion generated is approximately 1.4×10^9, which is an order of magnitude below the observed yields.

Simple energetics arguments suggest that explaining the results with a shock-reflected ^{3}He population is implausible. A ^{3}He ion traveling at this speed contains 168 keV of kinetic energy. If 20% of the ^{3}He ions were reflected, as would be required to explain the observed yield using this mechanism alone, this population would contain 160 joules of kinetic energy, which is approximately the total energy delivered to the ^{3}He plasma by the implosion. Even a fraction of this number would begin to significantly drain the energy of the rebound shock, thereby inhibiting further reflection.

Non-thermalized Shock Energy If upon shock convergence the ^{3}He plasma is not fully thermalized due to long thermalization times, the radially inward-directed ^{3}He fluid might directly produce a population of radially outward-directed ^{3}He ions after convergence. At shock convergence, the calculated ion-ion thermalization times are in excess of 1 ns, which is long compared

to dynamical timescales ($\sim$ 200 ps). Such a population would be expected to maintain velocity v_{3He} equal to or less than the fluid velocity behind the incoming shock, v_1. In simulations of these experiments, the mass-average incoming fluid velocity $\langle v_1 \rangle = 1100$ μm/ns just prior to shock convergence, which is approximately 70% of the rebound shock velocity. The center-of-mass energy would thus be $\sim 0.14\times$ that of the shock-accelerated ^{3}He considered above, and the fusion reactivity reduced by a factor of approximately 400. The predicted yield from this mechanism was calculated using the same technique as was used for the shock acceleration mechanism. Assuming all ^{3}He are radially directed outward at $\langle v_1 \rangle$, the predicted yield due to non-thermalized, shocked ^{3}He is less than 1×10^8, over two orders of magnitude lower than the observed yields.

Long Mean-Free-Paths Loss of ion confinement due to long ion-ion mean-free-paths[42] provides another kinetic source of radially-directed, high-energy ^{3}He ions in these experiments. Given the low density and high temperatures produced in the central plasma, the mean-free-path of ^{3}He ions at peak compression are expected to be approximately equal to the radius of the shell at peak convergence. In this scenario, kinetic effects have been shown to play a strong role in the dynamics of fusion yield production.[26] In particular, the mean-free-path of the energetic ions which dominate fusion production is several times longer than the thermal mean-free-path. The energetic ^{3}He ions are free to stream into the remaining CD plasma, where fusion reactions can occur with a probability determined by the collisional center-of-mass energy as the ions slow down.

An upper bound to the total yield generated from this mechanism was calculated by assuming all ^{3}He ions in the plasma are in a thermalized distribution and escape radially into the CD plasma without first slowing on the ^{3}He.[h] The fusion probability was calculated for each initial ion energy as above, and then weighted by the number of ions with that energy in a Maxwell-Boltzmann distribution for the selected ion temperature. This calculation produces approximately 6×10^9 D^{3}He reactions, a factor of 5$\times$ less than the yields observed.

Diagnostic Signatures of Beam-Target Fusion Although it has been shown that these mechanisms are not likely to be strong enough to play a significant role in the experiments, it is worth considering what experimental signatures might be used to differentiate between yield produced by various mechanisms. One signature of a beam-target mechanism would be broadening of the fusion product spectral lines. For thermal plasmas, the fusion spectral line width is Doppler broadened by center-of-mass velocity of the reacting ions, and is roughly proportional to the square root of the ion temperature,[56,57] as described in Section 1.3.1. This effect is exacerbated in the "spherical beam-target" scenario described above, as the center-of-mass velocity of each reaction is radially directed outward from the plasma. Following Reference [57], the observed particle energy of a fusion product from a reaction with center-of-mass velocity V_{CM} is

$$E_1' = \frac{1}{2} m_1' V_{CM}^2 + \frac{m_2'}{m_1' + m_2'} (Q + K) + |V_{CM}| \cos\theta \sqrt{\frac{2 m_1' m_2'}{m_1' + m_2'} (Q + K)}, \tag{3.10}$$

where m' are the fusion product masses, Q is the energy released by the fusion reaction, K is the total kinetic energy in the center-of-mass system ($K \ll Q$), and θ is the angle between the center-of-mass velocity and the direction of the nuclear product. The broadening of the spectral peak is governed

[h]The scenario described is an upper bound, as energy loss by ions escaping during thermalization would prevent such a state from forming. ^{3}He ions are not expected to acquire significantly more energy through collisions than the energy at which $\lambda_{ii} = R_{fuel}$, which in this case is $\sim$ 20 keV: well below the energies expected to dominate fusion reactions.

by the (directional) $\cos\theta$ term. In a thermal plasma, V_{CM-th} will have a roughly normal distribution and θ will be independent of where the reaction occurs in the plasma. In the beam-target reactions described above, $|V_{CM-beam}|$ is roughly constant and θ is correlated to reaction location: for the 'near' side of the implosion, $\theta = 0$, whereas for the 'far' side, $\theta = \pi$. The fusion product energy is thus a function of angle, $E'(\theta) = E'_0 + E'_{beam}\cos\theta$, where $E'_{beam} = V_{CM-beam}\sqrt{Qm'_1m'_2/(m'_1+m'_2)}$. Taking the 2nd moment of $E'(\theta)$, and rewriting $V_{CM-beam}$ in terms of the beam-particle energy $E_1 = (m_1+m_2)^2V^2_{CM-beam}/2m_1$, the spectral width of the fusion products is obtained as

$$\sigma^2_{beam} = \frac{4}{3}\frac{m'_1m'_2}{(m'_1+m'_2)}\frac{m_1}{(m_1+m_2)^2}(Q+K)E_1. \tag{3.11}$$

This derivation is identical to the thermal case, except with $E_1 \propto V^2_{CM-beam}$ in lieu of $\langle V^2_{CM-th}\rangle$. In the case of energetic ^{3}He fusing with a static shell of D, the formula for proton spectral width may be simplified to $\sigma^2_{beam} \approx E_1(2340\text{ keV})$. By comparison with the well-known relationship for D^{3}He protons from a thermal fusion source, $\sigma^2_{th} \approx T_i(5880\text{ keV})$, it is clear that a radially symmetric population with energy E_1 in excess of 2.5 times the thermal energy will produce a wider spectral line than the thermal ions.[56] For the calculations described above, ^{3}He ions at the shock velocity carry 40 keV, and would generate a proton line width ($\sigma \approx 300$ keV) equivalent to 16 keV thermal temperature. Such temperatures are reasonably achieved in these and similar experiments, and as such could not be discriminated using this technique. However shock-accelerated ^{3}He ions carrying 160 keV would generate a proton line width ($\sigma \approx 600$ keV) equivalent to 64 keV, which would be unreasonably high and represent a measurable signature of this effect.

3.7 Summary

In summary, measurements of nuclear yield from direct-drive implosions of thin CD-shells show the same yield of D^{3}He-protons from capsules filled with pure ^{3}He and from capsules filled with a hydroequivalent 50:50 mixture of deuterium and ^{3}He. The observed yields indicate that the number density of deuterium in the ^{3}He gas is of order 10% the ^{3}He number density before fusion burn. Hydrodynamic mix mechanisms have been ruled out as explanations for this observation, as they do not introduce sufficient fuel-shell mix prior to shock rebound. Integrated 1D-radiation-hydrodynamic calculations including ion diffusion indicate that the amount of mix generated by ion diffusion is sufficiently high to explain the observations. Fluid simulations including reduced ion kinetic models match the observed trends of yield and ion temperature in these implosions, strengthening the case for ion diffusion.

Several kinetic mechanisms were considered as possible contributing factors to mix in these implosions. Of the other models considered, electric field acceleration of the deuterium ions at the shock front is predicted to have the strongest effect. As shocks break out across the fuel-shell interface, a substantial fraction of deuterons near the interface are accelerated to approximately twice the shock speed, and deuterons within a mean-free path of the interface are free to stream into the ^{3}He plasma. An upper bound for the number of deuterons accelerated is calculated to be comparable to the number required to explain the yield results. Several 'beam-target' fusion mechanisms were considered, but all are predicted to produce yield at least an order of magnitude below what was observed. Fully kinetic simulations of such implosions, especially during the dynamic epoch of shock breakout across the fuel-shell interface, will be highly informative in terms of better understanding the detailed mechanics of kinetic mix in these implosions, and their application to other experiments of interest, such as CH/DT interfaces in ignition experiments.

3.8 References

1. J. Lindl, "Development of the indirect-drive approach to inertial confinement fusion and the target physics basis for ignition and gain," Physics of Plasmas, **2**(11), 3933 (1995).
2. Y. Aglitskiy, A. L. Velikovich, M. Karasik *et al.*, "Direct Observation of Mass Oscillations Due to Ablative Richtmyer-Meshkov Instability in Plastic Targets," Physical Review Letters, **87**, 265001 (2001).
3. V. A. Smalyuk, S. X. Hu, J. D. Hager *et al.*, "Rayleigh-Taylor Growth Measurements in the Acceleration Phase of Spherical Implosions on OMEGA," Physical Review Letters, **103**(10), 105001 (2009).
4. S. E. Bodner, "Rayleigh-Taylor Instability and Laser-Pellet Fusion," Physical Review Letters, **33**(13), 761 (1974).
5. Henshaw, M. J. de C. and Pert, G. J. and Youngs, D. L., "Non-linear Rayleigh-Taylor Instability in (Spherical) Laser Accelerated Targets," Plasma Physics and Controlled Fusion, **29**(3), 405 (1987).
6. K. O. Mikaelian, "Oblique shocks and the combined Rayleigh-Taylor, Kelvin-Helmholtz, and Richtmyer-Meshkov instabilities," Physics of Fluids, **6**(6), 1943 (1994).
7. A. L. Velikovich, A. J. Schmitt, J. H. Gardner *et al.*, "Feedout and Richtmyer-Meshkov instability at large density difference," Physics of Plasmas, **8**(2), 592 (2001).
8. R. D. Petrasso, J. A. Frenje, C. K. Li *et al.*, "Measuring Implosion Dynamics through ρR Evolution in Inertial-Confinement Fusion Experiments," Physical Review Letters, **90**(9), 095002 (2003).
9. J. R. Rygg, J. A. Frenje, C. K. Li *et al.*, "Time-Dependent Nuclear Measurements of Mix in Inertial Confinement Fusion," Physical Review Letters, **98**(21), 215002 (2007).
10. D. C. Wilson, P. S. Ebey, T. C. Sangster *et al.*, "Atomic mix in directly driven inertial confinement implosions," Physics of Plasmas, **18**(11), 112707 (2011).
11. V. A. Smalyuk, R. E. Tipton, J. E. Pino *et al.*, "Measurements of an Ablator-Gas Atomic Mix in Indirectly Driven Implosions at the National Ignition Facility," Physical Review Letters, **112**, 025002 (2014).
12. V. A. Smalyuk, M. Barrios, J. A. Caggiano *et al.*, "Hydrodynamic instability growth and mix experiments at the National Ignition Facility," Physics of Plasmas, **21**(5), 056301 (2014).
13. D. T. Casey, V. A. Smalyuk, R. E. Tipton *et al.*, "Development of the CD Symcap platform to study gas-shell mix in implosions at the National Ignition Facility," Physics of Plasmas, **21**(9), 092705 (2014).
14. S. W. Haan, J. D. Lindl, D. A. Callahan *et al.*, "Point design targets, specifications, and requirements for the 2010 ignition campaign on the National Ignition Facility," Physics of Plasmas, **18**, 051001 (2011).
15. C. Bellei, H. Rinderknecht, A. Zylstra *et al.*, "Species separation and kinetic effects in collisional plasma shocks," Physics of Plasmas, **21**(5), 056310 (2014).
16. General Atomics, see `https://fusion.gat.com/global/IFTRole`.
17. S. P. Regan, J. A. Marozas, J. H. Kelly *et al.*, "Experimental investigation of smoothing by spectral dispersion," Journal of the Optical Society of America B, **17**(9), 1483 (2000).
18. Y. Lin, T. J. Kessler and G. N. Lawrence, "Distributed phase plates for super-Gaussian focal-plane irradiance profiles," Optics Letters, **20**(7), 764 (1995).
19. J. T. Larsen and S. M. Lane, "HYADES - A plasma hydrodynamics code for dense plasma studies," Journal of Quantitative Spectroscopy and Radiative Transfer, **51**, 179 (1994).
20. J. R. Rygg, J. A. Frenje, C. K. Li *et al.*, "Tests of the hydrodynamic equivalence of direct-drive implosions with different D_2 and ^{3}He mixtures," Physics of Plasmas, **13**(5), 052702 (2006).
21. F. H. Séguin, J. A. Frenje, C. K. Li *et al.*, "Spectrometry of charged particles from inertial-confinement-fusion plasmas," Review of Scientific Instruments, **74**(2), 975 (2003).
22. V. Y. Glebov, C. Stoeckl, T. C. Sangster *et al.*, "Prototypes of National Ignition Facility neutron time-of-flight detectors tested on OMEGA," Review of Scientific Instruments, **75**(10), 3559 (2004).
23. R. A. Lerche, D. W. Phillion and G. L. Tietbohl, "25 ps neutron detector for measuring ICF-target burn history," Review of Scientific Instruments, **66**(1), 933 (1995).
24. J. A. Frenje, C. K. Li, F. H. Séguin *et al.*, "Measuring shock-bang timing and ρR evolution of D^3He implosions at OMEGA," Physics of Plasmas, **11**(5), 2798 (2004).
25. W. Seka, H. A. Baldis, J. Fuchs *et al.*, "Multibeam Stimulated Brillouin Scattering from Hot, Solid-Target Plasmas," Physical Review Letters, **89**(17), 175002 (2002).

26. M. J. Rosenberg, H. G. Rinderknecht, N. M. Hoffman *et al.*, "Exploration of the Transition from the Hydrodynamiclike to the Strongly Kinetic Regime in Shock-Driven Implosions," Physical Review Letters, **112**, 185001 (2014).
27. D. K. Bradley, P. M. Bell, O. L. Landen *et al.*, "Development and characterization of a pair of 30-40 ps x-ray framing cameras," Review of Scientific Instruments, **66**(1), 716 (1995).
28. J. Hubbell and S. Seltzer, "Tables of X-Ray Mass Attenuation Coefficients and Mass Energy-Absorption Coefficients from 1 keV to 20 MeV for Elements Z = 1 to 92 and 48 Additional Substances of Dosimetric Interest," see `http://www.nist.gov/pml/data/xraycoef/index.cfm` (2013).
29. M. J. Rosenberg, F. H. Séguin, P. A. Amendt *et al.*, "Assessment of Ion Kinetic Effects in Shock-Driven Inertial Confinement Fusion (ICF) Implosions Using Fusion Burn Imaging," Physics of Plasmas (in preparation).
30. S. Atzeni and J. Meyer-Ter-Vehn, *The Physics of Inertial Fusion: Beam Plasma Interaction, Hydrodynamics, Hot Dense Matter*, International Series of Monographs on Physics, (Oxford University Press, 2004).
31. S. W. Haan, "Onset of nonlinear saturation for Rayleigh-Taylor growth in the presence of a full spectrum of modes," Physical Review A, **39**(11), 5812 (1989).
32. J. R. Fincke, N. E. Lanier, S. H. Batha *et al.*, "Postponement of Saturation of the Richtmyer-Meshkov Instability in a Convergent Geometry," Physical Review Letters, **93**, 115003 (2004).
33. Private Communication with M. Schoff.
34. D. Keller, T. Collins, J. A. Delletrez *et al.*, "DRACO — A New Multidimensional Hydrocode," Bull. Am. Phys. Soc. 44, 37 (1999).
35. P. B. Radha, T. J. B. Collins, J. A. Delettrez *et al.*, "Multidimensional analysis of direct-drive, plastic-shell implosions on OMEGA," Physics of Plasmas, **12**(5), 056307 (2005).
36. P. Amendt, J. D. Colvin, R. E. Tipton *et al.*, "Indirect-drive noncryogenic double-shell ignition targets for the National Ignition Facility: Design and analysis," Physics of Plasmas, **9**(5), 2221 (2002).
37. L. Welser-Sherrill, J. H. Cooley, D. A. Haynes *et al.*, "Application of fall-line mix models to understand degraded yield," Physics of Plasmas, **15**(7), 072702 (2008).
38. P. Amendt, J. Milovich, L. J. Perkins *et al.*, "An indirect-drive non-cryogenic double-shell path to 1ω nd-laser hybrid inertial fusion–fission energy," Nuclear Fusion, **50**(10), 105006 (2010).
39. P. Amendt, C. Bellei and S. Wilks, "Plasma adiabatic lapse rate," Physical Review Letters, **109**, 075002 (2012).
40. G. Kagan and X.-Z. Tang, "Thermo-diffusion in inertially confined plasmas," Physics Letters A, **378**(21), 1531 (2014).
41. R. W. Schunk, "Mathematical structure of transport equations for multispecies flows," Reviews of Geophysics, **15**(4), 429 (1977).
42. K. Molvig, N. M. Hoffman, B. J. Albright *et al.*, "Knudsen Layer Reduction of Fusion Reactivity," Physical Review Letters, **109**, 095001 (2012).
43. N. M. Hoffman, G. B. Zimmerman, K. Molvig *et al.*, "Reduced models for the ion-kinetic regime in inertial-confinement-fusion capsule implosions," Physics of Plasmas (to be submitted).
44. P. Amendt, C. Bellei, S. Wilks *et al.*, "Shock-driven resistive heating in mixed species thermonuclear fuels," Physical Review E ((to be submitted)).
45. C. K. Li, F. H. Séguin, J. R. Rygg *et al.*, "Monoenergetic-Proton-Radiography Measurements of Implosion Dynamics in Direct-Drive Inertial-Confinement Fusion," Physical Review Letters, **100**(22), 225001 (2008).
46. Y. B. Zel'dovich and Y. P. Raizer, *Physics of Shock Waves and High-Temperature Hydrodynamic Phenomena*, Dover Books on Physics, (Dover Publications, 2002).
47. D. W. Forslund and C. R. Shonk, "Formation and Structure of Electrostatic Collisionless Shocks," Physical Review Letters, **25**, 1699 (1970).
48. L. O. Silva, M. Marti, J. R. Davies *et al.*, "Proton Shock Acceleration in Laser-Plasma Interactions," Physical Review Letters, **92**, 015002 (2004).
49. F. Vidal, J. P. Matte, M. Casanova *et al.*, "Ion kinetic simulations of the formation and propagation of a planar collisional shock wave in a plasma," Physics of Fluids B: Plasma Physics (1989-1993), **5**(9), 3182 (1993).
50. J. R. Rygg, F. H. Séguin, C. K. Li *et al.*, "Proton radiography of inertial fusion implosions," Science, **319**(5867), 1223 (2008).

51. P. A. Amendt, J. L. Milovich, S. C. Wilks *et al.*, "Electric field and ionization-gradient effects on inertial-confinement-fusion implosions," Plasma Physics and Controlled Fusion, **51**(12), 124048 (2009).

52. S. D. Baalrud, "Transport coefficients in strongly coupled plasmas," Physics of Plasmas, **19**(3), 030701 (2012).

53. G. Kagan and X.-Z. Tang, "Electro-diffusion in a plasma with two ion species," Physics of Plasmas, **19**(8), 082709 (2012).

54. H.-S. Bosch and G. M. Hale, "Improved formulas for fusion cross-sections and thermal reactivities," Nuclear Fusion, **32**(4), 611 (1992).

55. C.-K. Li and R. D. Petrasso, "Charged-particle stopping powers in inertial confinement fusion plasmas," Physical Review Letters, **70**(20), 3059 (1993).

56. H. Brysk, "Fusion neutron energies and spectra," Plasma Physics, **15**, 611 (1973).

57. L. Ballabio, J. Källne and G. Gorini, "Relativistic calculation of fusion product spectra for thermonuclear plasmas," Nuclear Fusion, **38**(11), 1723 (1998).

4

Studies of Kinetic Fuel Dynamics in ICF using Shock-Driven Implosions

4.1 Introduction

In the current ignition design for ICF, four weak shocks compress the cryogenic deuterium-tritium (DT) fuel, then combine into a single strong shock with Mach number ~10–50.[1] This strong shock transits the central gas, a DT-vapor with initial density 0.3 mg/cc, and converges at the center of the implosion. The properties of this shock set the initial entropy of the central plasma hotspot. As introduced in Section 1.1.2, the rebounding shock then strikes the imploding fuel, beginning the deceleration phase in which the hotspot is compressed and heated to fusion-relevant conditions.

Understanding the evolution of the plasma during the shock transit phase is fundamentally important for achieving ICF ignition, because the shock sets the initial conditions for hotspot formation, compression, ignition and burn.[2] However the plasma produced by the shock transit is both relatively low in density and high in temperature. As described by Equation 1.24, strong shocks can compress a plasma only up to a constant factor (4, in an ideal gas). Increased shock strength then raises the temperature of the shocked plasma proportionally to M^2. These conditions produce long ion-ion mean-free-paths, which scale as $\lambda_{ii} \propto T^2/n \propto M^4$. Quantitatively, the ion-ion mean-free-paths in the shocked central plasma of the ICF simulation shown in Figure 1.7 reach $\lambda_{ii} \approx 100$ μm, which is comparable to the scale size of the experiment. As was described in Section 1.2.2, such conditions are precisely those in which the hydrodynamic equations begin to break down and kinetic physics becomes important.

The simulations used to design ICF experiments generally assume a single average-ion hydrodynamic framework, in which the equations of motion for a single ion-species plasma are solved iteratively to model the implosion. Multiple ion species are not treated separately: the ion mass and charge are set as a weighted average of the individual species. As long as ion-ion mean-free-paths are short relative to the zone size, this approximation is expected to be accurate. However, recent experimental and theoretical work has questioned the validity of the average-ion assumption for ICF experiments.[3–13] Anomalous reduction of the compression-phase nuclear yield has been observed in implosions filled with multiple fuel species, such as deuterium-helium-3 (D^3He),[3] DT,[4] DT with added ^3He,[5] and D^3He with trace amounts of argon, krypton, or xenon.[6] The reduction is described as *anomalous* because the ratio of the observed yield to the modeled yield varies by over 50% as a function of ion species fraction. The yield is observed to drop compared to the model as the plasma approaches equal ion number density for the different species, and recover as the plasma approaches a 'pure' single-ion composition. Anomalous reduction of the shock yield has been ambiguous in these studies: the results from compressive D^3He implosions indicate that shock

yields are anomalously reduced in some implosions, but not in others, while the DT+^{3}He study appears to indicate that the shock-yield effect is small.

Diffusive separation of the ion species in the fuel is a potential cause of these anomalous observations. As introduced in Section 1.2.2, such diffusion can be driven by gradients in pressure,[7] electric potential,[8,9] and temperature.[10] The separation could directly cause the yield reductions by changing the local ion densities in the fuel prior to burn. Additionally, the viscosity between the counter-diffusing species can also resistively heat the plasma, which increases its entropy and resists compression.[11] Kinetic physics has been observed to impact the evolution and nuclear performance of multi-species plasmas in computational studies,[12–14] although no fully kinetic model is yet capable of simulating an entire ICF implosion.

Despite the importance of the shock phase to establishing the initial conditions for compression and burn, this phase is difficult to diagnose directly. These challenges were described in the introduction to Chapter 2, and motivated the development of the PTOF and MagPTOF diagnostics described in that chapter. In brief, the rebounding shock generates a brief period of fusion production ("shock-bang"), which is uniquely observable for implosions filled with deuterium and ^{3}He fuel via the D^{3}He-fusion protons, and provides direct information on the fusing plasma through nuclear diagnosis. However the development of nuclear diagnostics on the NIF is an ongoing effort, and does not yet approach the number available on the OMEGA laser. Moreover, other fusion products generated at shock-bang are not observed on the NIF: shock DD-neutrons are overwhelmed by the main period of nuclear production ("compression burn"), which occurs less than 1 ns after shock rebound; also, DD-protons do not escape the capsule due to high ρR.

To directly study the physics of the shock-phase, a series of shock-driven implosions were performed using the OMEGA laser. By using the shock-driven implosions introduced in Section 1.1.3, all the fusion products can escape the implosion and be detected because of low total ρR, on the order of 1 mg/cm^2. The lack of a subsequent compression phase allows highly precise diagnosis of the shock-generated fusion products to evaluate the state of the plasma at shock-bang time. The experiments described in this chapter demonstrate for the first time signatures of two multiple-ion kinetic physics effects in a series of D^{3}He-gas-filled, strongly-shocked implosions: thermal decoupling and diffusive separation of the ion populations. The observations suggest that these kinetic effects, which hydrodynamic simulations do not capture, have an important impact on ICF-relevant plasmas.

In this chapter, Section 4.2 describes the design of these experiments. The experimental results are presented in Section 4.3. Hydrodynamic instability growth is shown not to produce the observed anomalous yield trends in Section 4.4. In Section 4.5 the theory of thermal decoupling between the ion species is developed and a model is applied to explain the low-initial gas density implosions. Section 4.6 evaluates a burn-averaged deuterium fraction in the plasma, and uses this to demonstrate ion species separation in an ICF implosion for the first time. Finally, the results are summarized in Section 4.7.

4.2 Experimental Design

The experiments were performed in two campaigns at the 60-beam OMEGA laser facility.[15] Spherical glass capsules produced by the drop-tower method and with a diameter of 860 μm, a wall thickness of 2.2 μm, and glass density of 2.15 g/cm^3 were used. These capsules were filled with various concentrations of D_2 and ^{3}He gas, shown in Figure 4.1. The atomic deuterium fraction ($f_D \equiv n_D/(n_D + n_{^3He})$) of the gas fills ranged from 1 (pure deuterium) to 0.07 (^{3}He-rich), while

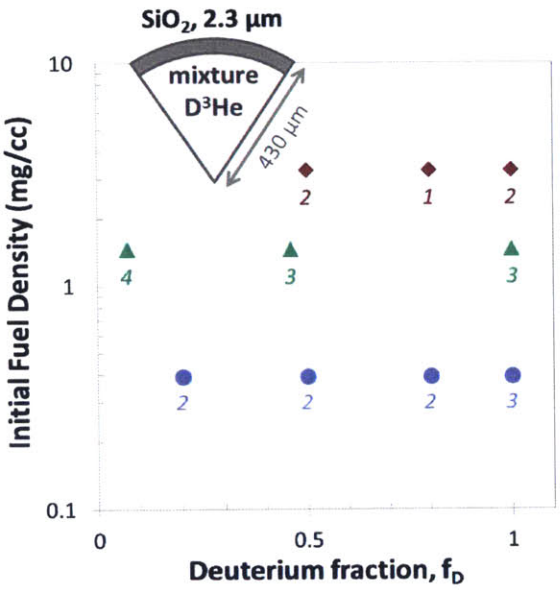

Figure 4.1. Initial gas fill used in the kinetic plasma dynamics experiments. The targets were thin-glass spherical capsules, with an outer diameter of ~860 μm and a wall thickness of 2.2 μm, filled with mixtures of deuterium and ^{3}He gas. The initial mass density was held constant at 3.3 (red), 1.5 (green), and 0.4 (blue) mg/cc, while the deuterium fraction ($f_D = n_D/(n_D + n_{^3He})$) was varied. The number of implosions performed using each initial gas fill are indicated. The 1.5 mg/cc implosions were performed on February 8th, 2011 using a 1 ns, 23 TW laser impulse; the 0.4 and 3.3 mg/cc implosions were performed on April 4th, 2013 using an 0.6 ns, 23 TW impulse.

maintaining a constant initial mass density of $\rho_0 = 0.4$, 1.5, or 3.3 mg/cc.[a] The initial campaign, performed on February 8th, 2011, imploded the 1.5 mg/cc capsules using a 1 ns square, 23 TW laser pulse. The second campaign was performed on April 4th, 2013, and imploded the 0.4 and 3.3 mg/cc capsules using an 0.6 ns square, 23 TW laser pulse.[b] For all implosions, distributed phase plates were used in all cases to generate a fourth-order super-Gaussian (SG4) beam profile,[16] and the beams were smoothed by spectral dispersion (SSD).[17] These implosions mimic the density and shock strength in the ignition-target central gas. Because the shell burns through and the compression of the fuel by remaining shell mass is minimal, the implosions produce primarily shock yield. A summary of the shot parameters for this series is given in Table 4.1.

The choice of equal mass density in the fuel is beneficial for several reasons. As already noted, this selection maintains an equal Atwood number at the fuel-shell interface. Additionally, the mass density of the gas affects the velocity of the shock that is launched into the gas by the shell. Since the shell and laser impulse are selected to be identical, the ram pressure of the shock is expected to be identical as well. Ram pressure is defined as $P_{ram} = \rho v_{sh}^2$, so equal mass-density gas fills will also have equal shock velocity. This principle is confirmed by 1D-hydrodynamic simulations. Additional details related to the scaling of the shock velocity versus initial gas pressure are presented in Appendix F.

For D^{3}He mixtures in particular, equal-mass-density mixtures often share the property of *hydroequivalence*, which was introduced in Section 3.2. Hydrodynamically, the evolution of the shocked plasma is determined from the equation of state, which for an ideal gas is given by:

$$P = n_i T_i + Z n_i T_e = \frac{\rho_i (1 + Z\Gamma) T_i}{A m_p}, \tag{4.1}$$

where Γ is the ratio of electron to ion temperature (T_e/T_i). If the electron-ion thermalization time

[a] I will refer to these three series as the low-, medium-, and high-density implosions throughout this chapter.

[b] The laser pulse was shortened in the second campaign, to turn the laser off prior to nuclear bang-time. The laser impulse charges the capsule, which upshifts the charged fusion products. Turning the laser off prior to nuclear burn allows the electric charge to decay so that the spectra are not affected.

Table 4.1. Shot information for kinetic plasma dynamics studies using implosions of glass (SiO_2) shells filled with mixtures of D and ^{3}He on the OMEGA laser.

Shot #	Initial gas fill		Capsules		Laser Information		
	ρ_0 (mg/cc)	f_D	OD (μm)	wall (μm)	Energy (kJ)	Abs %	Pulse
61085	1.461	1	890.4	2.2	23.06		SG1018
61086	1.461	1	886.4	2.2	22.59		SG1018
61087	1.461	1	885.4	2.2	22.66		SG1018
61089	1.444	0.067	879.6	2.3	22.78		SG1018
61090	1.469	0.066	868.0	2.0	22.60		SG1018
61091	1.457	0.066	850.2	2.1	22.83		SG1018
61093	1.444	0.067	881.2	2.1	22.64		SG1018
61094	1.453	0	871.8	2.3	29.42		SG1018
61095	1.453	0	858.8	2.3	29.32		SG1018
61096	1.436	0.464	865.0	2.0	22.48		SG1018
61097	1.436	0.464	849.0	2.0	22.74		SG1018
61099	1.436	0.464	890.4	2.2	22.41		SG1018
average	1.45±0.01		873±14.9	2.16±0.12	23.79±2.61		
69249	0.384	0.509	883.2	2.3	14.52	60%	SG0604
69250	0.388	0.835	845.6	2.3	14.65	57%	SG0604
69251	0.385	0.217	845.1	2.4	14.65	57%	SG0604
69254	0.385	0.507	844.4	2.3	14.60	54%	SG0604
69256	0.399	0.819	853.0	2.2	14.69	55%	SG0604
69257	0.424	0.198	868.5	2.3	14.36	58%	SG0604
69258	0.390	1	858.4	2.4	14.58	57%	SG0604
69259	0.390	1	836.2	2.2	14.62	54%	SG0604
69263	0.390	1	836.3	2.3	14.45	55%	SG0604
average	0.39±0.01		852±15.5	2.3±0.07	14.57±0.11	56%±2%	
69252	3.299	0.840	852.3	2.4	14.56	58%	SG0604
69261	3.305	1	878.6	2.4	14.56	60%	SG0604
69262	3.305	1	846.2	2.3	14.63	55%	SG0604
69264	3.174	0.510	869.2	2.2	14.71	58%	SG0604
69265	3.378	0.484	881.0	2.2	14.84	59%	SG0604
average	3.29±0.07		865±15.6	2.3±0.1	14.66±0.12	58%±2%	

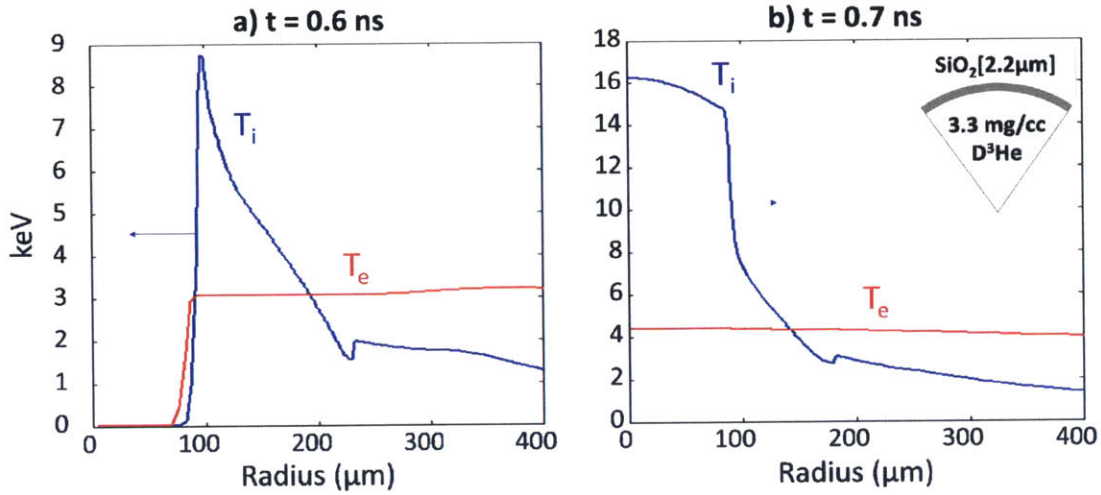

Figure 4.2. Electron and ion temperature profiles in a 1D-HYADES simulation of a high initial-gas density shock-driven implosion, a) before (0.6 ns) and b) after (0.7 ns) shock rebound. The electron and ion temperatures are decoupled throughout the implosion. Electron temperature is primarily set by the laser, while ion temperatures are set by the shock heating process.

is short, then $\Gamma \approx 1$. Fully ionized D^3He mixtures have the special property that $(1+Z)/A = 1$ regardless of the deuterium fraction, so equal mass density implies equal total particle number $(1+Z)n_i$ and the equation of state is identical regardless of deuterium fraction. This implies that, given the same dynamic history of outside pressure influences, the systems are expected to evolve identically. For example, the ion temperature of the shocked plasma would be given by $T_i = P/\rho_i$, with the pressure and density given in terms of the Mach number and the sound speed in the upstream plasma by Equations 1.24 and 1.25.

In practice, this is not expected to occur for shock-driven implosions because the electron-ion equilibration times are generally quite long compared to the experimental timescales. Thermal equilibration rates are comparable to the collision rate in Equation 1.15, and are given by:[18]

$$\nu_\epsilon^{j/k} = \frac{(A_j A_k)^{1/2} Z_j^2 Z_k^2 n_k \log\Lambda}{(A_j T_k + A_k T_j)^{3/2}} \left[4.4 \times 10^{-12} Hz\right], \tag{4.2}$$

where temperatures have units of keV and the density is in cm^{-3}. For temperatures of 3 keV and densities of 5×10^{21} cm^{-3}, the electron-ion thermal equilibration is calculated to be on the order of 1 ns, longer than the duration of the implosion. Figure 4.2 presents profiles of the electron and ion temperature both before and after shock rebound in a simulation of the high-density, $f_D = 0.5$ experiments. These figures demonstrate clearly that the electrons and ions are not equilibrated at shock rebound and during fusion production. If Γ is retained in the ideal equation of state, the solution for the shocked ion temperature becomes:

$$T_i = \frac{P}{\rho_i} \frac{(3 - f_D)}{(1 + (2 - f_D)\Gamma)}. \tag{4.3}$$

For long thermalization times, $\Gamma \ll 1$, and the shocked ion temperature will be expected to vary with deuterium fraction by up to a factor of 3/2. This behavior is observed in the simulated burn-averaged ion temperatures, as will be discussed in the next section.

4.3 Experimental Results

Comprehensive nuclear diagnosis was performed to record the behavior of these implosions. For all experiments, yields of DD-fusion neutrons (2.45 MeV) were measured using the neutron Time-of-Flight (nTOF) diagnostic suite.[19] Yields and spectra of D^3He-fusion protons (14.7 MeV) were recorded using the Charged Particle Spectrometers (CPS1 and CPS2) and Wedge-Range-Filter proton spectrometers (WRF).[20] Burn-averaged ion temperatures were inferred from the spectral widths of the nuclear products, after correcting for instrumental broadening[21,22] as introduced in Section 1.3.1. 1D-radiation hydrodynamic simulations were performed using the code HYADES[23] for comparison to the observed values. The simulations were constrained using the laser absorption fraction,[24] which was measured to be 57% in these experiments, and the measured DD-neutron and D^3He-proton nuclear-bang times, recorded using the NTD[25] and PTD[26] instruments, respectively. In addition, for the low- and high-density implosions on April 4th, 2013 the spatial burn profiles of D^3He-protons and DD-protons (3.0 MeV) were measured by penumbral imaging.[27] Time-resolved self-emission x-ray images were also recorded on this shot day.[28] The results from these diagnostics will be discussed in this section.

4.3.1 Yields

The measured yields show anomalous trends relative to the hydrodynamically simulated values, as shown in Figure 4.3.[c] For each ρ_0, the yield drops relative to the predicted yield as the deuterium fraction is reduced from $f_D = 1$. This trend occurs in addition to the reduction in yield with decreasing ρ_0, which was previously reported in Reference [29] and can be clearly seen in the plots of measured yield divided by the simulated yield ('Yield-over-clean' or YOC) shown in Figure 4.3c) and d). The decrease in nuclear production with reduced fuel density was shown to be caused by the increased importance of kinetic effects associated with long ion-ion mean-free-paths: ion diffusion and reduction in fusion reactivity due to the loss of high-energy ions on the Maxwellian tail, the so-called *Knudsen reactivity reduction* presented in Section 1.2.2.[29] The study that demonstrated this trend in YOC with fuel density was performed on the OMEGA laser on March 14th, 2013 using identical targets and laser impulses to the high- and low-density implosions presented in this chapter. A key finding from that work showing the reduction in YOC with reduced fuel density and increased Knudsen number is reproduced in Figure 4.4 for reference.

To highlight the trend with deuterium fraction, the observed yield divided by the predicted yield is plotted in Figure 4.3e) and f), where each dataset has been normalized to the equimolar value ("Yield-over-clean normalized," or YOCn). The YOCn for each series varies by approximately 50% with f_D. These results provide the first conclusive experimental demonstration of a shock-yield anomaly with fuel ion fraction. The YOCn increase monotonically in the range $f_D > 0.2$. The experiments with $\rho_0 = 1.5$ mg/cc and a 1 ns, 23 TW laser pulse were performed down to $f_D = 0.07$, and show a flattening of YOCn in the limit of low f_D, rather than a continuous decay. These results are unlike the anomalous trends in the compression yield, which showed a maximal reduction for equimolar D^3He and yield recovery approaching pure ^3He,[3] suggesting that a different mechanism may be at work. The observed trend cannot be explained by turbulent fuel-shell mix, since the Atwood number does not change with f_D; Section 4.4 presents a more detailed investigation of this claim. Two models including additional kinetic physics, decoupling of the D and ^3He ion temperatures ("2-Ti"), and species separation by ion diffusion (Reduced Ion Kinetic, or "RIK"), capture the observed trends, and will be discussed in Sections 4.5 and 4.6.2, respectively.

[c] In subsequent figures, results from multiple implosions with the same nominal design are averaged.

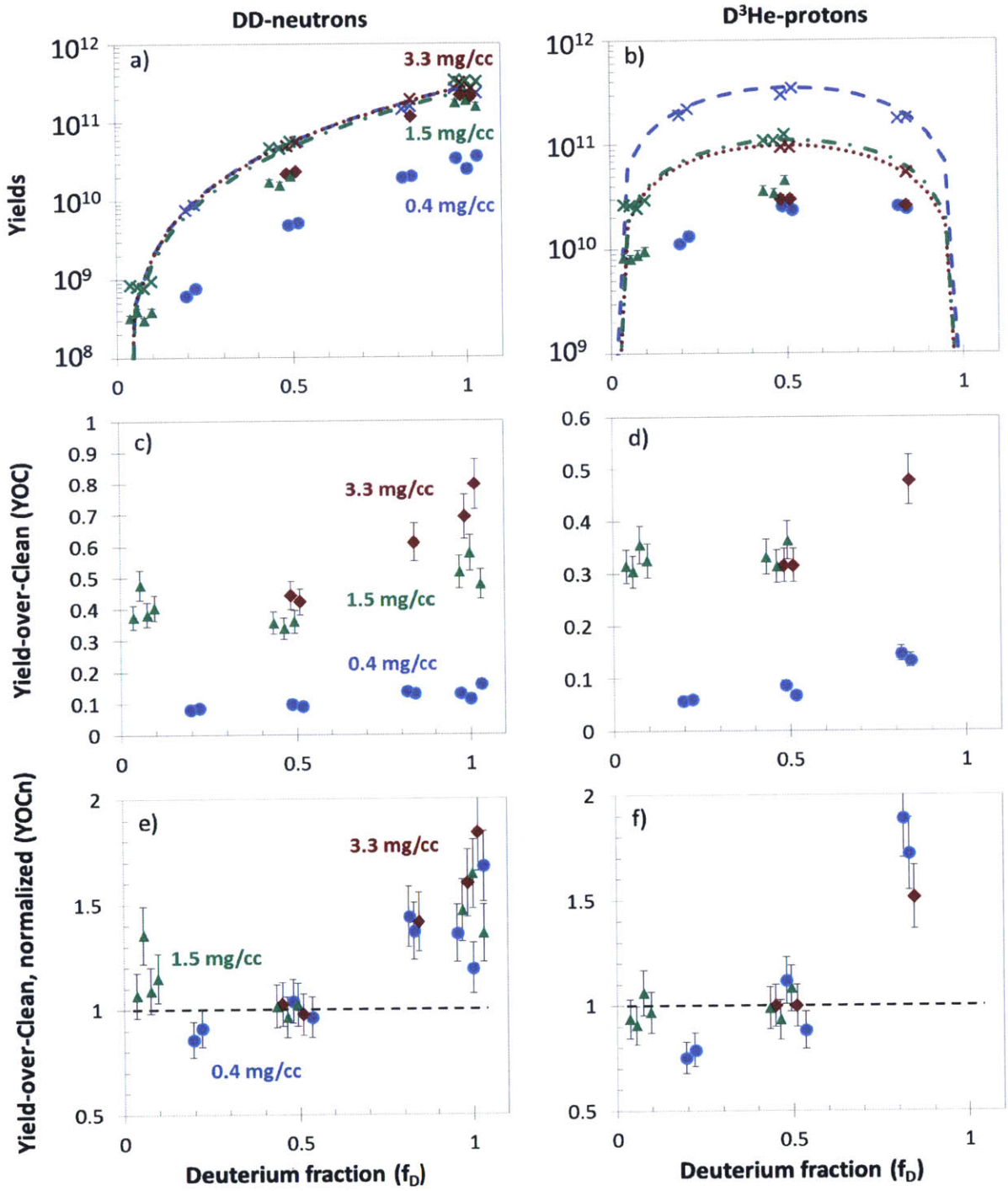

Figure 4.3. Yields of DD-neutrons (left) and D^3He-protons (right) for the kinetic plasma dynamics implosions. High- (3.3 mg/cc, red), medium- (1.5, green) and low-density (0.4, blue) are shown. (a,b) Absolute yields for the campaigns (points). 1D-simulated yields for the shots (x's) and simulated nominal trends with deuterium fraction (lines) are shown for comparison. (c,d) The measured yield divided by the 1D-simulated yield ('Yield-over-clean' or YOC) and (e,f) the yield-over-clean normalized to the value of each series at $f_D = 0.5$ (YOCn) emphasize the anomalous trend in the data as deuterium fraction is varied. (The black dashed line in (e,f) represents agreement with the simulated trend, though not the absolute simulated values.)

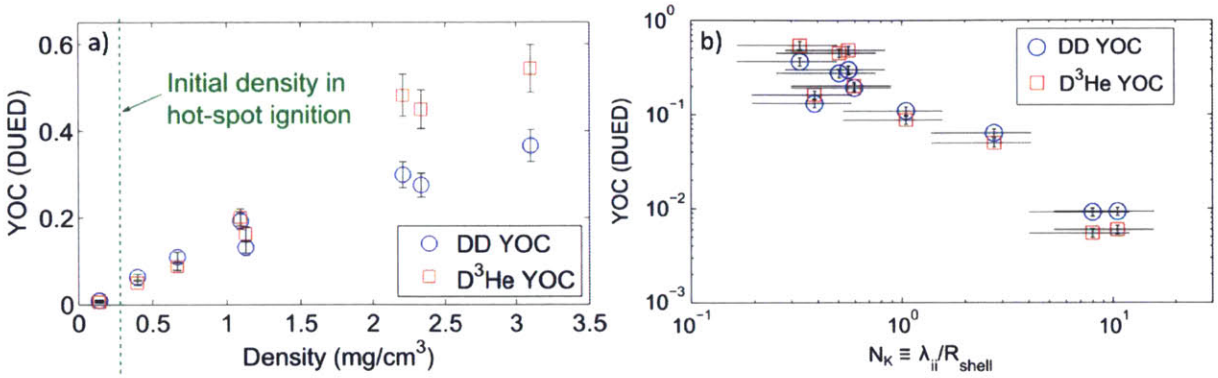

Figure 4.4. YOC relative to 1D DUED simulations for both DD-neutron and D^3He-proton reactions, as a function of a) the initial gas-fill density ρ_0 and b) the Knudsen number N_k, defined as the ratio of the ion-ion mean-free path at bang time to the minimum shell radius. The experiments in this figure used identical shell and laser parameters to the low- and high-density implosions presented in this chapter. Figures were originally published by M. Rosenberg, et al. as Fig. 2b) and Fig. 3 in Reference [29]

The modeled nuclear yields, which deviate significantly from the experiments, are given by:

$$\begin{aligned} Y_{DD} &= \int \left(n_D^2/2\right) \langle \sigma v \rangle_{DD} dV dt, \\ Y_{D^3He} &= \int n_D n_{^3He} \langle \sigma v \rangle_{D^3He} dV dt. \end{aligned} \tag{4.4}$$

Yields depend on the evolution of the ion species densities n_D, $n_{^3He}$ and the Maxwellian-averaged fusion reactivities $\langle \sigma v \rangle_{DD,D^3He}$, which are strong functions of the ion temperature T_i. Examining the density and ion temperature in the experiments, which are accessible via other nuclear diagnostics, will help isolate the physics behind the anomaly.

Mean-free-path effects

Although the mean-free-path in the plasma is a function of deuterium fraction for a given ρ_0, these long ion-ion mean-free-path effects do not directly cause the yield anomaly with f_D. The physical mechanisms that cause reduced yield with increased Knudsen number will play a role in these experiments as well; however, careful examination indicates that the observed trend is opposite to the trend expected from the long mean-free-path effects alone. Following Equation 1.15, the mean-free-path for a fuel ion of species j for collisions with ions of species k scales as $\lambda_{jk} \propto T^2 m_j / n_k Z_j^2 Z_k^2 m_{red} \log \Lambda$. The total mean-free-path is the inverse sum of the mean-free-paths for species j relative to all plasma species: $\lambda_j = \left(\sum_i \lambda_{ji}^{-1}\right)^{-1}$. Assuming thermalized ion species and ignoring variations in $\log \Lambda$, the scaling of the mean-free-path for deuterons and ^3He in the plasma can be calculated as a function of deuterium fraction:

$$\begin{aligned} \lambda_D &= \frac{10(3-f_D)}{(24-19f_D)} \lambda_C, \\ \lambda_{^3He} &= \frac{5(3-f_D)}{8(5-4f_D)} \lambda_C, \end{aligned} \tag{4.5}$$

where the constant of proportionality $\lambda_C = (3/4\pi)(4\pi\epsilon_0/e^2)^2 T^2 m_p/(\rho \log \Lambda)$. While the deuteron mean-free-path is always 3.3× that of a ^3He ion to within 5%, the mean-free-path for each species increases by a factor of over 3× as f_D increases from 0 to 1. This reduced confinement with increasing deuterium fraction stems from two sources. As the ratio of deuterium to ^3He increases, the average field ion charge decreases, allowing the mean-free-path to grow as Z^{-2}. This is partially

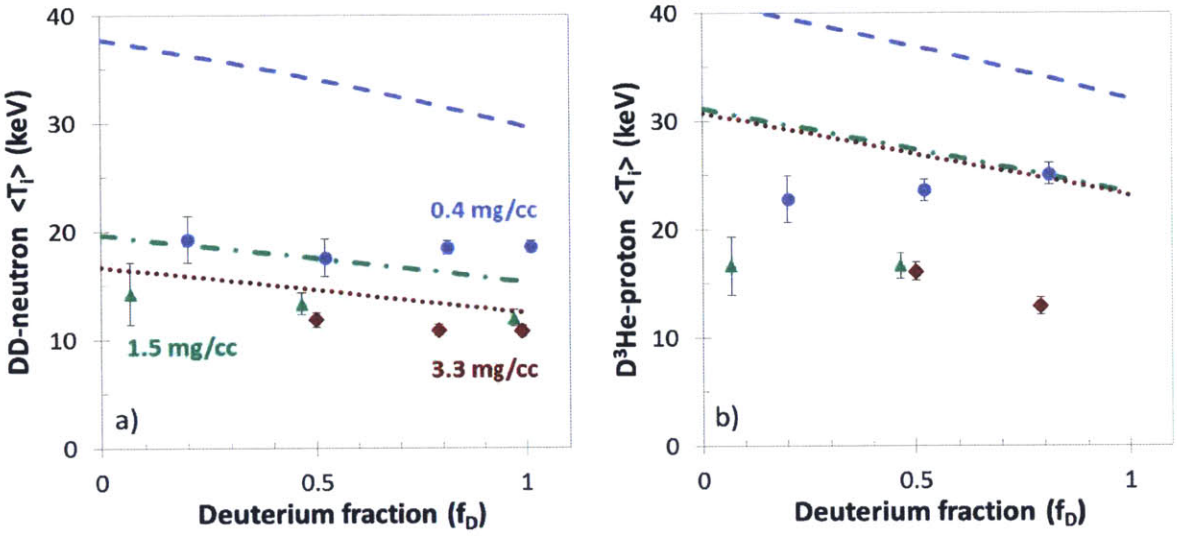

Figure 4.5. Comparison of measured (points) and simulated (lines) burn-averaged ion temperatures $\langle T_i \rangle$ for the a) DD- and b) D^3He-fusion reactions. The low- (blue, dashed), medium (green, dot-dashed), and high-density (red, dotted) data and simulations are shown. The 'clean' 1D-simulations predict an increased $\langle T_i \rangle$ with decreased f_D, which is roughly in agreement with the trends in the medium- and high-density data but is not observed in the low-ρ_0 data. Measurement uncertainties for the data are comparable to the size of the points where not shown. DD-neutron data courtesy of Vladimir Glebov, LLE.

balanced by an increase in the ion number density required to maintain the same mass density with the intrinsically lighter deuterons. An average mean-free-path for the plasma, calculated by weighting the species-specific mean-free-paths in Equation 4.5 by the ion species fraction, is then:

$$\langle \lambda_{ii} \rangle = (3 - f_D) \frac{24 + 37 f_D - 45 f_D^2}{(24 - 19 f_D)(5 - 4 f_D)} \frac{5 \lambda_C}{8}, \tag{4.6}$$

which is more than a factor of 10 greater for the pure deuterium plasma than for pure ^3He. Based on the scaling observed in Figure 4.4b), pure deuterium implosions would be expected to underperform substantially compared to the D^3He-filled implosions: this is the opposite of what is shown in Figure 4.3. A very strong, heretofore unidentified physical mechanism must be at play in these implosions to counteract, and in fact produce the opposite of, this expected trend.

The analysis as presented implicitly assumes that density and temperature evolve similarly as deuterium fraction is changed. While this is not necessarily guaranteed in shock-driven implosions, the following sections examine further nuclear data and demonstrate that the plasma does not deviate from this assumption to within a factor of ~2.

4.3.2 Burn-averaged ion temperatures

The measured burn-averaged ion temperatures $\langle T_i \rangle$ also demonstrate anomalous behavior compared to the average-ion simulations, as shown in Figure 4.5. The 'clean' simulations predict increasing temperature for reduced f_D, because the equation of state depends on the deuterium fraction for equal-mass-density mixtures, as introduced in Section 4.2. Equation 4.3 suggests that the shocked plasma temperature, and therefore the burn-averaged temperature, should scale as $\langle T_i \rangle \propto (3 - f_D)$. The simulated temperatures closely follow this expected trend. The observations for the medium-

and high-density series also increase with reduced deuterium fraction, roughly in agreement with the expected trend.[d] In contrast, in the low-density implosions the measured $\langle T_i \rangle$ are roughly constant with f_D.

The observed anomaly in burn-averaged ion temperatures for the low-density fuels has not been previously reported, and cannot be explained by invoking either atomic mix or long mean-free-path effects, for the same reasons given in the preceding section. (For a simulation study of the impact of atomic mix, see Section 4.4.) This result indicates that a new, non-hydrodynamic physical process is dominant during the nuclear production in the low-density implosions. The observations can be explained as a signature of ion thermal decoupling, which will be presented in Section 4.5 below.

4.3.3 Burn histories

The measured bang-times and burn-durations for these experimental campaigns are shown in Table 4.2. One trend is notable in this data: the DD-neutron bang-time is observed to be earlier for the low-density than the high-density implosions by about 10%, despite the fact that these experiments had the same laser impulse. This trend is not observed in the D^3He-proton bang-time. This trend may offer some additional evidence for a separation of the ion species at the shock front. However, caution is urged in interpreting this trend, since a fall-line mix model also shifts the DD-neutron bang-time earlier for low-density implosions, without strongly affecting the D^3He-proton bang-time.

These implosions were used in the development of the multiPTD instrumental technique to measure the DD-neutron and D^3He-proton burn histories with high relative precision. However, high-quality multiPTD data was not recorded for these implosions, so the relative bang-times are only as precise as the instrumental cross-timing uncertainty of ± 50 ps. The development of this capability is ongoing work which may in the future shed light on the details of the kinetic processes that are important during shock propagation and shock-yield production.

4.3.4 Nuclear imaging

The radial profiles of nuclear production were measured using penumbral imaging of the DD-protons and D^3He-protons on the low- and high-density campaigns. The PCIS instrument was fielded in TIM 2, with the aperture positioned 3.95 cm from TCC and the CR-39 59 cm behind the aperture. Two pieces of 1000 μm thick CR-39 were fielded to record both DD-protons and D^3He-protons along the same line of sight. The front piece of CR-39 was filtered with 5 μm Ta + 12.5 μm Al, while the rear piece was filtered with 400–450 μm Al, depending on the thickness of the front piece. As described in Section 1.3.4, a model of the nuclear production profile is fit to the data to constrain two parameters: the radius containing 50% of the nuclear yield (r_{50}), and the 'peakedness' (p). As a reminder, a p of zero indicates a volumetrically uniform ('flat') burn profile; a positive p indicates a centrally-peaked profile, while a negative p indicates the profile is 'hollow'. The measured values of these parameters are shown in Figure 4.6, along with predictions from the 1D-HYADES simulations for comparison.

In the high-density implosions, the burn radii are measured to be significantly larger than the simulated values: the DD-proton profile is nearly 2× larger than simulations, while the D^3He-proton profile is $\sim 1.5\times$ larger. At the same time, the shape of the burn profiles is in approximate agreement with the simulations. This result suggests an undercompression of the high-density implosions. Undercompression due to multiple-ion effects has been proposed as one explanation for

[d]The disagreement in the absolute value of yields and $\langle T_i \rangle$ between measurements and 1D-simulations is comparable to that observed in Reference [29].

Table 4.2. Bang-times and burn durations (full-width at half maximum, or FWHM) from the kinetic dynamics campaigns for DD-neutrons and D^3He-protons, as measured using the NTD and PTD diagnostics, respectively. All time values are in picoseconds. Typical cross-timing uncertainties are ±50 ps. Instrument analysis courtesy of Christian Stoeckl, LLE.

Shot #	Initial gas fill		Laser	DD-neutrons		D^3He-protons	
	ρ_0 (mg/cc)	f_D	Energy (kJ)	BT	FWHM	BT	FWHM
61085	1.461	1	23.06	801	180	–	–
61086	1.461	1	22.59	818	165	–	–
61087	1.461	1	22.66	780	180	–	–
61089	1.444	0.067	22.78	790	160	807	137
61090	1.469	0.066	22.60	–	–	780	121
61091	1.457	0.066	22.83	–	–	734	142
61093	1.444	0.067	22.64	–	–	756	148
61094	1.453	0	29.42	–	–	–	–
61095	1.453	0	29.32	–	–	–	–
61096	1.436	0.464	22.48	759	182	753	132
61097	1.436	0.464	22.74	773	155	742	143
61099	1.436	0.464	22.41	803	166	797	137
average	1.45±0.01		23.79±2.61	789±20	170±11	767±28	137±9
69249	0.384	0.509	14.52	727	189	–	–
69250	0.388	0.835	14.65	713	162	865	211
69251	0.385	0.217	14.65	747	174	856	148
69254	0.385	0.507	14.60	730	174	835	188
69256	0.399	0.819	14.69	707	161	855	192
69257	0.424	0.198	14.36	731	185	855	159
69258	0.390	1	14.58	731	165	–	–
69259	0.390	1	14.62	695	165	–	–
69263	0.390	1	14.45	750	154	–	–
average	0.39±0.01		14.57±0.11	726±18	170±12	853±11	180±26
69252	3.299	0.840	14.56	800	173	857	151
69261	3.305	1	14.56	813	172	–	–
69262	3.305	1	14.63	791	168	–	–
69264	3.174	0.510	14.71	764	184	834	147
69265	3.378	0.484	14.84	780	179	851	146
average	3.29±0.07		14.66±0.12	790±19	175±6	847±12	148±2

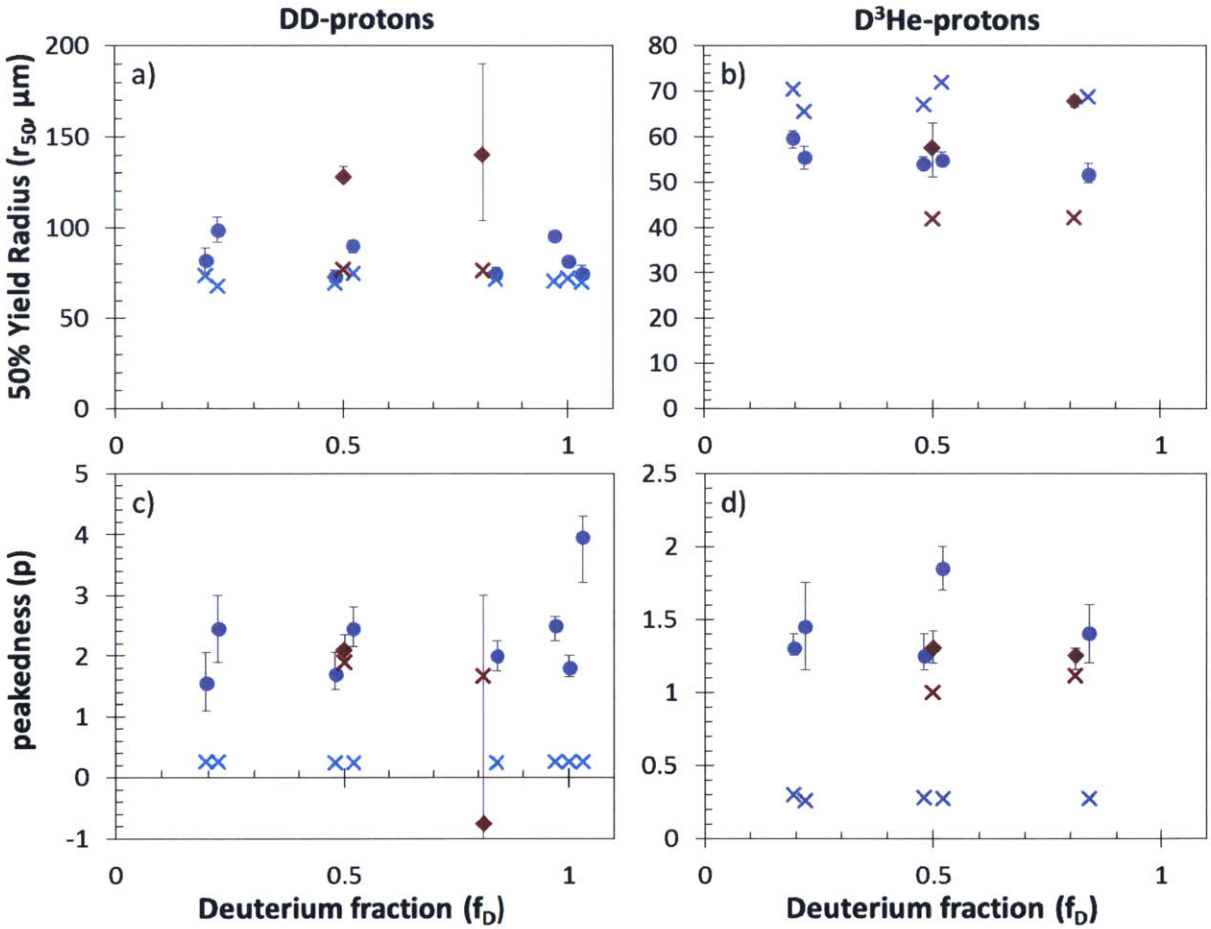

Figure 4.6. Measured (points) and simulated (x) parameters for the profiles of DD-proton and D^3He-proton nuclear production in the low- (blue) and high-density (red) implosions. Parameters shown include (a,b) radii containing 50% of the nuclear production (r_{50}) and (c,d) the 'peakedness' of the profile (p), as defined in Equation 1.36. For the high-density implosions, the burn radii are measurably larger than simulations, but the profile shape is roughly in agreement with simulations. For the low-density implosions, the radii are more accurately modeled, but the measured profile shape is much more centrally-peaked than in the simulations.

the yield anomaly observed in compression yield.[11] The relative flow of the deuterium and ^{3}He due to ion diffusion introduces a source for *resistive heating* of the ion species. Additional heating of the plasma by diffusion during the shock and implosion phase increases the adiabat of the fuel and makes it harder to compress. The reduced density at shock burn also reduces the yield. However these data are not of sufficiently high quality to address whether the radius at peak burn has a trend with deuterium fraction. The data suggest that the r_{50} for the DD reaction is increased more than the r_{50} for D^{3}He. This is also a possible indicator of species separation, in that outward diffusion of the deuterons compared to the ^{3}He would weight the DD reactions to larger average radius than the D^{3}He-reactions. Performing higher-quality convergence measurements is a valuable direction for future research.

In the low-density implosions, the burn radii are generally comparable to the simulations. The DD-burn-radius is on average slightly larger than simulations, while the D^{3}He-burn-radius is slightly smaller (~80%). No clear trend with deuterium fraction is observed. The peakedness of the profiles shows a clear difference between the data and simulations: the measured profiles are strongly centrally peaked ($p \sim 2$ for DD and ~ 1.5 for D^{3}He), while the simulations predict a nearly flat burn profile ($p \sim 0$). Recent work has demonstrated that the shape of the profile in simulations of shock-driven implosions is highly sensitive to the treatment of plasma viscosity and diffusion.[30] The 1D-HYADES simulations shown here do not include diffusion or physical viscosity.[e] The data suggest that these effects are important in the plasma, and must be better understood.

4.3.5 Time-resolved x-ray imaging

The x-ray framing camera (XRFC1) was fielded in TIM3 to image the time-resolved self-emission of the high- and low-density implosions.[28] The camera setup described in Section 3.3.5 was used on these experiments, with the exception that the filter material was varied from shot to shot: the filtering used included 0.5, 1, and 2 mil Al, and 4 and 5 mil Be. The camera was fielded with a magnification of 6× and the pinholes had a diameter of 10 μm. An example of the recorded x-ray framing camera data from both a high- and a low-density implosion is shown in Figure 4.7a) and b), respectively. For both of the images shown, the filtering was 5 mil beryllium and strip bias was 200 V. In both experiments, the first strip begins after the laser has already turned on. The target mounting stalk is visible in the lower-right corner of the images.

In the low-density data, the first image is distorted by arcing on the micro channel plate. As in the thin-CD implosions shown in Figure 3.9, the shell limb is clearly visible into the third strip, but then disappears. A blurry background is apparent in the images near peak compression, which is likely due to direct interaction of high-energy x-rays with the x-ray film. However the image of emission from the compressed fuel is still visible. In contrast, in the high-density data the limb of shell emission is clearly visible in all images, including at peak compression and the beginning of expansion.

Since the electron density in the shell plasma is substantially higher than that in the fuel, the bremsstrahlung emission is expected to be dominated by the shell plasma. The glass also has additional pathways for the emission of recombination (line) radiation. In light of this expectation, the clear limb in the high-density x-ray images at peak compression suggest that the implosion remains highly spherical and the fuel-shell interface remains intact: that is to say, the fuel and shell are not diffusively mixed. The blurriness of the low-density x-ray images at peak compression may suggest that the fuel and shell are more mixed than in the high-density case. However the presence of a background makes quantitative emission profile calculations from these images difficult. Future

[e] A 'numerical viscosity' is included to prevent unphysical solutions (such as negative zone volumes), but this is not based on any physical theory.

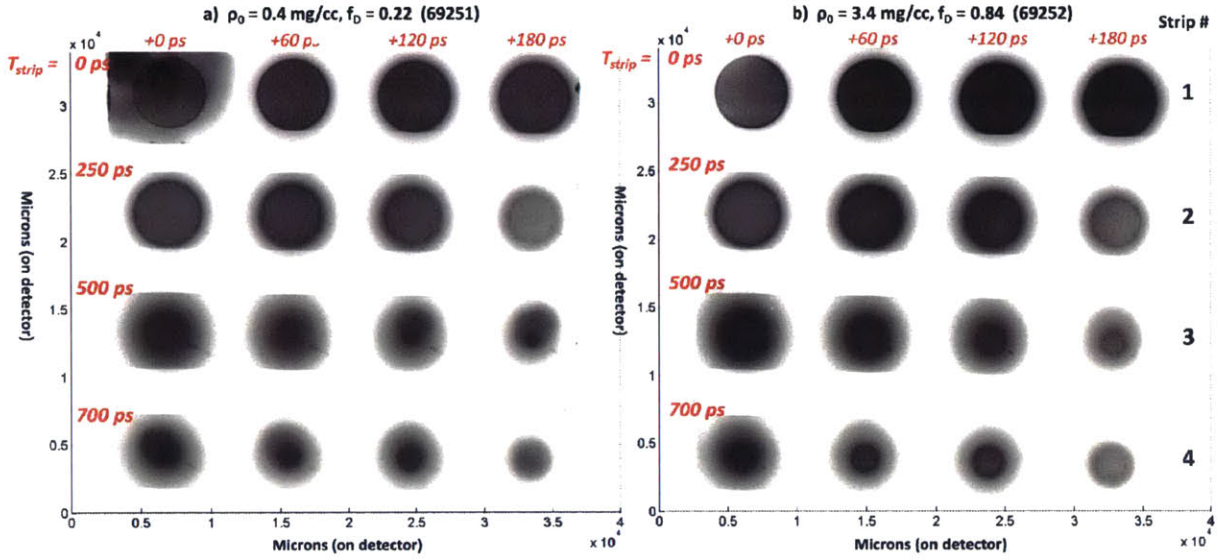

Figure 4.7. Example XRFC images from a) low-density (shot 69251) and b) high-density (69252) implosions, recorded on April 4th 2013. For both experiments the camera was fielded with magnification of 6×, pinhole diameter of 10 μm, 5 mil beryllium filtering, and strip bias of 200 V.

experiments could include a tracer layer at the fuel-shell interface that emits at a characteristic, high-energy line. Filtering to observe this line emission would provide a precise location of the fuel-shell interface and give a distinct signature for diffusion studies.

The analysis procedure presented in Section 3.3.5 was used to determine the implosion radius as a function of time. Measured trajectories for the low- and high-density images in Figure 4.7 are shown in Figure 4.8, compared with the simulated location of the fuel-shell interface. For both sets of data, the measured data follows the simulated location of the fuel-shell interface closely, although for the low-density data the radius is more difficult to infer due to background.

The results from the high-density implosions hint at under-compression of the 50:50 D^3He-filled targets, relative to the D_2-filled targets, as shown in Figure 4.9. To zeroth order, the density of the plasma at burn scales as CR^{-3}, where the convergence ratio CR is equal to the ratio of the initial fuel radius to the radius at peak compression, R_0/R_{peak}. Since the yield scales as the density squared times the volume, the yield is estimated to scale very sensitively with the convergence ratio: $Y \propto CR^{-3}$. The ~60% yield scaling factor observed for 50:50 D:^{3}He mixtures in Figure 4.3 could thus be caused by a reduction in compression ratio of approximately 19%, relative to the value for pure D_2. The observed minimum x-ray emission radius for implosions with $f_D = 0.5$ is approximately 11% larger than that predicted from 1D-radiation hydrodynamic simulations. In contrast, the minimum x-ray emission radius for implosions with $f_D = 1$ is approximately 5% larger than predictions. From this difference, the yield for the D^3He-filled targets would be expected to be only 70–80% of the scaled yield from the pure-deuterium implosions, comparable to what was observed. Unfortunately, the uncertainty in the measurement is comparable to the scale of the effect; however the data is not inconsistent with resistive heating and inhibited compression as a contributing factor for the observed yield anomaly. Improved future experiments might include a high-Z dopant on the inner shell layer, so that line radiation may be used for more accurate characterization of the fuel radius evolution during the implosion.

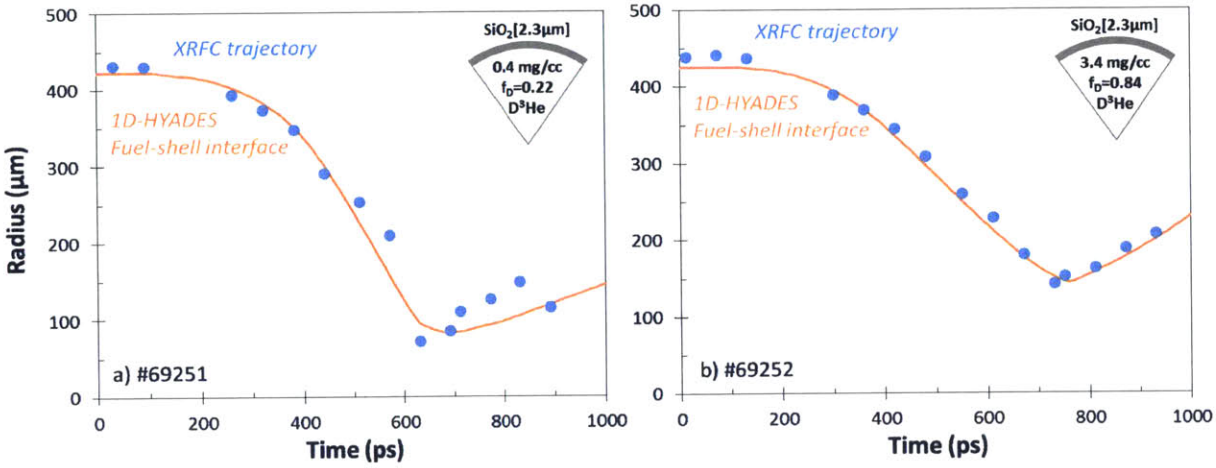

Figure 4.8. Implosion radius as a function of time inferred from the XRFC images (points), for the a) low-density (69251) and b) high-density (69252) images shown in Figure 4.7. The trajectory of the fuel-shell interface in 1D-HYADES simulations of the implosions is shown for comparisons (orange line).

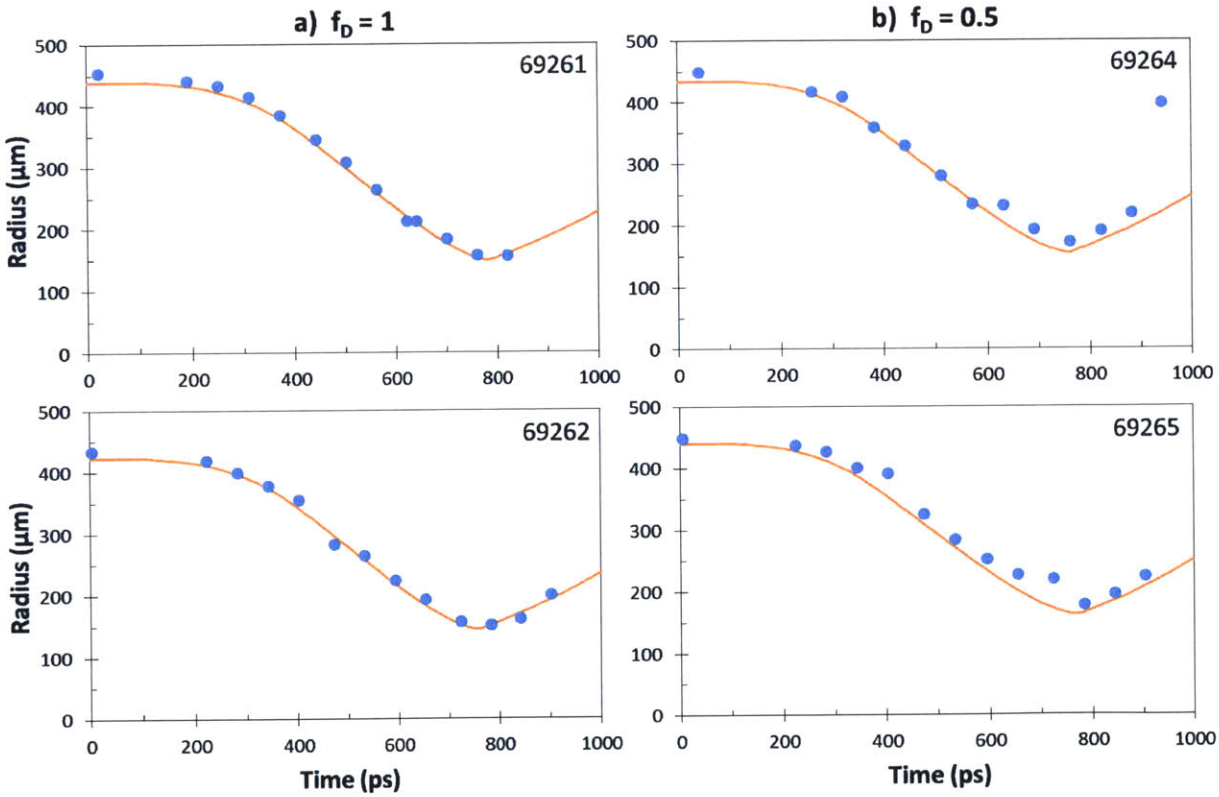

Figure 4.9. Comparison of the XRFC-inferred implosion radius as a function of time (points) and simulated fuel-shell interface trajectory (lines), for the high-density implosions filled with a) pure deuterium (69261, 69262) and b) 50:50 D^3He (69264, 69265). The $f_D = 1$ implosions present very good agreement between the measured and simulated trajectories; in comparison, the $f_D = 0.5$ implosions appear to reach a minimum radius that is approximately 5% larger than expected.

4.4 Trends in Fall-Line Mix Model

As has been noted, these shock-driven implosions are insensitive to hydrodynamic instability growth.[31] The physics of these capsules is similar to the implosions of thin-CD shells discussed in Chapter 3, and instability growth is minimal for similar reasons, which will be summarized here. Firstly, a high mass ablation velocity of the shell material (approximately 8 μm/ns) stabilizes the ablation-front instability growth. Glass ablates very efficiently due to a high ratio of average ion mass to average charge. Glass also has a high laser absorption efficiency: the absorption was measured to be 57% for these experiments, compared to 53% for the $CD_{1.4}$ used in Chapter 3, when imploded with a comparable laser impulse.[f] Secondly, the entire shell rapidly ablates ("burns through"), which limits the time available for ablation-front instability growth. In these experiments, burn-through occurs at ~0.35 ns, after which the density gradient that drives the ablative Rayleigh-Taylor instability is eliminated and the instability growth is truncated. Thirdly, the comparatively small radial convergence of these shock-driven implosions limits the scale of Rayleigh-Taylor instability growth: the x-ray framing camera images indicate these implosions converge radially by only ~3–5×. This should be contrasted to the values of ~30–40x typical of the 'compressively-driven' implosions used for ignition designs, where Rayleigh-Taylor growth plays an important role. Finally, the negligible compression phase limits late-time instability growth. Because the shell burns through, the imploding shell mass is not large enough to significantly compress the fuel after the initial shock rebounds. The 2D-hydrodynamic simulations of thin-CD shell implosions described in Section 3.4.2, which showed negligible instability growth at peak nuclear production, had comparable shell mass and gas-fill density to these experiments.

Although atomic mix may occur in a 1D manner to some extent, this will not impact the observed trends with varying deuterium fraction. Hydrodynamic instability growth is governed by the Atwood number at the fuel-shell interface, which is defined in Equation 3.1 and is a function of the shell and fuel density only. By design, the fuel density remains unchanged as the deuterium fraction is varied; as such, the Atwood number and the resulting hydrodynamic mix at peak nuclear production is also constant with varying deuterium fraction. Thus, even though 1D mix might occur at some level, it cannot lead to a yield or temperature trend with varying deuterium fraction.

In support of this argument, a fall-line analysis of the 1D-hydrodynamic simulations was performed, which showed that no level of mixing was able to produce the observed trends in yield and temperature. Figure 4.10 shows a Lagrangian (radius vs time) plot for a hydrodynamic simulation of a low-initial density target, illustrating the fall-line mix model and its effect on the yield. The "fall-line," which was introduced in Section 3.4.2, is defined as the projection of the fuel-shell interface from the point of the fastest implosion velocity, and therefore defines the furthest distance that shell material can penetrate into the fuel kinematically. A penetration depth for mix is defined as a fraction of the distance from fuel-shell interface to the fall-line. For this simple model, it is assumed that no yield is produced within the penetration region. Following the results of the 2D-simulations presented in Section 3.4.2, a 20% penetration fraction is taken as an extreme upper bound for the amount of mix present in the experiment. This value only reduces the simulated yield by ~5% for the high-density implosions and ~30% for the low-density implosions. The trends of simulated yield and temperature with deuterium fraction for a fall-line mix model with 20% penetration fraction are shown as dashed lines in Figure 4.11. The trends in YOCn are virtually indistinguishable from the 'clean' 1D hydrodynamic simulation, as expected. The burn-averaged ion temperatures are slightly *increased* by the fall-line mix model, since the penetration region truncates the coldest part of the nuclear production that occurs near the fuel-shell interface; however the trend is unchanged

[f] These values were measured with a laser intensity of 10^{15} W/cm^2.

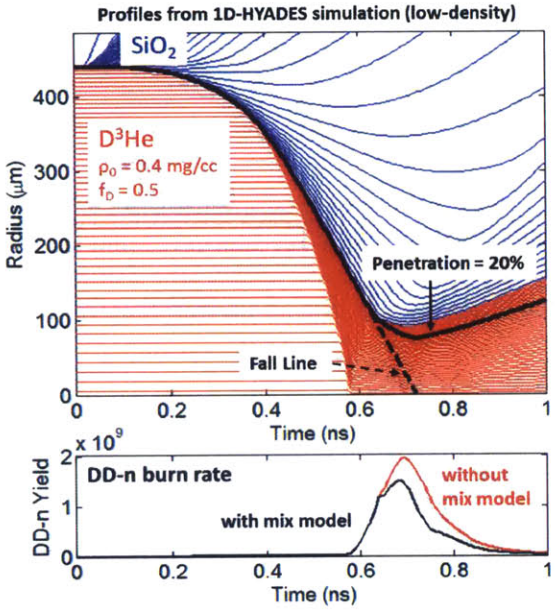

Figure 4.10. (top) Plot of Lagrangian mass-element profiles from 1D-HYADES simulation of an implosion with 0.4 mg/cc, $f_D = 0.5$ initial gas fill, illustrating the fall-line mix model. The fall line (black dashed line) is defined as the projection of the fastest velocity point on the trajectory of the interface between the fuel (red) and the shell (blue). Atomic mix is assumed to penetrate some fraction of the distance between the fuel-shell interface and the fall line: this is called the penetration fraction, and is shown here as 20% (black solid line), which is an extreme upper bound for these experiments. Yield above the penetration line is truncated. (bottom) The DD-n burn rate in the simulation, with 20% penetration mix model (black) and 'clean' or without the mix model (red). The total DD-n yield is reduced by ~30% with the mix model.

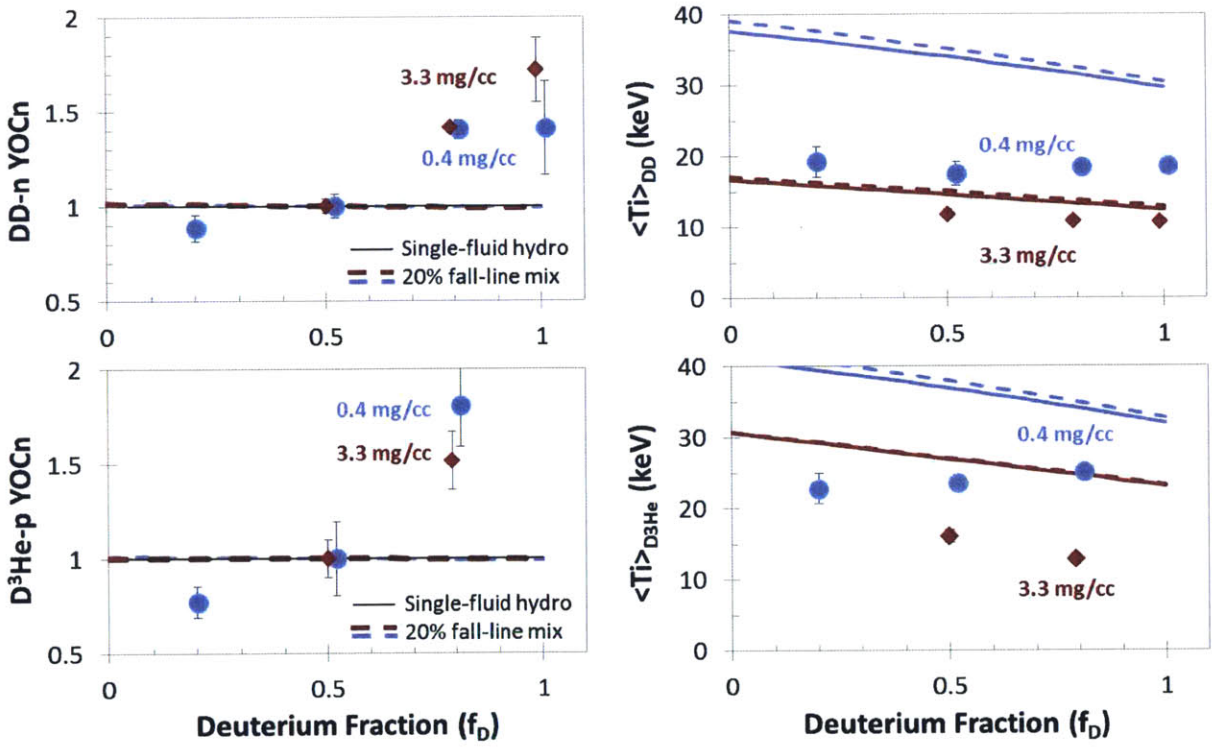

Figure 4.11. Comparison of the DD-neutron and D^3He-proton normalized yield-over-clean (points) with the results from the fall-line mix model, assuming 20% mix penetration fraction (dashed lines). Data and simulations for both the 3.3 mg/cc (red) and 0.4 mg/cc (blue) fills are shown. (left) The trend of yield-over-clean normalized (YOCn) with deuterium fraction is not changed, although the absolute yields are changed by the mix model. (right) The trend for burn-averaged ion temperature in the mix model is the same as the trend in the clean model, and is in slightly worse agreement with the data due to the truncation of the coldest regions of nuclear burn.

from the clean model. In summary, hydrodynamic mix is not significant in these implosions and also cannot produce the observed trends with deuterium fraction.

4.5 Ion Thermal Decoupling

The observed 'flat' trend in the low-density burn-averaged ion temperature data is a signature of thermal decoupling between the deuterium and helium-3. Two physical processes play a role in creating this trend: differential heating of the ion species by the shock, and a long ion-ion equilibration time that allows this differential heating to subsist for experimentally-relevant timescales. The shock delivers different amounts of energy to the two ion species as it transits the fuel, depending on their charges and masses. Ion heating from collisional strong shocks scales with the ion mass ($T_i \propto m_i v_{sh}^2$, where v_{sh} is the shock velocity), as a consequence of the hydrodynamic shock equations derived in Section 1.2.1. If the shock is an electrostatic collisionless shock, it gives the shocked ions an amount of energy that scales with the ion charge ($T_i \propto Z_i \Delta\Phi_{sh}$, where Φ_{sh} is the electric potential). In either scenario, the ^{3}He ions receive more energy than the D, by a factor of 1.5 or 2, respectively. This difference persists for the thermal equilibration timescale. Table 4.3 shows the calculated timescales for thermal equilibration between ion species using the measured plasma conditions at shock burn.[18,g] Comparing the inter-species equilibration timescales to the measured burn durations, it is likely that ion temperatures are unequilibrated during shock burn in the low-density implosions.[h]

Because the shell and laser drive are the same within each experimental series, the shock properties ($v_{sh}, \Delta\Phi_{sh}$) are expected to be constant for a fixed ρ_0, regardless of the deuterium fraction.[i] The shocked ion temperatures depend only on these shock properties and ρ_0, so the shocked deuterium- and ^{3}He-temperatures are also constant with deuterium fraction for a fixed ρ_0. Assuming the species do not equilibrate prior to nuclear burn, the burn-averaged ion temperatures will then be constant as well. This signature of ion thermal decoupling is observed in the low-density data in Figure 4.5, and contrasts with the fully equilibrated expectation that scales with the average-ion mass $\langle m_i \rangle = (3 - f_D)\, m_p$. The observed $\langle T_i \rangle$ indicate that multi-ion kinetic physics is important for thermal evolution in the low-ρ_0 experiments.

To determine the effect of thermal decoupling on the yield, the low-ρ_0 simulations were post-processed with an empirical model that was fit to the measured $\langle T_i \rangle$. The D and ^{3}He temperatures were defined in terms of the simulated ion temperature (T_{sim}) and f_D as:

$$T_{^3He} = T_D R_T = T_{sim} f_T \frac{R_T}{f_D + R_T(1 - f_D)}, \tag{4.7}$$

where the ratio of temperatures $R_T (\equiv T_{^3He}/T_D)$ and the scalar f_T are free parameters. This formulation conserves the thermal energy in the plasma up to the scalar f_T, since $T_1 f_T = f_D T_D + f_{^3He} T_{^3He}$. The effective temperature for fusion reactivity was defined as $T_{eff,ij} = (m_i T_j + m_j T_i)/(m_i + m_j)$, following Reference [12]. The effective temperature that was burn-averaged for comparison with the spectral $\langle T_i \rangle$ measurements was defined as $T_{spect,ij} = (m_i T_i + m_j T_j)/(m_i + m_j)$, following Ref [13]. The best-fit of this model to 15 measured $\langle T_i \rangle$ from the low-ρ_0 experiments was given

[g]The medium-density series are not included, as this calculation makes use of the PCIS data for burn-averaged number density.

[h]The calculated values in Table 4.3 confirm the previous argument in Section 4.2 that the electrons will be fully thermally decoupled from the ions for most of the experiment: ion-electron equilibration requires approximately $\sqrt{m_i/m_e} > 60\times$ longer than ion-ion equilibration.

[i]The 1D-HYADES simulations confirmed the invariance of shock speed in the fuel with the deuterium fraction for a constant fuel mass-density.

Table 4.3. Thermal equilibration timescales between ion species ($\tau_{D/^3He}, \tau_{^3He/D}$) and thermalization timescales within ion species ($\tau_D, \tau_{^3He}$) for various ρ_0 and f_D, calculated according to Ref [18]. Bold values exceed the measured DD-burn duration τ_{burn} (full-width at half maximum), which are also included. All time values are in picoseconds.

Density (mg/cc)	f_D	Ion-ion equilibration time				
		$\tau_{D/^3He}$	$\tau_{^3He/D}$	τ_D	$\tau_{^3He}$	τ_{burn}
0.4	0.2	**240**	**930**	**2730**	70	180
	0.5	**330**	**320**	**980**	90	180
	0.8	**890**	**190**	**600**	**250**	160
	1		140	**440**		160
3.3	0.5	120	130	**380**	40	180
	0.8	**240**	50	150	70	170
	1		40	120		170

by $R_T = 1.3 \pm 0.1$, $f_T = 0.61 \pm 0.02$, and is shown in Figure 4.12a) and b). This model improves agreement with the observed yield trends, as shown in Figure 4.12c) and d). No reasonable fit to the high-ρ_0 $\langle T_i \rangle$ data could be found using this model, suggesting that thermal decoupling is not a dominant effect. This is not surprising given the much shorter equilibration times for the high-density implosions, as shown in Table 4.3.

It is worth noting that the long ion-ion equilibration times at shock convergence imply that neither ion species is well-described as a thermal distribution. Thermalization and collisional timescales are comparable, implying that decoupled plasmas are also collisionless. If the shock itself is collisionless, this does not change the argument presented in this section: as noted earlier, a collisionless shock also delivers less energy to the D than to the ^{3}He. While this condition holds, long equilibration times imply that the average deuteron energy will remain low compared to the thermal expectation. The average center-of-mass energy for D-D collisions is then also low compared to the thermal expectation, directly reducing the inferred $\langle T_i \rangle$ and the yield. Fully kinetic simulations incorporating Monte Carlo fusion production are required to better evaluate the effects of non-thermal ion distributions on the measured data.

4.6 Measurements of Species Separation

Separation of the ion species by diffusion has been put forward as an additional explanation for the observed yield trends.[7,9] To determine whether the ion species are separated prior to fusion production, the comprehensive nuclear data were examined. Although the ion species fraction during burn is not measured directly, quantities proportional to the ion densities can be inferred by inverting Equations 4.4. The yield, $\langle T_i \rangle$, burn duration, and radius containing 50% of the nuclear burn (r_{50}) are measured for both the DD and D^{3}He reactions. Using these quantities, the burn-averaged density products can be calculated for ion species i,j as:

$$\langle n_i n_j \rangle = \left(\frac{(1+\delta_{ij})Y}{\langle \sigma v \rangle (\langle T_i \rangle)(4\pi r_{50}^3/3)\tau_{burn}} \right)_{ij}, \tag{4.8}$$

where quantities are measured for the i-j fusion reaction, and δ_{ij} is the Kronecker delta. This value was calculated for eight low-density implosions and two high-density implosions on which all of the requisite data was available, and the results are shown in Figure 4.13. The 1D-HYADES simulations were also post-processed using the same formulation, and the simulated burn-averaged

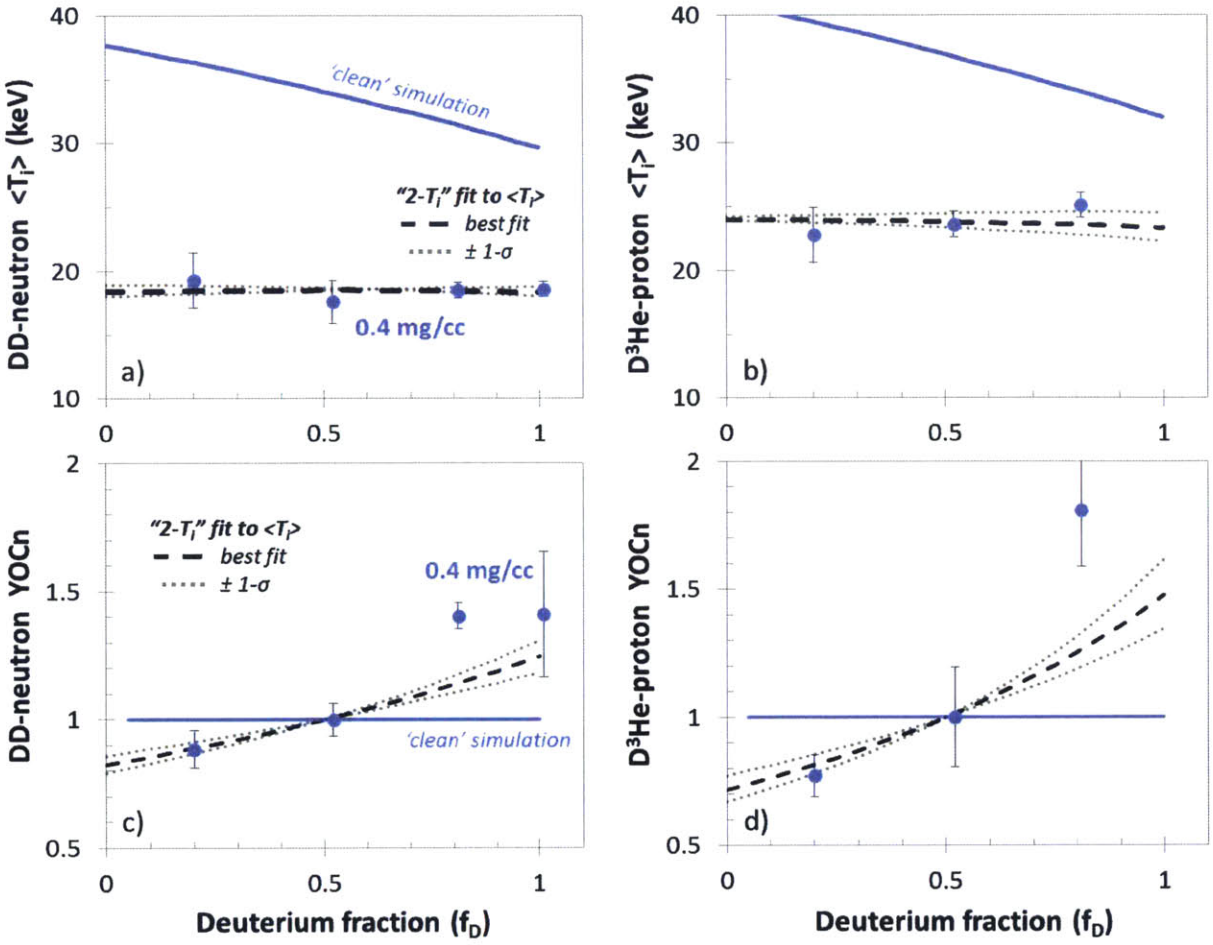

Figure 4.12. A model of decoupled D and ^{3}He ion temperatures in 1D-simulations ("2-T_i") was fit to the measured burn-averaged ion temperatures in the low-ρ_0 series. The data used in the fit (blue points), 'clean' simulated trend (blue line), the best-fit of the "2-T_i" model (black dashed) and the $\pm 1\sigma$ models (grey dotted) are shown for a) DD-neutron $\langle T_i \rangle$ and b) D^{3}He-proton $\langle T_i \rangle$ data. The best-fit parameters for the model were: $R_T = 1.3 \pm 0.1$, $f_T = 0.61 \pm 0.02$. The yield produced by the best-fit and $\pm 1\sigma$ models is compared to the measured yields of c) DD-neutrons and d) D^{3}He-protons, and better captures the observed trend in the data. Note that the yield data was not used in the fitting procedure.

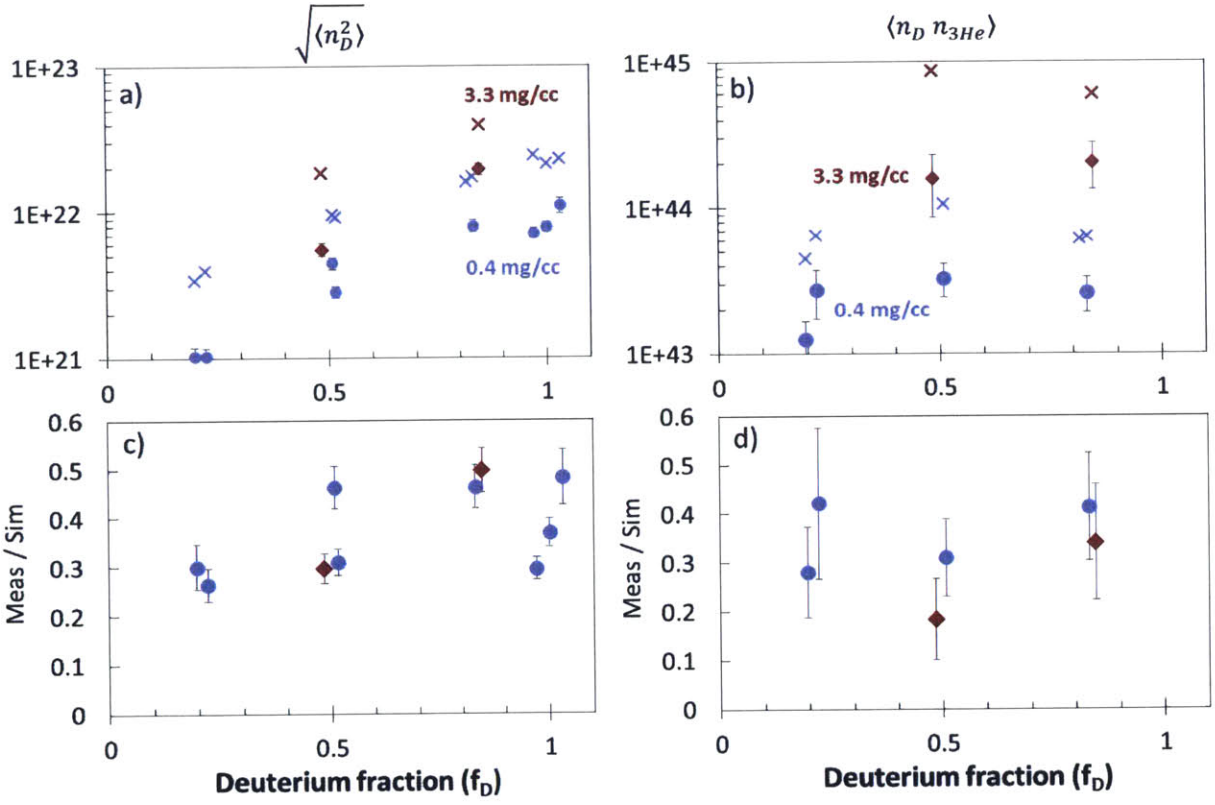

Figure 4.13. The burn-averaged density products inferred as a function of deuterium fraction: a) $\langle n_D n_D \rangle$, calculated using the DD-fusion observables (the square-root is plotted, for comparison to the deuterium ion density) and b) $\langle n_D n_{^3He} \rangle$, calculated using the D^3He-proton observables. Measured data (points) and simulations (x) follow similar trends, though slight undercompression may be observed with reduced f_D. The ratio of measured to simulated values is shown in (c,d), respectively.

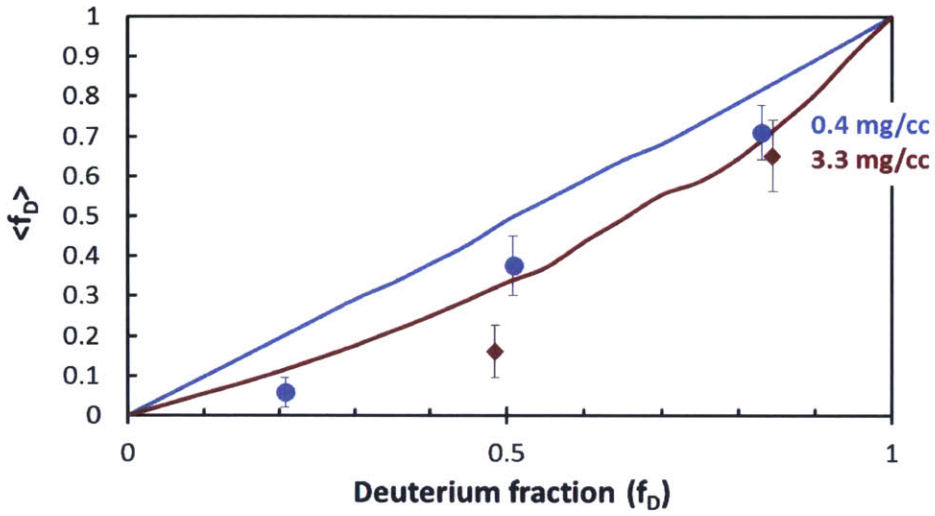

Figure 4.14. "Burn-averaged deuterium fraction" $\langle f_D \rangle$ evaluated from the experiments for low-density (blue) and high-density (red) implosions, compared to 1D-clean simulations (lines). Simulated values for $\langle f_D \rangle$ differ slightly from the fuel f_D due to differences in the D^3He and DD reactivity. Reduction of the deuterium in the core prior to burn is inferred for all implosions.

density products are shown for comparison. Note that in the simulations, the 'burn-averaged' densities calculated in this way were approximately half of the actual plasma density during burn.

The measured values are lower than the predictions by a factor of 2–3 in all cases. Because the density naively scales as $n_i \propto CR^3$, this reduction in the deuterium density would seem to imply radial undercompression of 26–44%, which is greater than is expected from the time-resolved x-ray images but comparable to the result for the nuclear burn region, especially for the high-density implosions. While there is significant scatter in the data, they suggest that the deuterium-poor shots have a lower burn-averaged deuterium density than the deuterium-rich shots (this trend appears more evidently in the high-density data). In contrast, the burn-averaged product $\langle n_D n_{^3He} \rangle$ is less suggestive of a trend with deuterium fraction. As introduced in Section 1.2.2, the mass flux from ion diffusion between two ion species is expected to be equal and opposite in direction. If diffusion, rather than undercompression, is causing a trend in the deuterium density as a function of fuel deuterium fraction, then the helium-3 density would be expected to show the opposite trend, and the product $\langle n_D n_{^3He} \rangle$ would be nearly constant. The uncertainties in the data are unfortunately too large to assert that these expected trends are clearly observed; however, the data are suggestive that ion diffusion is redistributing the D and ^3He in the fuel.

Based on the burn-averaged density products defined in Equation 4.8, the burn-averaged deuterium fraction is then defined as:

$$\langle f_D \rangle = \left(1 + \frac{\langle n_D n_{^3He} \rangle}{\langle n_D^2 \rangle}\right)^{-1}. \tag{4.9}$$

This definition is mathematically equivalent to the definition of f_D in the limit $\langle n_i \rangle = n_i$. The value of $\langle f_D \rangle$ is not expected to be identical to the initial gas f_D, because the D^3He and DD reactions are weighted differently by the plasma temperature in the implosion. However, the definition is proportional to ion species fraction to first order, and can be compared directly to simulations.

Figure 4.14 shows the inferred burn-averaged deuterium fractions during burn for the low- and high-density implosions, compared to the 1D-simulated value of the same quantity. The measured

$\langle f_D \rangle$ are lower than the predicted values, implying that species separation significantly perturbs the ion distributions prior to bang-time. This is the first direct evidence of ion species separation in an ICF-relevant plasma. For the high-density implosions, the amount of species separation appears to depend on the deuterium fraction. Comparing the high-ρ_0 equimolar result to the simulated trend, the fuel deuterium fraction at bang-time is reduced from $f_D = 0.48$ to 0.277 [+0.094, −0.107]. In contrast, the high-ρ_0 implosion with $f_D = 0.84$ implies a fuel deuterium fraction at bang-time of 0.804 [+0.057, −0.095], which is consistent with little or no species separation. For the low-density implosions, all the experiments appear to be similarly affected: the initial deuterium fractions of $f_D = 0.21$, 0.51, and 0.83 were reduced to 0.059 [+0.038, −0.038], 0.395 [+0.073, −0.084], and 0.729 [+0.065, −0.077], respectively.

While these measurements are indicative of species separation, they do not require a particular mechanism for the species separation. Ion diffusion is a likely candidate for the high-density implosions, which behave relatively hydrodynamically. For the low-density implosions, which have already been shown to be nearly collisionless during burn, diffusion is unlikely to play a significant role, because it is fundamentally a collisional mechanism. Several possible explanations for the low-density species separation exist. Diffusion early in the implosion may seed the species separation, which subsists when the plasma becomes collisionless. Alternatively, the deuterium may be 'more collisionless' than the ^{3}He (the mean-free-path of a deuteron was shown to be ~3.3× that of a ^{3}He-ion in Section 4.3.1) and fuse at larger radii than the ^{3}He. A third possibility is that the bulk fuel ions may remain collisional throughout the implosion and the species separate diffusively, while the high-energy ions on the tail of the Maxwellian distribution become collisionless, producing the flat trend in $\langle T_i \rangle$ observed in Section 4.5. Distinguishing the actual dynamics underlying the species separation in the plasma remains as future work, and may require improved diagnostic precision. Because eight measurements are involved in each calculated value for $\langle f_D \rangle$, the final uncertainty of the inferred value is difficult to control. Improvements in the diagnostic accuracy – in particular, better knowledge of the plasma burn-averaged ion temperatures – could improve the accuracy of this technique in future experiments.

4.6.1 Burn-averaged mean-free-path

To demonstrate that long ion-ion mean-free-path effects are not the cause of the observed yield and temperature anomalies, a burn-averaged ion-ion mean-free-path has been evaluated based solely on the experimental data. From the burn-averaged density products inferred using Equation 4.8, the burn-average density can be estimated, providing the necessary information for a burn-average ion-ion mean-free-path.

The result of these calculations is shown in Figure 4.15. A factor of ~5× increase in the Knudsen number is observed in the low-density implosions, as deuterium fraction increases from 20% to 100%. This trend is approximately half as extreme as is expected from the theoretical arguments given in Section 4.3.1, due in part to an observed reduction in burn-average total ion density with reduced deuterium fraction. However the finding confirms that the kinetic physics which has previously been studied as a source for anomalous reduction of the shock yield, such as Knudsen-layer ion loss and ion diffusion, are not responsible for the yield variation as a function of deuterium fraction.

4.6.2 Reduced Ion Kinetic simulations

Using a 1D-radiation hydrodynamic simulation incorporating a model of plasma ion kinetic transport and other reduced ion kinetic (RIK) models,[32] the effect of species separation in these experi-

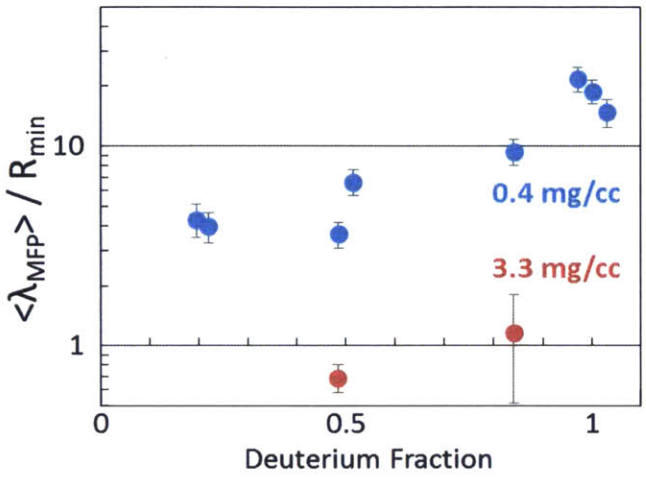

Figure 4.15. Knudsen number inferred from experimental observables ($N_k \equiv \langle\lambda_D\rangle/R_{min}$). The Knudsen number is calculated to be five times larger for the pure deuterium implosions ($f_D = 1$) compared to deuterium poor implosions ($f_D = 0.2$). Increased Knudsen number is associated with reduced nuclear performance due to the effect of kinetic physics, as shown in Figure 4.4.

Table 4.4. Parameters for the Reduced Ion Kinetic (RIK) simulations, calibrated to a high-density (ρ_0 = 3.1 mg/cc) and a low-density (0.4 mg/cc) 50:50 D^3He-gas filled thin-glass implosion performed on March 14th, 2013. Parameter used include laser absorption fraction (f_{ls}); electron flux limiter (f_e); Knudsen-layer reactivity reduction (f_{Knu}), ion kinetic transport (f_{idifm}), ion thermal conduction (f_{icndm}), and ion thermal flux-limit multiplier (f_{iflxm}). The atomic mix model parameter (f_{mix}) was set to zero.

Shot #	ρ_0	f_{ls}	f_e	f_{Knu}	f_{idifm}	f_{icndm}	f_{iflxm}
69055	3.1	0.63	0.06	0.1	1.2	1	0.3
69066	0.4	0.63	0.06	0.1	0.1	6	1.0

ments was investigated. The RIK simulations were provided by Nels Hoffman, LANL. Two sets of RIK model parameters were calibrated using an earlier set of shock-driven implosions performed on March 14th, 2014 using identical targets and laser impulses to the high- and low-density campaigns described here.[29] The best-fit to five observables from equimolar ($f_D = 0.5$) high- and low-ρ_0 implosions (3.1 and 0.4 mg/cc, respectively) was found by varying the RIK parameters, which were introduced in Section 3.5.1. The best-fit RIK parameters for the high- and low-density cases are shown in Table 4.4. For the high-density model, a slightly better fit was obtained by allowing the ion thermal flux limit multiplier f_{iflxm} to vary, which was set to 1 for the thin-CD study presented in Section 3.5.1. These high- and low-density models were applied while varying f_D to obtain RIK-simulated yield and temperature trends, which are compared to the observed high- and low-density data in Figures 4.16a-b) and c-d), respectively. The RIK simulations captured the yield trend for the high-density experiments, while also matching the measured $\langle T_i\rangle$.

A radial profile of the ion species densities at bang-time from the equimolar, high-ρ_0 RIK simulation is shown in Figure 4.17. In this simulation, ion diffusion had reduced f_D in the core from 0.5 to 0.33 prior to shock-bang, in agreement with the results in Figure 4.14. The deuterium was redistributed to the outer regions of the fuel, where it fuses less efficiently due to lower temperatures and admixture with the shell plasma.

As discussed in Section 3.6, the RIK models include flux-limited ion thermal conduction, and account for Knudsen-layer reactivity reduction. Due to these effects, the model closely matches the absolute observed temperatures and yields for both the high- and low-density data. However, the RIK simulations do not capture the observed $\langle T_i\rangle$ trends for the low-ρ_0 data. This is not surprising, as the models do not include separate ion thermal distributions. More fundamentally, the RIK models are kinetic perturbations on bulk hydrodynamic evolution, which may not extend

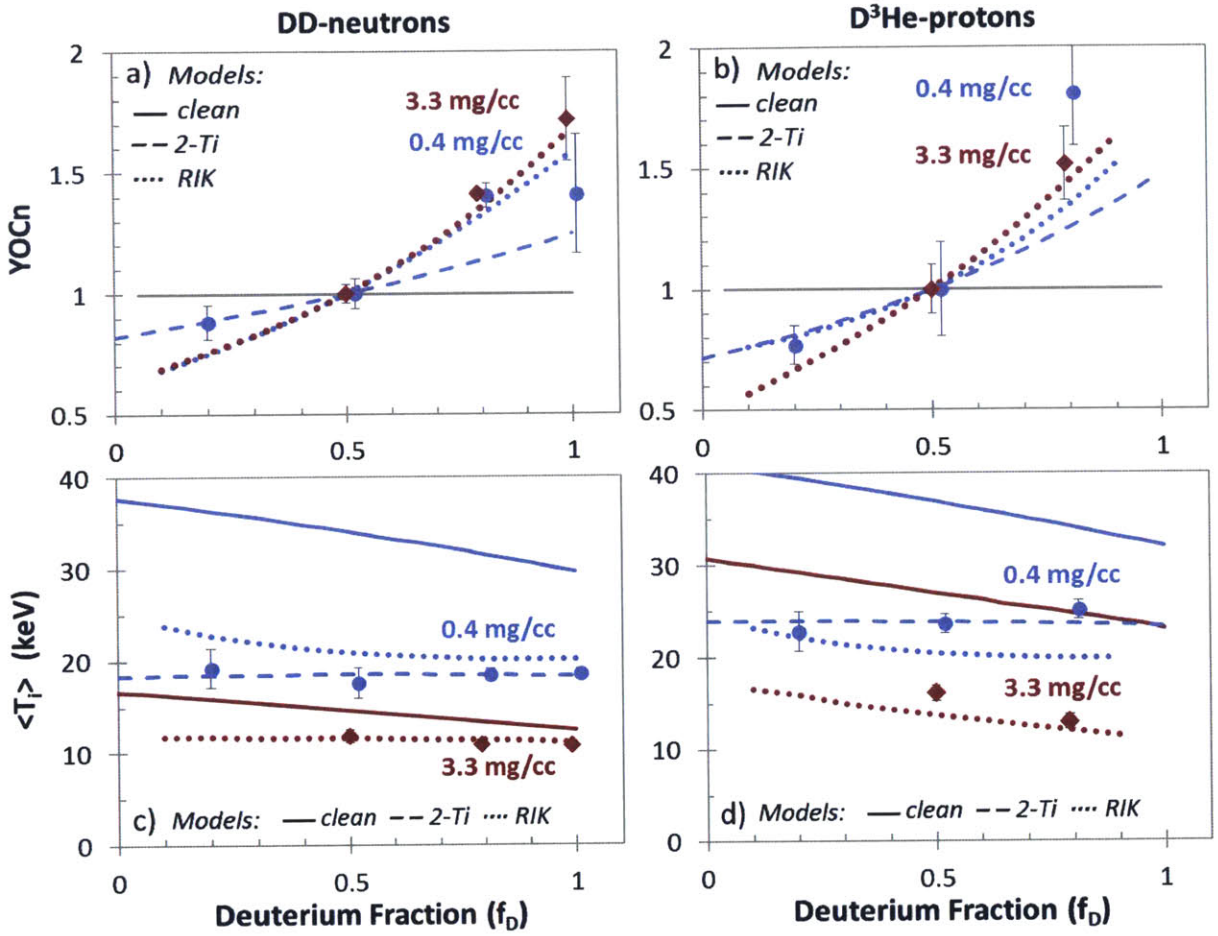

Figure 4.16. Trends with deuterium fraction in (a,b) DD-n and D^3He-p Yield-over-clean, normalized and (c,d) DD-n and D^3He-p burn-averaged ion temperature, from the Reduced Ion Kinetic simulations (dotted lines), compared to the high- (red points) and low-density data (blue points), and 1D-simulations (solid lines). The "2-T_i" model best-fit to the low-density $\langle T_i \rangle$ is included for comparison (dashed blue). The RIK simulations, which include models of kinetic ion mass- and energy-transport as well as Knudsen-layer fusion reduction, match the trend in both yield and temperature for the high-density implosions. The absolute temperatures of the low-density implosions are closely matched, but the observed 'flat' trend is not captured. RIK simulations provided by Nels Hoffman, LANL.

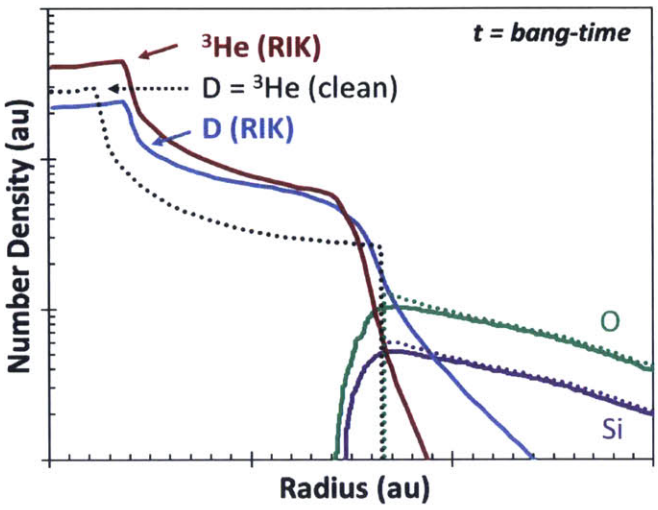

Figure 4.17. Density profiles near bang-time for an equimolar D^{3}He implosion with ρ_0 = 3.3 mg/cc, comparing 1D-average-ion 'clean' simulations (dotted) with simulations including reduced ion kinetic models of ion diffusion, ion thermal conduction, and tail-ion loss (solid). The deuterium (blue) diffuses to larger radii and ^{3}He (red) is concentrated in the core, such that at peak burn f_D = 0.33. The RIK simulations reproduce the observed yields, as shown in Figure 4.16. RIK simulations provided by Nels Hoffman, LANL.

to describe the fully kinetic behavior implied by thermal decoupling. This discrepancy supports ion thermal decoupling as a dominant physical effect in the low-density regime.

4.7 Summary

A series of D^{3}He-gas-filled shock-driven implosions have demonstrated anomalously low yields as deuterium fraction is reduced. In addition, the implosions containing the lowest initial gas density (0.4 mg/cc) generated burn-averaged ion temperatures that were anomalously invariant with deuterium fraction. These anomalies were shown not to be caused by hydrodynamic instabilities, turbulent atomic mix, or previously-observed kinetic plasma effects associated with long ion-ion mean-free-paths. Two kinetic processes associated with multiple ion species were proposed to explain these anomalies: ion thermal decoupling and species separation.

The 'flat' burn-averaged ion-temperature trend in the low-density implosions was found to be a signature of thermal decoupling between the deuterium and ^{3}He ion populations. Ion-ion thermalization times in the low-density implosions were calculated to be in excess of the burn duration, suggesting that the preferential heating of ^{3}He ions by the shock subsists through the peak nuclear production. This thermal decoupling leads to constant deuterium and ^{3}He ion temperatures as deuterium fraction is varied, producing the observed invariant trends in $\langle T_i \rangle$. A 1D-radiation hydrodynamic simulation was post-processed to allow for different D and ^{3}He temperatures, and fit to the burn-averaged temperature data. The best fit of this model to the observed $\langle T_i \rangle$ produces yields in better agreement with the observed trends.

A burn-averaged deuterium fraction was inferred from comprehensive nuclear measurements, and was lower than expected in all experiments. This result provided the first direct evidence of ion species separation in ICF implosions. Simulations including ion diffusion, among other reduced ion kinetic (RIK) models, demonstrate significant reduction of the core deuterium fraction prior to bang-time, in agreement with the experimental data. These simulations produce trends in yield and burn-averaged temperature in agreement with the high-density observations.

These experimental results strongly imply that ion kinetic effects play an important role in the low-density, strongly-shocked plasma of the incipient hotspot in ICF ignition implosions. The incipient hotspot plasma has both a comparable mass density (0.3 mg/cc) and a comparable shock-strength (M$\sim$10–50) as the experiments presented in this chapter. The kinetic effects described

here may impact the hotspot adiabat, affecting the efficiency of the compression phase. Moreover, species separation seeded prior to shock-bang may persist until peak compression and burn. Fully kinetic simulations, which are now under development, will be required to simultaneously capture the impact of both non-thermalized ions and species separation, and help us to better understand the role these kinetic effects play in ICF ignition designs.

4.8 References

1. S. W. Haan, J. D. Lindl, D. A. Callahan *et al.*, "Point design targets, specifications, and requirements for the 2010 ignition campaign on the National Ignition Facility," Physics of Plasmas, **18**, 051001 (2011).
2. W. H. Goldstein, "Science of Fusion Ignition on NIF," Technical Report LLNL-TR-570412, Lawrence Livermore National Laboratory (2012).
3. J. R. Rygg, J. A. Frenje, C. K. Li *et al.*, "Tests of the hydrodynamic equivalence of direct-drive implosions with different D_2 and ^{3}He mixtures," Physics of Plasmas, **13**(5), 052702 (2006).
4. D. T. Casey, J. A. Frenje, M. Gatu Johnson *et al.*, "Evidence for stratification of deuterium-tritium fuel in inertial confinement fusion implosions," Physical Review Letters, **108**, 075002 (2012).
5. H. W. Herrmann, J. R. Langenbrunner, J. M. Mack *et al.*, "Anomalous yield reduction in direct-drive deuterium/tritium implosions due to ^{3}He addition," Physics of Plasmas, **16**(5), 056312 (2009).
6. D. C. Wilson, G. A. Kyrala, J. F. B. Jr. *et al.*, "The effects of pre-mix on burn in ICF capsules," Journal of Physics: Conference Series, **112**, 022015 (2008).
7. P. Amendt, O. Landen, H. Robey *et al.*, "Plasma Barodiffusion in Inertial-Confinement-Fusion Implosions: Application to Observed Yield Anomalies in Thermonuclear Fuel Mixtures," Physical Reviev Letters, **105**, 115005 (2010).
8. P. Amendt, S. C. Wilks, C. Bellei *et al.*, "The potential role of electric fields and plasma barodiffusion on the inertial confinement fusion database," Physics of Plasmas, **18**(5), 056308 (2011).
9. G. Kagan and X.-Z. Tang, "Electro-diffusion in a plasma with two ion species," Physics of Plasmas, **19**(8), 082709 (2012).
10. G. Kagan and X.-Z. Tang, "Thermo-diffusion in inertially confined plasmas," Physics Letters A, **378**(21), 1531 (2014).
11. P. Amendt, C. Bellei, S. Wilks *et al.*, "Shock-driven resistive heating in mixed species thermonuclear fuels," Physical Review E ((to be submitted)).
12. C. Bellei, H. Rinderknecht, A. Zylstra *et al.*, "Species separation and kinetic effects in collisional plasma shocks," Physics of Plasmas, **21**(5), 056310 (2014).
13. A. Inglebert, B. Canaud and O. Larroche, "Species separation and modification of neutron diagnostics in inertial-confinement fusion," EPL (Europhysics Letters), **107**(6), 65003 (2014).
14. B. E. Peigney, O. Larroche and V. Tikhonchuk, "Ion kinetic effects on the ignition and burn of inertial confinement fusion targets: A multi-scale approach," Physics of Plasmas, **21**(12), 122709 (2014).
15. T. R. Boehly, D. L. Brown, R. S. Craxton *et al.*, "Initial performance results of the OMEGA laser system," Optics Communications, **133**(1-6), 495 (1997).
16. Y. Lin, T. J. Kessler and G. N. Lawrence, "Distributed phase plates for super-Gaussian focal-plane irradiance profiles," Optics Letters, **20**(7), 764 (1995).
17. S. P. Regan, J. A. Marozas, J. H. Kelly *et al.*, "Experimental investigation of smoothing by spectral dispersion," Journal of the Optical Society of America B, **17**(9), 1483 (2000).
18. J. D. Huba, "NRL Plasma Formulary," (online), Naval Research Laboratory, Washington, D.C. (2006).
19. V. Y. Glebov, C. Stoeckl, T. C. Sangster *et al.*, "Prototypes of National Ignition Facility neutron time-of-flight detectors tested on OMEGA," Review of Scientific Instruments, **75**(10), 3559 (2004).
20. F. H. Séguin, J. A. Frenje, C. K. Li *et al.*, "Spectrometry of charged particles from inertial-confinement-fusion plasmas," Review of Scientific Instruments, **74**(2), 975 (2003).
21. H. Brysk, "Fusion neutron energies and spectra," Plasma Physics, **15**, 611 (1973).

22. L. Ballabio, J. Källne and G. Gorini, "Relativistic calculation of fusion product spectra for thermonuclear plasmas," Nuclear Fusion, **38**(11), 1723 (1998).

23. J. T. Larsen and S. M. Lane, "HYADES - A plasma hydrodynamics code for dense plasma studies," Journal of Quantitative Spectroscopy and Radiative Transfer, **51**, 179 (1994).

24. W. Seka, H. A. Baldis, J. Fuchs *et al.*, "Multibeam Stimulated Brillouin Scattering from Hot, Solid-Target Plasmas," Physical Review Letters, **89**(17), 175002 (2002).

25. R. A. Lerche, D. W. Phillion and G. L. Tietbohl, "25 ps neutron detector for measuring ICF-target burn history," Review of Scientific Instruments, **66**(1), 933 (1995).

26. J. A. Frenje, C. K. Li, F. H. Séguin *et al.*, "Measuring shock-bang timing and ρR evolution of D^3He implosions at OMEGA," Physics of Plasmas, **11**(5), 2798 (2004).

27. F. H. Séguin, J. L. DeCiantis, J. A. Frenje *et al.*, "Measured dependence of nuclear burn region size on implosion parameters in inertial confinement fusion experiments," Physics of Plasmas, **13**(8), 082704 (2006).

28. D. K. Bradley, P. M. Bell, O. L. Landen *et al.*, "Development and characterization of a pair of 30-40 ps x-ray framing cameras," Review of Scientific Instruments, **66**(1), 716 (1995).

29. M. J. Rosenberg, H. G. Rinderknecht, N. M. Hoffman *et al.*, "Exploration of the Transition from the Hydrodynamiclike to the Strongly Kinetic Regime in Shock-Driven Implosions," Physical Review Letters, **112**, 185001 (2014).

30. M. J. Rosenberg, F. H. Séguin, P. A. Amendt *et al.*, "Assessment of Ion Kinetic Effects in Shock-Driven Inertial Confinement Fusion (ICF) Implosions Using Fusion Burn Imaging," Physics of Plasmas (in preparation).

31. C. Bayer, M. Bernard, D. Billon *et al.*, "Laser implosion of microballoons: study of the transition from exploding-pusher to ablative regime," Nuclear Fusion, **24**(5), 573 (1984).

32. N. M. Hoffman, G. B. Zimmerman, K. Molvig *et al.*, "Reduced models for the ion-kinetic regime in inertial-confinement-fusion capsule implosions," Physics of Plasmas (to be submitted).

5

Conclusion

In this thesis, laser-driven spherical implosions were used to produce strongly shocked, high-energy-density plasmas, with the goal of studying the emergence of kinetic dynamics in plasmas relevant to inertial confinement fusion (ICF). The implosions were performed on the OMEGA laser facility, and are comparable in both initial vapor density (~0.4 mg/cc) and shock strength (Mach number M~10–50) to the central plasma of hot-spot ignition experiments on the National Ignition Facility (NIF) during the shock-transit phase. Due to a combination of low plasma density and high plasma temperature, the ions have an average mean-free-path that is comparable to the scale size of the experiment. In this situation, the hydrodynamic equations that are typically used to predict the evolution of the plasma begin to break down. The work of this thesis documents the emergence of kinetic behaviors in shock-driven implosions, primarily through the interpretation of comprehensive nuclear diagnostic signatures.

In support of this research and the broader ICF ignition effort, new diagnostics for the nuclear bang-time were developed, as described in Chapter 2. The Particle Time-of-Flight (PTOF) diagnostic, a CVD-diamond based high-voltage diode detector, provides unique diagnostic capability at both OMEGA and the NIF. The time of peak nuclear fusion production in ICF experiments is inferred from the PTOF data by subtracting the time-of-flight for these products to the PTOF detector from the recorded detection time. On OMEGA, PTOF can measure the bang-time using D^3He-proton yields of 10^6, well below the sensitivity of other burn history diagnostics. On the NIF, PTOF is the only diagnostic capable of reporting the nuclear bang-time using neutrons with yields below 10^{13}, and is the only diagnostic capable of measuring the bang-time using DD-neutron and D^3He-proton signals. Additionally, PTOF has recently measured the bang-time of both D^3He-protons from the shock-phase and DD-neutrons from the compression-phase on a single implosion: a first at the NIF. This accurate measurement of the compression-shock bang-time differential ("ΔBT") strongly constrains the modeling of implosion dynamics, especially in combination with the measurement of the areal density of the implosion at shock bang-time from the WRF proton spectra.

The PTOF detector cannot record the D^3He-proton shock-bang time if the x-ray background is too large, as is the case for the standard gas-filled hohlraum target used in the ignition design and ignition-surrogate implosions. To provide this dual shock- and compression-bang time measurement on ignition-scale implosions, a diagnostic upgrade of the PTOF was also designed. The Magnetic Particle Time-of-Flight (MagPTOF) diagnostic includes a magnet to bend the charged D^3He-protons onto the detector around substantial line-of-sight x-ray shielding. The detectors, cabling, and electronics are identical to the PTOF to preserve cross-timing. The MagPTOF is predicted to reduce the x-ray background by a factor of 1000 compared to the unshielded detector, while delivering D^3He-protons in the energy range 6–16 MeV to the detector. Simulations of neutron

transport indicate that the DD-neutron signal, while reduced by scattering, will provide a robust DD-neutron bang-time. This new diagnostic will directly probe the shock dynamics of the D^3He-gas filled surrogate-ignition implosions, and should directly confirm that the ΔBT varies by a factor of 2 with shot parameters, which is not predicted by the hydrodynamic simulations and suggests that kinetic physics is playing an important role in the shock phase. The MagPTOF is currently being manufactured for initial shot operations in 2015.

Experiments using the OMEGA laser to directly investigate the role of kinetic physics in fuel-shell mix were presented in Chapter 3. Implosions of thin-walled (5 μm) deuterated plastic targets filled with pure ^3He produced D^3He-proton yields comparable to implosions of identical targets filled with pre-mixed 50:50 D^3He gas. The targets with the initially-separated reactants can only produce the observed D^3He-proton yields by substantial atomic mixing of the deuterium from the shell into the gas. The turbulent mix processes that have been studied extensively in ICF are produced by hydrodynamic instability growth at the fuel-shell interface, which was shown to be negligible in these experiments. Rapid burn-through of the shell material truncates ablation-phase instability growth; small radial convergences (~4–5) and negligible remaining shell mass make Rayleigh-Taylor mode growth in the compression phase insignificant. This expectation was confirmed by 2D-DRACO simulations of the implosions, which demonstrated highly 1D implosion behavior. Of several kinetic mechanisms considered, diffusive ion mass transport is the likeliest explanation for the substantial mix observed. In the 200 ps between shell burn-through and peak nuclear production, the temperature of the fuel-shell interface increases by over an order of magnitude, dramatically increasing the diffusion coefficient which scales as $D \propto T^{5/2}$. Post-processing of 1D-simulations with a simple diffusion model demonstrated the development of a diffusion layer prior to shock rebound. Simulations with an integrated ion diffusion model along with other reduced ion kinetic (RIK) models were able to capture the trends in both D^3He-proton and DD-neutron yields and burn-averaged ion temperatures in these experiments. Several alternative kinetic models were investigated, including electrostatic ion acceleration at the shock front and beam-target fusion scenarios. An upper bound on the shock-acceleration of shell deuterons into the ^3He fuel is calculated to be comparable to the level required to produce the observed yields. All the beam-target mechanisms were predicted to produce yields an order of magnitude below those observed. These experiments provide a valuable benchmark for ion diffusion theory and simulations in high-energy-density plasmas. Ion mass transport in plasmas remains an active area of research, and is important in the ablation of the cryogenic DT fuel that forms the main mass of the hotspot in the ICF ignition design.

A series of experiments to study multiple-ion kinetic dynamics relevant to the shock-phase of ICF implosions was presented in Chapter 4. Thin-walled (2.3 μm) glass targets were filled with various ratios of deuterium and ^3He at high-, medium-, and low-initial mass density, and imploded on the OMEGA laser. The nuclear production in these implosions scaled anomalously with the deuterium ion fraction, when compared to simulations. The ^3He-rich implosions produced less nuclear yield by 50% compared to the pure deuterium implosions with the same gas density. Additionally, in the lowest initial-density implosions (0.4 mg/cc) the burn-averaged ion temperatures were observed to be invariant with deuterium fraction, while hydrodynamic simulations predicted an increase in $\langle T_i \rangle$ with reduced deuterium. Two kinetic effects were invoked to explain these anomalous observations: thermal decoupling of the D and ^3He ion populations, and separation of the ion species by diffusion.

The invariance of the burn-averaged ion temperature was shown to be a signature of ion thermal decoupling. The shock heats the ^3He ions more than the deuterium ions, and the shocked temperatures of the individual species depend only on the properties of the shock, which are identical for a given mass density in the gas. If the equilibration time is short compared to the burn, these ion temperatures equilibrate to an intermediate value that depends on the ion species fractions, as simulated. If the equilibration time is long enough that the temperature difference subsists through

nuclear production, as was calculated for the low-density implosions, then the burn-averaged temperatures will be invariant for a given mass density, as observed. This is the first demonstration of thermal decoupling between multiple ion species in an ICF implosion. A model of thermal decoupling was implemented by post-processing of 1D-simulations, and produced a good fit to the measured ion temperatures. This model was found to produce better agreement with the observed yield trends as well.

Comprehensive nuclear data (including the yields, temperatures, burn durations, and burn profile radii from two reactions) were used to calculate a burn-averaged deuterium fraction in the experiments. This value was reduced from the expected value for all experiments: for example, in the high-density 50:50 D^3He implosion, the burn-averaged deuterium fraction was consistent with $f_D = 0.28 \pm 0.10$ in the core plasma. This is the first observation in an ICF implosion of ion species separation, which has been proposed as an explanation for previously-reported anomalies in the compression yield. Reduced ion kinetic simulations including ion diffusive mass transport demonstrate diffusion of deuterium out of the core, producing a deuterium fraction during burn in agreement with the measured values. These simulations recapture both the absolute yields and yield trends observed in the data.

The experiments presented in this thesis conclusively demonstrate that the kinetic effects associated with multiple-ion species – in particular, ion diffusion and ion thermal decoupling – play an important role in ICF-relevant plasmas. Ion diffusion actively redistributes the ion species in plasmas with moderate bulk ion-ion mean-free-paths relative to the scale lengths of the experiment. This redistribution is shown to occur during the shock phase in multiple-ion species plasmas, such as the DT plasma in the ignition design, and is predicted to occur during the compression phase as well. Hydrodynamic modeling of the ignition experiments does not incorporate ion diffusion, which may significantly impact the assembly of the fuel at the precise levels required for ignition. Future experiments may directly measure the species separation in the compression phase using similar techniques to those developed here. For example, the burn-averaged deuterium fraction may be measured in compressively-driven D^3He-filled implosions by imaging the DD-neutrons to obtain the burn region (rather than the DD-protons, which will not escape). Such experiments would conclusively determine whether species separation directly causes the anomalies observed in the compression-yield, or whether a related effect (for example, resistive heating) is the primary cause. In contrast, thermal decoupling is a fully-kinetic phenomenon that occurs only in the shock-phase of the low-density experiments. The shock phase of the ignition design has a comparable density and shock strength to these experiments, strongly suggesting that the central plasma may go through a decoupled period prior to the deceleration phase. Such decoupling could redistribute mass and energy in the incipient hotspot and modify its entropy, thereby changing the initial conditions for compression and ignition. Additional experiments will help to better understand the scale of this effect and the properties of the resulting plasma. To fully account for the impact of these effects in ICF, fully kinetic simulations of the ICF implosion must be developed: the results in this thesis will provide a valuable benchmark for verification of these new techniques.

Ultimately, the work presented in this thesis contributes to a better understanding of the physical processes that are important in these highly dynamic, high-energy-density states, which is an essential prerequisite for the success of inertial confinement fusion.

Appendix A

Definitions of Plasma Parameters

A.1 Derivation of the Collision Frequency and the Mean-Free-Path

The collision frequency in a thermal plasma ν_{th} is typically derived from the rate of momentum loss for a particle in that plasma:[a]

$$\frac{dp}{dt} = -\nu p \quad \rightarrow \quad \nu_{th} \equiv -\frac{1}{p}\frac{dp}{dt}. \tag{A.1}$$

Under this definition, the thermal collision frequency is essentially the rate at which the directed momentum of a particle is lost: one might think of it as the rate at which the particle's momentum is 'scrambled.' This momentum is not lost to the system as a whole, but is redistributed through collisions to other particles.

This definition suggests that the mean free path of a particle λ can be analogously defined as the distance scale for momentum loss, as follows:

$$\frac{dp}{dl} = -\frac{p}{\lambda} \quad \rightarrow \quad \frac{1}{\lambda} \equiv -\frac{1}{p}\frac{dp}{dl}. \tag{A.2}$$

The momentum loss for a particle (1) from a single interaction with another particle (2) follows from Coulomb scattering as $\Delta p_x = 2p_x(m_r/m_1)(1 - \cos\chi_c)$, where m_r is the reduced mass and $\chi_c = 2\cot^{-1}(b/b_{90})$ is the scattering angle in the center-of-mass frame. Here, b is the impact parameter and $b_{90} = q_1 q_2/(4\pi\epsilon_0 m_r v_1^2)$ is the impact parameter for 90° scattering. Assuming small-angle scattering, the term $(1 - \cos\chi_c) \approx 2b_{90}^2/b^2$. The rate of momentum loss as a function of unit distance for a single particle colliding with a field of (identical) particles is then given from an integral over the impact parameter, which results in:

$$\frac{dp_1}{dl} = n_2 p_1 \frac{m_2}{m_1 + m_2} 4\pi b_{90}^2 \ln\Lambda. \tag{A.3}$$

The time derivative of momentum is simply $dp/dt = (dp/dl)v_r$, where v_r is the relative velocity of the particles.

To obtain the thermal collision frequency and mean-free-path, the rate of momentum loss must be integrated over the distribution function of both the 'test' and 'field' species. As discussed,

[a] This derivation follows closely the derivation of collision frequency found in Reference [1], which has been extended here to derive the mean free path as well.

the mean-free-path is given directly by $\lambda_{th}^{-1} = -(1/p)\int (dp/dl) f_1 f_2 d^3v_1 d^3v_2$, whereas the collision frequency is given by $\nu_{th} = -(1/p)\int v_r (dp/dl) f_1 f_2 d^3v_1 d^3v_2$. The two distributions f_1, f_2 are treated as counter-flowing Maxwellians with a temperature T and drift velocity v_d in the center-of-mass frame,

$$f_i = n_i \left(\frac{m_i}{2\pi T}\right)^{\frac{3}{2}} \exp\left[-\frac{m_i(\vec{v}_i - \vec{v}_{di})^2}{2T}\right], \tag{A.4}$$

where $m_r\vec{v}_d = m_1\vec{v}_{d1} = -m_2\vec{v}_{d2}$ and $v_d^2 \ll 2T/m$.[b] The product $f_1 f_2$ can be expanded to first order in $\vec{v}_d$ as follows:

$$f_1 f_2 = n_1 n_2 \left(\frac{m_1}{2\pi T}\right)^{\frac{3}{2}} \left(\frac{m_2}{2\pi T}\right)^{\frac{3}{2}} \exp\left[-\frac{m_1 v_1^2}{2T} - \frac{m_2 v_2^2}{2T}\right] \left(1 + \frac{\vec{v}_1 \cdot m_1\vec{v}_{d1}}{T} + \frac{\vec{v}_2 \cdot m_2\vec{v}_{d2}}{T}\right), \tag{A.5}$$

or, in the center-of-mass frame ($\vec{v}_r = \vec{v}_1 - \vec{v}_2$, $V = (m_1v_1 + m_2v_2)/(m_1 + m_2)$, $M = m_1 + m_2$):

$$f_1 f_2 = n_1 n_2 \left(\frac{M}{2\pi T}\right)^{\frac{3}{2}} \left(\frac{m_r}{2\pi T}\right)^{\frac{3}{2}} \exp\left[-\frac{MV^2}{2T} - \frac{m_r v_r^2}{2T}\right] \left(1 + \frac{m_r}{T}\vec{v}_d \cdot \vec{v}_r\right). \tag{A.6}$$

This formulation breaks the symmetry of the integral of dp/dl over d^3v_r allowing an answer to be evaluated.

After removing constant terms and evaluating the integral over center-of-mass velocity, the remaining integral for mean free path becomes

$$\frac{1}{\lambda_{ij}} = -\frac{1}{p_i} 4\pi \left(\frac{q_i q_j}{4\pi\epsilon_0}\right)^2 \ln\Lambda n_i n_j \left(\frac{m_r}{2\pi T}\right)^{\frac{3}{2}} \left(\frac{m_r v_d}{T}\right) \int \frac{v_{rx}^2}{v_{red}^4} \exp\left[-\frac{m_r v_r^2}{2T}\right] d^3v_r, \tag{A.7}$$

where we have selected without loss of generality $\vec{v}_d = v_d\hat{x}$. Since v_r is spherically symmetric, there is nothing special about v_{rx}, and so $\int v_{rx}^2 f(v_r) = \int v_{ry}^2 f(v_r) = \int v_{rz}^2 f(v_r) = (1/3)\int v_r^2 f(v_r)$. The remaining integral is then a Gaussian integral. Taking species 1 for the test species, the momentum density is $p_1 = n_1 m_1 v_d$ and the answer follows:

$$\frac{1}{\lambda_{12}} = \frac{4\pi}{3} \left(\frac{q_1 q_2}{4\pi\epsilon_0}\right)^2 \frac{n_2 m_r}{T^2 m_1} \ln\Lambda. \tag{A.8}$$

The collision frequency follows from similar evaluation of its integral:

$$\nu_{12} = \frac{4\sqrt{2\pi}}{3} \left(\frac{q_1 q_2}{4\pi\epsilon_0}\right)^2 \frac{n_2\sqrt{m_r}}{m_1 T^{3/2}} \ln\Lambda. \tag{A.9}$$

From these two equations, the relationship between the mean free path and the collision frequency is determined to be

$$\nu_{12}\lambda_{12} = \sqrt{\frac{2T}{\pi m_r}}. \tag{A.10}$$

The common definition, $\lambda_{12,common} = v_{th,1}/\nu_{12}$ for $v_{th,1} = \sqrt{2T/m_1}$, is observed to be equal to the more accurate value derived here multiplied by a factor of $\sqrt{(\pi m_2)/(m_1 + m_2)}$. This factor determines that the actual mean free path varies from $\pi^{-1/2} \sim 56\%$ of the typical value up to

[b] Effectively we are looking at small fluctuations in the relative drift velocities. There has to be some momentum flux in order for it to change over time (or distance): taking $v_d = 0$ causes the total momentum to be zero and the integral vanishes due to symmetry. Random scattering in the plasma will generate such small fluxes that do not persist for more than a few collision times.

$\sqrt{m_1/m_2\pi} \gg 1$, depending on the masses of the colliding particles. For example, in deuterium-helium-3 scattering, the mean free path is ~73% the common value; whereas for ^{3}He-D scattering the mean free path is ~89% the common value. Except in the case of heavy particles scattering on light ones, this multiplier is less than 1. This implies that in the cases of ion-ion collision considered in this thesis, the mean free path effects become important in slightly lower-density or higher-temperature plasmas than is naively expected.

A.2 The Coulomb Logarithm

The Coulomb logarithm $\ln\Lambda$ appears generally in collisional plasma processes from the integral over possible impact parameters. For Coulomb collisions, collisional quantities of interest (for example, the energy or momentum lost in a collision) scale as $((b/b_{90})^2 + 1)^{-1}$, for the impact parameter b and the impact parameter for 90° scattering $b_{90} = q_1 q_2/(4\pi\epsilon_0 m_r v_1^2)$. The integral of this quantity over possible impact parameters:

$$\int_0^\infty \frac{1}{(b/b_{90})^2+1} 2\pi b db = \pi b_{90}^2 \ln\left(1+\frac{b^2}{b_{90}^2}\right)\Big|_0^\infty \equiv 2\pi b_{90}^2 \ln(\Lambda), \tag{A.11}$$

diverges in the limit $b \to \infty$.[2] This occurs because while the Coulomb field falls off as r^{-2}, the differential area available for collisions increases as $b^2 \sim r^2$ and so collisions are important out to arbitrarily large distances.

The divergence is resolved by limiting the upper limit of the integration b_{max}. In a plasma, this limitation is justified because the field due to a point charge is screened by attracting oppositely-charged particles and repulsing same-charged particles. The screening distance is given by the Debye length, of which a general form is as follows:[3]

$$\lambda_{De} = \left[\frac{e^2}{\epsilon_0}\sum_j^f \left(\frac{n_j Z_j^2}{T_j}\right)\right]^{-\frac{1}{2}}. \tag{A.12}$$

It is important to note that all species in the plasma participate in screening, not just the two colliding species.

Interestingly, as b_{90} approaches the radius of the nucleus, quantum effects can become important for scattering. The theoretical lower limit on the impact parameter is approximately the de Broglie wavelength of the two colliding particles, given by $(\hbar/pc) \approx (\hbar/2m_r v_r)$ in the non-relativistic limit.[c] (The factor of 2 includes the de Broglie wavelengths of both colliding particles.) In practice, it is convenient to replace b_{90} in Equation A.11 with the root-mean-square sum of b_{90} and the de Broglie wavelength, $p_\perp = \left[b_{90}^2 + (\hbar/2m_r v_r)^2\right]^{1/2}$. This results in the following definition for the Coulomb logarithm:

$$\ln(\Lambda) = \frac{1}{2}\ln\left[1+\left(\frac{\lambda_{De}}{p_\perp}\right)^2\right]. \tag{A.13}$$

In strongly-coupled plasmas where $\ln(\Lambda) \lesssim 1$, the kinetic mechanisms of individual collisions become important to calculating the average value of $\ln(\Lambda)$. A recent parametrization by Scott Baalrud extends to $\ln(\Lambda) \ll 1$, in which regime it agrees well with molecular dynamics simulations (see

[c] For ICF plasmas with temperatures no greater than T ~ 10 keV $\ll M_e \approx 511$ keV, the non-relativistic limit is a good approximation for all particles.

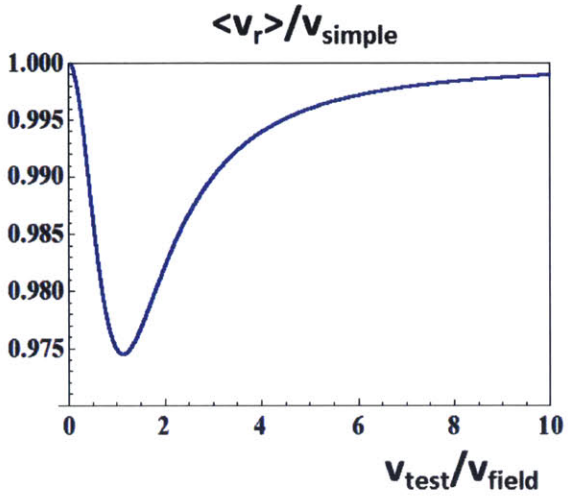

Figure A.1. Ratio of the thermal average relative velocity $\langle v_r \rangle$, defined by Equation A.14, to the 'simple' approximation $v_{simple} = (v_t^2 + v_f^2)^{1/2}$, where v_t is the test particle velocity and $v_f = \sqrt{8T/\pi m_f}$ is the Maxwellian-averaged thermal velocity of the field particle. The ratio is plotted as a function of v_t/v_f. The correct average is reduced from the simple value; the maximum reduction is approximately 2.5%, near $v_t = v_f$. This form is relevant primarily in stopping power calculations.

Reference [4]). This parametrization is occasionally used in this thesis for numerical calculations of $\ln(\Lambda)$ when dealing with simulations of plasmas that may be moderately- or strongly-coupled.

Note on thermal-average relative velocity

Equation A.13 is technically valid only for collisions of particle species with well-defined relative velocities, $v_r = (v_1 - v_2)$. When the Coulomb logarithm appears in an integral (such as in the derivation of the mean free path in Sec. A.1), it should in principle be integrated along with other terms over the particle distributions. However this approach is typically analytically intractable. Instead, the Coulomb logarithm is usually carried out of the integral and the velocity terms are replaced with a thermal-average relative velocity, $\langle v_r \rangle$. This term is often approximated as $\langle v_r^2 \rangle^{1/2} = (\langle v_1^2 \rangle + \langle v_2^2 \rangle)^{1/2}$, which is readily evaluated using the Maxwellian-averaged thermal velocities, $v_{th}^2 = \langle v^2 \rangle = 8T/\pi m$. However in the case of a test particle with velocity v_t transiting a thermal field plasma with $v_f = v_{th,f}$, $\langle v_r \rangle$ can be calculated directly. This case arises in stopping power calculations, and the correct form is evaluated as:

$$\langle v_r \rangle = \frac{v_f}{2} \exp\left[-\frac{4v_t^2}{\pi v_f^2}\right] + v_t \left(1 + \frac{\pi v_f^2}{8v_t^2}\right) \operatorname{erf}\left[\sqrt{\frac{4v_t^2}{\pi v_f^2}}\right]. \tag{A.14}$$

Figure A.1 plots the ratio of Eqn. A.14 with the typical approximation, $v_{simple} = (\langle v_t^2 \rangle + \langle v_f^2 \rangle)^{1/2}$. The thermal average relative velocity differs from the approximate equation near $v_t = v_f$, where it is lower by a maximum of ~2.5%.

A.3 References

1. I. Hutchinson, "Introduction to Plasma Physics (MIT 8.613J), course notes," see http://ocw.mit.edu/courses/nuclear-engineering/22-611j-introduction-to-plasma-physics-i-fall-2003/lecture-notes/ (2003), Chapter 3, Collisions in Plasmas.
2. M. A. Leontovich, (editor), *Reviews of Plasma Physics*, volume 1, chapter B.A. Trubnikov, "Particle Interactions in a Fully Ionized Plasma", (Consultants Bureau, New York, 1965).
3. I. Hutchinson, *Principles of Plasma Diagnostics*, (Cambridge University Press, 2005).
4. S. D. Baalrud, "Transport coefficients in strongly coupled plasmas," Physics of Plasmas, **19**(3), 030701 (2012).

Appendix B

Line Broadening due to the CPS Aperture

The charged particle spectrometers (CPS1 and CPS2) described in Section 1.3.3 provided valuable measurements for the work presented in Chapters 3 and 4, including both the absolute yields and spectral widths for nuclear fusion products. The D^3He-proton spectra were especially critical for providing the burn-averaged ion temperature of the D^3He-reaction, which presents the signature of thermal decoupling in the low-density shock-driven implosions (see Sections 4.3.2 and 4.5).

As discussed in Section 1.3.1, the burn-averaged ion temperature $\langle T_i \rangle$ can be inferred from the spectra of the nuclear products, which have a characteristic width proportional to the square root of the ion temperature:[1]

$$W_{FWHM} = 2\sqrt{2\ln 2}\sigma_{th} = \omega_0 \left(1 + \delta_w\right) \sqrt{T_i}, \tag{B.1}$$

where W_{FWHM} is the full-width at half-maximum of the spectral peak, T_i is the ion temperature of the fusing plasma, σ_{th} is the Gaussian width, ω_0 is a constant of proportionality for the reaction in question with units of $\text{keV}^{1/2}$, and δ_w is a positive, temperature-dependent correction (less than 2.5% for $T_i < 20$ keV). The constants of proportionality ω_0 and δ_w have been calculated by Ballabio, et al. in Reference [1], including relativistic corrections; a few of the most commonly-used values of ω_0 are copied in Table B.1.

From a diagnostic point of view, a spectral width $\sigma_{measured}$ is recorded. This width includes not only the incident spectral width produced by the fusing plasma, but also the instrumental broadening of the diagnostic instrument. For CPS, the instrumental broadening function is not a Gaussian, but is approximately a square response or 'boxcar.' The characteristic boxcar width (W) depends on both the width of the CPS aperture and the energy and species of the incident particle; however the MIT CPS Analysis program includes the capability to calculate W from the CPS magnetic fields, given these inputs. The convolution of the boxcar with an incident Gaussian spectrum produces a measured spectrum that is nearly Gaussian, as illustrated in Figure B.1. To obtain the burn-averaged ion temperature from this measured data, the instrumental broadening must be removed.

Practically speaking, the removal of the instrument broadening can be readily performed if one knows the *effective* Gaussian broadening of a boxcar with width W, designated as σ_{eff}. This

Table B.1. Common coefficients relating plasma ion-temperature and produced fusion-product spectral width. Values taken from Ballabio, et al., 1998 (Reference [1])

Reaction	$D(d,n)^3He$	D(d,p)T	$T(d,n)\alpha$	$D(^3He,p)\alpha$
ω_0 ($\text{keV}^{1/2}$)	82.542	91.599	177.259	180.985

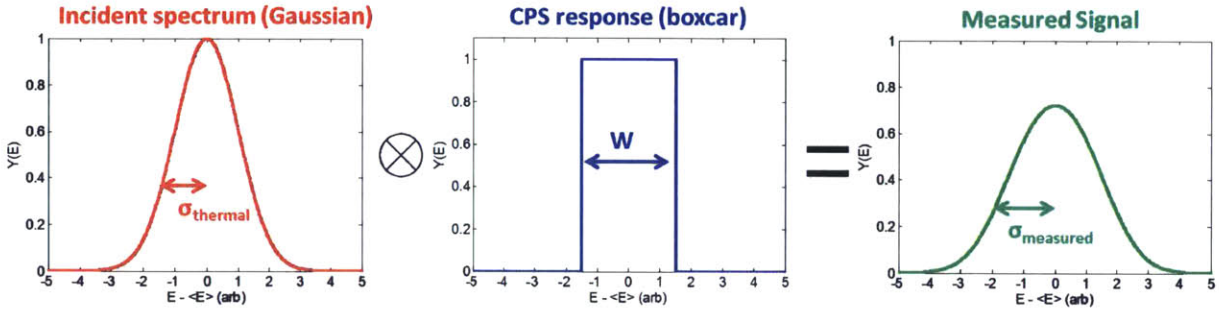

Figure B.1. Illustration of spectral broadening of an incident spectrum (red) by the CPS instrument response function (blue). The instrument response is approximately a boxcar, such that the convolution with an incident Gaussian of spectral width $\sigma_{thermal}$ creates a signal (green) that is almost, but not quite, Gaussian with a spectral width $\sim \sigma_{measured}$. The instrument response must be removed to determine the incident spectral width and determine a burn-averaged ion temperature.

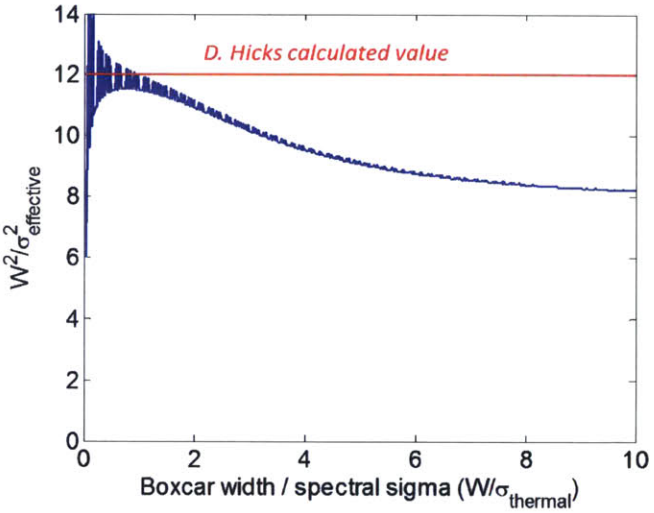

Figure B.2. Calculated ratio of effective CPS response width σ_{eff} to the boxcar response width W, as a function of the dimensionless ratio of boxcar width to spectral thermal width σ_{th} (blue). The ratio is plotted as $(W/\sigma_{eff})^2$, to highlight the limiting value of 12 which was calculated by D. Hicks (red).[2] Corrections to this limiting value become important for $W > \sigma_{th}$, and approach a constant limiting value of approximately 8 in the limit $W \gg \sigma_{th}$.

quantity is defined as the RMS difference between the incident and measured widths: $\sigma_{eff}^2 \equiv \sigma_{meas}^2 - \sigma_{th}^2$. Although in principle the convolved signal is not Gaussian, in the data analysis the signal is usually fit with a Gaussian to obtain a yield and spectral width. As such σ_{meas} is defined here as the width of the Gaussian fit to the measured signal.

The effective width σ_{eff} is a function of both the response width W and the thermal width σ_{th}; however the dimensionless ratio W/σ_{eff} is a function only of W/σ_{th}. This function was calculated numerically, by convolving boxcars with Gaussian spectra and fitting a Gaussian to the resulting signal; the results of this study are shown in Figure B.2. In the limit of a narrow boxcar compared to the incident spectral width ($W/\sigma_{th} \ll 1$), the ratio (W/σ_{eff}) approaches a value of $\sqrt{12}$. This value was reported by Damien Hicks in his PhD thesis,[2] and can be determined by analytical arguments. However as the boxcar width becomes comparable to and exceeds the thermal width, corrections to this coefficient become important. As an example of this, Figure B.3 compares the real plasma ion temperature to the 'measured' $\langle T_i \rangle$ inferred using Hicks' coefficient value of 12. For a ratio $W/\sigma_{th} = 2$, the inferred $\langle T_i \rangle$ is higher than the actual value by 3%; for $W/\sigma_{th} = 3$, this discrepancy increases to 14%.

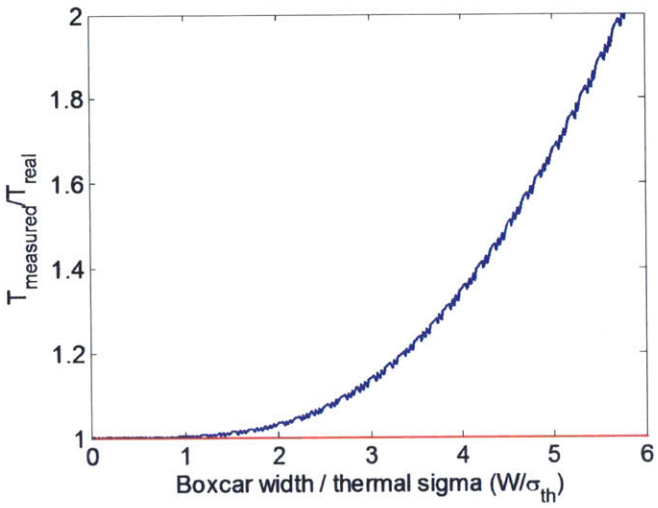

Figure B.3. Error introduced in the burn-averaged ion temperature due to using the Hicks limit of $W = 12\sigma_{eff}$. The ratio of the 'measured' temperature to the 'real' plasma temperature is plotted as a function of the width ratio W/σ_{th} (blue). Unity (red) indicates agreement. The correction is negligible for $W < \sigma_{th}$, but becomes important for $W/\sigma_{th} > 2$.

Ratios W/σ_{th} in excess of 3 are readily possible in experimental data, especially on low-yield shots for which broad apertures must be fielded. The physical slit widths range from 0.1 to 10 mm, which correspond to an energy range of W from 61 keV to 6.1 MeV for D^3He-protons. In comparison, by using Equation B.1 and the values in Table B.1 it is calculated that a 10 keV ion temperature produces a D^3He-proton spectral line with a thermal width of $\sigma_{th} = 146$ keV. Thus, significant corrections are necessary for D^3He-proton measurements made using slit widths of 0.5 mm or more.

In practice, the thermal width is not known a priori (it is, after all, the value we are trying to determine). However the trend in the effective broadening can be recast as a function of the boxcar width W and the measured signal width σ_{meas}, as shown in Figure B.4a). This trend was fit with a 3rd-order polynomial, to facilitate calculating the correct value of the effective broadening for a given dataset. The best-fit to the numerical calculations is as follows:

$$\sigma_{eff}^2 = \frac{W^2}{-0.00664R^6 + 0.0373R^4 - 0.398R^2 + 12.02}, \tag{B.2}$$

written as a function of $R \equiv W/\sigma_{meas}$, the ratio of the boxcar width to the measured spectral width. The fit was not constrained to the limiting value of 12, in order to minimize the total error of the fit: as shown in Figure B.4b), the fit matches the numerical trend to better than 0.5% over the entire range. Equation B.2 was used to remove the instrumental broadening from Gaussian fits to the measured CPS data, in order to determine the incident spectral width and the burn-averaged ion temperatures presented in this thesis.

The approach developed here represents a significant improvement over the previous technique of using a constant correction. However, it is not ideal. In reality, the response width W is dependent on the incident particle energy, and is not a perfect boxcar. In pursuit of a more accurate model of the instrument response, one could construct a 2-dimensional response matrix for each slit width from the model of the magnetic field: $\mathbb{W}_{slit} = \mathbb{W}_{slit}(E_{in}, E'_{out})$. This matrix translates an impulse of particles with energy E_{in} to a spectrum of particles with "energy" E'_{out} inferred from their position in the detection plane.[a] Having constructed this matrix, the model of the CPS signal S is then obtained by: $S(E'_j) = Y(E_i)\mathbb{W}_{slit}(E_i, E'_j)$. The model signal can be

[a]It might be preferable to parametrize in terms of a spatial coordinate rather than E'_{out}, as this is not a real energy.

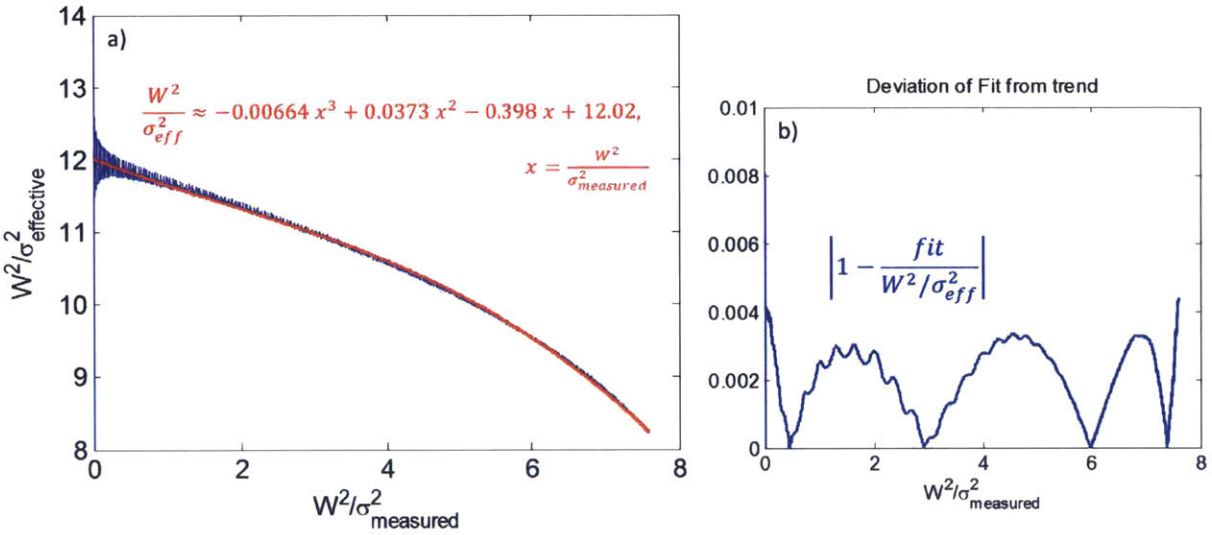

Figure B.4. a) Effective instrumental broadening for CPS as a function of the ratio of the boxcar width to the total measured width, W/σ_{meas} (blue). A 3rd-order polynomial (red) was fit to the numerical function to facilitate estimates of the correct effective broadening value for a particular dataset. b) The error in the parametrized function relative to the numerical trend is less than 0.5% for the entire range.

fit to the actual CPS signal while varying the model spectrum Y(E) to obtain the best fit. Such an approach would require highly detailed understanding of the CPS magnets, and might require remapping the magnetic fields, after more than a decade of operation in the high neutron-fluence environment of the OMEGA laser. Both the difficulty and the importance of developing such a detailed model are unclear at this time, and therefore this significant effort is left to future work.

B.1 References

1. L. Ballabio, J. Källne and G. Gorini, "Relativistic calculation of fusion product spectra for thermonuclear plasmas," Nuclear Fusion, **38**(11), 1723 (1998).

2. D. Hicks, *Charged-Particle Spectroscopy: A New Window on Inertial Confinement Fusion*, Ph.D. thesis, Massachusetts Institute of Technology (1999).

Appendix C

The Effect of Aperture Charging on Penumbral Imaging Data

Penumbral imaging of the charged fusion products was used to measure the size and profile of the nuclear burn region, as reported in Chapters 3 and 4. The principles of penumbral imaging as implemented in the Proton Core Imaging Diagnostic (PCIS) on OMEGA were introduced in Section 1.3.4. On several shots, the recorded images presented unexpected radial structures; an example is shown in Figure C.1. The fluence on the axis of the DD-proton (3.0 MeV) image is clearly reduced from the peak by nearly a factor of 2; a slight reduction in the fluence is also observed at ~80% of the image radius, well inside the edge of the penumbra. Similar features are not observed in the D^3He-proton (14.7 MeV) image, which was recorded coaxially with the DD-proton image on the same shot.

The anomalous features were hypothesized to be produced by electric charging of the aperture during the shot. Given the circular shape and axial alignment of the unexpected features, the most likely source was considered to be the imaging aperture or its surrounding hardware. The apertures are well characterized and verified to be free of obstructions prior to their assembly, so scattering is an unlikely candidate for these features. Large fluences of electrons are produced by the laser-plasma interactions, which can charge the target to an electrical potential of hundreds of kV while the lasers are on.[1] These electrons could collect on the PCIS nose tip hardware, which is positioned 3 or 4 cm from the target chamber center, charging it negatively before the fusion products arrive. Alternatively, x-rays generated by the target could liberate electrons from the aperture itself, charging it positively. The electric fields thus generated would perturb the path of the charged fusion products as they pass through the aperture. Since the D^3He-protons have approximately five times the kinetic energy of the DD-protons, they would spend less time in the vicinity of the aperture and therefore would be affected less by the fields, as is observed.

Two approaches were used to determine the impact of aperture charging on the PCIS data. An analytical model of particle deflection was developed to assess and correct for the aperture charging in the measured data, and is presented in Section C.1. This model is a generalization of a technique originated by Fredrick Séguin[2] to include relativistic effects. Monte Carlo transport simulations through a numerical model of the electric fields produced by aperture charging were also used to produce synthetic PCIS images, which are presented in Section C.2.

C.1 Analytical correction for electric field effects

The DD-proton and D^3He-proton images exhibit different apparent magnifications, as determined from the radius of the image on the detector and the known radius of the aperture. Since the

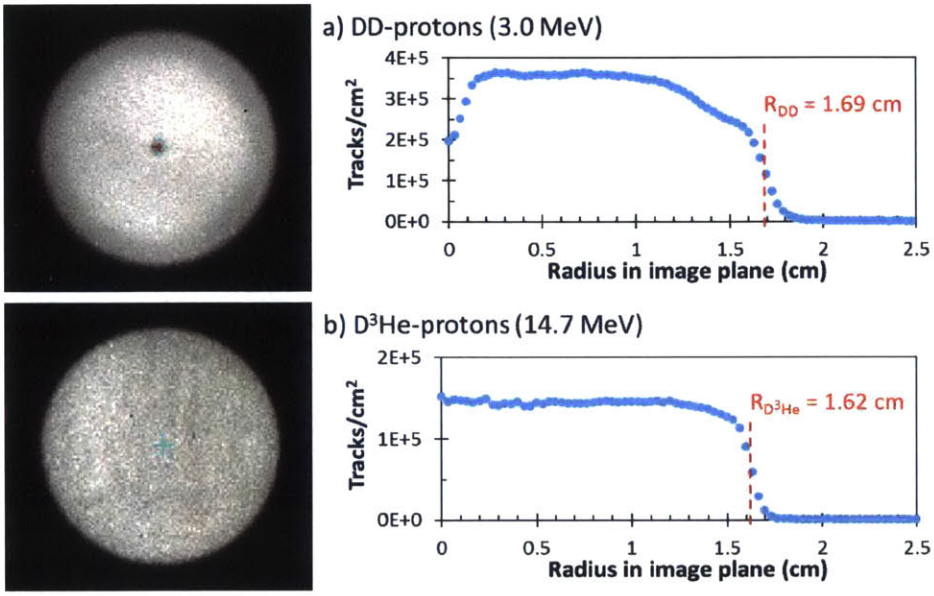

Figure C.1. Example of PCIS penumbral imaging data recorded on OMEGA shot 69250 (Om130404) showing anomalous radial features. a) The DD-proton aperture image (left) shows clear evidence of fluence variation in the aperture image, which is expected to be uniform except near the edge. The radial lineout (right) indicates a reduction of fluence on axis (R = 0 cm), and a 'lip' (near R = 1.3 cm) where the fluence is reduced slightly before the edge of the image (R = 1.6–1.8 cm). The radius of the DD-proton aperture image is $R_{DD} = 1.69$ cm (red dashed). b) The D^3He-proton aperture image (left) and radial lineout (right) do not show the features observed in the DD-proton image and lineout, although they were recorded coaxially with the DD-proton image. The radius of the D^3He-proton aperture image is $R_{D^3He} = 1.62$ cm, approximately 4% smaller than the DD-proton image. The experiment was a D^3He-filled thin-glass target with $\rho_0 = 0.4$ mg/cc, $f_D = 0.8$, imploded with a 14.4 kJ, 0.6 ns laser impulse; the PCIS magnification was $M = 15.1$.

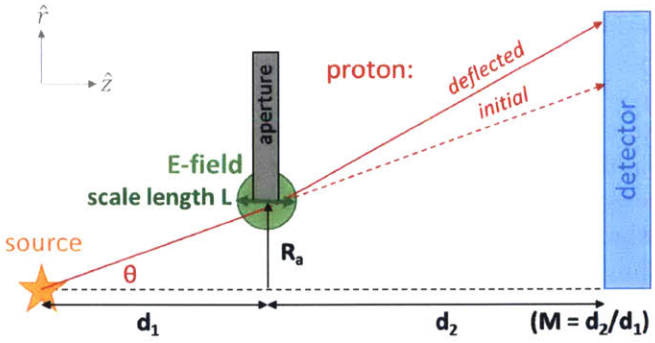

Figure C.2. Geometry for an analytical model of proton deflection by electric fields at the PCIS aperture. The protons (red) that define the outer radius of the image on the detector pass near to the radius of the aperture, R_a. The aperture is positioned an axial distance d_1 from the source; the detector is an axial distance d_2 from the aperture. The pinhole magnification is $M = d_2/d_1$. The electric field, present near the aperture and covering a scale-length L, deflects the protons (red) from their initial trajectory (red dashed) and changes the radius of the image on the detector.

particles have different energies, this measured difference can be used to constrain the strength of the electric fields at the aperture. The particles that define the radius of the image are those that pass closely to the edge of the aperture, as shown schematically in Figure C.2. These particles have an initial velocity $\vec{v_{tot}} = v_r\hat{r} + v_z\hat{z}$, with $v_r/v_z = \tan\theta = R_a/d_1$. Assuming that the electric field introduces a radial impulse on the particle as it passes the aperture, the radial velocity will be shifted by $\Delta v_r = qE\Delta t/m\gamma$, where q is the particle charge, E the electric field, Δt the amount of time spent near the electric field, m the particle mass, and γ is the relativistic gamma. The electric field has a fixed geometry with a spatial scale L, and so the product $v_{tot}E\Delta t \equiv$ EL is taken to be a constant with units of volts. The radius of the image on the detector is given by:

$$r_{det} = R_a + \frac{v_r + q(\mathrm{EL})/(m\gamma v_{tot})}{v_z} M d_1, \tag{C.1}$$

where M is the 'true' (expected) pinhole magnification $M = d_2/d_1$. The radius of the aperture is known, and the radius of the image is measured using two particles with different velocities. Equation C.1 can therefore be solved for the two unknowns, M and (EL). For the case of measuring DD- and D^3He-protons, the mass and charge of the particles are equal and fall out of the algebra. This results in the following equations:

$$M = \frac{1}{R_a}\left[\frac{(\gamma\beta^2 r_{det})_{DD} - (\gamma\beta^2 r_{det})_{D^3He}}{(\gamma\beta^2)_{DD} - (\gamma\beta^2)_{D^3He}}\right] - 1, \tag{C.2}$$

$$\mathrm{EL} = \frac{mR_a\cos\theta}{qd_1}\left[\frac{(r_{det,DD} - r_{det,D^3He})(\gamma\beta^2)_{DD}(\gamma\beta^2)_{D^3He}}{(\gamma\beta^2)_{D^3He}(r_{det,D^3He} - R_a) - (\gamma\beta^2)_{DD}(r_{det,DD} - R_a)}\right] \tag{C.3}$$

where $\beta = v_{tot}/c$ is the relativistic velocity. The true magnification M is a function only of r_{det}, R_a, and the particle velocities, while the electric deflection constant EL depends additionally on the particle mass, charge, and aperture offset.

This technique was applied to determine the correct magnification for the analysis of the PCIS data reported in Sections 3.3.4 and 4.3.4. This typically resulted in a 4% correction to the measured burn radius for DD-protons, and a 1% correction to the measured burn radius for D^3He-protons. The measured electric deflection constants had an average value and standard deviation of EL = 6.6 ± 1.0 kV over seven thin-glass shell implosions recorded on April 4th, 2013. Considering that the scale length L should be comparable to the thickness of the apertures, which were made of 500 μm-thick tantalum, this value implies an electric field on the order of 10^5 V/cm. The greater outward deflection of the DD-protons relative to the D^3He-protons implies that the apertures were negatively charged.

C.2 Monte Carlo particle transport simulations

To confirm that the observed features were generated by electric charging of the aperture, Monte Carlo simulations of proton transit through an electrically-charged PCIS aperture were performed. The electric field structure near the PCIS aperture was estimated using a partial differential equation solver. The simulated electric potential and electric field structures are shown in Figure C.3. The dimensions for the PCIS nosecone hardware were taken from LLE mechanical drawings. The program solved Poisson's equation assuming cylindrical symmetry to determine the fields that would arise from surface charge density distributions. In this model, the pinhole, nosecap, nosecone, and entire inner surface of the PCIS hardware was held at a potential of 1, while the target chamber

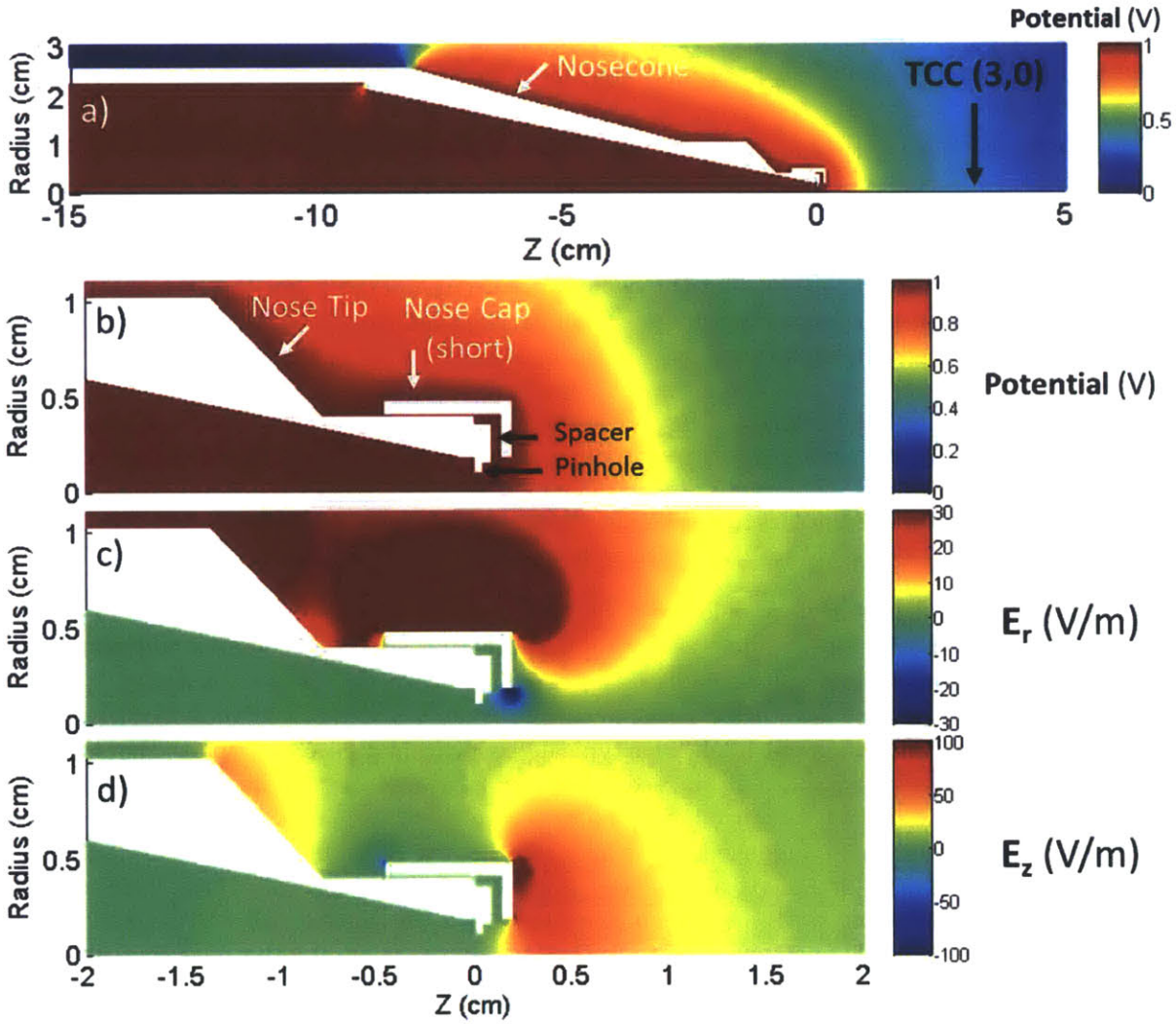

Figure C.3. Simulated electric potential a) surrounding the PCIS nosecone and b) near the PCIS aperture, assuming uniform charging of the pinhole, nosecap, nosecone, and the entire inner surface of the PCIS hardware. The model was positioned such that the inside surface of the aperture was at Z = 0; the implosion occurs at Z = +3 cm. The resulting electric fields in the c) radial and d) axial direction were calculated from the gradient of the potential, and were used for Monte Carlo particle trajectory calculations.

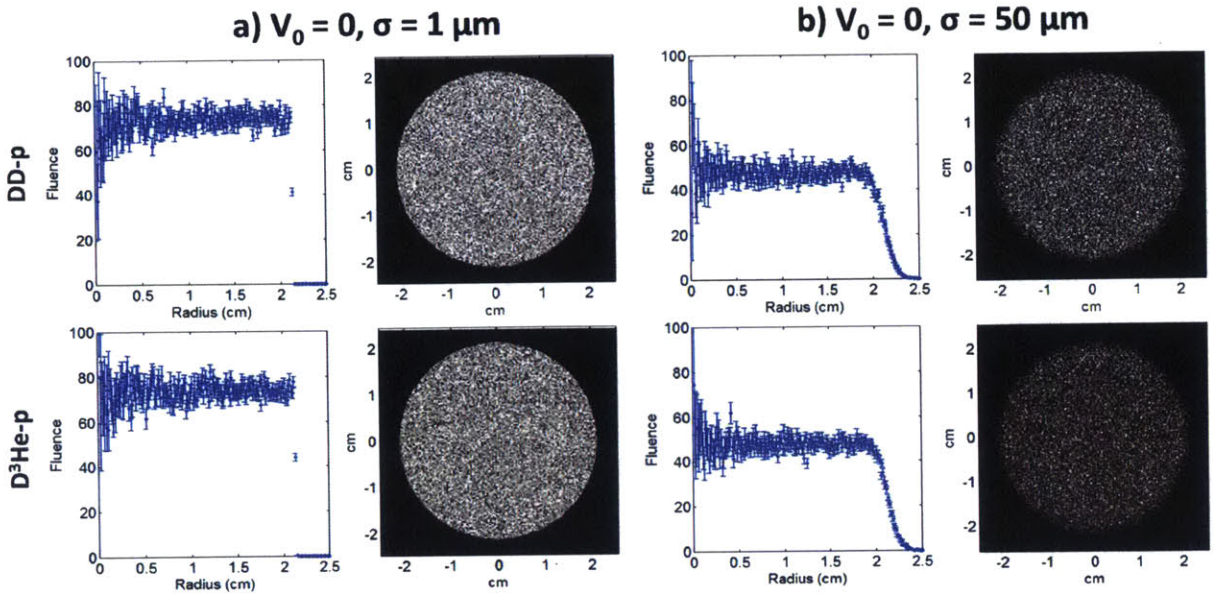

Figure C.4. Simulated PCIS data with no electric field and a) Gaussian burn radius $\sigma = 1$ μm, b) $\sigma = 50$ μm. Fluence vs radius (left, blue) and fluence maps (right, greyscale) are shown for both DD-protons (top) and D^3He-protons (bottom). The magnification is $M = 20$. The simulated PCIS behaves as expected: fluence in the image is flat, and the width of the penumbral region is correlated to the burn radius.

and the remainder of the outside of the PCIS hardware was held at a potential of 0. This choice was made so that the particles would experience fields at the pinhole only, and not inside the nosecone. In reality, the PCIS hardware is dynamically charging and discharging during the experiment; however that level of detail is beyond the scope of this work. The radial and axial electric fields are calculated as the gradient in the field potential: $E_r = -\partial V/\partial r, E_z = -\partial V/\partial z$.

Monte Carlo particle transport calculations were performed using the simulated field maps to determine the effect of the electric fields on the resulting PCIS image. For each particle, the Lorentz force was numerically calculated to determine its trajectory through the field structure. The simulations were performed in three spatial dimensions, to correctly account for off-axis particle origins. The particle source probability distribution was a spherical Gaussian with a characteristic width σ, positioned at the target chamber center. The fields were multiplied by a scalar V_0 to simulate different amounts of charging. Protons with both 3.0 and 14.7 MeV were simulated for σ from 1 to 60 μm and V_0 from 0 to -100,000 Volts. Each run transported 10^5 particles.

The results of two null simulations, with the electric field set to zero and the burn radius set to 1 μm and 50 μm, are shown in Figure C.4. The null simulations demonstrate the expected results: the fluence across both the DD-proton and D^3He-proton images are flat, and the width of the penumbral region is correlated to the burn radius.[a] Analysis of the simulated PCIS data produced agreement with the input burn radii to within statistical uncertainties. The radii of the DD-proton and D^3He-proton images agree to approximately 0.1%.

Simulations with negative electric potentials and the burn radius set to 1 μm reproduce the axial fluence depletion observed in the data, as shown in Figure C.4. For potentials of -10 kV, the DD-proton exhibits a slight central depletion and the D^3He-proton image appears normal. For

[a]The absolute level of fluence varies with the burn radius for numerical reasons: 100000 particles were launched in each case, however a greater number of these are rejected by collision with the aperture in the simulation with larger σ.

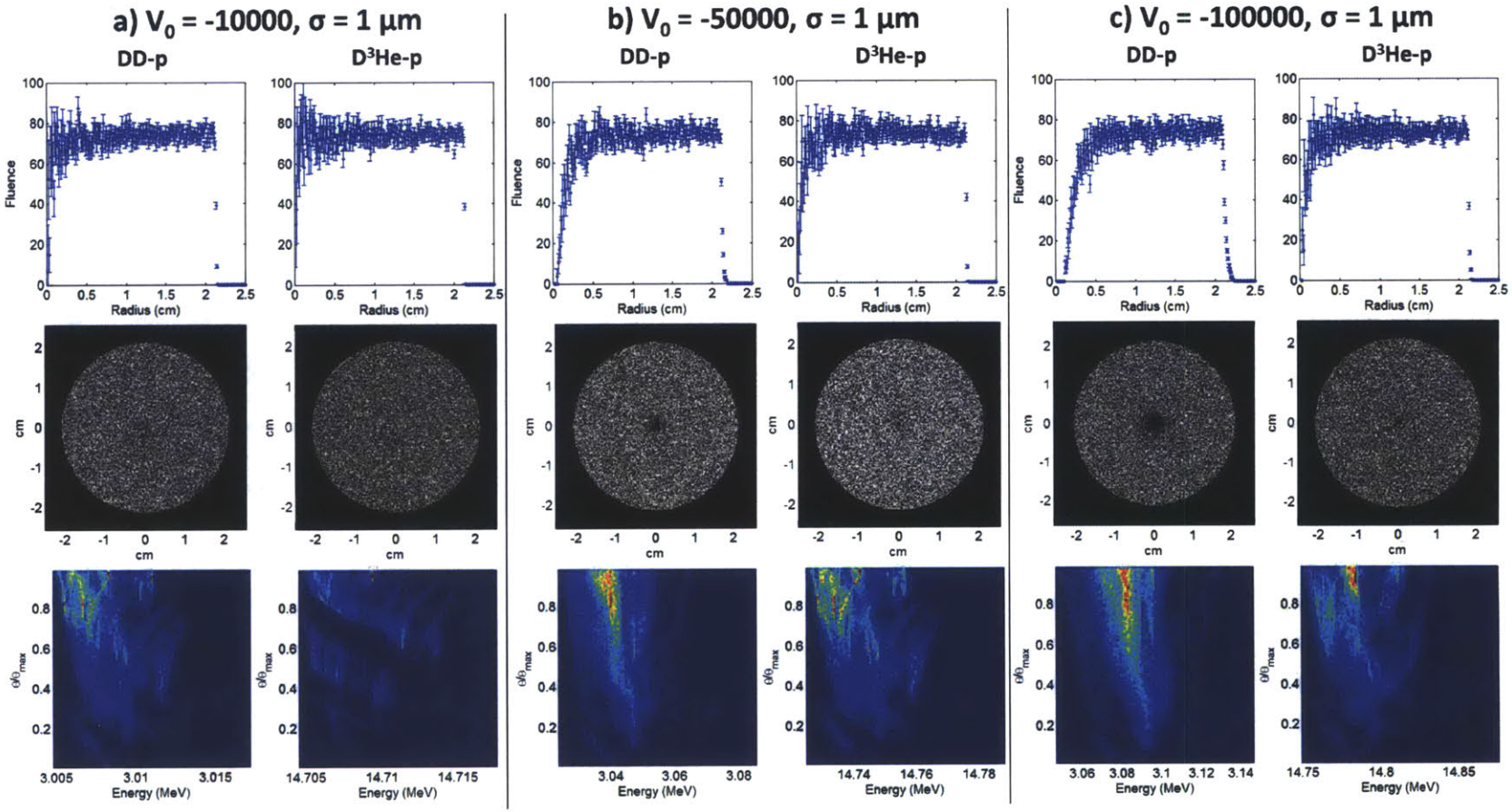

Figure C.5. Simulated PCIS data for a fixed burn radius $\sigma = 1$ μm and varying electric field at a) -10,000 Volts, b) -50,000 V and c) -100,000 V. For each case, fluence vs radius (top, blue), fluence maps (middle, greyscale), and particle incident angle vs energy (bottom, heat map) are shown for both DD-protons (left) and D^3He-protons (right). The electric field introduces a visible perturbation on the DD-proton profile between -10 and -50 kV. The D^3He-proton profile is also visibly perturbed at -100 kV. The particles are also up-shifted from their birth energy, however the amount of upshift is negligible from a diagnostic point of view (< 100 keV).

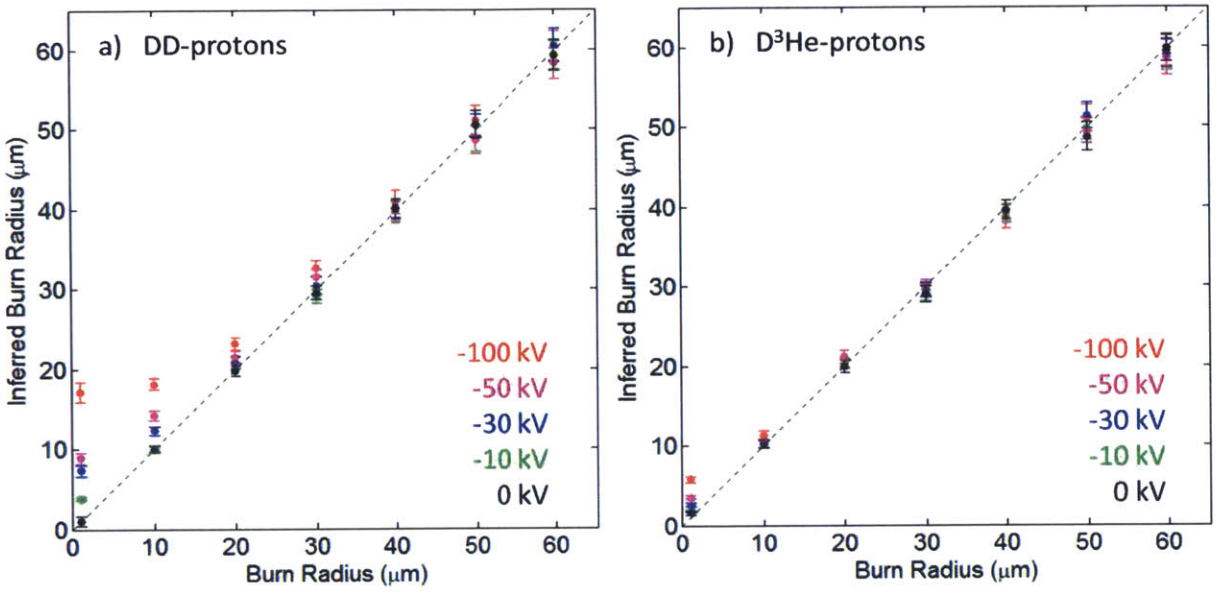

Figure C.6. The inferred burn radius compared to the actual burn radius σ for simulated images using a) DD-protons and b) D^3He-protons, showing the effect of PCIS aperture charging. The electric fields introduce an effective broadening of the penumbra, causing the inferred burn width to approach a positive value $\sigma_E(V_0)$ in the limit $\sigma \to 0$. The electric field broadening appears to add in quadrature with σ, such that for $\sigma > \sigma_E$ the inferred width is correct to within uncertainties. The DD-protons are more severely broadened than the D^3He-protons.

potentials of -50 kV, the DD-proton image is clearly depleted in the center, and the D^3He-proton image is beginning to be affected. Finally, potentials of -100 kV produce the depletion feature in both DD- and D^3He-proton images. From the electric field maps, the -100 kV potential generates radial fields near the aperture with a peak strength of $E_r \approx -10^4$ V/cm, and peak axial fields of $E_z \approx -5 \times 10^4$ V/cm. The total field strength is the same order of magnitude as the estimate from radial deflections in the measured data using Equation C.3.

The burn radii inferred from the data are shown in Figure C.6. The electric fields appear to broaden the penumbral region slightly, causing the inferred burn radius to be larger than the input value. The shape of the curves suggest that an additional broadening σ_E, which is a function of the electric potential, is added in quadrature to the input burn radius σ to produce the inferred value. For $\sigma > \sigma_E$, the input burn radius dominates and the inferred values are in agreement with σ to within statistical uncertainties. The inferred width in the limiting case of small burn radius ($\sigma = 1$ μm) is shown in Figure C.7, as a function of potential. In this limit, σ_E dominates the inferred width, and is seen to grow roughly linearly with increased $|V_0|$. A linear fit to the data has a slope of approximately -0.18 μm/kV for the DD-protons and -0.05 μm/kV for the D^3He-protons.

Interestingly, the radii of the DD-proton and D^3He-proton aperture images in the simulations agree to approximately 0.1% regardless of the electric potential, as shown in Figure C.8. The aperture image radii also agree with the expected radii to within uncertainties. This finding contrasts with the observed PCIS data, for which the DD-proton aperture image had a measurably larger radius than the D^3He-proton image (see Figure C.1); this difference was the initial motivation for the development of the analytical model presented in Section C.1. Additionally, the slight decrease of the particle fluence at $\sim$ 80% of the image radius that was observed in the PCIS data is not observed in the simulations. These features must be caused by electric- or magnetic-field structures

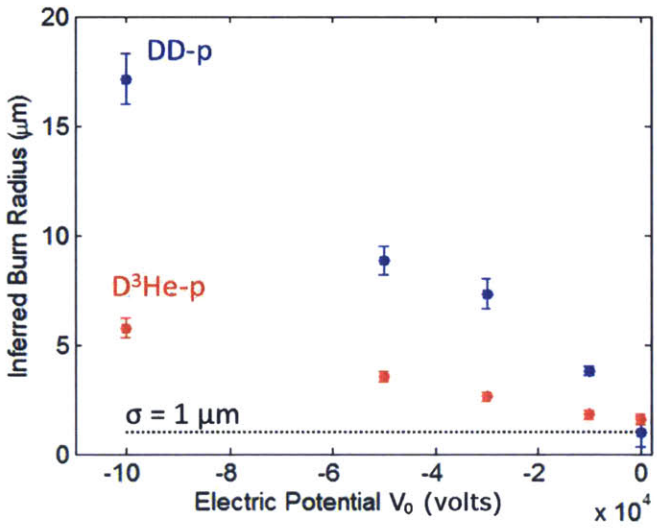

Figure C.7. The inferred burn radius for the limiting case $\sigma = 1$ μm as a function of the electric potential V_0, illustrating the effective broadening due to the electric fields σ_E. The broadening appears to be linear in V_0; the DD-proton penumbra is broadened approximately 3 times more than the D^3He-proton penumbra.

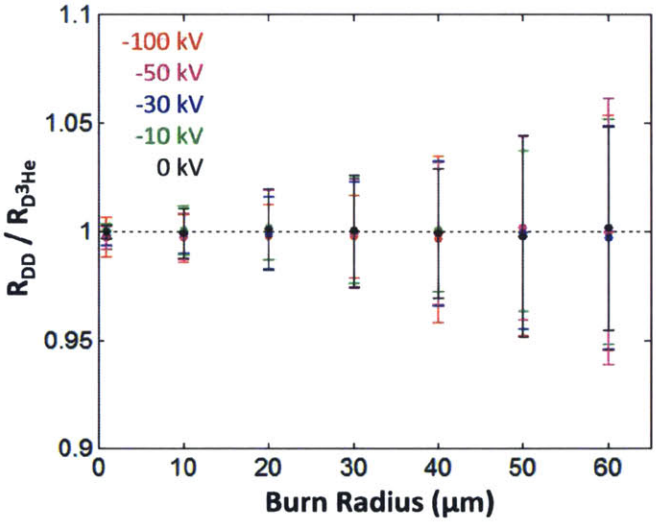

Figure C.8. Ratio of the simulated image radius for DD-protons to the image radius for D^3He-protons, plotted as a function of burn radius σ for several electric potentials. The ratio is invariant with both σ and V_0, and is equal to unity to within statistical uncertainty for all points. This finding is contrary to an observed ratio greater than 1 in PCIS data.

that are not represented in the static PCIS field model developed here.

C.3 Summary

The PCIS charged particle images recorded in this work showed several anomalous features which were hypothesized to be caused by electric fields near the aperture. A simple analytical model was developed to use the difference in the radius of coaxially-recorded DD-proton and D^3He-proton images to correct for the electric field effect in the PCIS analysis. This analytical model corrected the inferred burn radii by ~4% for DD-protons and ~1% for D^3He-protons, and also inferred an electric field strength on the order of 10^5 V/cm. A partial differential equation solver was used to calculate the static electric field structures surrounding a charged, cylindrically symmetric model of the PCIS nosecone. The electric field models were then used in 3D Monte Carlo simulations of charged particle trajectories, to create simulated PCIS images with various aperture electric potentials and burn radii. These simulations produced the expected PCIS behavior with no electric

field, and also recreated the anomalous axial fluence depletion seen in the data for radial electric fields on the order of 10^4 V/cm. The electric fields also broadened the image penumbra, resulting in a slight broadening of the inferred burn radius. The additional broadening was determined to grow linearly with the aperture potential, and add in quadrature with the actual burn radius to produce the inferred burn radius. For most cases examined, the actual burn radius σ was the dominant term. The enlargement of the DD-proton aperture image relative to the D^3He-proton image and the reduction of fluence at ~80% of the image radius that was observed in the data was not recreated by the simulations. These features may be due to dynamic discharging of the PCIS aperture or some other electromagnetic source not considered, and explaining these additional features remains as future work. That being said, the static electric effects considered here appear to have only a small effect (<10%) on the analyzed PCIS data.

C.4 References

1. N. Sinenian, M. J.-E. Manuel, J. A. Frenje *et al.*, "An empirical target discharging model relevant to hot-electron preheat in direct-drive implosions on OMEGA," Plasma Physics and Controlled Fusion, **55**(4), 045001 (2013).
2. Private Communication with F. Séguin.

Appendix D

Using Combined Secondary Fusion Products to Infer Fuel ρR, Electron Temperature, and Mix in D_2-filled Implosions

Nuclear fusion products have been used extensively to explore the behavior of the high energy-density plasmas generated in inertial confinement fusion implosions. The high sensitivity of thermonuclear fusion yield rate to plasma ion temperature and density (see Equation 1.4) makes the nuclear reaction histories and profiles valuable for studying the core plasma. Because the fusion reactions produce nearly monoenergetic fusion products, the measured fusion product spectra contain information about the kinematics of the fusing plasma and the areal density of the plasma traversed by escaping charged particles.

Certain fusion products are themselves fusion reactants, and can react in-flight as they transit and escape the fuel: these are called *secondary* fusion reactions. In an ICF implosion filled with deuterium, densities and temperatures near peak compression are sufficiently high for fuel ions to undergo thermonuclear fusion:

$$\begin{array}{rcl} D + D & \rightarrow & T \quad (1.01\ \text{MeV}) + p \quad (3.02\ \text{MeV}) \quad (50\%), \\ & \rightarrow & {}^3He \quad (0.82\ \text{MeV}) + n \quad (2.45\ \text{MeV}) \quad (50\%). \end{array} \tag{D.1}$$

A fraction of the reactant products, ^{3}He and T, will themselves fuse in-flight with thermal deuterons:

$$\begin{array}{rcl} T \quad (\leq 1.01\ \text{MeV}) + D & \rightarrow & n \quad (11.9\text{–}17.2\ \text{MeV}) + \alpha \quad (6.7\text{–}1.4\ \text{MeV}), \\ {}^3He \quad (\leq 0.82\ \text{MeV}) + D & \rightarrow & p \quad (12.5\text{–}17.4\ \text{MeV}) + \alpha \quad (6.6\text{–}1.7\ \text{MeV}). \end{array} \tag{D.2}$$

The secondary proton and neutron yields produced by these reactions is known to depend sensitively on fuel-ρR, plasma temperatures, and plasma composition in implosions of deuterium-filled targets.[1] Nuclear diagnostics have been used to assess the profiles of the imploded fuel at bang time on implosions at OMEGA.[2,3] Implosions with low fuel areal density were found to produce consistent yields of secondary protons and neutrons for laser intensities of $\sim 6 \times 10^{14}$ W/cm^2. However shots with intensity above 10^{15} produced a yield of secondary neutrons congruent with a fuel ρR nearly double the value inferred from secondary protons.[3] Mix of shell material into the fuel was proposed as an explanation for this discrepancy. A similar discrepancy has recently been observed in high-intensity, deuterium filled, polar-direct-drive, spherical CH targets imploded at the National Ignition Facility (NIF). The mix of shell material into the DT-fuel and the hotspot is a matter of extensive research in ICF, due to the extremely detrimental effects of small amounts of mix on attaining high yield. The electron temperature of the core plasma is also of interest. As seen in

Chapter 4, shock driven implosions can have fully decoupled electron- and ion-temperatures for the duration of the experiment; but compressively-driven implosions can also exhibit unequilibrated temperatures. Since fast ions stop primarily through collisions with the electrons, the electron temperature has a major impact on stopping power in the core of such implosions, and will play a significant role in alpha heating. Secondary yields, which probe the entire fuel area and are sensitive to changes in the stopping power, provide a unique view on these important aspects of the final fuel assembly at bang time.

A technique for analyzing both the secondary DT-neutron and D^3He-proton yields produced in deuterium-filled implosions was developed to assess fuel ρR, electron temperature, and mix. In warm D_2-filled implosions with moderate fuel ρRs in the range 5 - 100 mg/cm^2, increased stopping power reduces the secondary D^3He-proton yield but increases the secondary DT-neutron yield relative to the primary yield. Both the fuel electron temperature and mixing of shell material into the fuel impact the fuel stopping power and can affect the secondary yield ratio. By using the combined yields of secondary DT-neutrons and secondary D^3He-protons, these important and difficult-to-measure properties of the fuel assembly are addressed. This technique has been successfully applied to three classes of experiments at the NIF: direct-drive exploding pushers, indirect-drive 1- and 2-shock implosions, and direct-drive mix experiments.

This appendix is organized as follows: Section D.1 presents a model for how the secondary yields change as a function of fuel-ρR and stopping power, and outlines how the combined information of the secondary yields is used to infer $\rho R_{fuel}, T_e$, and mix. The simplest form of the model assumes a uniform deuterium plasma, and is directly applicable to implosions containing deuterium fuel with dopants such as argon and krypton, or additional fuels such as ^3He or T. Section D.2 presents the results of applying this model to experiments at the NIF.

The technique described here is contingent upon robust measurements of both the D^3He-proton and the DT-neutron spectra in deuterium-filled implosions. Proton spectra are routinely recorded at both OMEGA and the NIF using the Wedge Range Filter (WRF) spectrometers.[4–6] At OMEGA, the Charged Particle Spectrometer (CPS) diagnostics also record proton spectra by magnetic deflection of charged particles onto CR-39.[4] Secondary neutron yields are recorded by neutron Time-of-Flight (nTOF) detectors at both OMEGA and the NIF.[7,8] Time-of-flight is used to resolve neutron energy and differentiate secondary neutrons from the primary 3.0 MeV neutrons, which are 10^2 to 10^4 times more plentiful.

D.1 Model of Secondary Yields

Secondary yield production depends on the path-averaged fusion reactivity of the D-D fusion products ^3He and T as they transit the plasma. Since fusion reactivity is a strong function of center-of-mass energy of the reactant particles, the stopping power of the plasma along the path of these products will have a strong impact on the secondary yields. An example of a DD-^3He and DD-t slowing in a pure deuterium plasma, and the resulting cross-section for fusion with background deuterons, is shown in Figure D.1. More generally, for a ^3He or T born at location $\vec{x}_0$ and following path $\vec{x}$, the probability of undergoing secondary fusion is:

$$P_2 = \int_{\vec{x}} n_D\left(\vec{r}\right) \sigma_{fus}\left(E\left(\vec{r}\right)\right) d\vec{r}, \tag{D.3}$$

$$E\left(\vec{r}\right) = E_0 - \int_{\vec{x}_0}^{\vec{r}} \frac{dE}{dx}\left(E\left(x'\right), T\left(x'\right), n\left(x'\right)\right) dx' \tag{D.4}$$

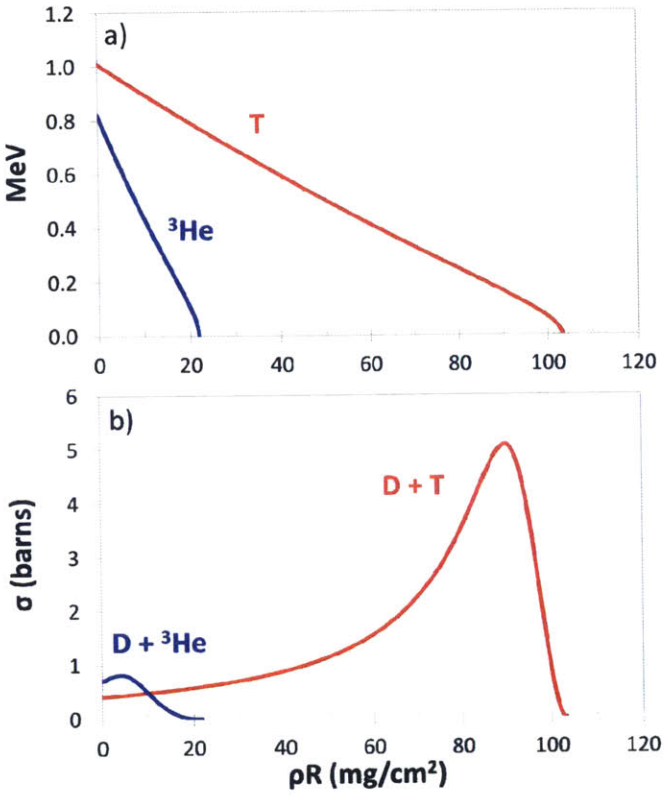

Figure D.1. Example of a DD-^{3}He (blue) and DD-t (red) slowing in a pure deuterium plasma (ρ = 30 g/cc, $T_e = T_i$ =3 keV), and fusion reactivity along their paths. a) The initially 0.8 MeV DD-^{3}He and 1.01 MeV DD-t lose energy to the plasma as a function of the areal density transited. If the areal density is sufficiently high the particles are ranged out in the plasma: in this example, the ^{3}He and T have ranges of ~20 and ~100 mg/cm^2, respectively. b) The cross-section for fusion with a thermal deuteron is a strong function of the collisional center-of-mass energy, and therefore varies with the ρR transited as well. The ^{3}He ion is born near the peak in the D-^{3}He reactivity, so additional ρR tends to decrease the cross-section; in contrast, the triton is born with substantially more energy than the reactivity peak, and so the cross-section increases with higher ρR.

The probability of fusion for any one particle averages over the plasma density and cross-section along its path. The cross-section in turn depends on the plasma stopping power along the path, which is set by plasma temperature, density, and composition. The DD-^{3}He birth energy (0.82 MeV) is near the peak of the D^{3}He-fusion cross section (0.66 MeV). Because of this, increasing the plasma stopping power tends to reduce the average reactivity. In contrast, the DD-triton birth energy (1.01 MeV) is approximately six times more energetic than the peak of the DT-fusion cross section (0.16 MeV): the DT reactivity increases by as much as a factor of 12 as the triton slows in the fuel. These changes in the reactivity with slowing in the fuel are illustrated in Figure D.1b).

The measured ratio of secondary yield to primary yield, Y_2/Y_1, is a double-average of the probability in equation D.3: an average of the trajectory direction $\vec{x}$ over 4π of solid angle, and a primary burn-weighted average of the initial reactant location $\vec{x}_0$. This calculation is analytically intractable even for simple cases, but is accessible to numerical methods. A numerical model of secondary yield production was developed, using the Li-Petrasso stopping power formulation to range reactant products in a plasma,[9] and the fusion cross-section parametrization of Bosch and Hale to calculate the probability of secondary fusion for both D^{3}He-protons and DT-neutrons.[10] This model, which calculates the probability of secondary production assuming a uniform plasma with a known density, temperature, and composition, is applied here to study the trends in secondary yield production.

As an illustrative case, the secondary yield production from a uniform, spherical deuterium plasma with various average areal densities ($\rho R_{deuterium}$) is shown in Figure D.2.[a] The secondary yield production probability Y_2/Y_1 scales approximately linearly with average fuel-ρR, until the ^{3}He or T are stopped by the plasma, at which point the ratio saturates.[1] The range of the reactant

[a]Here and throughout this work, the nuclear production is assumed to occur volumetrically.

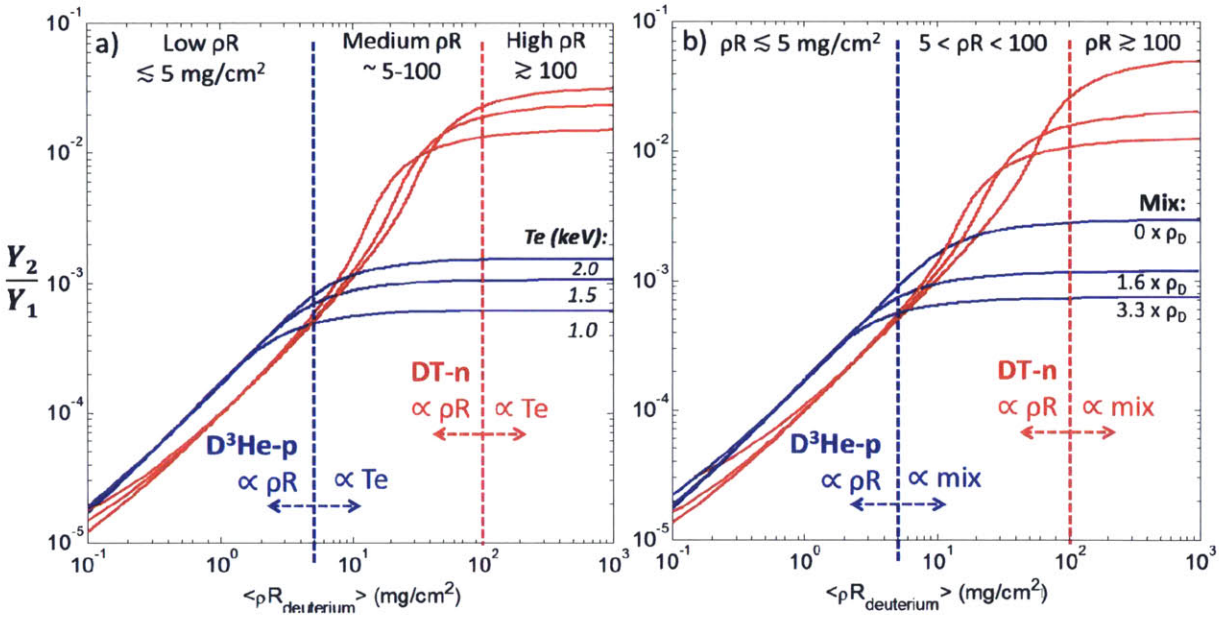

Figure D.2. Production probability for secondary D^3He-protons (blue) and DT-neutrons (red) as a function of ρR for various a) electron temperatures T_e and b) uniform CH mix. The example assumes a uniform deuterium plasma with $\rho = 0.21$ g/cc, $T_i = 3.4$ keV (for the mix study, $T_e = T_i$). The range of the DD-^{3}He (blue dashed) and DD-t (red dashed) divide the plot into three regions: low ρR ($\lesssim$5 mg/cm^2), for which both secondary products are produced proportionally to ρR; medium ρR ($5 \lesssim \rho R \lesssim 100$ mg/cm^2), for which the D^3He-proton yield saturates at a level governed by the stopping power (T_e or mix) and the DT-neutron yield continues to scale with ρR; and high ρR ($\gtrsim$100 mg/cm^2), for which both yields saturate and ρR cannot be inferred.

ions, and therefore the saturation value of Y_2/Y_1, depends sensitively on the stopping power of the plasma. The stopping power scales approximately linearly with the fuel electron temperature, as shown in Figure D.2a), but is also affected by the plasma composition as shown in Figure D.2b). Since the DD-^{3}He is ranged out at a lower ρR than the DD-t, the trends in secondary yield probability are divided into three regions: low-ρR, for which both the ^{3}He and T escape the plasma; medium-ρR, for which the ^{3}He is ranged out but the T escapes, and high-ρR, for which both products are ranged out. In the middle region, which occurs between approximately 5 and 100 mg/cm^2, measuring both secondary yields provides a strong constraint on both the ρR and the total stopping power in the plasma.

To highlight this behavior, Figure D.3 shows the ratio of secondary neutron to secondary proton yields versus the deuterium areal density in the fuel (ρR_d) for a uniform plasma with a variety of temperatures and compositions.[b] Each curve is divided into three regions, defined by the respective ranges of a DD-^{3}He and DD-triton in that plasma. At low average fuel ρRs, both reactant ions escape the plasma, and the ratio of secondary yields varies slowly, with a value of approximately 0.6. As the ^{3}He is ranged below the peak of its fusion cross section, the ratio of secondary yields begins to rise rapidly. The curve plateaus at a value of approximately 20 when the triton is ranged out.

[b]Deuterium areal density, $\rho R_d = n_d m_d R$, is the areal density value relevant to secondary yield production – effectively, how many deuterons the reactant particle 'sees' in-flight – while the total areal density in the fuel ρR_{tot} is relevant for stopping power. In Figure D.3a) the plasma is pure deuterium so $\rho R_d = \rho R_{tot}$. In Figure D.3b) the horizontal shift between the curves is set almost entirely by the scaling factor $\rho R_d = (f_d A_d / \langle A \rangle) \rho R_{tot}$, where $\langle A \rangle$ is the average ion mass in the plasma.

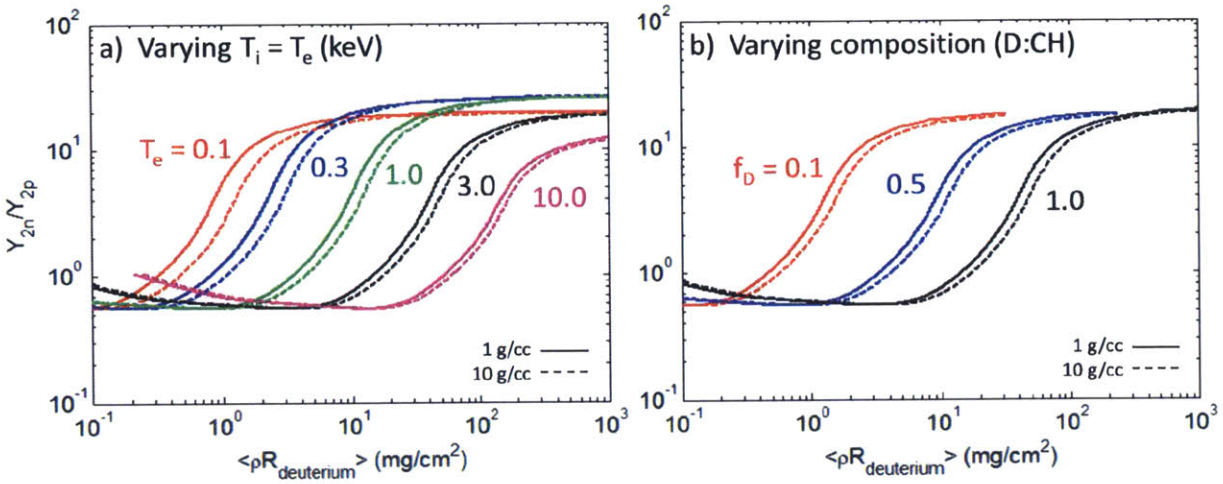

Figure D.3. The ratio of secondary DT-neutron yield to secondary D^{3}He-proton yield varies with the deuterium areal density in the fuel, ρR_d. The curve is affected by the plasma stopping power, which changes with a) temperatures ($T_i = T_e$, from 0.1 to 10 keV in a pure deuterium plasma) and b) plasma composition (deuterium with plastic admixture: the deuterium fraction $f_D = n_D/(n_D + n_{CH})$ ranges from 0.1 to 1.0; $T_i = T_e = 3$ for this calculation). Curves are plotted for plasma density of 1 g/cc (solid) and 10 g/cc (dashed). Each curve varies rapidly for values of ρR in between the respective ranges of the DD-^{3}He and DD-t. The region of rapid variation changes depending on the plasma stopping power. Below and above the region of rapid change, the ratio of secondary neutrons to secondary protons is nearly constant.

The ranges of ρR_d for which the curve varies rapidly is highly sensitive to the stopping power of the plasma, which depends on the plasma temperature and composition. This presentation highlights the fact that by measuring both of the secondary yields, the ratio between them (Y_{2n}/Y_{2p}) contains information on the stopping power of the plasma, as long as the ρR is within a certain range. Since both mix and plasma electron temperature affect the stopping power, these two values are degenerate in terms of inferring a change in stopping power from the secondary yields.

The effect of mix on the stopping power can be calculated numerically, as above; however, an analytical approach offers some insight into how the secondary yields scale with mix. Consider a uniform deuterium plasma with n uniformly mixed ion species, with charge state $Z_1, \ldots, Z_n$, atomic mass $A_1, \ldots, A_n$, and ion number fraction $f_1, \ldots, f_n$, with $f_k = n_k/n_{i,tot}$ such that $f_D + \sum_k^n f_k = 1$. The electron density in such a plasma will be $n_e = n_{i,tot}(f_D + \sum_k^n Z_k f_k)$. Since the reactant ions slow down primarily on electrons in this regime, $dE/dx \propto n_e$. Assuming the fuel areal density is high enough to stop the reactant ions, the probability of secondary fusion will then scale in the following manner:

$$P_2 = \int_{E_0}^{0} \frac{n_D \sigma_{fus}(E)}{dE/dx} dE = \frac{f_D}{f_D + \sum_k^n Z_k f_k} P_2^0. \tag{D.5}$$

Here, the probability of secondary fusion from equation D.3 has been recast as an integral over energy, and P_2^0 is the probability for secondary fusion in a pure deuterium plasma with the same deuterium density. Adding uniformly mixed ions into the plasma inhibits secondary yield production by simultaneously increasing the stopping power through increased electron density, and diluting the deuterium ions. This scaling holds regardless of fuel density, so long as the reactant ions are stopped in the plasma and stopping is primarily on electrons.

The integral in Equation D.5 can be generalized to all plasmas for which the final energy of

the reactant particle is fixed at a non-zero value. That is to say, if the areal densities ρR_{equal} that provide equal stopping for a reactant species in pure deuterium and multi-species plasmas can be determined, then the following is true:

$$P_2 \frac{f_D + \sum_k^n f_k Z_k}{f_D} = F(\rho R_{equal}), \tag{D.6}$$

where F is a function of ρR_{equal} only. For many cases, in particular those for which the charge-to-mass ratio (Z/A) is close to that for deuterium (1/2), the formula is approximately valid under the assumption $\rho R_{equal} = \rho R_{total}$ as the plasma composition is varied. In the limit of low ρR, F is then approximately equal to ρR_{tot} multiplied by a constant: $0.1/(\mathrm{g/cm^2})$ for secondary DT-neutrons, and $0.17/(\mathrm{g/cm^2})$ for secondary D^3He-protons. Numerical studies were used to study the accuracy of Equation D.6 for a wide variety of plasma conditions over the entire range of areal density. This secondary yield scaling appears to be accurate to within 25% for both secondary products, for densities below 1 g/cc and electron temperatures above 1 keV. An exception is for deuterium-hydrogen mixtures, for which the scaling is not accurate even in the low-ρR regime. This appears to be due to the increased importance of stopping on the hydrogen ions. An improved derivation of Equations D.5 and D.6 to better account for the change of stopping power in the plasma with arbitrary species remains as future work. The full numerical modeling of the stopping power used in the remainder of this work intrinsically incorporates the details of plasma composition.

The uniform mix model presented here is most directly relevant to the case of ICF targets initially filled with deuterium and additional gases, such as low levels of dopants for x-ray imaging (Ar, Kr) or other fusion fuels (^{3}He, T). The DD implosion database for indirect drive at OMEGA includes several examples of implosions with 10 atm D_2 fuel doped with 0.05 atm Ar.[11] In such an implosion, assuming Helium-like Argon (Z = 16), the scaling in equation D.5 predicts that the secondary yield will only be reduced by ~4% compared to the pure-deuterium case. However, in targets with 50:50 mixtures of D^3He, which are routinely imploded on the OMEGA laser as backlighters for monoenergetic proton radiography experiments[12] or for studies of kinetic plasma dynamics (see Chapter 4 and, for example, Reference [13]), the secondary yields are expected to be reduced by 67% compared to a pure-deuterium case. Diagnosis of the secondary D^3He-protons from D^3He-gas filled implosions is exceptionally difficult due to a primary D^3He-proton yield several orders of magnitude larger. The secondary DT-neutrons may in principle be measured. In symmetry (SymCap) and convergent-ablator (ConA) surrogate experiments at the NIF, for which D^3He fuel with deuterium fraction of 30% are imploded and reach average fuel areal densities exceeding 100 $\mathrm{mg/cm^2}$, the above scaling indicates that the secondary yields will be reduced by 80% compared to a pure deuterium implosion.

D.2 Analysis of Experimental Data from the NIF

The combined secondary yield analysis was applied to data recorded on several experiments performed at the National Ignition Facility. The indirect-drive ignition relevant experiments produce fuel assemblies with very high areal density on the order of hundreds of $\mathrm{mg/cm^2}$, and as such this technique cannot be applied to them. However several experimental campaigns have investigated plasmas with moderate areal density and pure deuterium fuel. This section will present the secondary yield data and combined secondary analysis for three campaigns: polar-direct-drive exploding pushers, indirect-drive 1-shock and 2-shock implosions, and the polar-direct-drive defect-induced mix experiments (DIME).

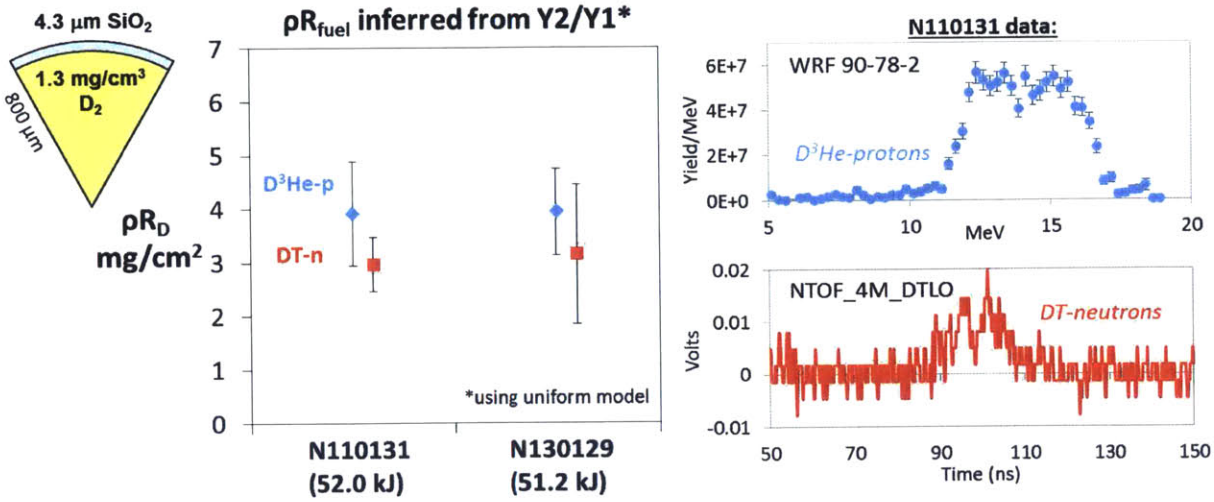

Figure D.4. Fuel ρR was inferred from both secondary D^{3}He-p and DT-n yields on two NIF polar-direct drive (PDD) Exploding Pushers, N110131 and N130129. For both shots, the ρR inferred from each secondary product was in agreement. These experiments have a low fuel ρR such that the DD-^{3}He are not ranged out and only ρR can be robustly inferred.

Table D.1. Shot parameters and yields for NIF Exploding Pushers used in combined secondary yield analysis study.

Shot	OD μm	wall μm	Energy kJ	Pulse ns	T_i keV	Y_{DD} $\times 10^{11}$	$Y2_{D^3He}$ $\times 10^8$	$Y2_{DT}$ $\times 10^7$
N110131	1555	4.5	52	2.1	5.4 ± 0.2	3.0(±0.1)	2.0(±0.4)	8.6(±1.0)
N130129	1533	4.6	51.4	1.4	3.9 ± 0.3	2.5(±0.2)	1.7(±0.3)	7.6(±2.8)

D.2.1 Polar-direct-drive exploding pushers

Shock-driven 'exploding pusher' implosions are used on the NIF primarily for diagnostic calibration, although careful analysis of the experimental data has provided insights into kinetic processes in the shock-convergence phase of ICF.[14] Because these implosions are gas-filled (ρ_0=1.6 mg/cc) and have low convergence (CR~5), the fuel ρR at bang-time is expected to be low. Specifically, the initial fuel areal density $\rho R_0 \approx 0.13$ mg/cm^2 is expected to grow by a factor of CR$^2 \sim 36$, so a final value of < 5 mg/cm^2 is expected.[c] This expectation is confirmed by the data from two implosions, shown in Figure D.4. The fuel ρR inferred from both secondary products were found to agree with each other, with a value of ~ 4 mg/cm^2. This value is in the 'low' ρR region of Figure D.2, and as such the yield of both secondary products is expected to scale linearly with ρR, and neither T_e nor mix can be robustly inferred. The shot parameters and measured yields are given in Table D.1.

The data was used to infer an upper bound on the amount of fuel-shell mix present in the experiments. Introducing mix increases the total areal density in the fuel without increasing the deuterium areal density. Therefore sufficient mix would range out the DD-^{3}He sooner than expected, and increase the secondary neutron-to-proton ratio. The amount of mix required for inconsistency with the measured secondary yield data was determined to be 3.4 μg for N110131 and 1.3 μg for N130129. Figure D.5 shows the χ^2 map as a function of mix mass and ρR for both shots. Both sets of data are most consistent with a clean implosion. The upper limit on mixed mass can be

[c] This calculation, performed in reverse, is used to determine the convergence ratio in the experiment.

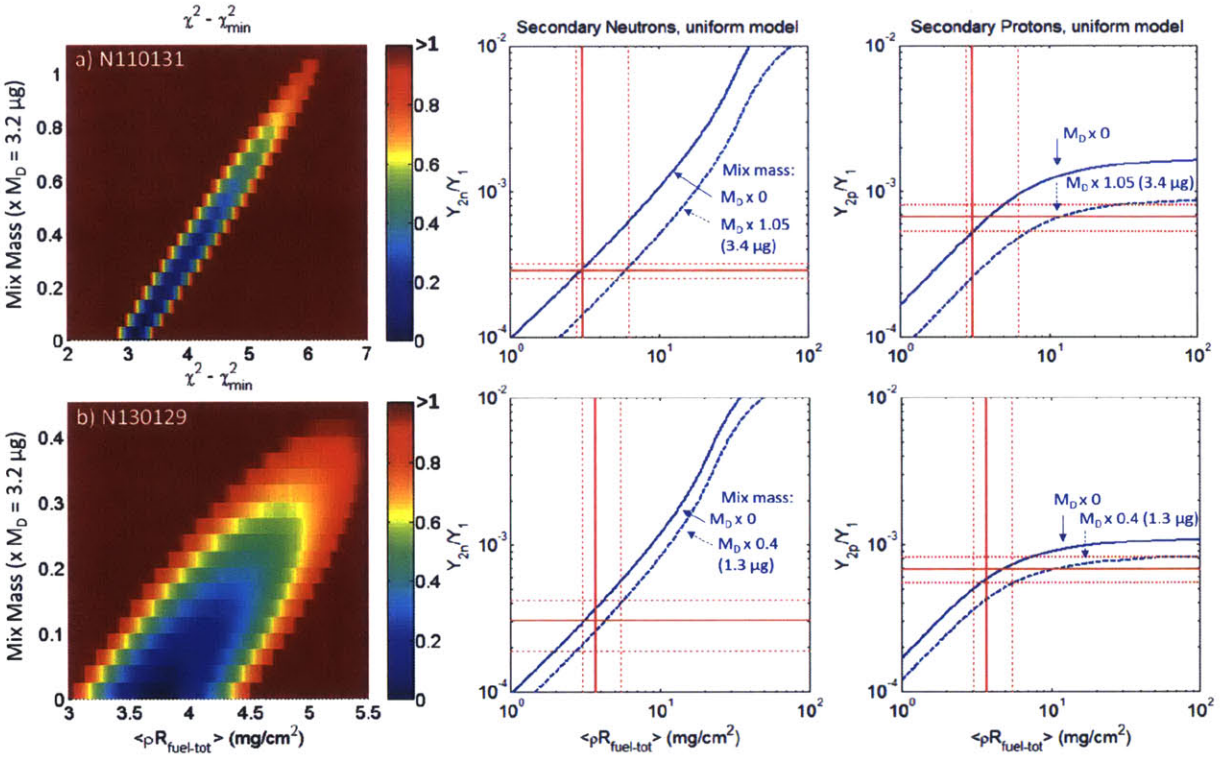

Figure D.5. Upper bound calculation for mix mass in two NIF Exploding Pusher implosions: a) N110131 and b) N130129. The χ^2 map (left) shows the values of mix mass (as a fraction of the total deuterium mass $M_D = 3.2$ μg) and total fuel ρR that are consistent with the observed secondary yield production. Regions with $\chi^2 \leq 1$ are consistent with the data. The simulated secondary yield production curves as a function of fuel ρR are shown for neutrons (middle) and protons (right), for both a clean fuel and including the upper bound mix mass. Measured secondary yields with uncertainties (red horizontal lines), and inferred ρR with uncertainties (red vertical lines) are also shown.

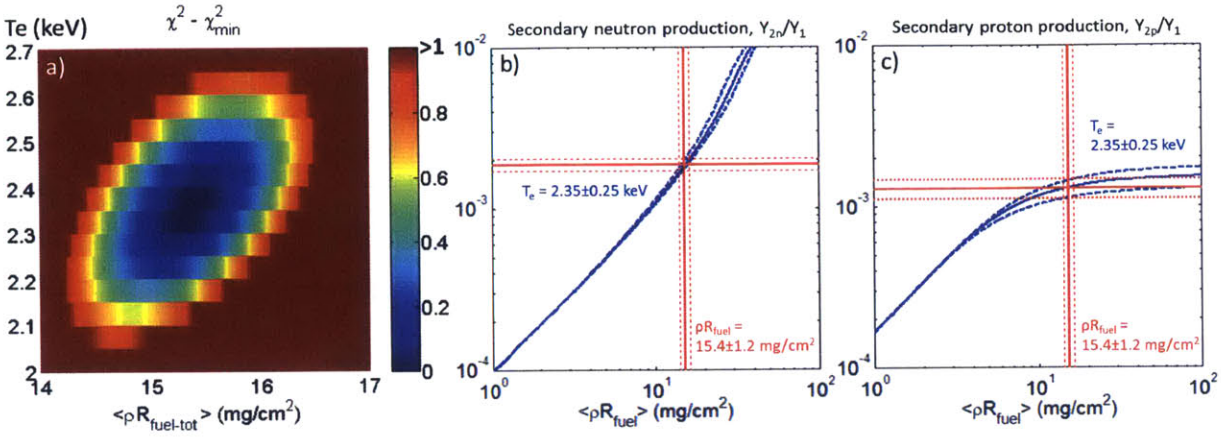

Figure D.6. Combined secondary yield analysis for the D_2-filled Indirect Drive Exploding Pusher implosion (N130312). The analysis assumes a pure deuterium plasma with $\rho = 1.4 \pm 0.43$ mg/cc and $T_i = 3.53 \pm 0.18$ keV. a) The χ^2 map showing regions of electron temperature and average total fuel areal density that are consistent with the data: the best-fit values are $\rho R_{fuel} = 15.4 \pm 1.2$ mg/cm^2 and $T_e = 2.35 \pm 0.25$ keV. A χ^2 in excess of the minimum value plus one (red areas) indicates inconsistency. The calculated secondary yield production ratio for b) DT-neutrons and c) D^{3}He-protons is shown for the best-fit T_e (blue solid) and the range of acceptable T_e (blue dashed), along with the measured data and uncertainty (red horizontal lines) and inferred average ρR_{fuel} and uncertainty (red vertical lines). The ranging out of the DD-^{3}He ions is evident.

understood as the amount of additional mass necessary to range out DD-^{3}He ions. The slightly higher fuel ρR inferred for N130129 and the slightly lower temperature on this shot translates into a higher average stopping power, and a reduced upper bound on the mix mass. The simulated secondary generation curves for both the no-mix case and the upper-bound mix are also shown for each shot.

D.2.2 Indirect-drive 1- and 2-shock implosions

The 'Indirect Drive Exploding Pusher' was a 1-shock implosion that was designed to provide a simple 1D-hydrodynamic implosion for verification of hydrodynamic codes. A D_2-filled and a DT-filled implosion using this platform demonstrated optimally 1D performance and agreement across the board with simulated predictions.[15] Both secondary D^{3}He-protons and DT-neutrons were measured on the DD-filled implosion N130312, and the combined secondary analysis was performed as shown in Figure D.6. The target and laser parameters and the observed yields are shown in Table D.2. In this implosion, the average ρR_{fuel} was sufficiently high to range out the DD-^{3}He. Since the implosion was observed to evolve in an exceptionally 1D manner, hydrodynamic mix is considered to be negligible. As such, the data was used to determine the average $\rho R_{fuel} = 15.4 \pm 1.2$ mg/cm^2 and the average fuel electron temperature $T_e = 2.35 \pm 0.25$ keV.

This electron temperature is approximately 66% of the measured DD-neutron burn-averaged ion temperature ($\langle T_i \rangle = 3.53 \pm 0.18$ keV). This is not a discrepancy, but reflects a difference in what these measured quantities represent. Because of the strong reactivity scaling with ion temperature, the burn-averaged ion temperature is weighted toward the hotter regions of the plasma. In contrast, the electron temperature measured by the secondary yield analysis is averaged over the entire deuterium-containing volume, weighted to nuclear burn. The electrons will also cool more rapidly than the ions due to radiative emission and electron thermal conduction out of the hotspot.

Table D.2. Shot parameters and yields for NIF 1- and 2-shock indirect-drive implosions used in combined secondary yield analysis study.

Shot	OD μm	wall μm	Energy kJ	Pulse	T_i keV	Y_{DD} $\times 10^{12}$	$Y2_{D^3He}$ $\times 10^9$	$Y2_{DT}$ $\times 10^{10}$
N130312	2110	120 CH	892	1-shock	3.5 ± 0.2	5.2 ± 0.2	6.6 ± 0.9	0.96 ± 0.08
N130813	2167	83.5 HDC	1290	2-shock	3.6 ± 0.2	22 ± 2	14 ± 7	13.5 ± 1.3

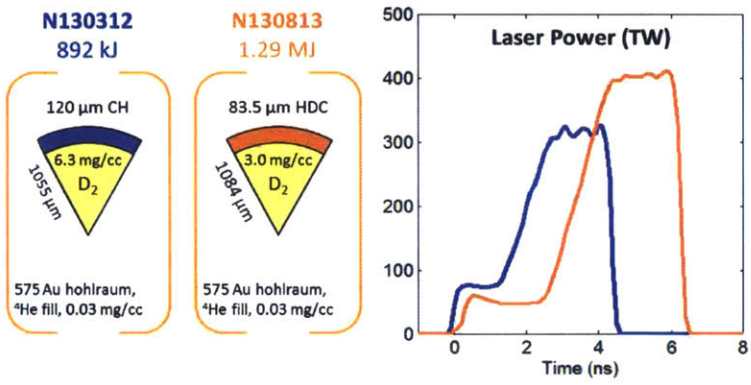

Figure D.7. Comparison of the targets and laser impulses for the 1- and 2-shock implosions on NIF (N130321 and N130813, respectively). In addition to increased laser energy for N130812, the major difference between the two implosions is the choice of shell material (CD and HDC, respectively).

A followup experiment to this 1-shock implosion was performed using a 2-shock implosion to achieve higher density and convergence. Both secondary products were also observed on the 2-shock, deuterium-filled implosion N130813: the target and laser parameters and the observed yields are shown in Table D.2. In addition to the laser pulse shape change, this implosion also used a high-density carbon target rather than CH. A comparison of the two targets and laser impulses is shown in Figure D.7. The combined secondary analysis was performed with the results shown in Figure D.8. The fuel ρR was found to be larger than in the 1-shock implosion, as expected. The measured electron temperature is colder than in the 1-shock implosion by almost a factor of two, although the burn-averaged ion temperatures are comparable. The 2-shock implosion produces a lower adiabat than the 1-shock implosion, and therefore a lower fuel-averaged temperature is reasonable.

D.2.3 Defect-induced mix experiments (DIME)

A series of six deuterium-filled, polar-direct-drive experiments was performed at the NIF in 2012 and 2013, as part of the defect induced mix experiments (DIME) campaign at the NIF.[16] These experiments imploded 2.2 mm diameter CH capsules with shell thickness 42 μm and filled with 0.6 mg/cc D_2. The targets were illuminated with 630–690 kJ of laser energy, reaching a peak power of 325 TW. Observed primary DD-neutron yields were in the range 3–9 $\times$ 10^{11}, and secondary proton and neutron yields were recorded on all shots. A summary of the experiment information and recorded data is given in Table D.3.

Substantial mix was inferred in these experiments by x-ray spectroscopic methods.[17] Since the electron temperature is unknown, both of these parameters may be expected to play a role in the plasma stopping power. The measured burn-averaged ion temperatures provide an upper limit on the volume-averaged plasma electron temperature during burn; setting $T_e = \langle T_i \rangle$ in the analysis results in the ρR_{fuel} and mix masses shown in Figure D.9. Because of the degeneracy in stopping power between colder T_e and increased mix, these mix masses can be taken as an upper bound, and correspond to a maximum of the innermost ~2 μm of the shell mixing completely into the

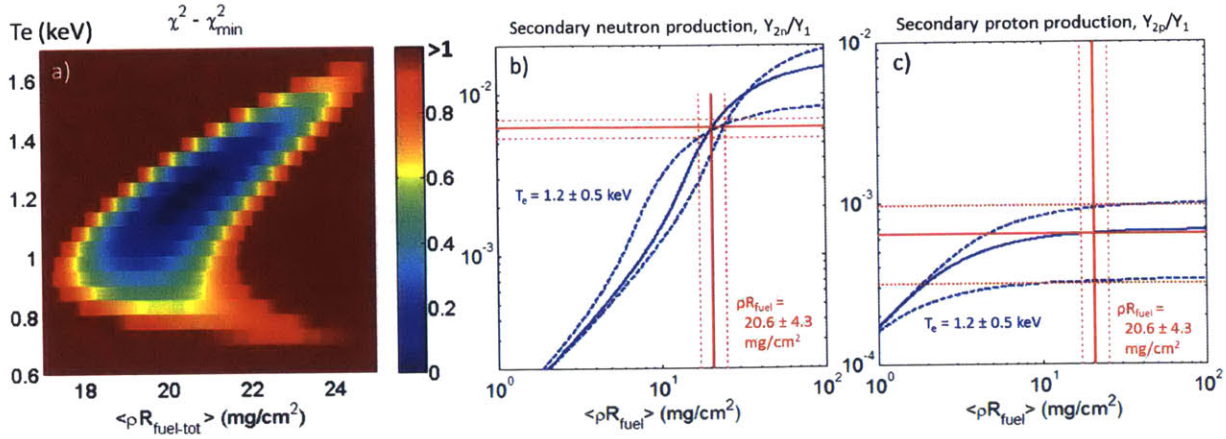

Figure D.8. Combined secondary yield analysis for the Indirect Drive 2-shock implosion, N130813. The analysis assumes a pure deuterium plasma with $\rho = 2.96 \pm 0.89$ mg/cc and $T_i = 3.6 \pm 0.2$ keV. a) The χ^2 map showing regions of T_e and ρR_{fuel} that are consistent with the data: the best-fit values are $\rho R_{fuel} = 20.6 \pm 4.3$ mg/cm^2 and $T_e = 1.2 \pm 0.5$ keV. $\chi^2 - \chi^2_{min} > 1$ (red) indicates inconsistency. The calculated secondary yield production ratio for b) DT-neutrons and c) D^{3}He-protons is shown for the best-fit T_e with uncertainties (blue), along with the measured data and uncertainty (red horizontal lines) and inferred average ρR_{fuel} and uncertainty (red vertical lines).

fuel. Each of these implosions had an initial total deuterium mass of 4.1 μg. Given the average mass of the mixed CH ions is 3.25× the deuteron mass, the number density of mix inferred for the implosions is comparable to the initial number density of deuterium.

Although Figure D.9 shows three quantities, only two independent quantities are inferred from the data. Mixed mass and total deuterium areal density in the fuel (b and c) are the most well-constrained quantities by the secondary data, while the total ρR is degenerate with the other two. In effect, the secondary neutron analysis constrains the deuterium ρR, while the secondary proton analysis constrains the stopping power (in this case, mix).

In the indirect-drive 1-shock and 2-shock implosions, the electron temperature was significantly lower than the burn-averaged ion temperature, and it is likely the same is true in the DIME implosions. To assess the dependence of the inferred mix on the electron temperature, the mix was evaluated for various T_e in one of the implosions (N121207). The resulting trends, which are shown

Table D.3. Shot parameters and yields for the defect induced mix experiments (DIME) campaign on the NIF. All capsules were composed of CH, filled with 0.6 mg/cc of pure D_2 gas, and imploded using a 2 ns square laser impulse in polar-direct-drive mode. The capsule for N120730 was fabricated with an equatorial groove to induce mix; all others were spherical.

Shot	OD μm	wall μm	Energy kJ	T_i keV	Y_{DD} $\times 10^{11}$	$Y2_{D^3He}$ $\times 10^8$	$Y2_{DT}$ $\times 10^8$
N120728	2200	40	688	4.4 ± 0.3	5.8 ± 0.4	2.1 ± 0.4	2.8 ± 0.3
N120730	2200	40	689	4.2 ± 0.3	6.5 ± 0.4	2.2 ± 0.4	3.5 ± 0.3
N121119	2200	40	659	4.3 ± 0.4	8.6 ± 0.4	3.7 ± 0.7	6.2 ± 0.6
N121207	2200	42	631	3.4 ± 0.2	3.7 ± 0.2	1.9 ± 0.4	2.4 ± 0.2
N130320	2200	42	319	3.7 ± 0.2	7.3 ± 0.2	5.8 ± 1.2	10.3 ± 1.0
N130321	2200	42	463	3.8 ± 0.2	6.0 ± 0.2	4.0 ± 0.8	5.1 ± 0.5

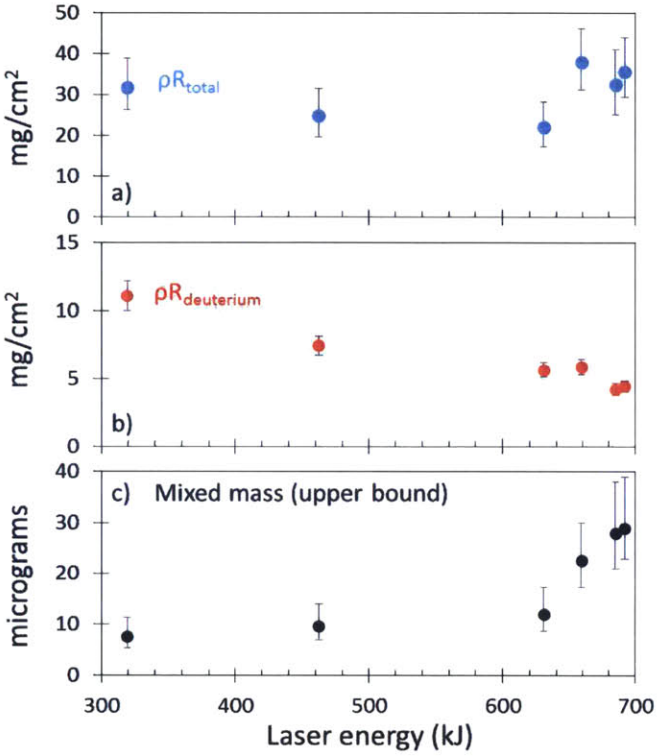

Figure D.9. Inferred values from secondary yield data recorded on the defect induced-mix experiments (DIME) performed on the NIF, plotted as a function of laser energy: a) the total average ρR in the fuel region (blue) and b) the average deuterium ρR in the fuel region (red); c) the mixed mass inferred in the fuel region (black). Increased laser energy is associated with increased mix. T_e, which is degenerate with mix for this analysis, was set equal to the measured burn-averaged ion temperature in this calculation; therefore the mixed mass should be taken as an upper bound.

in Figure D.10, show an approximately linear relationship between increased T_e and increased inferred mix. The measured $\langle T_i \rangle$ is shown for reference. For this implosion, an x-ray spectroscopic method was also used to constrain the mixed mass, which is also shown on the figure along with a simulated value.[17] The secondary-inferred mix is consistent with the x-ray mix measurement for electron temperatures in the range $\sim 2.4 \pm 0.4$, which is generally plausible. This data illustrates that use of the secondary yields to robustly measure a mixed mass in the fuel requires additional knowledge of the electron temperature in the fuel.

D.3 Summary

A technique has been developed to infer the average fuel areal density during burn, and either the average fuel electron temperature or the average mix mass in the fuel during burn, using the combined information from the secondary DT-neutron and D^{3}He-proton yields from deuterium-filled implosions. The secondary yields are produced by in-flight reactions of the primary fusion products DD-^{3}He (0.82 MeV) and DD-t (1.01 MeV) with thermal deuterons. The reactivity for the secondary D^{3}He (DT) reaction decreases (increases) as the ^{3}He (t) ion slows in the plasma. Because of this difference, and because the range of the triton is a factor of ~ 20 larger than that of the ^{3}He ion, the ratio of the secondary proton to secondary neutron yields changes with both the average deuterium ρR and with the average stopping power of the plasma. The stopping power is primarily sensitive to plasma electron temperature and plasma composition.

By invoking a model of the stopping power, the combined primary and secondary yield information is used to infer the areal density as well as the T_e or the mix mass for implosions with moderate fuel ρR, in the range ~ 0.5 to ~ 100 mg/cm^2. Implosions with areal density below ~ 5 mg/cm^2 do not range out the ^{3}He ion, such that only ρR may be inferred robustly. Implosions with areal

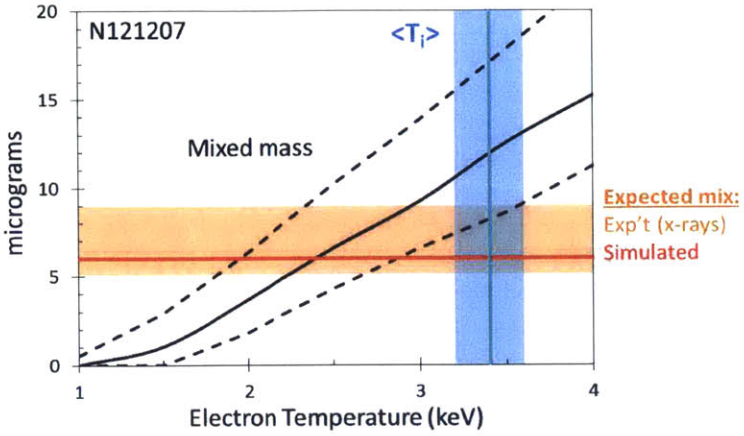

Figure D.10. Variation of the inferred mix mass with the value assumed for T_e in the analysis of the secondary yields from the DIME implosion N121207. The inferred mix mass (black) and uncertainty (black dashed) increase approximately linearly with the assumed plasma electron temperature, because both T_e and mix affect the plasma stopping power. The mix values inferred from x-ray spectroscopic measurements (orange) and simulations (red) are in agreement with the secondary-inferred mix values for $T_e \approx 2.4 \pm 0.4$. This value is somewhat lower than the measured burn-averaged ion temperature $\langle T_i \rangle = 3.4 \pm 0.2$ (blue), which was also observed in the 1- and 2-shock implosions discussed in Section D.2.2

density above $\sim$ 100 mg/cm^2 range out both reactant ions, such that the stopping power-related quantities (T_e and mix) may be inferred, but only a lower bound can be put on ρR. This technique has been applied to three classes of NIF implosions: polar-direct-drive exploding pushers with low ρR; indirect-drive 1-shock and 2-shock implosions, for which mix was negligible and T_e was inferred; and the polar-direct-drive DIME campaign, for which significant mix was observed.

Much future work can be done to improve this technique. The model developed here is essentially zero-dimensional, assuming a uniform plasma during burn. Temperature and density profiles vary with radius in 1D-simulations, which would have an effect on reactant slowing in the plasma and secondary production. More precise comparisons with experiments will require incorporation of more realistic spatial models. Previous research has implemented Monte Carlo simulation for secondary yields based on 1D profiles,[3] which could be done for this analysis as well. Fundamentally, only three pieces of information are being used in this approach – the primary and secondary yields – and as such at most three pieces of information can be inferred, which is not sufficient to constrain profiles of density, temperature, and mix. The ultimate application of this analysis is in support of a larger diagnostic effort to understand as well as possible the state of the fusing plasma.

D.4 References

1. F. H. Séguin, C. K. Li, J. A. Frenje *et al.*, "Using secondary-proton spectra to study the compression and symmetry of deuterium-filled capsules at OMEGA," Physics of Plasmas, **9**(6), 2725 (2002).
2. P. B. Radha, J. Delettrez, R. Epstein *et al.*, "Inference of mix in direct-drive implosions on OMEGA," Physics of Plasmas, **9**(5), 2208 (2002).
3. S. Kurebayashi, J. A. Frenje, F. H. Séguin *et al.*, "Using nuclear data and Monte Carlo techniques to study areal density and mix in D_2 implosions," Physics of Plasmas, **12**(3), 032703 (2005).
4. F. H. Séguin, J. A. Frenje, C. K. Li *et al.*, "Spectrometry of charged particles from inertial-confinement-fusion plasmas," Review of Scientific Instruments, **74**(2), 975 (2003).
5. F. H. Séguin, N. Sinenian, M. Rosenberg *et al.*, "Advances in compact proton spectrometers for inertial-confinement fusion and plasma nuclear science," Review of Scientific Instruments, **83**(10), 10D908 (2012).

6. A. B. Zylstra, J. A. Frenje, F. H. Séguin *et al.*, "The effect of shock dynamics on compressibility of ignition-scale National Ignition Facility implosions," Physics of Plasmas, **21**(11), 112701 (2014).
7. V. Y. Glebov, C. Stoeckl, T. C. Sangster *et al.*, "Prototypes of National Ignition Facility neutron time-of-flight detectors tested on OMEGA," Review of Scientific Instruments, **75**(10), 3559 (2004).
8. V. Y. Glebov, T. C. Sangster, C. Stoeckl *et al.*, "The National Ignition Facility neutron time-of-flight system and its initial performance (invited)," Review of Scientific Instruments, **81**(10), 10D325 (2010).
9. C.-K. Li and R. D. Petrasso, "Charged-particle stopping powers in inertial confinement fusion plasmas," Physical Review Letters, **70**(20), 3059 (1993).
10. H.-S. Bosch and G. M. Hale, "Improved formulas for fusion cross-sections and thermal reactivities," Nuclear Fusion, **32**(4), 611 (1992).
11. J. D. Lindl, P. Amendt, R. L. Berger *et al.*, "The physics basis for ignition using indirect-drive targets on the National Ignition Facility," Physics of Plasmas, **11**(2), 339 (2004).
12. C. K. Li, F. H. Séguin, J. A. Frenje *et al.*, "Monoenergetic proton backlighter for measuring E and B fields and for radiographing implosions and high-energy density plasmas (invited)," Review of Scientific Instruments, **77**(10), 10E725 (2006).
13. J. R. Rygg, J. A. Frenje, C. K. Li *et al.*, "Tests of the hydrodynamic equivalence of direct-drive implosions with different D_2 and ^3He mixtures," Physics of Plasmas, **13**(5), 052702 (2006).
14. M. J. Rosenberg, A. B. Zylstra, F. H. Seguin *et al.*, "Investigation of Ion Kinetic Effects in Direct-Drive Exploding-Pusher Implosions at the NIF," Physics of Plasmas (submitted).
15. S. Le Pape, L. Divol, L. Berzak Hopkins *et al.*, "Observation of a Reflected Shock in an Indirectly Driven Spherical Implosion at the National Ignition Facility," Physical Review Letters, **112**, 225002 (2014).
16. M. J. Schmitt, P. A. Bradley, J. A. Cobble *et al.*, "Development of a polar direct-drive platform for studying inertial confinement fusion implosion mix on the National Ignition Facility," Physics of Plasmas, **20**(5), 056310 (2013).
17. P. Hakel, G. A. Kyrala, P. A. Bradley *et al.*, "X-ray spectroscopic diagnostics and modeling of polar-drive implosion experiments on the National Ignition Facility," Physics of Plasmas, **21**(6), 063306 (2014).

Appendix E

Investigation of Yield Anomaly in Indirect-Drive Glass-Capsule Implosions on OMEGA

The primary physics findings presented in Chapters 3 and 4 were obtained in direct-drive implosions of thin-glass targets using the OMEGA laser. Since the kinetic physics effects occur in the fuel and at the fuel-shell interface, it was expected that they should be insensitive to the type of drive. To explore this question, three series of indirect-drive, glass-capsule implosions filled with various densities and ratios of D^3He-gas were performed on the OMEGA laser.

The first five experiments were implosions of thin ($\sim$ 5 μm) glass shell, 50:50 D^3He-gas filled targets performed on September 1st, 2011. The implosions produced significantly fewer DD-neutrons than expected by 1D-LASNEX simulations, while the D^3He-proton yields agreed well with the models, as shown in Figure E.1. As for the direct-drive implosions, which were discussed in Chapter 4, the D^3He-proton yields were observed to agree better with the simulations than the DD-neutron yields. To follow up on this result, two additional experiments were performed using the same hohlraums but increased laser power. Thirteen thick ($\sim$ 24 μm) glass shells filled with various combinations of D_2 and ^3He gas were imploded on May 7th, 2013, and six additional thin-glass shells filled with 50:50 D^3He or pure D_2 were imploded on August 1st, 2013. The design of these experiments is presented in Section E.1, and experimental data is presented in Section E.2. A discussion interpreting these results is included in Section E.3.

E.1 Experimental Design

All the experiments described in this appendix used a gold vacuum hohlraum with an outer diameter of 1.6 mm and a length of 2 mm ('OMEGA scale 1'), and 0.8 mm diameter laser entrance holes (50% of the hohlraum radius). In the first experimental series, which was performed on a half-day of OMEGA-only shots as part of a joint OMEGA/OMEGA–EP shot day on September 1st, 2011, these hohlraums were used to implode glass capsules with a $\sim 623.6 \pm 2.2$ μm outer diameter and $\sim$ 5.2 μm-thick wall. These capsules were filled with 6.23 ± 0.01 mg/cm^2 of 50:50 D^3He gas. A 1 ns square impulse using 30 of the OMEGA beams and containing $\sim$ 12.8 kJ was used to drive the hohlraum. These beams included ten 'Cone 2' beams, which enter the hohlraum at a 42.0 ° angle relative to the axis, and twenty 'Cone 3' beams, which enter the hohlraum at a 58.9 ◦ angle. These beams were focused and pointed at the center of the laser entrance holes. The SG4 phase plates were used, although they were designed for spherical implosions.

The second experimental series was performed on a full-day of OMEGA shots awarded through the LLNL-NIC program on May 7th, 2013. Identical hohlraums were used to drive glass capsules with a similar $\sim$ 603 μm outer diameter but a thicker, $\sim$ 24.4 μm wall. The thicker wall was

Table E.1. Shot information for indirect-drive thin- and thick-glass implosions on OMEGA. Shots 63416–63421 were performed on Sept. 1st, 2011; 69656–69672 were performed on May 7th, 2013; and 70540–70551 were performed on Aug. 1st, 2013. All shots used a 1 ns square (SG1018) laser impulse.

Shot #	Capsules		Initial gas		Laser Information	
	OD (μm)	wall (μm)	ρ_0 (mg/cm^2)	f_D	Energy (kJ)	Cones
63416	623.4	5.2	6.23	0.498	12.69	2, 3
63417	626.4	5.2	6.21	0.499	12.82	2, 3
63419	623.4	5.2	6.23	0.498	12.80	2, 3
63420	624.4	5.2	6.25	0.497	12.80	2, 3
63421	620.4	5.2	6.23	0.498	12.66	2, 3
average	623.6±2.2	5.2	6.23±0.01	0.498±0.001	12.75±0.07	
69656	601.4	24.3	4.61	0.506	16.68	1, 2, 3
69657	598.0	24.6	4.67	0.501	16.78	1, 2, 3
69658	609.8	24.2	4.64	0.787	16.78	1, 2, 3
69660	600.9	24.4	4.55	0.799	16.66	1, 2, 3
69661	604.4	24.4	4.62	1	16.61	1, 2, 3
69663	600.1	24.4	4.63	1	16.60	1, 2, 3
69665	601.9	24.5	4.62	0.202	16.82	1, 2, 3
69666	605.1	24.5	4.61	0.189	16.46	1, 2, 3
69667	606.1	24.3	2.99	0.497	16.61	1, 2, 3
69668	604.0	24.3	1.54	0.501	16.55	1, 2, 3
69669	599.0	24.4	1.55	0.499	16.67	1, 2, 3
69671	605.8	24.3	4.61	0.506	16.41	1, 2, 3
69672	601.2	24.4	4.63	1	16.69	1, 2, 3
average	602.9±3.3	24.39±0.11	4.62±0.03[†]		16.64±0.12	
70540	622.4	5.2	6.21	0.500	17.36	1, 2, 3
70543	626.2	5.1	6.23	0.498	17.56	1, 2, 3
70545	623.4	5.2	5.75	0.532	17.68	1, 2, 3
70547	627.2	5.1	6.20	1	17.46	1, 2, 3
70549	624.2	5.1	6.18	1	17.63	1, 2, 3
70551	626.2	5.1	6.18	1	17.64	1, 2, 3
average	624.9±1.9	5.13±0.05	6.12±0.19	0.51±0.02[‡]	17.55±0.12	

[†] High-density implosions only
[‡] f_D = 50% shots only

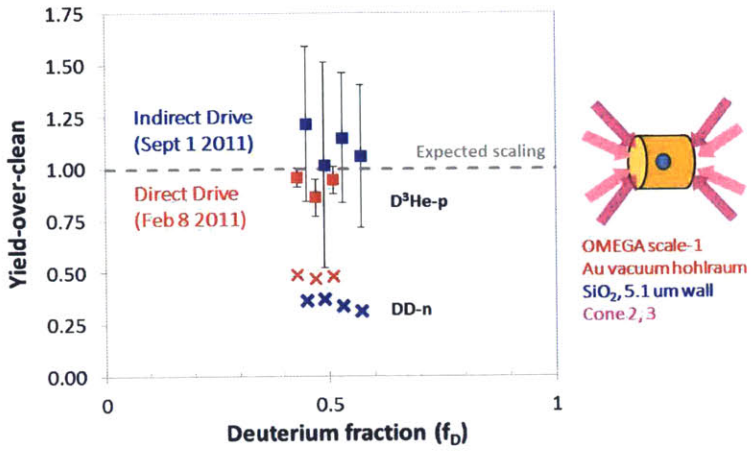

Figure E.1. Comparison of yield-over-clean (LASNEX) for indirect-drive shock-driven implosions on OMEGA performed on Sept 1st, 2011 (blue) and direct-drive implosions performed on Feb 8th, 2011 (red). The D^3He-proton yields (squares) were in reasonable agreement with the simulations (grey dashed line), while the DD-neutron-yields underperform by a factor of 2–3. Direct-drive LASNEX simulations were performed by Aaron Miles; indirect-drive simulations were performed by Peter Amendt. Points spread out for legibility.

selected due to predictions of the LASNEX code, which indicated that the M–band radiation of the gold hohlraum was very strongly absorbed by the glass. The capsules were filled with combinations of D_2 and ^3He gas with an initial mass density of $\rho_0 = 4.6$ mg/cc and deuterium fraction ranging from $f_D = 0.2$ to 1, to examine the scaling of the nuclear yield with deuterium fraction. Three shots were also performed with 50:50 D^3He and reduced ρ_0, to examine the scaling of yield with initial mass density. A 1 ns square impulse was again used, but this time the 'Cone 1' beams were added, for a total of 40 OMEGA beams containing $\sim$ 16.6 kJ. The Cone 1 beams enter the hohlraum at a very shallow angle (21.4° relative to the axis) and pass very close to the target. To avoid accidental direct illumination the spherical target with the Cone 1 beams, these beams were pointed and focused at 1.5 mm from TCC, or 0.5 mm outside the LEH. Elliptical phase plates (E-IDI-300) were used to maximize the laser energy entering the hohlraum and produce more uniform drive of the hohlraum wall.

The third experimental series was performed on the OMEGA-only shots of a joint OMEGA/OMEGA–EP shot day on August 1st, 2013, and revisited the thin-walled glass capsules used in the initial series. However the laser setup was identical to that used in the May 7th experiments, including all three laser cones (40 beams). These experiments compared three shots of 50:50 D^3He-gas fill with three shots of pure D_2 with an equal initial gas density of $\rho_0 = 6.1$ mg/cc. Shot information for all indirect-drive shock-driven implosions in this study is provided in Table E.1.

E.2 Experimental Results

The primary diagnostics on these implosions were those that recorded the nuclear yields. DD-neutron yields and burn-averaged temperatures were recorded with the neutron time-of-flight diagnostic suite. D^3He-proton yields and spectra were recorded using the Wedge-Range-Filter (WRF) compact proton spectrometers only. The charged particle spectrometers (CPS) were not sensitive enough to record the observed yields below 10^7. Neutron yields were below 10^9, such that the neutron temporal diagnostic (NTD) could not be used to record the nuclear burn history. However,

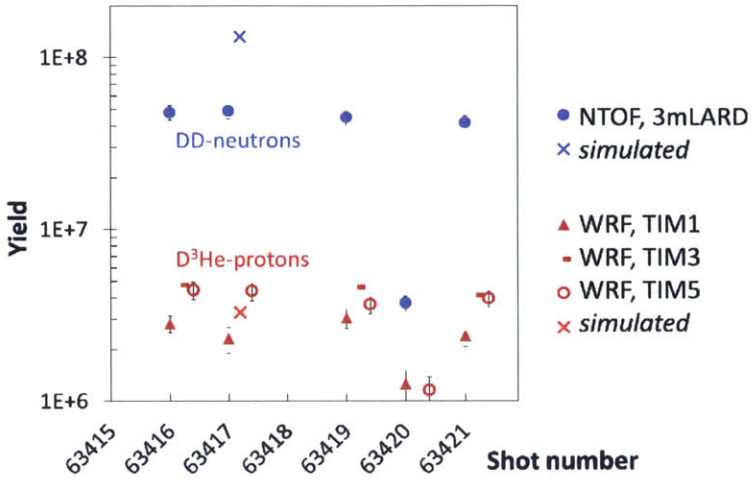

Figure E.2. Yields observed on the thin-glass shell indirect-drive implosions using Cones 2 and 3 (30 beams), performed on OMEGA on Sept. 1st, 2011. Expected yields from LASNEX simulations by Peter Amendt are also shown (x). All experiments contained 50:50 D^3He-gas fill with $\rho_0 = 6.23 \pm 0.01$ mg/cc. Several D^3He-proton diagnostics were fielded along different lines-of-sight (red triangle, bar, and open circle), and reported systematically different results. Shot 63420 significantly underperformed relative to the other shots for an unknown reason.

the PTOF diagnostic described in Chapter 2 was successfully used to measure the D^3He-proton bang-time on several of the implosions. X-ray framing cameras were fielded on the second and third campaigns; however a design flaw on the May 7th experiments interferes with the interpretation of the x-ray framing camera data on that shot day.

The DANTE diagnostic[1,2] was used to measure the peak radiation temperature of the hohlraums. In the initial, 12.8 kJ experiments, DANTE recorded a peak radiation temperature of 225.5 ± 0.7 eV, with a peak radiation flux of 337 ± 4 GW/sr. By adding the additional ten Cone 1 beams and increasing the laser energy, the peak radiation temperature increased only marginally to 232.7 ± 2.5 eV, but the peak radiation flux increased by $\sim 12\%$ to 378 ± 16 GW/sr.[a]

Because of the different nature of the implosions, this section will first introduce the experimental results of the thin-glass shell implosions performed on September 1st, 2011 and August 1st, 2013; this will be followed by a discussion of the results from the thick-glass shell implosions performed on May 7th, 2013.

E.2.1 Thin-glass shell experiments

The nuclear yields observed on the thin-shell implosions with 30 laser beams (2 cones) are shown in Figure E.2, and yields observed on the thin-shell implosions with 40 beams (3 cones) are shown in Figure E.3. Simulated values using the LASNEX code are shown in both figures for comparison to the data; these simulations were performed by Peter Amendt. In the 2-cone implosions, the DD-neutron yields were approximately 1/3 the simulated value, while the D^3He-proton yields were roughly consistent with the simulated value. In contrast, the 3-cone implosions with equimolar gas-fill produced D^3He-proton and DD-neutron yields that were both approximately 60% of the simulated values. Additionally, the 3-cone implosions with pure D_2-gas fill produced DD-neutron yields that were only $\sim 30\%$ of the simulated values. This anomalous trend with deuterium fraction is the opposite of that observed for direct-drive implosions in Chapter 4.

In the 2-cone implosions, several WRFs were fielded along various lines-of-sight, and produced systematically different results: the WRF in TIM1 systematically reported lower yields, while the WRFs in TIM3 and TIM5 systematically reported higher yields. This difference is likely due to different magnetic field structures created by laser irradiation of the hohlraum wall. Figure E.4

[a] These values were measured on the May 7th, 2013 shot day. The hohlraum and drive are nominally identical to the subsequent thin-shell shots on Aug 1st, 2013.

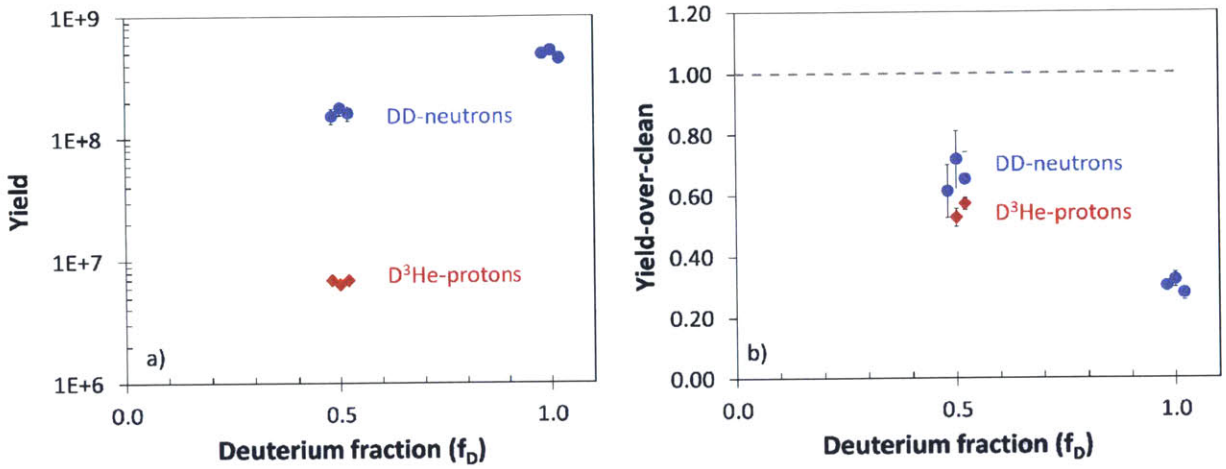

Figure E.3. Yields observed on the thin-glass shell indirect-drive implosions using Cones 1, 2 and 3 (40 beams), performed on OMEGA on Aug. 1st, 2013. Experiments contained either 50:50 D^3He-gas fill or pure D_2-gas fill with $\rho_0 = 6.12 \pm 0.19$ mg/cc. a) Absolute DD-neutron yields (blue) and D^3He-proton yields (red) were increased relative to the 2-cone implosions shown in Figure E.2 by a factor of 2–3×. b) Yields divided by the expected yields from LASNEX simulations performed by Peter Amendt ("Yield-over-clean"). Unlike the 2-cone implosions, both the D^3He-proton and DD-neutron yields are $\sim 60\%$ of the expected values. The DD-neutron yields from the pure D_2-filled targets are anomalously low, compared to the 50:50 implosions. This trend with deuterium fraction is the opposite of that observed previously in Chapter 4.

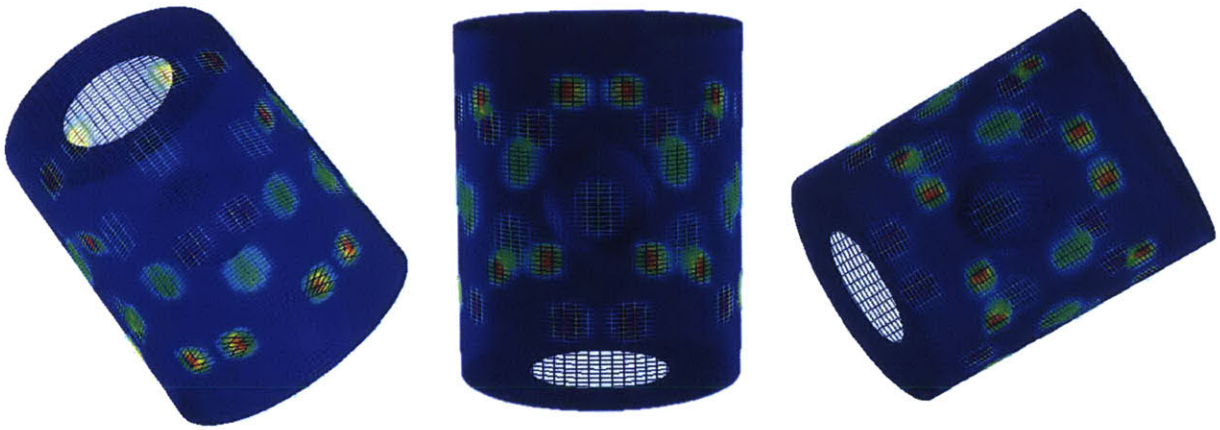

Figure E.4. WRF views of the hohlraum and implosion from a) TIM1, b) TIM3, and c) TIM5, for the 2-cone implosions performed on Sept. 1st 2011. Color indicates the total energy deposition on the inside of the hohlraum wall by the lasers. The protons observed from the TIM1 line-of-sight pass between two laser spots, and may experience scattering in the buildup of gold plasma from the colliding plasma bubbles. The protons observed from TIM3 and TIM5 pass directly through the center of a laser spot, and will tend to be concentrated by the magnetic field structure of the plasma bubble.

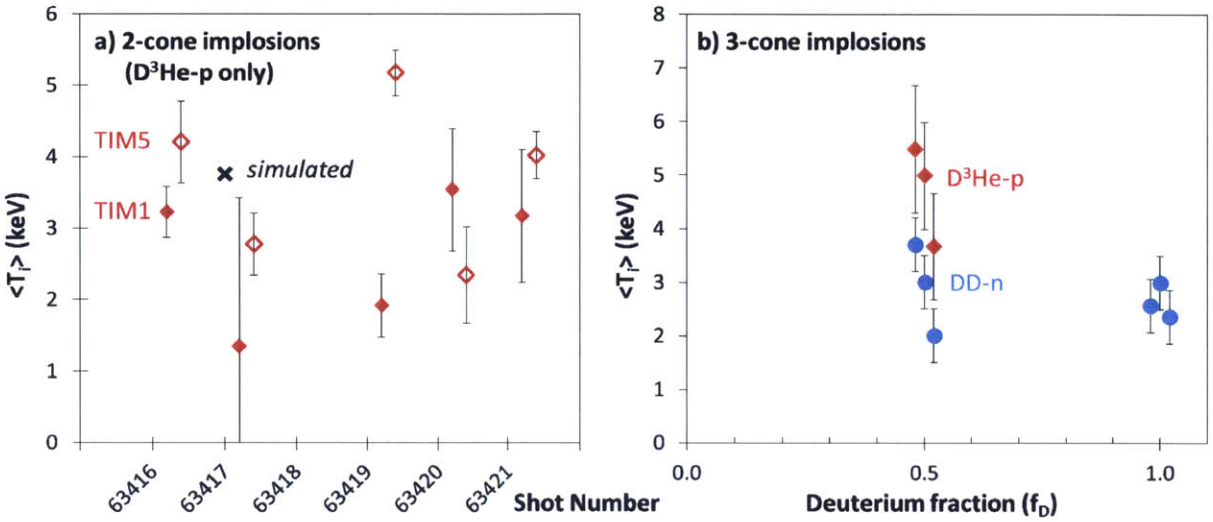

Figure E.5. Burn-averaged ion temperatures for the indirect-drive, thin-glass shell implosions. a) D^3He-proton burn-averaged ion temperatures for the 2-cone implosions on Sept. 1st, 2011, as measured by the WRFs in TIM1 (red solid) and TIM5 (red hollow). The LASNEX-simulated value of 3.7 keV is shown (black x). b) Measured D^3He-proton (red) and DD-neutron (blue) burn-averaged ion temperatures for the 3-cone implosions on Aug. 1st, 2013, plotted relative to the deuterium fraction of the fuel. WRF-measured temperatures were in much better agreement with each other, compared to the 2-cone implosions; the average value of WRFs in TIM1, TIM5, and the P2-NDI is shown. LASNEX simulated $\langle T_i \rangle_{DD} \approx 8$ keV for the $f_D = 0.5$ implosions and ≈ 7.5 keV for $f_D = 1$.

shows the view of the hohlraum for each of the three lines-of-sight. The WRF in TIM1 views the target in between two laser spots on the hohlraum wall; in contrast, TIM3 and TIM5 view the implosion directly through the center of a laser spot. Based on the magnetic field structures observed in laser-target interactions, viewing the target through a laser-plasma bubble would be expected to concentrate protons on the detector.[3] In contrast, the reconnecting field structure produced near the two colliding bubbles on the TIM1 line-of-sight would not concentrate protons, and the buildup of gold plasma at that sight might preferentially scatter protons out of the line of sight.

The burn-averaged ion temperature was measured using the D^3He-proton and DD-neutron spectral line-widths, and are plotted in Figure E.5. On the 2-cone implosions, a DD-neutron burn-averaged ion temperature of $\langle T_i \rangle_{DD} = 6 \pm 3$ keV was inferred. The DD-neutrons were measured only be the detector NTOF_3mLARD due to the low neutron yields: this detector has an intrinsically slow response time, which generates the large uncertainty in the ion temperature measurement. The D^3He-proton-measured $\langle T_i \rangle$ are roughly in agreement with the simulated value of 3.7 keV on this shot day, however there is substantial scatter across the different lines of sight. For the 3-cone implosions, the 3mNTOF detector was used, which provides improved precision for the DD-neutron measurement. The D^3He-proton $\langle T_i \rangle$ agreed with each other across three lines-of-sight to within uncertainties. In these experiments, the measured burn-averaged temperature was substantially lower than the LASNEX-simulated values of $\langle T_i \rangle_{DD} \approx 8$ and 7.5 keV for $f_D = 0.5$ and 1.0, respectively.

The PTOF detector was fielded in TIM2 at 20 cm from the target to record the D^3He-proton bang-time on the 2-cone series. An accurate cross-timing to the NTD was obtained using seven backlighter implosions on the remainder of the shot-day. Including the absolute timing uncertainty

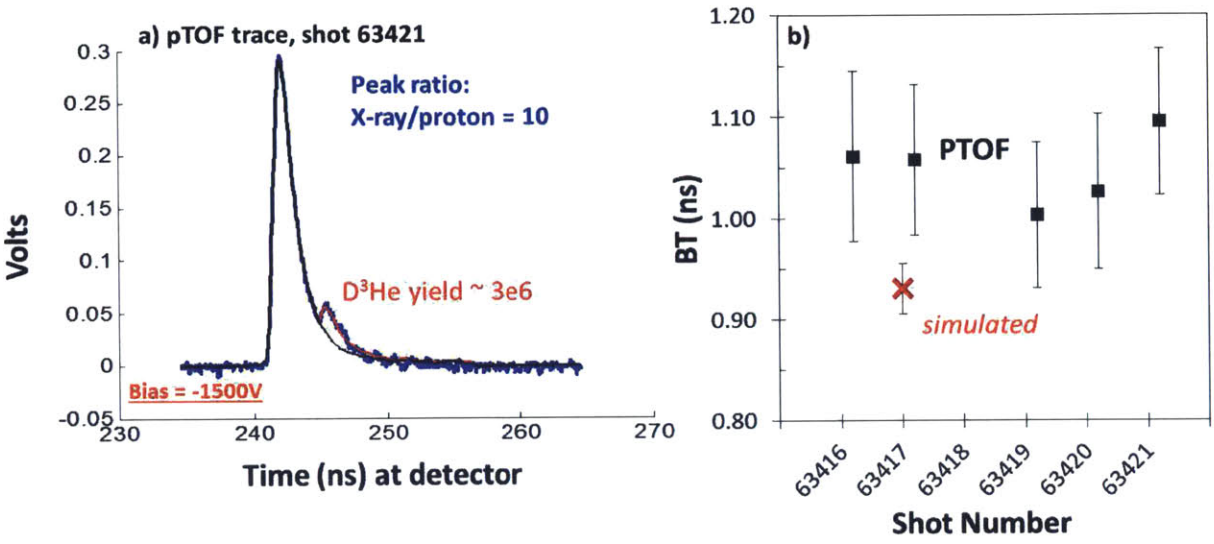

Figure E.6. PTOF data from the indirect-drive 2-cone implosions performed on Sept. 1st, 2011. a) An example PTOF trace recorded on shot 63421. Although the x-ray peak is approximately 10× larger than the D^3He-proton peak, an accurate bang-time was measured: filtering of [50 μm Ta + 100 μm Au] was sufficient to protect the detector from the hohlraum x-rays. b) Measured D^3He-proton bang-times from the PTOF diagnostic.

of ±50 ps quoted for the NTD, the total uncertainty in the PTOF bang-times was approximately ±70 ps. An example PTOF trace and the measured bang-times for the indirect-drive thin-glass shell implosions is shown in Figure E.6. PTOF measures the bang-time on all five shots to be 1.048 ± 0.035 ns, which is somewhat later than the simulated value of 0.93 ± 0.05 ns. This difference suggests that LASNEX may be coupling more energy to the fuel than in the experiment. PTOF was fielded on the 3-cone implosions of Aug. 1st, 2013, however the increased x-ray signal overwhelmed the proton signal on most implosions.

On the 3-cone shot day, self-emission x-ray framing camera images were obtained with a view through the LEH; an example of this data is shown in Figure E.7. The laser entrance hole is clearly seen in the images; the capsule appears near peak compression, and appears to be highly circular, as expected. Analysis of the images suggests a convergence ratio of $CR \sim 2.7$ at bang-time. After bang-time, dark radial 'fingers' can be seen in the images. These features are probably produced by radial jets of gold blowing off the hohlraum wall, as has been observed in related work.[4]

E.2.2 Thick-glass shell experiments

The experiments performed on May 7th, 2013 imploded glass shells with 24 μm wall using the 3-cone laser design. The yields and yields-over-clean from this shot day are presented in Figure E.8. The highest density implosions ($\rho_0 = 4.6$ mg/cc) demonstrate a clear anomalous reduction in both the DD-neutron and D^3He-proton yield as the deuterium fraction was reduced from $f_D = 1.0$ to 0.2. Additionally, the yield is observed to reduce anomalously as the initial gas pressure was reduced to $\rho_0 = 3.0$ and 1.5 mg/cc. The yield reduction with deuterium fraction shows a similar trend to that observed in Chapter 4, and is somewhat larger in magnitude: the pure deuterium implosions perform approximately 2× better than the equimolar D^3He-filled implosions.

Despite the design prediction that the shell would burn through, the data indicate that these implosions produced primarily compression yield. Several WRF-measured proton spectra are shown

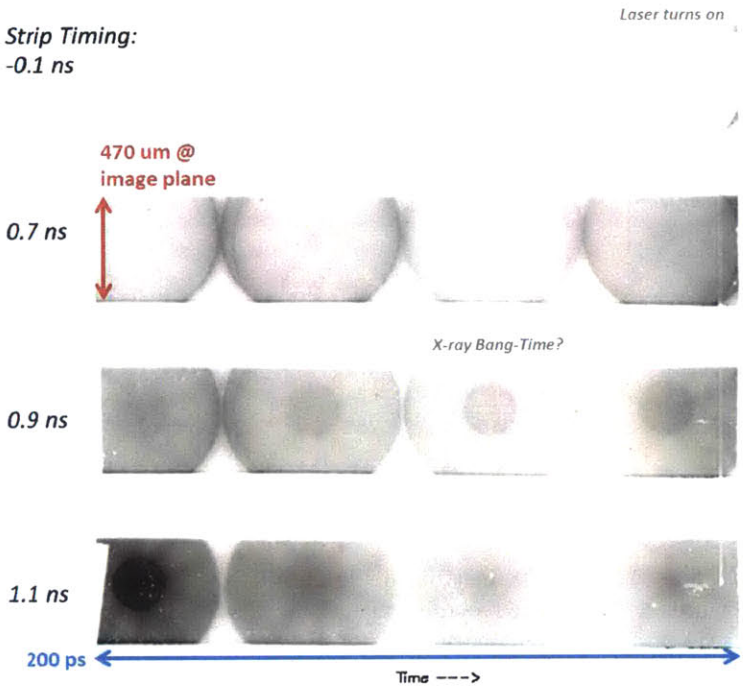

Figure E.7. Time-resolved self-emission x-ray images recorded through the laser entrance hole on the indirect-drive, 3-cone, thin-shell implosion 70547. The laser turns on at the end of the first strip. The laser entrance hole is clearly visible in each image; the imploded capsule becomes visible near bang-time, which occurs at around 1.0 ns. At bang-time, the imploded capsule has an outer diameter of $\sim$ 230 μm, implying a convergence ratio of $\sim$ 2.7. At the end of the implosion, the radial 'jets' produced by the laser ablation of the hohlraum wall are clearly seen.

in Figure E.9. The spectra are substantially non-Gaussian, which indicates substantial ρR evolution during the burn, and measure the D^3He-proton energy to be downshifted from the birth energy by $\sim$ 1 MeV.[b] Both of these features suggest that the yield is primarily produced during the compression phase. The width and shape of the peak is dominated by ρR evolution in the implosion, and the burn-averaged ion temperature cannot be inferred from this data.

Secondary D^3He-proton yields were measured on the pure deuterium implosions, as shown by the open blue diamonds in Figure E.8b). Secondary DT-neutron yields were also measured on these experiments, as shown in Figure E.10a) and b). As discussed in Appendix D, the secondary nuclear yields can be used to infer the fuel ρR during nuclear burn; the inferred values are shown in Figure E.10c). Averaging all the DT-neutron-inferred fuel areal densities, $\rho R_{\text{fuel}} = 8.44 \pm 0.28$ mg/cm^2 during burn in the experiments.

The burn-averaged ion temperature was inferred from the DD-neutron spectral width on several implosions with sufficiently high yield, as shown in Figure E.11. With the exception of one outlier implosion with $f_D = 0.5$, the data are consistent with a slight increasing trend as the deuterium fraction is reduced. This trend was predicted in the case of thermally equilibrated ions but thermally decoupled electrons, as discussed in Section 4.2 and observed in the high-density experiments presented in Chapter 4. In absolute terms, the temperatures are comparable to those observed in the thin-shell implosions, but are much lower than those observed in the direct-drive implosions of Chapters 3 and 4.

The DD-neutron yield was sufficiently high to measure the nuclear bang-time on several of the implosions, in particular those with high initial mass density ($\rho_0 = 4.6$ or 3.0 mg/cc) and $f_D \geq 0.5$. The measured nuclear bang-times are shown in Figure E.12. All the bang-times in this data set are consistent with a measured value of 1770 ± 50 ps, which is slightly later than the simulated value of

[b]The hohlraum wall downshifts the protons by $\sim$ 0.8 MeV in all experiments, which has not been corrected for in the displayed spectra.

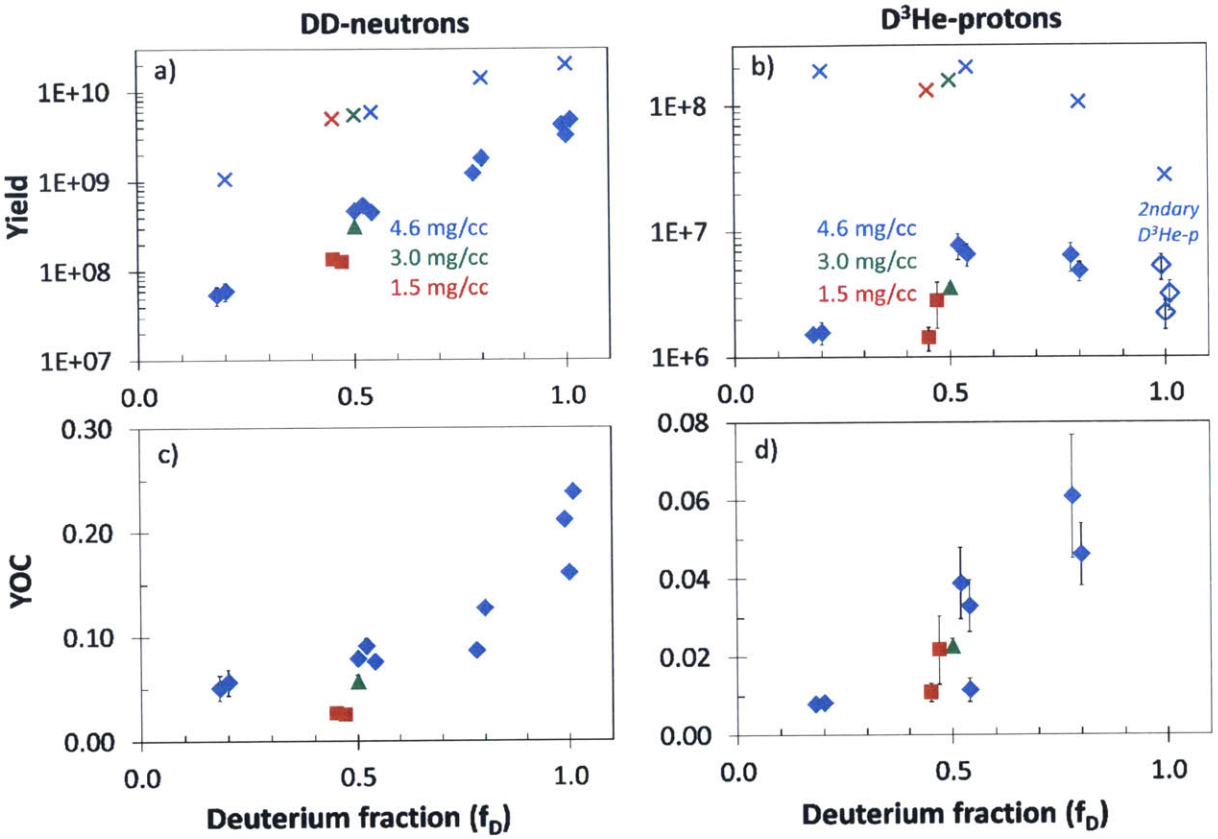

Figure E.8. Yields of a) DD-neutrons and b) D^3He-protons observed on the thick glass shell indirect-drive 3-cone (40-beam) implosions, performed on OMEGA on May 7th, 2013. Experiments contained combinations of D_2 and ^3He gas with initial gas density $\rho_0 = 4.6$ mg/cc (blue diamonds), or 50:50 D^3He-gas fill with $\rho_0 = 3.0$ (green triangles) or 1.5 mg/cc (red squares). D^3He-proton yields observed for $f_D = 1$ (open diamonds) were produced by secondary fusion processes. The expected yields from LASNEX simulations performed by Peter Amendt are shown for comparison (x). Yields divided by the expected yields ("Yield-over-clean") for c) DD-neutrons and d) D^3He-protons both demonstrate a clear anomalous yield trend with deuterium fraction, similar to that described in Chapter 4. Error bars are comparable to the data point sizes where not shown.

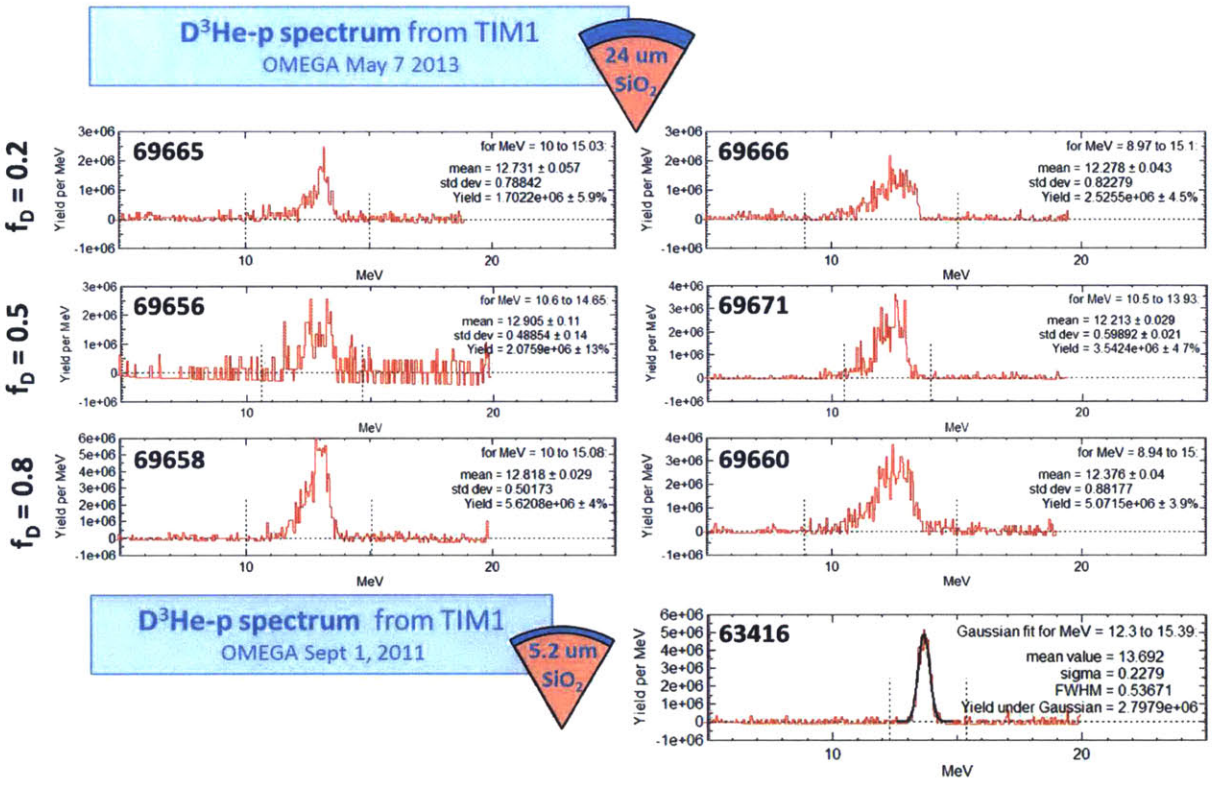

Figure E.9. D^3He-proton spectra recorded from thick-glass shell indirect-drive implosions on OMEGA, as measured by WRF compact proton spectrometers fielded in TIM1. Representative spectra are shown for $f_D = 0.2$ (top row), 0.5 (second row), and 0.8 (third row). The measured spectra are significantly non-Gaussian in shape. After accounting for 0.8 MeV energy loss in the hohlraum wall, the spectra indicate approximately 1 MeV proton energy loss while exiting the implosion. Both of these features indicate that the yield is predominantly produced in the compression phase. In comparison, a spectrum recorded from a TIM1 WRF on a thin-shell implosion (bottom row) is highly Gaussian and shows that < 0.2 MeV energy was lost exiting the implosion, both of which indicate that the yield was predominantly produced in the shock phase.

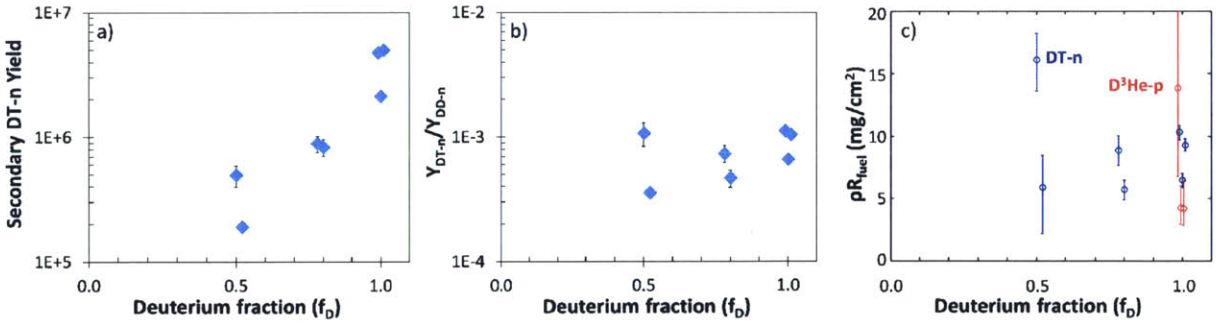

Figure E.10. Secondary DT-neutron yields measured from thick-shell indirect-drive implosions. Both a) absolute yields and b) ratio of secondary to primary neutron yields are shown (blue points). c) The ratio of secondary to primary yields for the DT-neutrons (blue) indicate an average fuel areal density of $\rho R_{\text{fuel}} = 8.7 \pm 2.0$ mg/cm^2 during burn. The D^3He-proton-inferred fuel areal density (red) is roughly consistent with that from the DT-neutrons.

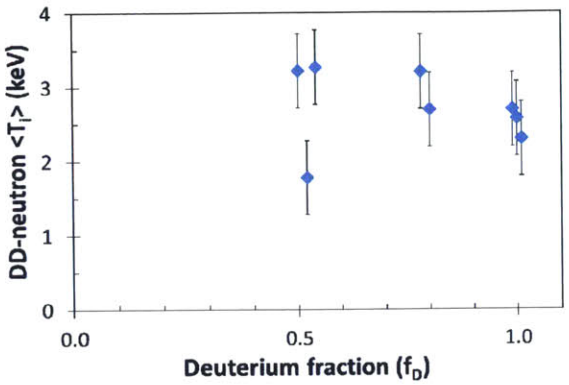

Figure E.11. Burn-averaged ion temperatures inferred from DD-neutron spectral width for thick-glass shell D^3He-gas filled indirect-drive implosions on OMEGA. Data (blue) were only inferred for the $\rho_0 = 4.6$ mg/cc implosions with $f_D \geq 0.5$; other implosions did not produce sufficient nuclear yield for this measurement.

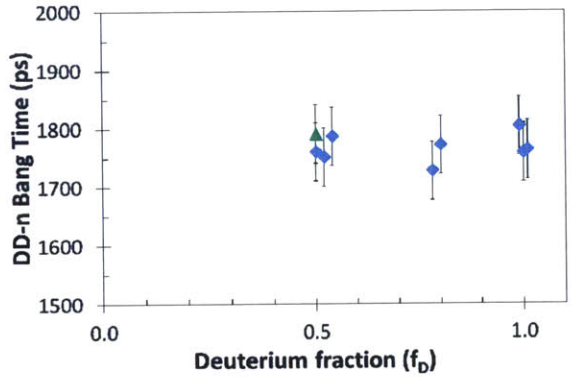

Figure E.12. Nuclear bang-time measured using DD-neutrons from thick-shell indirect-drive implosions on OMEGA. Data were only inferred for the $\rho_0 = 4.6$ (blue) and 3.0 mg/cc (green) implosions with $f_D \geq 0.5$; other implosions did not produce sufficient nuclear yield for this measurement. The bang-time was consistently 1770 ± 50 ps for all implosions.

~ 1640 ps. This result suggests that the experiment does not couple the laser energy to the target as efficiently as the simulation predicts.

E.3 Discussion

The thin-glass shell implosions were expected to produce a similar anomalous yield trend to that observed in the thin-shell direct-drive implosions discussed in Chapter 4. Instead, the opposite trend was observed: the pure deuterium implosions underperformed compared to the 50:50 D^3He-filled implosions, in both the DD-neutron and D^3He-proton yields. Similar behavior is observed in the DD-neutron yield from thin-CD direct-drive implosions discussed in Chapter 3. In that context, ion diffusion was found to explain the observed yield behavior. Deuterium was able to 'escape' from the core by diffusion, and because the mean free path increases with deuterium fraction in equal-mass-density mixtures of D^3He ($\lambda_D(f_D = 1) \approx 1.38 \times \lambda_D(f_D = 0.5)$: see Equation 4.5) the deuterium diffused out of the core more efficiently in the pure deuterium case. This is one possible explanation of the yield result.

A second possible explanation involves the loss of tail ions, which reduces the effective fusion reactivity and is expected to increase with the deuterium fraction as discussed in Section 4.3.1. Because of the high initial mass density, these experiments are most directly comparable to the high-density direct-drive implosions. The Knudsen number, which describes how kinetic the ion behavior should be, scales as $N_K \propto T_i^2 C R^{-2} \rho R_0^{-1}$. The initial fuel ρR was similar in the direct-drive high-density experiments and the thick-shell indirect-drive experiments ($\rho R_0 = 0.146$ and 0.139 mg/cm^2, respectively), and was somewhat higher in the thin-shell indirect-drive experiments (0.191 mg/cm^2).

The thin-shell indirect-drive implosions were less compressed by $\sim$ 10% compared to the direct-drive implosions, but also were colder by $\sim 4\times$, which would cause us to infer a Knudsen number that was about an order of magnitude lower compared to the direct-drive experiments. In absolute terms, the mean-free-path for the pure deuterium plasma at burn is estimated to be approximately 6 μm, such that the Knudsen number is $\sim$ 0.05. The radial convergence was not measured on the thick-shell implosions, but the fuel areal density at burn was inferred from the secondary yields. Comparing this value to the initial fuel areal density, a $CR \approx 7.9 \pm 1.0$ is inferred, from which the Knudsen number at burn is estimated to be $\sim$ 0.01. These values are small enough that hydrodynamic behavior dominates and ion thermal decoupling will not occur, but diffusive effects are probable and tail-ion loss will occur.

Although the thin-shell implosions appear to be dominated by shock yield, the burn-averaged ion temperatures in the range 2–4 keV are substantially lower than those observed in the direct-drive implosions (> 10 keV). The burn-averaged ion temperature is directly related to the shock strength in shock-driven implosions, so these results suggest that the shock was significantly weaker in the indirect-drive experiments. This is not surprising: although a similar total laser energy was used in both scenarios, the drive efficiency of the hohlraum is not as high as that of direct laser drive, and less energy is coupled into the shock. Ion kinetic effects are predicted to alter the shape of the shock front, producing for example a separate deuterium and ^{3}He shock.[5]. Such effects would depend on the strength of the shock front, which might explain the qualitative difference between the thin-shell implosions discussed here and the results from direct-driven implosions.

For the thick-shell implosions, the secondary data shown in Figure E.10 is suggestive of undercompression as a partial cause of the yield anomaly. With the exception of one outlier, there may be a slight trend in the fuel ρR that decreases as the fuel deuterium fraction is reduced. If true, that finding would suggest undercompression as ^{3}He is added to the fuel, consistent with the hypothesis of resistive heating. However given the uncertainties in the measurement, this claim is premature. The D^{3}He-proton-inferred fuel areal densities are only inferred for the pure deuterium case, and are roughly consistent with the DT-neutron-inferred values, although they are systematically lower on one experiment. This discrepancy is resolved by positing an electron temperature that is lower than the ion temperature by 10–20%.

That being said, as the yield is evidently produced due to compression of the fuel by the shell, it may be more natural to compare the thick-shell results to the directly-driven compressive experiments presented in Reference[6]. As has been discussed, the yield anomaly in compressive experiments was found to be maximal for a deuterium fraction of $f_D = 0.5$, and implosion performance recovered both in the limits of pure deuterium and pure ^{3}He. The behavior observed here — monotonically decreasing performance as f_D is reduced — is qualitatively different. A more concrete understanding of the compression yield anomaly must be developed to address this qualitative difference. Further experiments could reproduce the previous compressively-driven direct-drive implosions, while making use of comprehensive nuclear diagnostics including imaging to evaluate the burn-averaged deuterium fraction. This would help determine the mechanism underlying the compressive yield anomaly, and whether species separation or resistive heating is the primary cause.

E.4 Summary

Several experiments were performed on the OMEGA laser to determine whether anomalously low yields are produced in indirectly driven thin- and thick-glass shell implosions filled with D^{3}He. Initial implosions of thin-glass shells filled with 50:50 D^{3}He using 30 beams demonstrated underperformance of DD-neutron production compared to D^{3}He-proton production. In subsequent

implosions of thin-glass shells with 40 beams, this was not observed. Furthermore, implosions with pure deuterium fuel produced lower yields-over-clean than those filled with 50:50 D^3He fuel, in contradiction to observations in directly driven implosions. These results may be caused by the diffusive loss of deuterium to the shell plasma, or by "Knudsen-layer" tail-ion loss. In the thick-shelled indirect-drive implosions, D^3He-proton spectra indicate that the yield is produced during the compression phase. Anomalously reduced yields were observed as the deuterium fraction was reduced from $f_D = 1$ to 0.2. The observed trend appears qualitatively similar to that observed in thin-shell (shock-driven) direct-drive implosions, and differs from that observed in thick-shell (compressive) direct-drive implosions, for which a yield recovery was observed for $f_D < 0.5$. Further experiments are required to differentiate between the mechanisms present in these two classes of compressive experiments.

E.5 References

1. H. N. Kornblum, R. L. Kauffman and J. A. Smith, "Measurement of 0.1–3 keV x rays from laser plasmas," Review of Scientific Instruments, **57**(8), 2179 (1986).
2. M. J. May, K. Widmann, C. Sorce *et al.*, "Uncertainty analysis technique for OMEGA Dante measurements," Review of Scientific Instruments, **81**(10), 10E505 (2010).
3. R. D. Petrasso, C. K. Li, F. H. Séguin *et al.*, "Lorentz Mapping of Magnetic Fields in Hot Dense Plasmas," Physical Review Letters, **103**(8), 085001 (2009).
4. C. Li, F. Séguin, J. Frenje *et al.*, "Impeding Hohlraum Plasma Stagnation in Inertial-Confinement Fusion," Physical Review Letters, **108**, 025001 (2012).
5. C. Bellei, H. Rinderknecht, A. Zylstra *et al.*, "Species separation and kinetic effects in collisional plasma shocks," Physics of Plasmas, **21**(5), 056310 (2014).
6. J. R. Rygg, J. A. Frenje, C. K. Li *et al.*, "Tests of the hydrodynamic equivalence of direct-drive implosions with different D_2 and ^3He mixtures," Physics of Plasmas, **13**(5), 052702 (2006).

Appendix F

Analytical Model of Shock Speed versus Initial Gas-Fill Pressure

The shock-driven experiments described in Chapters 3 and 4 vary the initial gas-fill of the capsules while keeping the pressure drive from the laser and shell the same. The strength of the shock affects both the shock-generated nuclear yield and the time of peak nuclear production. For these experiments, the primary comparison was between fuels with equal mass density but differing ion species fractions. That being said, understanding how the shock coupling into the gas varies with initial gas pressure is useful for related experiments and physical understanding of the systems.

To evaluate how the strength of the shock launched into the gas depends on the gas pressure, an analytical model relating the shocked shell pressure to the shocked gas pressure across a fuel-shell interface was developed. This model follows P. Drake, who derived a model for the unloading of shocked solid material into a gas (see Sec. 4.4.1).[1] As such, the model assumes a constant pressure source on the outside of the shell, and is in a planar geometry. Although the implosions are spherical, the spherical correction is small at shock breakout because the aspect ratio of the shells is very large: the radius is typically 100× the wall thickness.

As the shock reaches the fuel-shell interface, the shocked pressure in the shell and the unshocked pressure in the gas are each approximately uniform. Thereafter, five regions are produced, as depicted in Figure F.1: 1. the shocked shell; 2. the shell rarefaction into the underdense gas; 3. the shell plateau at the pressure of the shocked gas; 4. the shocked gas; and 5. the unshocked gas. The fuel-shell interface is between regions 3 and 4. Throughout this derivation, P_j are pressures, u_j are

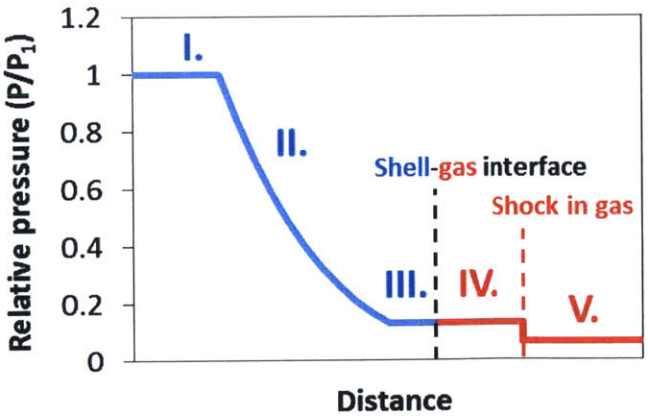

Figure F.1. Regions produced in the analytical model of shock breakout at the interface between a shocked shell (blue) and a fill gas (red): I. the shocked shell; II. the shell rarefaction into the gas; III. the shell plateau at equal pressure to the shocked gas; IV. the shocked gas; and V. the unshocked gas.

fluid velocities, and c_j are sound-speeds in the five regions designated by subscript j; $\gamma_{g,s}$ are the ratio of specific heats and $M_{g,s}$ are the Mach numbers of the shock, in the gas or shell as designated by subscript g or s, respectively. The pressure balance across the rarefaction wave (regions 1 to 3) is taken from Drake, Eqn. 4.114:

$$\frac{P_3}{P_1} = \left(1 - \frac{(\gamma_s - 1)\,U}{2c_1}\right)^{\frac{2\gamma_s}{\gamma_s - 1}}, \tag{F.1}$$

where $U = u_3 - u_1$ is the flow velocity difference between the plasma in region 1 and 3. The pressure and the flow velocity are expected to be equal across the fuel-shell interface: $P_3 = P_4$, $u_3 = u_4$. Finally, the pressure differential at the shock front can be written in terms of M_g following Equation 1.25. The flow velocities in each region are not known a priori; however assuming that the shell and the gas are initially stationary prior to being shocked, the resulting flow velocity in regions 1 and 4 can be written in terms of the Mach number and the sound speed:

$$u_1 = \frac{2M_s c_0}{\gamma_s + 1}, \qquad u_4 = \frac{2M_g c_5}{\gamma_g + 1}. \tag{F.2}$$

Here, c_0 refers to the sound-speed in the unshocked shell. This quantity is somewhat difficult to define, as it will vary dramatically due to preheat; however it should be constant for a given shell and laser irradiation. Since $c = \sqrt{\gamma P/\rho}$, Equations 1.24 and 1.25 can be used to rewrite c_0 in terms of c_1, M_s, and γ_s, specifically:

$$\frac{c_0}{c_1} = \frac{M_s\,(\gamma_s + 1)}{\sqrt{(2\gamma_s M_s^2 - (\gamma_s - 1))\,(M_s^2\,(\gamma_s - 1) + 2)}}. \tag{F.3}$$

Putting together these pressure balance equations, the pressure ratio between region 1 and 5 can be written as:

$$\frac{P_5}{P_1} = \frac{\left(1 + \left(M_s \frac{\gamma_s - 1}{\gamma_s + 1} - M_g \frac{(\gamma_s - 1)}{\gamma_g + 1} \frac{c_5}{c_0}\right) \frac{c_0}{c_1}\right)^{\frac{2\gamma_s}{\gamma_s - 1}}}{\frac{2\gamma_g M_g^2 - (\gamma_g - 1)}{\gamma_g + 1}}. \tag{F.4}$$

The fraction c_0/c_1 is just a function of M_s and γ_s (see Eqn F.3). Therefore, the formulation in Equation F.4 describes the pressure ratio P_5/P_1 as a function of four constants (c_5, c_0, γ_g, and γ_s) and two variables (M_g, M_s). It is worth noting that this formulation includes a limit in which the numerator vanishes: this is the limit of negligible gas-fill pressure, and produces the condition:

$$\frac{M_g}{M_s} = \frac{c_0}{c_5} \frac{(\gamma_g + 1)}{(\gamma_S + 1)} \left[1 + \frac{\sqrt{(2\gamma_s M_s^2 - (\gamma_s - 1))\,(M_s^2\,(\gamma_s - 1) + 2)}}{(\gamma_s - 1)\,M_s^2}\right]. \tag{F.5}$$

This represents the maximum possible shock-speed in the gas, which is a multiple of M_s that varies weakly with M_s. For weak $M_s \approx 1$, this multiple approaches $5c_0/c_5$; for strong $M_s \gg 1$, the multiple is $(1 + \sqrt{5})c_0/c_5 \approx 3.24c_0/c_5$.

In reality, P_1 and P_5 are fixed, and we wish to invert Equation F.4 to solve for M_g. In practice this is analytically difficult; however the function can be plotted and the appropriate value determined numerically. Several cases are shown in Figure F.2. In this figure, $\gamma_g = \gamma_s = 5/3$, and $T_0 \sim 100$ eV was used to calculate c_0. The pressure in region 1 was taken from a LILAC simulation to be ~ 30 Mbar, such that an initial gas pressure of 1 atm implies $P_5/P_1 \sim 3 \times 10^{-8}$. An order-of-magnitude change in the initial gas pressure is found to produce a <10% change in

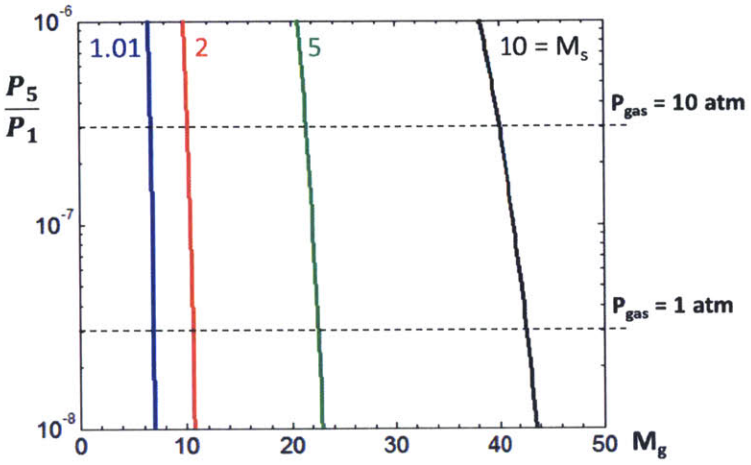

Figure F.2. Plot of the variation of the Mach number of the shock in the gas (M_g) versus the gas-to-shell pressure ratio P_5/P_1, for four initial Mach numbers in the shell: $M_s = 1.01$ (blue), 2 (red), 5 (green), and 10 (black). The ratio of initial gas pressure to shell pressure is approximately 3×10^{-8} for 1 atm of initial gas; both 1 atm and 10 atm are shown (dashed black). The shock Mach number in the gas varies by less than 10% for initial gas pressure changes of an order of magnitude.

the Mach number of the shock in the gas, with slightly stronger shocks predicted in lower-density gas fills. Since the sound speed in the unshocked gas depends primarily on the temperature of the gas, it is expected to be the same regardless of the initial gas pressure. Then, the ~10% higher Mach number in the lower-pressure gas fills will translate into a faster shock velocity, and an earlier bang-time by ~10% of the shock transit time. This effect may contribute to the ~10% difference observed between DD-neutron bang-times in the low- and high-density implosions of the shock anomaly study (see Table 4.2).

In summary, an analytical model was developed to evaluate the shock speed launched into the central plasma of a gas-filled target implosion as a function of the initial gas pressure. For a given drive pressure and shell, the Mach number of the shock launched in the gas was found to vary weakly with gas pressure. This effect does not strongly affect the experiments presented in Chapters 3 and 4, since the primary experimental variable in those studies was the composition of the gas, while the initial mass density was maintained at a constant value. In practice, the dynamics of the shock may behave very differently from this model in shock-driven implosions. HYADES simulations show that the shell plasma accelerates continuously until it burns through, and the shock only escapes from the fuel-shell interface after this period of strong acceleration is complete (see for example Figure 1.8). The acceleration is not considered in the model developed here, and appears to delay shock breakout and shell rarefaction in the simulations. This model will more accurately describe the shock dynamics in implosions with thick ablators, for which the shock breakout is better defined.

F.1 References

1. R. P. Drake, *High-energy-density physics : fundamentals, inertial fusion, and experimental astrophysics*, Shock wave and high pressure phenomena, (Springer, Berlin ; New York, 2006).

Appendix G

Supporting PTOF Research and Development

In the course of developing the PTOF nuclear bang-time diagnostic discussed in Chapter 2, many experiments were performed to test and characterize the PTOF detectors. This appendix describes the procedures and results of several of these experiments, and is organized based on the institution at which the experiments were performed. The results of experiments performed at MIT, including x-ray testing and single-proton counting experiments, are presented in Section G.1. Experiments performed on the OMEGA laser, including detector sensitivity calibration to nuclear products and related studies, are presented in Section G.2. Finally, the tandem accelerator in the State University of New York (SUNY) Geneseo's Department of Nuclear Physics was used to investigate the PTOF detector sensitivity to low-energy protons, which is discussed in Section G.3.

G.1 Detector Testing at MIT

The PTOF detectors were subjected to several tests at MIT, using both an X-ray Machine and the MIT Linear Electrostatic Ion Accelerator (LEIA).[a] These tests were performed to validate that newly constructed detectors were operating correctly, to establish a baseline performance for the PTOF detector design, and to attempt a sensitivity calibration of the detectors using single-proton counting.

G.1.1 X-ray tests

In May, 2011, the PTOF detectors were fielded in a series of calibration tests on a thick-target bremsstrahlung x-ray machine at MIT. This machine uses a water-cooled copper target, which is bombarded by an electron beam. The voltage and current of the beam are controllable, with maximum values of 35 kV and $\sim$ 20 mA, respectively. For these studies, the voltage was set at 35 kV and the current changed to alter the x-ray intensity. The x-ray intensity output at each port oscillates with a frequency of 120 Hz. Additional characteristics of this machine are described in Reference [1].

The experimental layout for these calibrations is shown in Figure G.1. A partially-depleted silicon surface barrier detector (SBD) was positioned at Port 1 for reference; the PTOF detectors being tested were positioned at Port 3. Each port could be configured with a 37 μm Cu filter, to

[a]The MIT IDs are used for individual PTOF detectors throughout this appendix. These IDs have the format "#X" where # indicates the CVD diamond thickness in microns, and X is the sequential letter ID assigned to the CVD diamond in question (e.g. "200B" is the second 200 μm detector constructed). In two cases, the old-style detector IDs are used: "10x1000" was a 10 mm diameter, 1000 μm thick CVD diamond wafer, and "5x250" was a 5 mm diameter, 250 μm thick wafer; both were provided by Vladimir Glebov and are no longer used for PTOF.

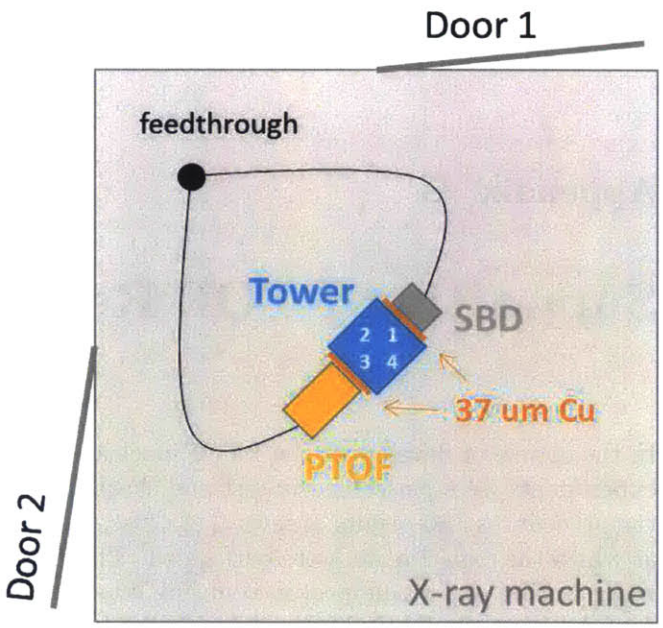

Figure G.1. Cartoon of the experimental design for PTOF detector x-ray testing using the MIT X-ray Machine. The PTOF detector is positioned against Port 3, while the reference SBD is positioned against Port 1. Copper filtering (orange) may be interposed between the source and the detectors to isolate the 8 keV line. The PTOF is connected to a battery box designed to deliver either $\sim$ 500 or $\sim$ 145 V; the SBD is connected to a 45 V battery box. Current through the detector is recorded on an oscilloscope as a voltage spike.

isolate the $\sim$ 8 keV Cu K_α x-ray emission line. Custom battery boxes were used to supply bias to the detectors: the PTOF was biased at either $\pm$502 V or $\pm$144 V, while the SBD was biased at 45 V. When x-rays are incident on the detector, electron-hole pairs are excited in the detector medium and current flows through the circuit. This current is detected using an oscilloscope with a 50 Ω termination and recorded as an oscillating voltage signal. Many oscillation peaks were averaged and the peak-to-peak voltage recorded for both the operating PTOF detector and the SBD reference. These measurements were recorded over the range of available x-ray machine currents.

Figure G.2 shows the measured peak-to-peak voltage for several 200 μm thick PTOF detectors compared to the SBD reference. Signals are approximately three orders of magnitude smaller than the bias voltage, so the observed linear scaling with increased x-ray intensity is expected. Across the set of five detectors tested, the sensitivity to x-rays varies by approximately $\pm$20%. For each detector, the sensitivity increases with bias voltage at a rate that is slower than linear. Assuming a power law for the sensitivity as a function of bias and based on the aggregate data shown here, the sensitivity appears to scale as bias to the power of 0.32 ± 0.06.

Several detectors were tested with both positive and negative biases, by switching the polarity of the battery boxes. These results are shown for detector 200B in Figure G.3 (no Cu-filter only) and for detector 200G in Figure G.4. While detector 200B appears to show 44% greater sensitivity with a positive bias, detector 200G appears to have comparable sensitivity for positive and negative biases. The reasons for the difference in behavior are unclear at this time.

G.1.2 Accelerator tests

A series of experiments was performed using the MIT Linear Electrostatic Ion Accelerator (LEIA) in January 2011 to evaluate whether single-proton signals could be detected using the PTOF detectors, and to use this capability for calibration of the detector sensitivity as a function of proton energy. The experimental layout is shown in Figure G.5. The accelerator's deuteron beam is incident on an erbium deuteride target doped with ^{3}He, which produces both 3.0 MeV DD-protons and 14.7 MeV D^{3}He-protons. These particles are ranged through aluminum filters to obtain the desired incident

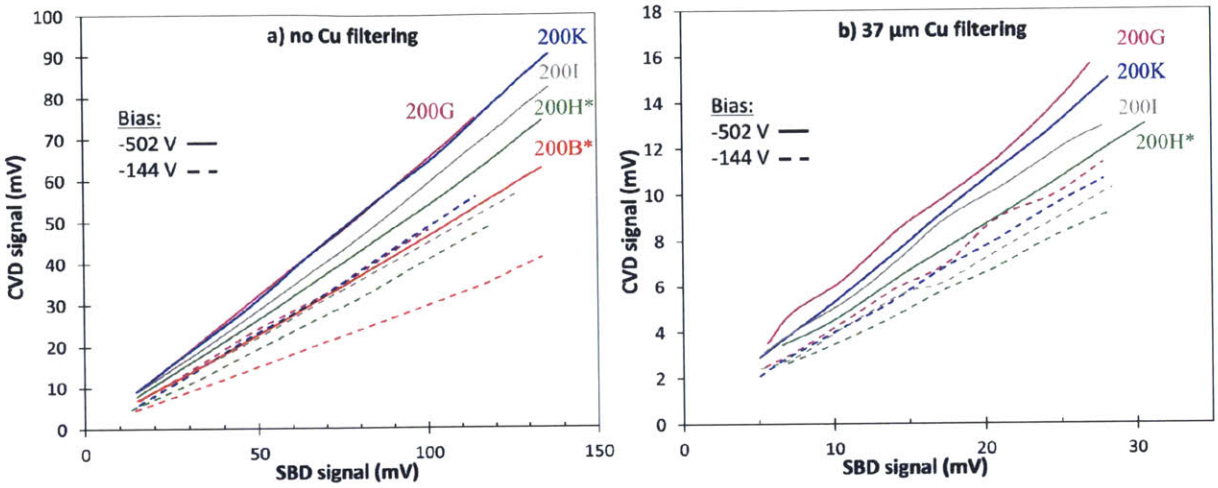

Figure G.2. Measured peak-to-peak voltage signal for five, 200 µm CVD-diamond detectors compared to signal from a partially-depleted SBD when exposed on the MIT X-ray Machine. Asterisks indicate detectors in active use on the NIF. Either a) no filtering or b) 37 µm Cu filtering was interposed between the source and the detectors. The CVD-diamonds were biased with -502 V (solid lines) or -144 V (dashed lines). The x-ray machine voltage was set to 35 kV, and the current was varied to modify the beam intensity.

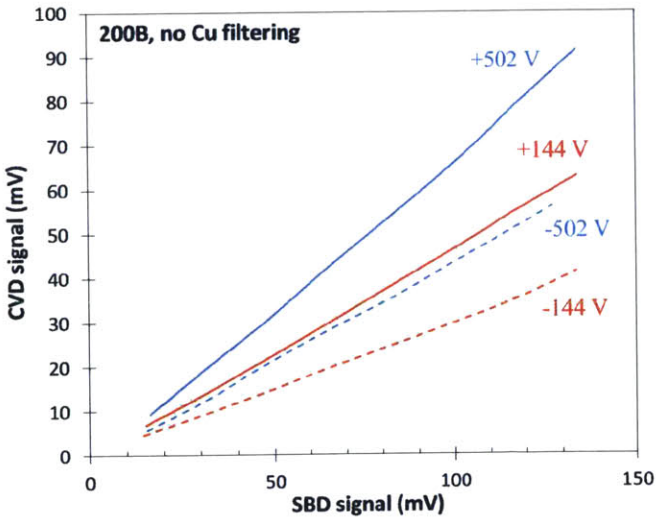

Figure G.3. Measured peak-to-peak voltage signal for PTOF detector 200B compared to a reference signal from an SBD when exposed on the MIT X-ray Machine. No filtering was interposed between the source and the detectors. The detector was biased positively (solid lines) or negatively (dashed lines) at 502 V (blue) or 144 V (red).

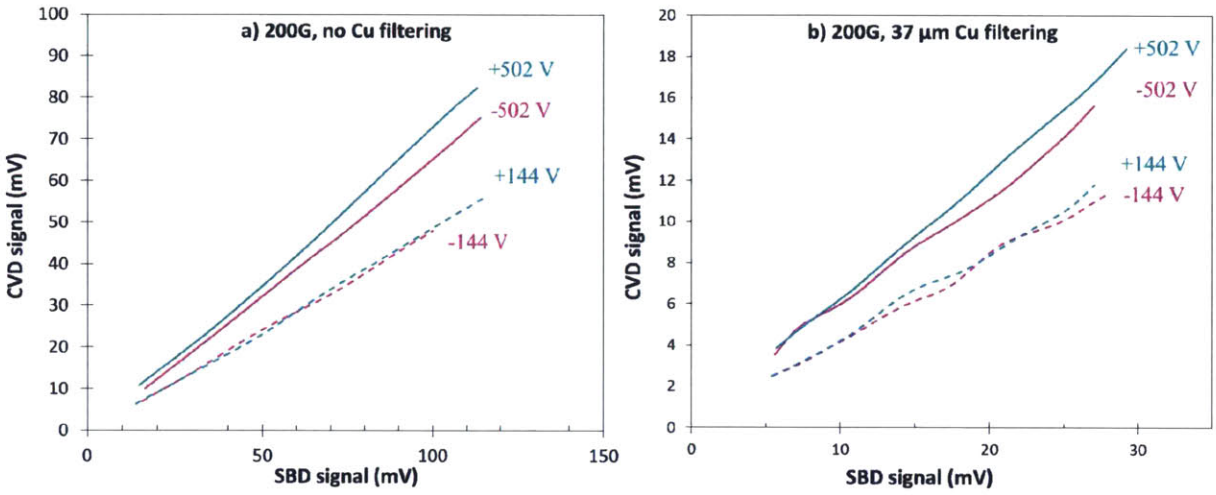

Figure G.4. Measured peak-to-peak voltage signal for PTOF detector 200G compared to a reference signal from an SBD when exposed on the MIT X-ray Machine. Either a) no filtering or b) 37 μm Cu filtering was interposed between the source and the detectors. The detector was biased positively (solid lines) or negatively (dashed lines) at 502 V (cyan) or 144 V (magenta).

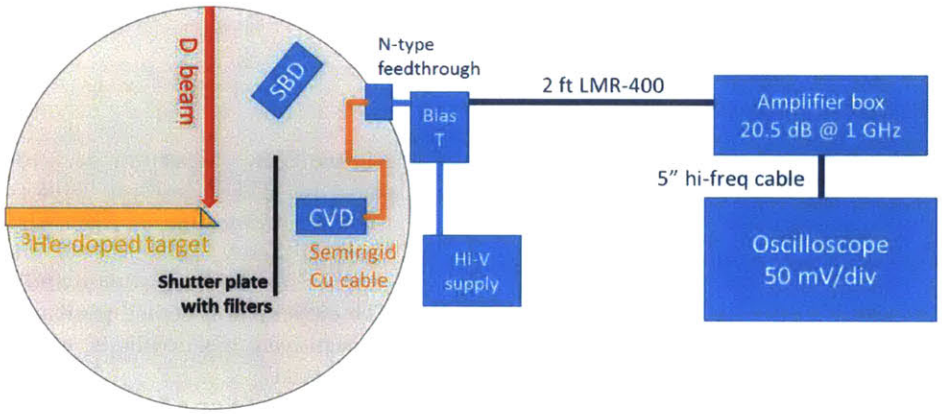

Figure G.5. Schematic of the experimental layout for single-proton counting using the PTOF detector on MIT's Linear Electrostatic Ion Accelerator (LEIA). Inside the target chamber (grey), a deuteron beam (red) is incident on an erbium-deuteride (ErD_2) target doped with ^{3}He (orange), producing 3.0 MeV DD-protons and 14.7 MeV D^{3}He-protons. These particles are ranged through filters fielded on a shutter plate (black) and then detected by the CVD-diamond detector positioned 15 cm from the target. An SBD detector positioned 16 cm from the target records the fusion rate. The detector is connected by a semirigid copper cable to an N-type feedthrough. A bias-T connected to the feedthrough delivers bias voltage from a bias supply to the detector, but transmits high-frequency signals through 2 feet of LMR-400 cable to a custom amplifier box containing a high-frequency amplifier. The amplified signal is transmitted by 5" high-frequency cable to an oscilloscope (Tektronix TDS6604B).

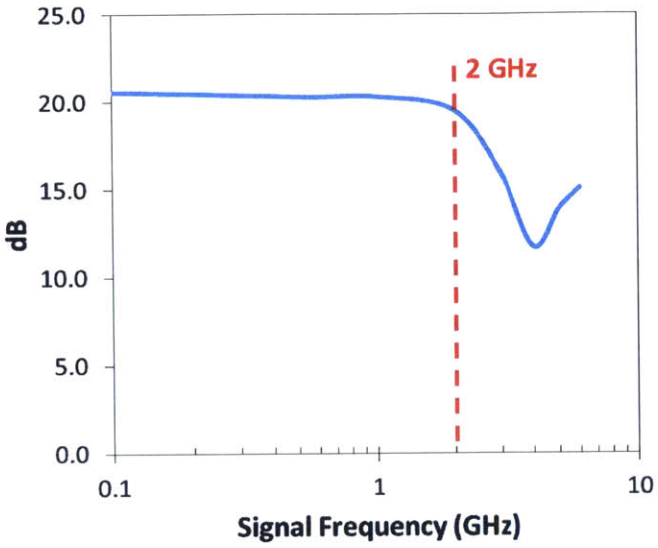

Figure G.6. The amplification as a function of signal frequency for the PTOF circuit (blue). This response curve was measured in situ as installed on the target chamber. Typical PTOF signals have a dominant frequency of approximately 2 GHz (red), for which the signal is amplified by 20 dB.

proton energy on the PTOF detector. An SBD is fielded in the target chamber to measure the DD- and D^3He-fusion rate. The PTOF detector is connected by a vacuum-compatible, semi-rigid copper cable to an N-type vacuum feedthrough. Outside the vacuum chamber, a bias-T supplies bias voltage to the detector while transmitting high-frequency signals to the detection circuit. The signals are amplified by a custom amplifier box, containing either one or two 13.5 GHz bandwidth, 21 dB amplifiers made by Picosecond Pulse Labs (model 5840B),[2] and then are recorded by a 6 GHz Tektronix TDS6604B oscilloscope.[3] The oscilloscope was set to trigger off peaks in the signal, and the trigger value was set at a level that would reject any noise peaks while the accelerator beam was off.

The amplification response of the circuit was measured in situ using a single amplifier, as shown in Figure G.6. The amplification was measured to be extremely flat at 20.5 dB up to approximately 2 GHz, where it drops below 20 dB. Based on impulse responses measured on OMEGA, the PTOF signals are expected to be approximately 1 ns wide, so the dominant frequency (1 GHz) is in the flat region and the expected signal amplification is approximately 20 dB.

The PTOF detector 200A was used in these experiments with a bias of -500 V. When the deuterium beam was on, single-event signals were recorded by the oscilloscope for all filter configurations. The count rate of the PTOF detector relative to the control SBD count rate is shown in Figure G.7 as a function of incident proton energy. The PTOF count rate did not equal the SBD count rate for any incident proton energy. The largest PTOF counting efficiency was 37% for 4.5 MeV protons; higher and lower proton energies resulted in reduced counting efficiency. Since the SBD has been demonstrated to record 100% of incident particles,[4] this result seems to imply that the oscilloscope is only registering a fraction of incident particle events.

For each incident proton energy, the recorded signals had a wide range of amplitudes, as shown in Figure G.8. For the 6 MeV incident protons shown, the mean peak amplitude is around 40 mV, but the distribution has a significant tail with amplitudes above 60 mV. The trigger value for this experiment was 30 mV, which appears to truncate the observed distribution. In combination with the proton observation efficiency being less than 100%, this data suggests that the mean peak amplitude is at or below the trigger value, and only the peaks on the tail of the amplitude distribution are observed and recorded. If this is the case, the observation efficiency contains some

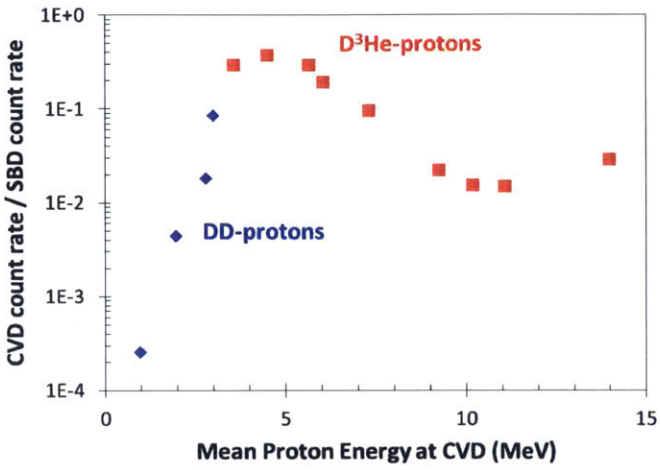

Figure G.7. Ratio of the proton count rate of PTOF detector 200A to the count rate of the SBD detector during accelerator tests as a function of the incident proton energy on the PTOF detector. Count rates are adjusted to account for the difference in CVD and SBD detector solid angle. DD-protons (blue) were ranged down from their birth energy of 3.0 MeV; D^3He-protons (red) were ranged down from 14.7 MeV. The SBD has been demonstrated to record 100% of incident charged particles,[4] so the data can be interpreted as the fraction of incident particles detected. The detection efficiency peaks at 37% for 4.5 MeV protons. Loss of detection efficiency for higher and lower energies may imply that the detection system triggers only for the largest peaks.

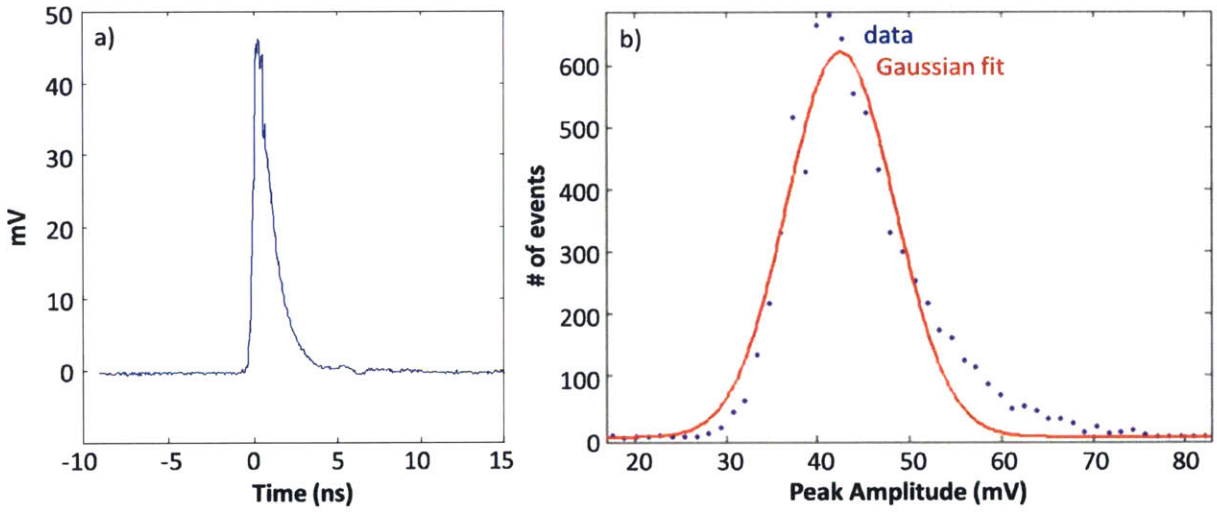

Figure G.8. a) Average of 7383 signal peaks for 6 MeV protons recorded using detector 200A in single-proton counting mode. D^3He-protons were ranged through 966 μm Al to achieve the desired energy. The PTOF detector was biased at -500 V for this experiment. b) Histogram of peak signal amplitude for the 6 MeV proton series (blue) and a Gaussian fit to the data (red). The oscilloscope was set to trigger for signals of 30 mV or larger (reducing the trigger point from this value resulted in many false triggers). The peak distribution appears to be non-Gaussian, suggesting that many events with lower peak amplitudes are not recorded.

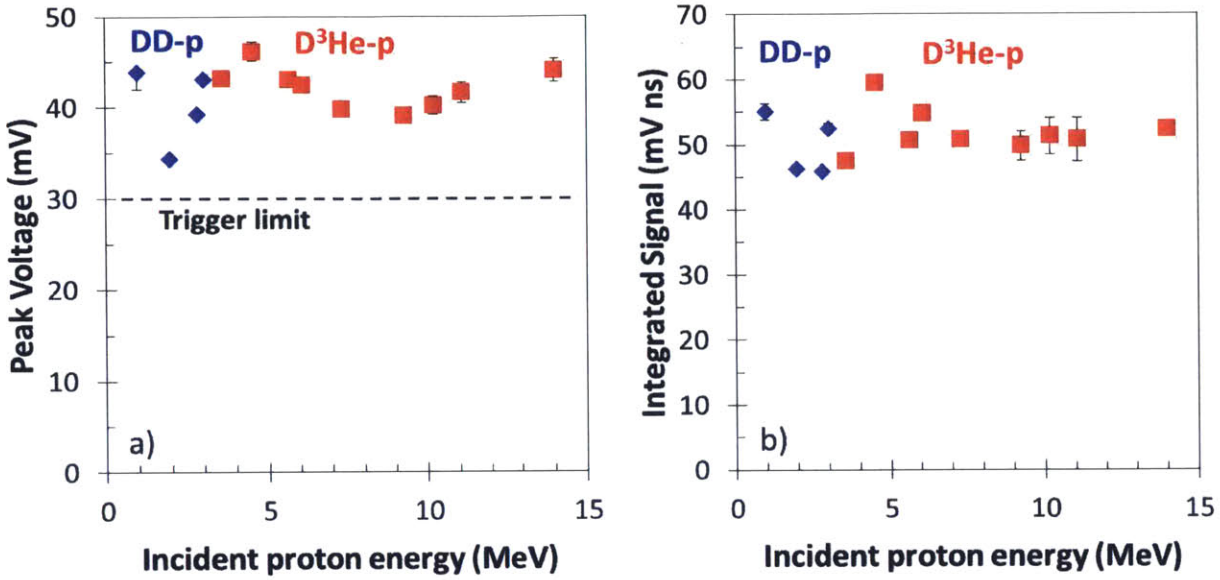

Figure G.9. a) Mean peak amplitude in mV as a function of incident proton energy for PTOF detector 200A in single-proton counting experiments on LEIA. DD-protons (blue) and D^3He-protons (red) were ranged down from their birth energies by aluminum filters. The trigger limit for recording data was 30 mV. The maximum value of 46.6 mV was measured for 4.5 MeV protons. b) Mean integrated signal in mV-ns as a function of incident proton energy. No systematic change in the integrated peak size is observed for different proton energies.

information about the relative sensitivity of the detector to protons: higher mean peak amplitudes will correlate to a greater efficiency of track observation. The data would then indicate that the PTOF detectors are most sensitive to ~ 5 MeV protons. This is slightly lower than the predicted peak sensitivity of 6.9 MeV from Figure 2.13. However broadening of the proton peak as it is ranged down from 14.7 MeV must also be taken into account, since the particles near the peak sensitivity are by definition those most likely to be recorded.

The average peak amplitude was also observed to change with incident proton energy, as shown in Figure G.9. The largest mean peak amplitude was for 4.5 MeV protons, which also had the greatest detection efficiency, providing additional evidence that the detector is most sensitive to protons near this energy. Above and below this energy the mean amplitude was decreased, however in the extremes of low- and high-energy protons, the amplitude appeared to recover. This recovery is likely to be fictitious given the extremely low particle counting efficiencies in those extremes. The detected particles in both the high- and low-energy measurements could be protons with moderate energy produced by large-angle scattering of D^3He-protons within the target chamber. Interestingly, while the peak amplitude appears to change, the integrated signal under the peak appears to be constant with proton energy. This further confirms the idea that only the high-amplitude tail of the peak distribution is being observed.

Taking these data at face value and correcting for the amplification, a sensitivity of approximately 4.5×10^{-4} V ns per incident proton is inferred for this detector. This is a factor of 2–3$\times$ larger than the value inferred for this detector in calibration experiments on OMEGA (1.6–2.2×10^{-4} V ns per proton). The systematically high sensitivity in the accelerator experiments is likely caused by the trigger detecting only the largest signal peaks produced the detector.

A second detector (200B) was also tested using the same procedure; however no signal peaks

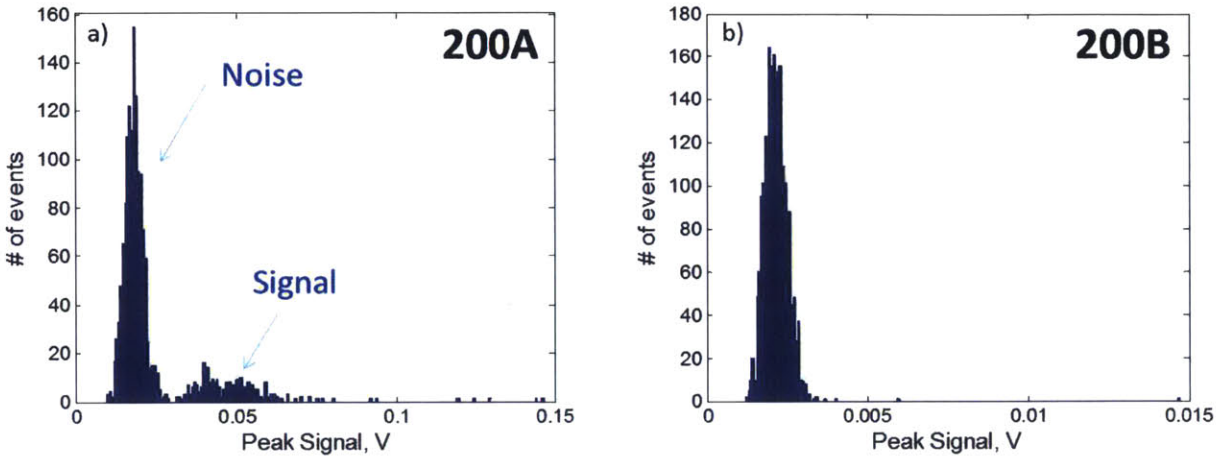

Figure G.10. Histogram of peak signal amplitude recorded during accelerator tests using a) detector 200A and b) detector 200B. The tests with detector 200B used only one amplifier, as the second amplifier was not found to increase the signal to noise ratio. While detector 200A recorded clear signal peaks with amplitudes in excess of 30 mV, detector 200B recorded no clear signal peaks during the experiment.

were observed, as shown in Figure G.10. The bias voltage was +500 V and only one amplifier was used for this test (the second amplifier was found not to improve the signal to noise ratio). In x-ray tests, 200B was approximately 30% less sensitive than 200A; in later experiments at the NIF, 200B was found to be approximately 5× less sensitive to DT-neutrons than 200A. The lack of visible signal peaks for 200B on the accelerator may be due to its lower sensitivity.

Based on these results, it was determined that the sensitivity of the PTOF detectors was not high enough to calibrate the proton sensitivity using single-proton counting methods. Further experiments to calibrate the PTOF detectors were performed using a proton beam from the tandem accelerator at SUNY Geneseo, as described in Section G.3.

G.2 Detector Testing on OMEGA

Implosions on the OMEGA laser have been the primary source of calibrations for the PTOF detectors. PTOF detectors were fielded in ride-along mode on many OMEGA shots to obtain calibrations to DD-neutrons, DT-neutrons, and D^3He-protons at various bias voltages. Neutron producing shots are relatively frequent on OMEGA, and detectors fielded in re-entrant tubes do not impact shot operations, making ride-along experiments an ideal means to acquire data on neutron sensitivity. D^3He-proton calibrations require installing the PTOF detector on a TIM and inserting it into the target chamber, which was done on several occasions.

This section presents the results of several PTOF tests performed on the OMEGA laser. Section G.2.1 discusses typical x-ray backgrounds measured on OMEGA and the correlation between PTOF x-ray signals and the Hard X-ray Detector (HXRD). Section G.2.2 presents the results of DD-neutron, DT-neutron, and D^3He-proton calibrations on OMEGA. Section G.2.3 shows the results of an attempt to increase the PTOF sensitivity to DD-neutrons by including a CH foil in front of the detector to generate knock-on protons. Section G.2.4 presents a failed attempt to measure DD-protons directly with PTOF.

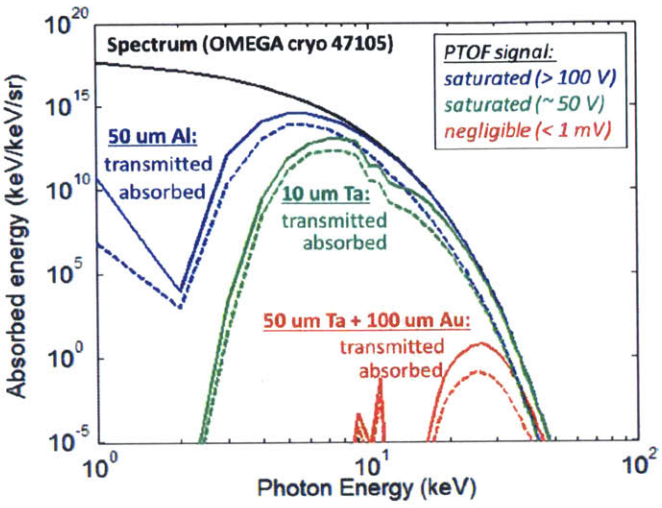

Figure G.11. Spectral intensity model (keV/keV sr) fit to an x-ray spectrum measured on the OMEGA cryogenic direct-drive implosion 47105 (black; see Reference [5]). The anticipated PTOF signal for this spectrum was calculated using three PTOF filters: 50 μm Al (blue), 10 μm Ta (green), and 50 μm Ta + 50 μm Au (red), assuming a 200 μm-thick PTOF detector is biased at −250 V and positioned 50 cm from TCC. The spectral intensity transmitted through PTOF filtering (solid) and photoabsorbed by the detector (dashed) are shown. With 50 μm Al filtering, the PTOF signal is expected to be deeply saturated (> 100 V), and with 10 μm Ta filtering, the signal is expected to be moderately saturated (∼ 50 V). In contrast, with 50 μm Ta + 100 μm Au filtering the signal is expected to be negligible (< 1 mV).

G.2.1 X-ray backgrounds on OMEGA

The x-ray background on OMEGA is generally lower than that on NIF, which alleviates some of the filtering requirements for the PTOF detectors. Figure G.11 shows an x-ray spectrum measured on the cryogenic direct-drive implosion 47105. This x-ray spectrum was processed to evaluate the predicted PTOF x-ray signal had a 200 μm detector been fielded on that shot. The predicted signal for the standard PTOF filtering (50 μm Ta + 100 μm Au) is negligible, while the predicted signal for very thin filtering (50 μm Al and 10 μm Ta) is saturated. Based on this example, x-ray filtering is necessary for shots on OMEGA, but there is more flexibility than for PTOF operations on the NIF. Note that 10 μm Ta will range DD-protons down to 2 MeV; based on this calculation, it is unlikely PTOF can be used to measure DD-protons directly on OMEGA.

The Hard X-ray Detector (HXRD) system is a facility diagnostic on the OMEGA laser that provides information about the high-energy x-ray spectrum. The HXRD has four channels, which have lower-energy cutoffs for x-ray detection of 20, 40, 60, and 80 keV.[6] Both PTOF and HXRD were fielded on the OMEGA indirect-drive implosions performed on May 7th, 2013, which were described in Appendix E.[b] The integrated signal from the PTOF detector on this shot day is compared to the integrated signals from the HXRD channels in Figure G.12.[c] All of the HXRD channels scale linearly with the PTOF x-ray signal on this shot day. However, only HXRD channel 4 appears to have an intercept at 0. If the spectral shape is fixed and only the intensity is varying, a linear scaling with an intercept of 0 would be expected for all channels. Therefore, the data suggest that the high-energy x-ray spectrum also varies from shot to shot, and that the heavily-filtered PTOF is most similar to HXRD channel 4 in spectral response.

G.2.2 DD-neutron, DT-neutron and D^3He-proton calibrations

Between 2010 and 2012, the response of thirteen PTOF detectors to fusion products was characterized using OMEGA capsule implosions as a particle source. The results of successful calibrations

[b]The notation "OmYYMMDD" is used as a searchable shorthand for the OMEGA shot day (e.g. May 7th, 2013 = Om130507).

[c]The PTOF integrated signal, which is typically reported in units of V ns, was converted into picocoulombs for this comparison by dividing out the 50 Ω termination resistance of the oscilloscope and multiplying by 1000.

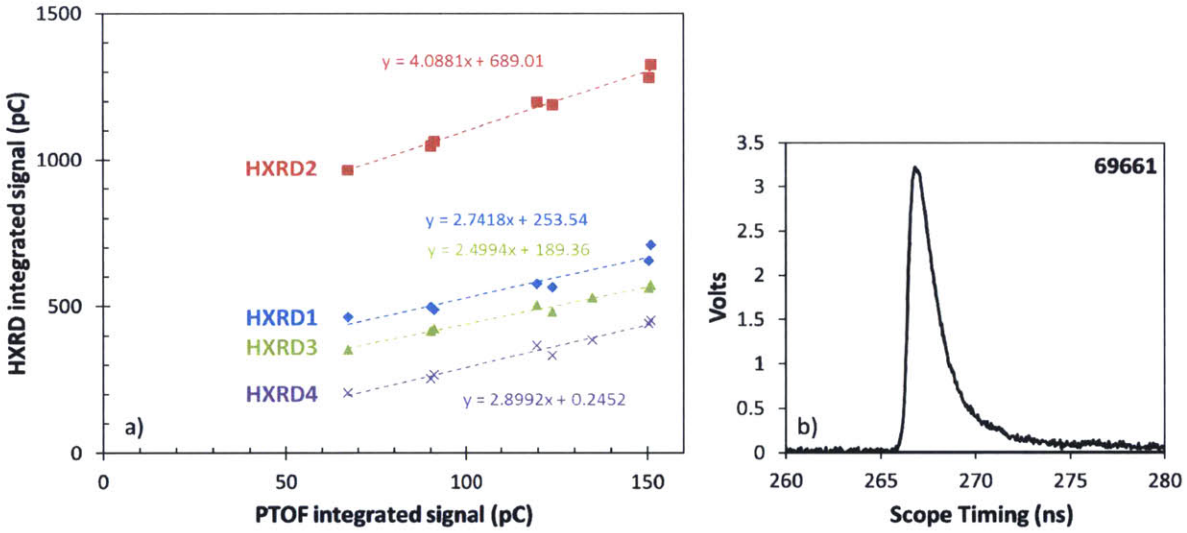

Figure G.12. a) Integrated signal for the four Hard X-ray Detector (HXRD) channels compared to integrated PTOF x-ray signal recorded on OMEGA indirect-drive implosions on May 7th, 2013 (Om130507). The PTOF detector 200T was fielded with filtering of 20 μm Ta + 178 μm U + 25 μm Au, biased at -1500 V and positioned 20 cm from TCC. HXRD channels 1 (blue), 2 (red), 3 (green) and 4 (purple) observe x-rays above 20, 40, 60, and 80 keV, respectively. Note that HXRD channel 1 uses a less sensitive scintillator than the other channels; for more information, see Reference [6]. Linear fits to the data are shown (dashed lines and formulas). Only the highest-energy channel has an intercept consistent with 0, suggesting that the PTOF is most sensitive to x-rays above 80 keV. b) Example PTOF trace recorded on shot 69661.

Table G.1. Sensitivity calibration values to DD-neutrons for PTOF detectors, recorded on OMEGA implosions. For a given detector and bias voltage, calibration values are averaged over multiple shots on a single shot day. Uncertainties are the standard deviation of the values in a given calibration series. The LLE-style PTOF housing was used instead of the standard ("NIF-style") housing where noted. Asterisks indicate detectors in active use on the NIF.

Detector	Shot Day	Bias (V)	Sensitivity (V ns/DD-n)	±	LLE Housing?
10x1000	Om100819	500	4.01E-07	5.33E-08	X
5x250	Om100819	500	3.16E-07	1.33E-07	X
1000A	Om110927	-1500	2.30E-07	5.45E-09	
"	Om111025	-1500	3.24E-07	6.44E-09	
1000B	Om110927	-1500	8.79E-07	3.36E-08	
1000C	Om110927	-1500	1.81E-07		
	Om111025	-1500	3.06E-07	1.86E-08	
100A	Om101102	-500	5.55E-08		X
100E	Om110524-26	-500	9.91E-08	1.62E-08	
200A	Om101102	-500	1.03E-07		X
200G	Om110524-26	-250	4.36E-09	2.30E-09	
"	"	-500	3.69E-08	1.76E-08	
"	"	-1500	9.66E-08	2.29E-08	
200M*	Om110524-26	-250	2.27E-08	6.27E-11	
"	"	-500	3.81E-08	2.37E-09	
200S	Om111025	-250	1.99E-08	1.01E-09	
"	Om110927	-1500	4.62E-08	2.99E-09	
200U	Om111025	-250	3.03E-08	1.79E-09	

Table G.2. Sensitivity calibration values to DT-neutrons for PTOF detectors, recorded on OMEGA implosions. For a given detector and bias voltage, calibration values are averaged over multiple shots on a single shot day. Uncertainties are the standard deviation in a given calibration series. Asterisks indicate detectors in active use on the NIF.

Detector	Shot Day	Bias (V)	Sensitivity (V ns/DT-n)	±
1000A	Om111019	-1500	6.90E-07	1.24E-07
1000C	Om111019	-1500	5.15E-07	1.94E-07
100E	Om110524-26	-500	3.92E-07	4.82E-08
200G	Om110524-26	-1500	3.34E-07	1.01E-08
200M*	Om110524-26	-250	2.39E-08	
"	"	-500	5.36E-08	2.46E-08
200S	Om111019	-1500	8.30E-09	1.92E-09†

† Two outlier points (100–1000× larger) not included.

using DD-neutrons are shown in Table G.1; calibration results using DT-neutrons are shown in Table G.2; and calibration results using D^3He-protons are shown in Table G.3. The PTOF experimental design, setup, operation, and data analysis was performed by M. Gatu Johnson for shots on May 24–26, September 1, September 27, October 19 and October 25 of 2011. Sensitivity values are reported in units of V ns per incident fusion particle. Frequently, multiple calibration shots were performed on a single day with the detector biased at a fixed voltage. In these cases, the average sensitivity recorded on this set of calibration shots is reported along with the standard deviation of the observed sensitivities. In the case of D^3He-proton calibrations, the x-ray filtering and the resulting incident proton energy on the detector is reported as well. If no minimum to maximum variation is reported, only a single calibration shot was performed.

The scaling of detector sensitivity with bias voltage for three, 200 μm and one 1000 μm detector are shown in Figure G.13. Generally, the sensitivity increases with bias voltage; however the rate of increase differs. Detector 200G showed a more rapid increase in DD-neutron sensitivity with bias voltage ($\sim V^{1.7}$) than the other 200 μm detectors ($\sim V^{0.5--0.8}$); however 200G also demonstrated large variability in sensitivity on a single shot day. For the proton sensitivity, the 1000 μm detector shows a more rapid increase with bias voltage ($\sim V^{1.1}$) than the 200 μm detector ($\sim V^{0.34}$). This may indicate that the 1500 V bias is beginning to sweep out all the charges produced in the 200 μm detector, but not in the 1000 μm detector.

The DT-neutron calibrations recorded on October 19, 2011 are notable because the detector 1000A was driven strongly into the regime of non-linear response. The detector sensitivity was observed to decrease during the shot day, as shown in Figure G.14a). This decrease appears to occur over the course of five shots on which the detector was driven into the non-linear regime of operation ("saturation"). As discussed in Chapter 2, the detector response becomes nonlinear when the peak voltage is greater than 10% of the bias voltage. While the sensitivity on the saturated shots was slightly reduced from the sensitivity at the beginning of the shot day, the peak voltage per neutron on the saturated shots was dramatically reduced, as shown in Figure G.14b). This is due to distortion of the impulse response function as the detector is driven into the non-linear regime, as shown in Figure G.15. When the signal voltage is greater than 10% of the bias voltage, the effective bias in the diamond is reduced as the charge is swept out, which in turn reduces the rate at which charge is extracted from the diamond. Interestingly, the sensitivity data suggest that

Table G.3. Sensitivity calibration values to D^3He-protons for PTOF detectors, recorded on OMEGA implosions. For a given detector, bias voltage, and filtering, calibration values are averaged over multiple shots on a single shot day. The proton energy incident on the detector (E_{proton}) is calculated from proton spectra recorded on the shot day using SRIM. Uncertainties are the standard deviation in a given calibration series. The LLE-style PTOF housing was used instead of the standard ("NIF-style") housing where noted.

Detector	Shot Day	Bias (V)	Filtering (μm)	E_{proton} (MeV)	Sensitivity (V ns/D^3He-p)	±	LLE Housing?
10x1000	Om100610	500	100Al+100Ta	12.1	1.47E-04	2.17E-05	X
"	"	"	100Al+200Ta	9.2	2.27E-04		X
"	"	1500	100Al+100Ta	12.1	5.12E-04	5.37E-06	X
"	Om100819	500	100Al+100Ta	11.1	1.72E-04	2.10E-05	X
5x250	Om100819	500	100Al+100Ta	11.1	4.79E-04	7.07E-06	X
100A	Om101102	-500	100Al+100Ta	11.1	1.18E-04	3.97E-05	X
200A	Om101102	-500	100Al+100Ta	11.1	2.24E-04	1.80E-05	X
"	"	"	100Al+200Ta	7.9	1.59E-04		X
200S	Om120110	-250	50Ta+200Au	6.6	5.13E-05	9.76E-06	
"	"	"	50Ta+250Au	4.0	7.27E-05	1.69E-05	
"	"	-500	50Ta+200Au	6.6	9.18E-05		
"	"	"	50Ta+250Au	4.0	8.55E-05	1.91E-05	
"	"	-1500	50Ta+250Au	4.0	1.32E-04	9.33E-06	
200T	Om110901	-1500	50Ta+100Au	11.0	1.61E-04	2.20E-05	

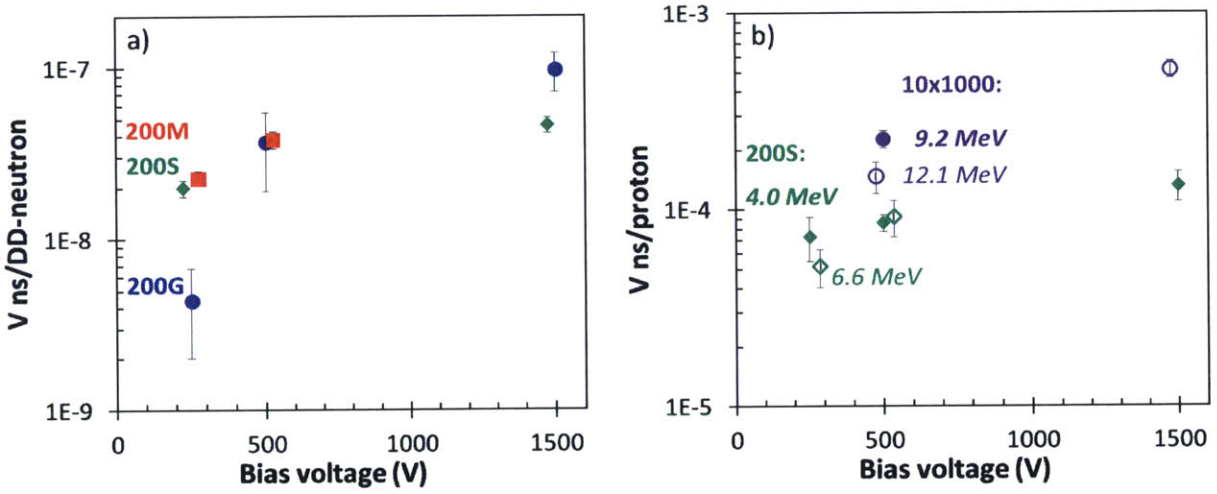

Figure G.13. Measured sensitivity of PTOF detectors 200M (red), 200S (green), 200G (blue) and 10x1000 (purple) to a) DD-neutrons and b) D^3He-protons as the bias voltage is changed. Negative biases were used for all detectors except for 10x1000, which was biased positively. Error bars show the RMS sum of the measured shot-to-shot standard deviation and a generic 10% yield uncertainty. In b), solid and hollow symbols indicate the incident proton energy: 4.0 and 6.6 MeV respectively for 200S; 9.2 and 12.1 MeV respectively for 10x1000. The sensitivity increases with the bias voltage, although the rate of increase differs from detector to detector.

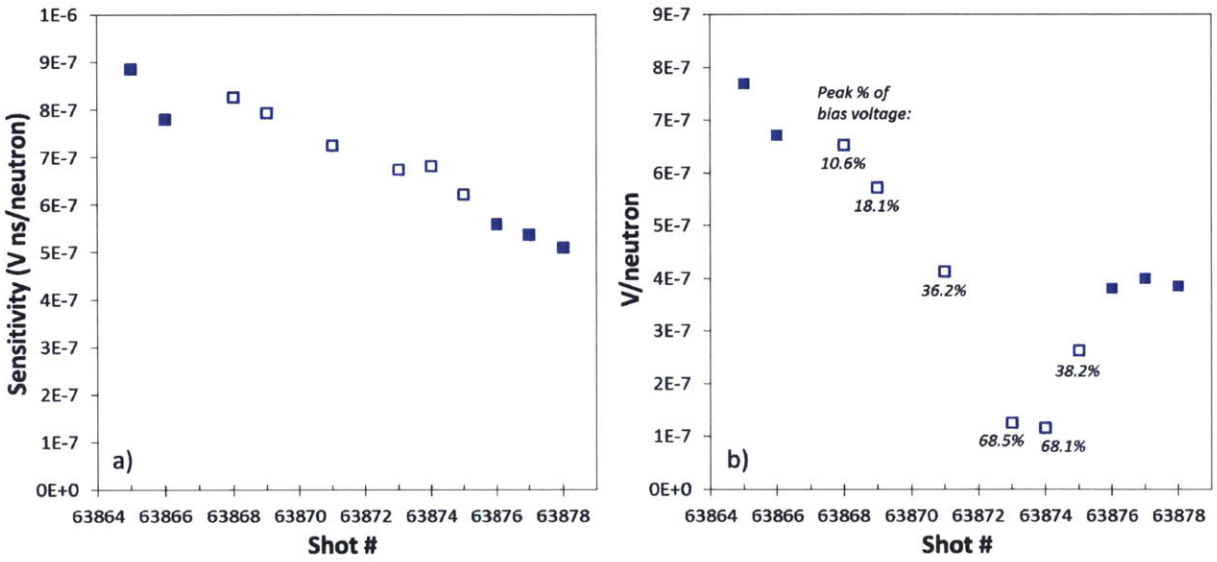

Figure G.14. a) Sensitivity of detector 1000A to DT-neutrons (blue squares) recorded on OMEGA implosions on October 19, 2011 (Om111019). The PTOF detector was biased to -1500 V for these calibrations, and the neutron fluence on the detector was controlled by varying the detector distance to TCC. Closed (open) squares indicate the peak signal was less (greater) than 10% of the bias voltage. The sensitivity decreased approximately linearly during the shot day, primarily over the course of five shots for which the peak voltage exceeded 10% of the bias voltage. b) Peak voltage of the recorded signal divided by the DT-neutron fluence on the detector. The peak percentage of the bias voltage is labelled for the high peak-voltage shots: the voltage per neutron is notably reduced for these experiments.

Figure G.15. Signal traces recorded using the 1000A detector on October 19, 2011 (Om111019), normalized to their peak value and aligned by the time of 20% peak rise. Signals from the start of the shot day with a peak voltage less than 10% of the bias voltage ($V/B = 10\%$, blue) are comparable but slightly narrower than signals with V/B in the range 10%–20% (green). Signals with $V/B \sim 35\%$ (purple) are clearly wider than the baseline signals, while signals with V/B above 60% (red) are several times wider. Signals from the end of the shot day with $V/B < 10\%$ (black) remain slightly wider than was observed at the beginning of the shot day. The shape of the impulse response function varies significantly in the nonlinear regime, and does not appear to return to the baseline value afterward.

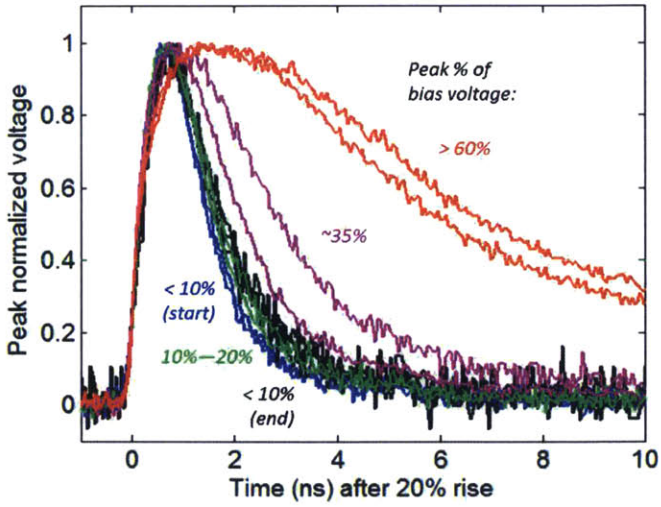

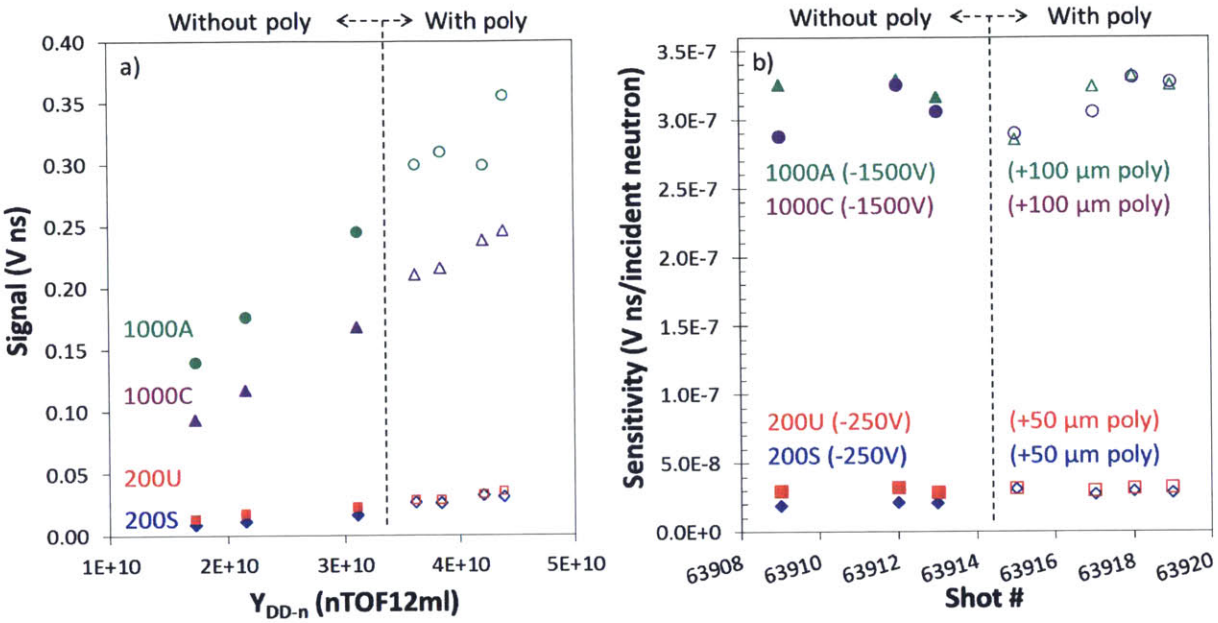

Figure G.16. a) Measured integrated signal (V ns) versus DD-neutron yield for four PTOF detectors fielded on OMEGA calibration implosions on October 25, 2011 (Om111025). The detectors were fielded with a layer of polyethylene (CH) on four shots (open symbols) to act as a signal multiplier for the DD-neutrons by (n,p) knock-on reactions. Two, 200 μm thick detectors, 200S (blue) and 200U (red), were fielded at -250 V and were tested with 50 μm poly; two, 1000 μm thick detectors, 1000A (green) and 1000C (purple), were fielded at -1500 V and were tested with 100 μm poly. b) DD-neutron sensitivity of the PTOF detectors inferred from the measured signals. No clear enhancement of the PTOF sensitivity was observed with the added poly filter.

the charge extracted per neutron is the same in non-linear and in linear operation, although the extraction occurs on a longer timescale in the non-linear case.

At the end of the shot day, the detector was again operated in the linear regime. The sensitivity did not fully recover to its initial value. Moreover, the IRF in the linear regime was wider at the end of the shot day than in the initial shots. This result suggests that the PTOF detectors have some 'memory' of non-linear excursions. These experiments all occurred on a single day of continuous operation: followup experiments are necessary to determine whether the changes to the IRF are permanent, if they fade over time, or if they can be reset.

G.2.3 Test with DD-neutron knock-on signal multiplier

An experiment was performed to determine whether the DD-neutron sensitivity of the PTOF detectors could be increased by including a thin polyethylene (CH) foil in front of the CVD-diamond disk. Some fraction of the DD-neutrons scatter protons out of the polyethylene foil; these protons then deposit all their energy in the PTOF detector. In principle, this technique would enhance the energy transferred from DD-neutrons into the PTOF detector.

Four PTOF detectors were fielded on OMEGA in ride-along mode on DD-neutron producing shots performed on October 25, 2011. Two, 200 μm thick detectors (200S and 200U) were fielded at -250 V; two, 1000 μm thick detectors (1000A and 1000C) were fielded at -1500 V. These detectors were fielded on three shots without poly to establish a baseline sensitivity. Afterward, 50 μm poly was inserted in front of the 200 μm detectors and 100 μm poly was inserted in front of the 1000 μm

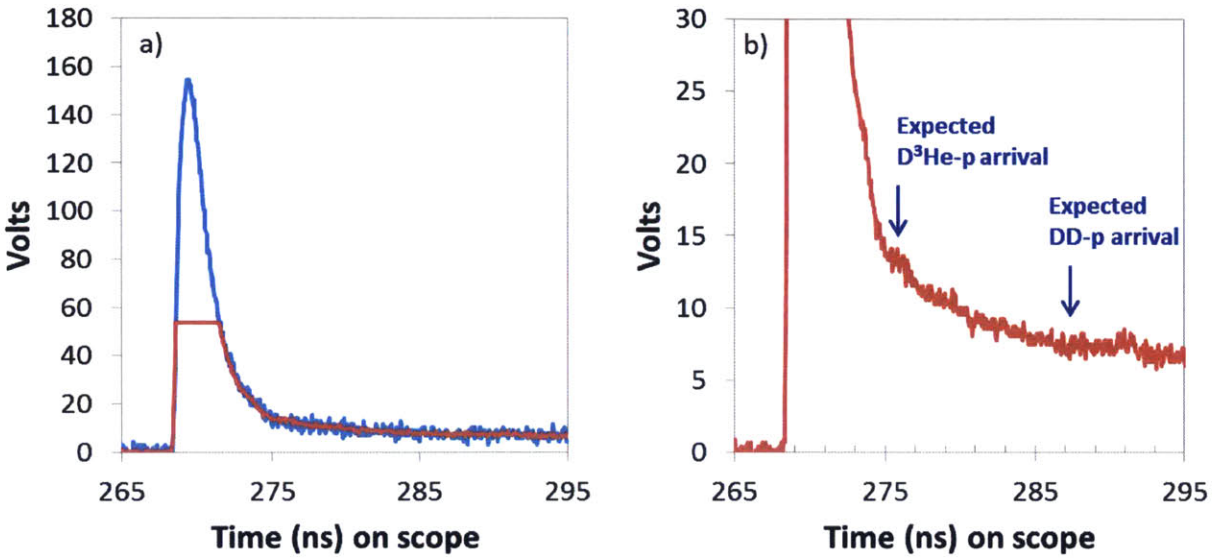

Figure G.17. PTOF trace recorded on OMEGA shock-driven D^3He-gas filled implosion 64609 (Om120110) in an attempt to measure DD-protons directly. The PTOF detector 200S was fielded with 50 μm Al, biased at -250 V and positioned 50 cm from TCC. a) An x-ray signal with a peak voltage of 155 V is observed (blue); one of the two scope channels is overvolted (red). The x-rays have driven the detector strongly into the non-linear regime. b) A zoom-in on the tail of the signal. The expected arrival time of D^3He-protons and DD-protons are indicated. While a small D^3He-proton signal may be observed, no clear DD-proton signal is seen.

detectors, and all detectors were fielded on four more experiments. The resulting data are shown in Figure G.16. The baseline sensitivity of the detectors to DD-neutrons was comparable to previous calibrations: 2.0×10^8 and 3.0×10^8 V ns per incident neutron for 200S and 200U, respectively; 3.2×10^7 and 3.1×10^7 V ns per incident neutron for 1000A and 1000C, respectively. Including the neutron signal multiplier did not systematically increase the recorded sensitivity. The sensitivities of 200U, 1000A, and 1000C with the poly were each within 5% of the baseline sensitivity value. The sensitivity of 200S appeared to increase by $\sim 44\%$ with the poly; however this detector showed oscillations in sensitivity when fielded on DT shots performed on October 19, 2011, and may not be trustworthy.

In summary, the inclusion of polyethylene in the PTOF housing as an enhancer for DD-neutron signals was evaluated and appears not to be worthwhile.

G.2.4 Attempts to measure DD-protons on OMEGA

On Jan 10, 2012, PTOF detector 200S was fielded on two shots in an attempt to directly measure DD-protons. The detector was filtered with 50 μm Al, biased at -250 V, and initially positioned at 20 cm from TCC. DD-proton yields of approximately 5×10^8 were produced on these experiments, which would be expected to produce a signal on the order of 1 V, if the proton sensitivity is assumed to be comparable to those observed for higher proton energies.

On the first experiment (64608), the oscilloscope was overvolted by a large x-ray peak, and no usable data was obtained. For the second experiment (64609), the scope attenuation was increased by an order of magnitude and the detector was retracted to 50 cm from TCC. The signal trace recorded on this experiment is shown in Figure G.17. An x-ray signal with a peak of 155 V is

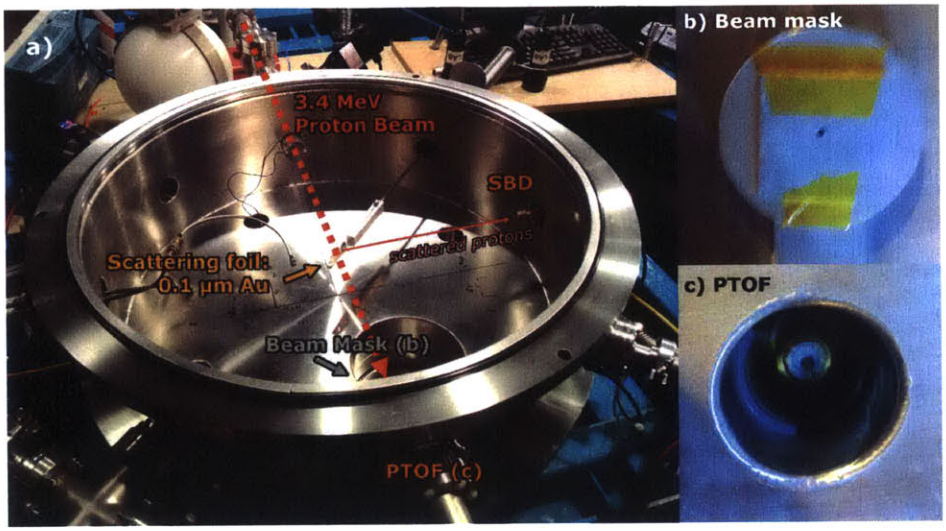

Figure G.18. a) The SUNY Geneseo Tandem Accelerator target chamber as configured for proton sensitivity calibration of a PTOF detector. The 3.4 MeV proton beam passes through an 0.1 μm gold foil, which scatters protons onto an SBD positioned at 90° to the beam trajectory with a probability of approximately 1.15×10^{-9}. The remainder of the beam strikes b) a beam mask, which limits the area of the beam incident on c) the PTOF detector, which is fielded in the beam dump. A piece of radiochromic film fielded in the PTOF detector shows the position of the proton beam on the detector.

observed, clipping one of the two scope channels on which the data was recorded. The PTOF was driven deeply into the regime of non-linear response by the x-ray peak. On the tail of the x-ray peak, a small D^3He-proton signal is possibly observed; however no peak is evident where the DD-proton signal is expected.

Based on this result, the attempt to measure DD-protons was abandoned. The small amount of x-ray filtering necessary for 3 MeV protons to reach the PTOF detector does not sufficiently block the x-ray spectrum, even on a directly-driven implosion. Filtering with higher Z, for example 10 μm Ta, will reject a greater portion of the x-ray spectrum while still transmitting the protons. However it is likely that the x-ray rejection must be improved by 2–3 orders of magnitude for the background to be small enough that DD-proton signals are observed. Given the marginal utility of the DD-proton measurement, as the DD-neutrons are much more readily detected and provide inherently higher precision for bang-time measurements, future attempts to detect DD-protons using PTOF are not recommended.

G.3 Detector Testing at the SUNY Geneseo Accelerator

Experiments were performed using the SUNY Geneseo Tandem Accelerator to calibrate the PTOF response to protons in current mode. The tandem accelerator at SUNY Geneseo is a National Electrostatics Corporation Model 5SDH 1.7 MV tandem Pelletron accelerator operated by the lab of Dr. Charles Freeman.[7] The experimental design for these calibrations is shown in Figure G.18. A beam of 3.4 MeV protons with a beam current on the order of 1 nA was produced by the accelerator and injected into the target chamber. The beam passed through a gold scattering foil with a thickness of 0.1 μm positioned at TCC, which both spread out the beam and scattered a small fraction ($\sim 1.15 \times 10^{-9}$) of the protons onto an SBD positioned at 90° relative to the beam trajectory. The proton beam was collimated by a beam mask, which was positioned to transmit a

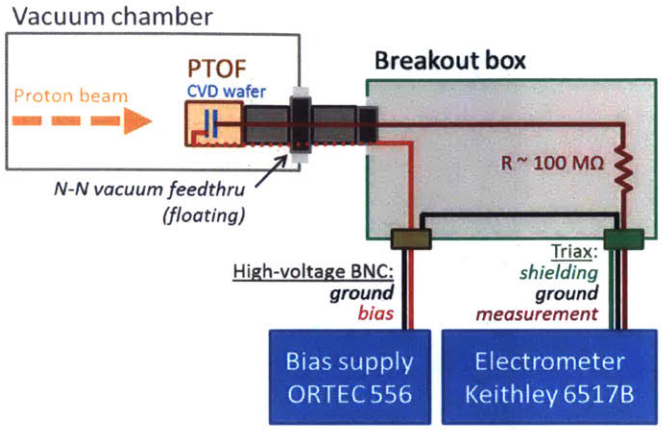

Figure G.19. Circuit used for the calibration of PTOF detectors to protons on the SUNY Geneseo accelerator. The PTOF detector is held in the vacuum chamber attached to a floating N-N vacuum feedthrough. A positive bias voltage (red) is supplied to the outside of the PTOF detector by an ORTEC model 556 bias supply; note that a positive bias supplied to the detector housing is equivalent to a negative bias supplied to the rear surface of the CVD diamond, which is the standard mode for NIF operation. A proton beam generates a current through the PTOF detector, which is integrated using a Keithley 6517B electrometer (dark red). A 100 MΩ resistor protects the electrometer input from breakdown in the detector. The electrometer ground (black) is connected to the bias supply ground (black) to provide the baseline for the charge integration. The shielding on the electrometer (green) is connected to the outside of the breakout box to reduce noise.

circular beam onto the active area of a PTOF detector positioned in the beam dump. The spot was measured using radiochromic film to have a diameter of 4.5 mm in the detector plane. A Faraday cup measured the beam current transmitted through the beam mask to be 0.222 ± 0.003 nA. This measurement was used to calibrate the ratio of the charge transmitted through the beam mask to the number of counts detected by the SBD, which was found to be 0.0106 counts/nC.

During PTOF calibration runs, the SBD was used as an on-shot reference for the number of protons incident on the PTOF. Aluminum filters with a thickness of 80 and 50 μm were inserted into the front of the PTOF detector to range the 3.4 MeV proton beam down to 1.2 MeV and 2.2 MeV, respectively, before hitting the detector itself.

The electronics used to read the PTOF current are shown in Figure G.19. The detector is held in the target chamber attached to an N-type to N-type floating vacuum feedthrough, and the outer conductor of the detector is biased to high voltage by an ORTEC model 556 bias supply. The proton beam generates current through the PTOF, which is integrated using a Keithley model 6517B electrometer. The electrometer ground is referenced to the bias supply ground. The electrometer also includes a shielding circuit in a triaxial configuration, which was connected to the shielding of the breakout box.

A 1000 μm-thick PTOF detector (1000B) was used in this experiment. The detector was tested with a positive bias of 100, 250, 500, 750, and 1000 V. When biased, the detector was found to produce a leakage current. The leakage current as a function of bias voltage is shown in Figure G.20. The leakage current appears to scale approximately exponentially with the bias voltage in this regime. For each calibration shot, the leakage current was measured both before the accelerator beam was turned on and after it was turned off. The expected charge due to the leakage current was then subtracted from the collected PTOF charge while the proton beam was on to evaluate the amount of charge produced by the proton beam.

The PTOF data recorded using this experimental setup is shown in Figure G.21. The sensitivity of the detector was 2–5× larger for the 3.4 MeV protons compared to the 1.2 and 2.2 MeV protons, depending on the bias voltage. The detector sensitivity was comparable to the 1.2 and 2.2 MeV protons, and was slightly ($\sim 10\%$) larger for the 1.2 MeV compared to the 2.2 MeV protons. The

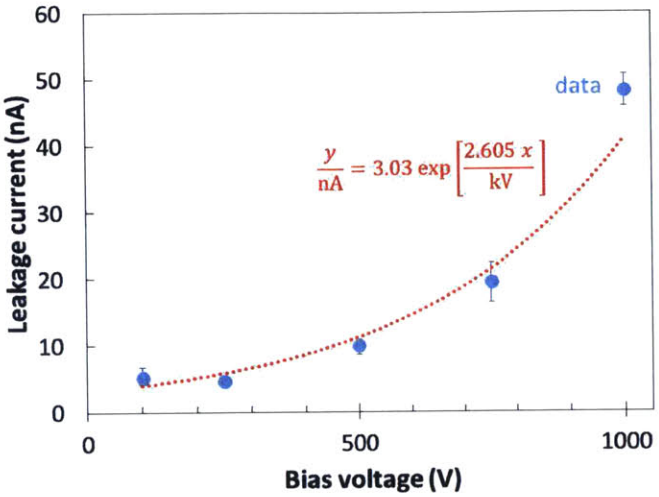

Figure G.20. Measured leakage current for a 1000 μm-thick PTOF detector (1000B) as a function of bias voltage. Points (blue) are the average of two or three measurements; error bars indicate minimum-to-maximum region. An exponential model (red) provides a reasonable fit to the data; the best-fit equation is shown.

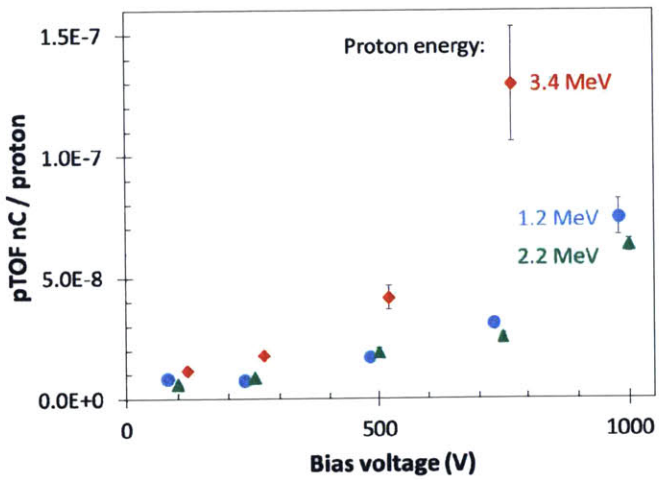

Figure G.21. Sensitivity (nC/proton) of the PTOF detector 1000B as a function of incident proton energy and bias voltage as measured on accelerator experiments performed at SUNY Geneseo. The bias voltage was varied from 100 V to 1000 V, and the detector was driven with 3.4 MeV (red), 2.2 MeV (green) and 1.2 MeV (blue) protons. The beam energy was 3.4 MeV for all experiments, and the proton energy was reduced using aluminum ranging filters. The measured leakage currents shown in Figure G.20 were accounted for in calculating the sensitivity values.

PTOF detector sensitivity appeared to increase exponentially with bias voltage: for the 3.4 MeV protons, the e-folding constant of the best fit was approximately 270 V.

The PTOF sensitivity to 3.4 MeV protons recorded using 500 V bias voltage was $(4.2 \pm 0.5) \times 10^{-8}$ nC/proton. For comparison to other calibrations, this value is equivalent to $(2.1 \pm 0.2) \times 10^{-6}$ V ns/proton.[d] This value is low compared to the proton sensitivities measured in OMEGA calibrations as shown in Section G.2.2. For example, a 1000 μm detector biased with 500 V was measured to have a sensitivity of 2.3×10^{-4} V ns per 8.2 MeV proton and 1.5×10^{-4} V ns per 11.4 MeV proton. As no implosion calibrations were performed using lower-energy protons, it is possible that all of these values are accurate. The fact that the detector is not observably more sensitive to 2.2 MeV protons than 1.2 MeV protons suggests that there is a sensitivity cutoff for protons below a certain energy. In this case, the observed signals for the low-energy protons may be due to pickup or some other background when the beam is on. In additional experiments, this should be tested directly by performing a null test in which the detector is shielded with a filter sufficiently thick to stop the proton beam. It is recommended that these experiments should be continued using a 200 μm PTOF detector, which would be better matched to the range of a 3.4 MeV proton in diamond ($\sim$ 60 μm). Such an experiment would provide a connection with both the single-proton counting data presented in Section G.1.2 and the standard PTOF detectors in use on the NIF.

G.4 References

1. J. Rojas-Herrera, H. G. Rinderknecht, A. B. Zylstra *et al.*, "Impact of x-ray dose on the response of CR-39 to 1-5.5 MeV alphas," Review of Scientific Instruments (submitted).
2. Picosecond Pulse Labs, see `http://www.picosecond.com/`.
3. Tektronix, see `http://www.tek.com/`.
4. N. Sinenian, M. J.-E. Manuel, A. B. Zylstra *et al.*, "Upgrade of the MIT Linear Electrostatic Ion Accelerator (LEIA) for nuclear diagnostics development for Omega, Z and the NIF," Review of Scientific Instruments, **83**(4), 043502 (2012).
5. F. Marshall, J. P. Knauer, T. C. Sangster *et al.*, "X-Ray Spectral Measurements of Cryogenic Capsules Imploded by OMEGA," Bulletin of the American Physical Society (2007).
6. C. Stoeckl, V. Y. Glebov, D. D. Meyerhofer *et al.*, "Hard x-ray detectors for OMEGA and NIF," Review of Scientific Instruments, **72**(1), 1197 (2001).
7. State University of New York Geneseo, Department of Physics and Astronomy, see `http://www.geneseo.edu/physics/nuclear`.

[d]The termination of the oscilloscope in PTOF measurements is 50 Ω. Thus, a typical sensitivity measured in (V ns)/proton actually represents a charge sensitivity measured in nC/proton multiplied by 50Ω.